DISSERTATION ZUR ERLANGUNG DES
NATURWISSENSCHAFTLICHEN DOKTORGRADES

# Background and sensitivity studies for the DARWIN low-background observatory


vorgelegt von

**Julia Dierle**




FAKULTÄT FÜR MATHEMATIK UND PHYSIK
ALBERT-LUDWIGS-UNIVERSITÄT FREIBURG

# Background and sensitivity studies for the DARWIN low-background observatory

Dissertation

zur Erlangung des Doktorgrades der
Fakultät der Mathematik und Physik der
Albert-Ludwigs-Universität
Freiburg im Breisgau

vorgelegt von
Julia Dierle

Februar 2022

| | |
|---|---|
| Betreuer der Arbeit: | Prof. Dr. Marc Schumann |
| Dekan der Fakultät: | Prof. Dr. Michael Thoss |
| Koreferent: | apl. Prof. Dr. Ulrich Landgraf |
| Prüfer: | Prof. Dr. Gregor Herten |
| | Prof. Dr. Joachim Dzubiella |
| Datum der Disputation: | 04.05.2022 |

## Abstract

Numerous astrophysical and cosmological observations indicate that the majority of the matter in the Universe is dark, i.e., does not interact electromagnetically nor strongly. One of the most promising dark matter candidates is the weakly interacting massive particle (WIMP). The DARWIN experiment, a proposed next-generation dark matter detector, aims to detect WIMPs directly by employing a dual-phase liquid xenon time projection chamber (TPC). DARWIN will have an unprecedented sensitivity for spin-independent WIMP-nucleon scattering cross-sections down to $\sim 10^{-49}\,\mathrm{cm}^2$ and will further explore the experimentally accessible parameter space for WIMP masses $> 5\,\mathrm{GeV}/c^2$. With its 40 t liquid xenon target, low-energy threshold, and ultra-low background, DARWIN will provide an environment, which is also suited for various other rare event searches.

The first part of this work is dedicated to the investigation of several science channels of DARWIN. Its sensitivities to the hypothetical lepton number violating processes neutrinoless double beta decay ($0\nu\beta\beta$) of $^{136}$Xe and neutrinoless double electron capture ($0\nu$ECEC) of $^{124}$Xe are reported. While for the former decay, DARWIN will yield a sensitivity limit of $T^{0\nu}_{1/2} > 2.4 \cdot 10^{27}\,\mathrm{yr}$ (90% C.L.) and could give important insights into the possible Majorana nature of neutrinos and their absolute mass scale, the sensitivity to the $0\nu$ECEC will be limited by the low natural abundance of $^{124}$Xe. DARWIN's ability to detect solar neutrinos by elastic $\nu$-electron scatterings is also presented, which can be used to estimate the electroweak mixing angle and neutrino oscillation parameters in a previously non-measured energy range of $< 200\,\mathrm{keV}$. Furthermore, material-induced radiogenic and muon-induced cosmogenic backgrounds relevant for the WIMP search are investigated, indicating that the cryostat, photosensors, and polytetrafluoroethylene (PTFE) are the most problematic sources. This yields important input for the design and construction of the future DARWIN detector.

The dominant radiogenic background producing electronic recoil signals in the search for WIMPs is $^{222}$Rn with the subsequent decays of its progenies. In the second experimental part of this work, the concept of a hermetic TPC is studied. It reduces the $^{222}$Rn-releasing material surfaces in contact with the xenon target and thus provides a possibility for $^{222}$Rn mitigation. The small-scale hermetic TPC prototype HUsXe was designed, commissioned, and operated in the Freiburg Astroparticle Physics laboratory. Its characterization, indicating a good detector performance, and hermeticity assessment are presented. The hermeticity results were further used to calculate the impact of a hermetic TPC on the expected DARWIN $^{222}$Rn activity, indicating its great potential for radon reduction. Again, this result provides relevant input for the design and construction of DARWIN.

## Kurzzusammenfassung

Zahlreiche astrophysikalische und kosmologische Beobachtungen weisen darauf hin, dass der Großteil der Materie im Universum dunkel ist, also weder elektromagnetisch noch stark wechselwirkt. Einer der vielversprechendsten Kandidaten für dunkle Materie ist das schwach wechselwirkende, massive Teilchen (WIMP). Das DARWIN-Experiment, ein vorgeschlagener Detektor der nächsten Generation, zielt auf eine direkte Detektion von WIMPs mithilfe einer Zweiphasen-Xenon-Zeitprojektionskammer (TPC) und die Erforschung des experimentell zugänglichen Parameterraums für WIMP-Massen $> 5\,\mathrm{GeV}/c^2$ ab. Mit seinem 40 t Flüssig-Xenon-Target, der niedrigen Energieschwelle und einem sehr niedrigen radioaktiven Untergrund wird DARWIN eine Umgebung bereitstellen, die auch für die Suche anderer seltener Ereignisse geeignet ist.

Der erste Teil dieser Arbeit widmet sich der Untersuchung mehrerer Physikkanäle von DARWIN. Seine Sensitivitäten zweier hypothetischer Leptonenzahl-verletzender Prozesse, des neutrinolosen doppelten Betazerfalls ($0\nu\beta\beta$) von $^{136}$Xe und des neutrinolosen doppelten Elektroneneinfangs ($0\nu$ECEC) von $^{124}$Xe, werden untersucht. Während DARWIN für den erstgenannten Zerfall ein Sensitivitätslimit von $T^{0\nu}_{1/2} > 2.4 \cdot 10^{27}\,\mathrm{yr}$ (90% C.L.) aufweist und wichtige Einblicke in die mögliche Neutrino-Majorana-Natur und ihre absolute Massenskala geben könnte, wird die Empfindlichkeit gegenüber dem $0\nu$ECEC durch die geringe natürliche $^{124}$Xe-Häufigkeit begrenzt. DARWINs Fähigkeit, solare Neutrinos durch elastische Neutrino-Elektron-Streuung nachzuweisen, wird ebenfalls vorgestellt, was zur Abschätzung des elektroschwachen Mischungswinkels und der Neutrino-Oszillationsparameter in einem zuvor nicht gemessenen Energiebereich von $< 200\,\mathrm{keV}$ verwendet werden kann. Darüber hinaus werden materialinduzierte und myoninduzierte kosmogene Hintergründe, die für die WIMP-Suche relevant sind, untersucht und die problematischsten Quellen, der Kryostat, die Photosensoren und das Polytetrafluorethylen (PTFE) diskutiert, was somit einen wichtigen Beitrag zum Design und Bau des zukünftigen DARWIN-Detektors darstellt.

Den dominanten radiogenen Untergrund, der elektronische Rückstoßsignale bei der Suche nach WIMPs induziert, stellt $^{222}$Rn mit den anschließenden Zerfällen seiner Nachkommen dar. Im zweiten, experimentellen Teil dieser Arbeit wird das Konzept einer hermetischen TPC untersucht, welche die $^{222}$Rn-freisetzenden Materialoberflächen in Kontakt mit dem Xenon-Target reduziert und somit eine Möglichkeit zur $^{222}$Rn-Minderung bietet. Der kleine hermetische TPC-Prototyp HUsXe wurde im Freiburger Labor für Astroteilchenphysik entworfen und betrieben. Seine Charakterisierung, die auf eine gute Detektorleistung hinweist, und die Bewertung der Hermetizität werden vorgestellt. Die hermetischen Ergebnisse wurden weiter verwendet, um den Einfluss einer hermetischen TPC auf die erwartete DARWIN $^{222}$Rn-Aktivität zu berechnen, was auf sein großes Potenzial zur Radonreduktion hinweist. Auch dieses Ergebnis liefert relevanten Input für das Design und die Konstruktion von DARWIN.

# Contents

# Chapter 1

# Introduction

As indicated by a large number of astrophysical and cosmological evidences, the majority of the matter content of the Universe is dark: baryonic matter only accounts for $\sim 16\%$, while dark matter, a yet undetected form of matter with unknown particle content, show a five times higher abundance [1]. One of the most promising particle candidates is the weakly interacting massive particle (WIMP), which might have been thermally produced in the early Universe.

Many experiments with different detection technologies aim at the direct detection of WIMPs; the most stringent exclusion limits for WIMP masses above $180\,\mathrm{MeV}/c^2$ are provided by experiments employing a dual-phase xenon time projection chamber (TPC) [2]. As of now, these experiments were able to exclude spin-independent WIMP-nucleon cross-sections down to $4.1 \cdot 10^{-47}\,\mathrm{cm}^2$ at 90% confidence level for WIMP masses of $30\,\mathrm{GeV}/c^2$ [3]. Current-generation experiments, such as XENONnT [4], LZ [5], or PandaX-4T [6], aim to improve the sensitivities by one order of magnitude. DARk matter WImp search with liquid xenoN (DARWIN), the proposed next-generation experiment, aims to do so by even two orders of magnitude. With its envisaged sensitivity of $2.5 \cdot 10^{-49}\,\mathrm{cm}^2$ for WIMP masses of $40\,\mathrm{GeV}/c^2$ [7], DARWIN will cover most of the experimentally accessible parameter space, which is limited by irreducible neutrino interactions [8]. Thus, DARWIN is also referred to as the *ultimate* dark matter detector. With its 40 t liquid xenon (LXe) target, low background, and low energy threshold, DARWIN will provide excellent conditions to also explore other rare event science channels beyond dark matter, e.g., related to neutrino physics.

After an introduction into the theory and the DARWIN experiment in chapters 2 and 3, respectively, DARWIN's sensitivity to various physics channels is presented in chapter 4. This includes the neutrinoless double beta decay ($0\nu\beta\beta$) of $^{136}$Xe and the neutrinoless double electron capture ($0\nu$ECEC) of $^{124}$Xe. Both isotopes will be naturally present in DARWIN's xenon target. The observation of these hypothetical second-order weak decays would prove lepton number violation, the Majorana nature of neutrinos, and could provide important information on the neutrino mass scale and ordering. DARWIN's sensitivity to these two decays is predicted by using detailed GEANT4 Monte Carlo (MC) simulations of xenon-intrinsic, cosmogenic,

and material-induced backgrounds. The impact of the latter source depends on the selection of materials, which are usually contaminated by long-lived radioactive isotopes. The double-walled cryostat, which houses the TPC and the cryogenic xenon, is expected to constitute the largest material background source due to its mass of several tonnes. Thus, a geometry- and material-dependent cryostat background study, based on detailed engineering calculations, is also presented in chapter 4. The expected backgrounds of other detector materials and the impact of shielding the detector with several meters of water is also investigated. These studies concentrate on the primary science goal of DARWIN, the WIMP search, and thus give input in terms of required improvements towards building the ultimate WIMP detector. Furthermore, the detailed model of the material background provided by this work allowed to study DARWIN's potential to detect solar neutrinos by elastic neutrino-electron scattering, which can be used to calculate neutrino oscillation parameters, such as the $\nu_e$ survival probability, and the electroweak mixing angle.

Besides the detector materials, the xenon itself is also contaminated by radioactive isotopes, such as $^{222}$Rn. The decay of its progenies, in particular $^{214}$Pb, is one of the main background sources for the WIMP search, for which a $^{222}$Rn concentration of 0.1 $\mu$Bq/kg is required to achieve the background goal of DARWIN [7]. $^{222}$Rn is permanently emanated from surfaces of all detector materials, which contain the mother isotope $^{226}$Ra. Due to its half-life of 3.8 d [9], $^{222}$Rn mixes homogeneously with the xenon target. Several radon reduction techniques, like online radon removal in distillation columns or the selection of materials with low $^{226}$Ra contamination, are already applied by current-generation detectors [4, 5]. However, DARWIN's challenging radon goal requires to additionally investigate new techniques. One possibility is constructing a hermetic TPC to drastically reduce the $^{222}$Rn-releasing surface areas, which are in contact with the xenon target. It separates the xenon contained in the TPC from the surrounding xenon, which mostly acts as shielding material. A small-scale hermetic TPC, the Hermetically Used Xenon TPC (HUsXe), was designed, built, and operated within this work. The analysis and results are described in chapter 5: a typical TPC characterization study is shown, which includes the calculation of detector-inherent gains, absolute scintillation and ionization yields, as well as LXe properties, the electron drift velocity and longitudinal diffusion. Furthermore, the hermeticity of HUsXe, sealed using the concept of cryofitting, exploiting the different thermal expansion coefficients of the implemented materials, is determined. The result are used to predict the impact of a hermetic TPC on DARWIN's radon activity.

The work presented in this thesis was performed as part of the DARWIN collaboration and, therefore, not everything mentioned is my sole original work. In the following, I give a short summary about my contributions:

- Chapter 4, DARWIN science channels: As part of a core team of four people, I participated in the initial adaption of the GEANT4 code to the specification of DARWIN, primarily by implementing the TPC geometry (section 4.1). The optimization of the DARWIN cryostat material and geometry (section 4.2) and the investigation of expected cosmogenic and radiogenic nuclear recoil

backgrounds for the WIMP search (section 4.3) were entirely performed by myself. The investigation of DARWIN's sensitivity to the $0\nu\beta\beta$ of $^{136}$Xe (section 4.4) was a collaborative effort, published in the European Physical Journal C [10], where I contributed the MC-based prediction of the material-induced backgrounds, a detailed background model, and the determination of the optimal fiducial volume. I supervised the study of DARWIN's sensitivity to the $0\nu$ECEC of $^{124}$Xe (section 4.5), performed by M. Rajado Nunes da Silva, and contributed the MC simulations; a publication is currently in preparation. I provided the material-induced electronic recoil background required to determine DARWIN's sensitivity to detect solar neutrinos (section 4.6), published in the European Physical Journal C [11].

- Chapter 5, HUsXe: Most of the work described in this chapter was performed by myself. I designed and assembled the HUsXe detector (section 5.2.1). I adapted the XeBRA cryogenic detector test platform (section 5.2.2) to the HUsXe requirements and installed and commissioned a second xenon gas system. At the beginning of my Ph.D., I also contributed to the commissioning of the XeBRA platform and to optimize and operate a small standard, i.e., non-hermetic TPC; a publication is currently in preparation. I planned and coordinated all three HUsXe runs: this included installing the TPC, detector operation and data taking, and shutting down the detector (section 5.3). However, since the several week-long operations required permanent detector shifts, I was supported by several members of the Freiburg Astroparticle Physics Group, notably M. Rajado Nunes da Silva, who also contributed to the analysis of the first HUsXe data. The measurements of LXe properties, S1-only, S2-only, and combined S1-S2 TPC characterizations are my own work (section 5.4). I also performed the analysis of the hermeticity of the HUsXe detector and predicted the impact of a (semi-)hermetic TPC on DARWIN's $^{222}$Rn concentration (section 5.5). A publication is currently in preparation.

- Further contributions: The impact of a novel single-phase technology for charge signal generation on DARWIN's expected nuclear recoil background rate was calculated using my expertise on neutron backgrounds, which is part of the study published in [12]. This study is not included in the thesis presented here since the investigation of the single-phase technology is beyond the scope of this work.

# Chapter 2

# Dark matter and neutrino physics

Almost one century has passed since the first gravitational evidence in the 1930s [13] pointed towards the existence of a new form of matter: *dark matter (DM)*. As of today, DM has not been detected yet, despite the great variety of cosmological and astrophysical evidence. Its observation and the determination of its properties constitute the primary science goal of many experiments, such as DARk matter WImp search with liquid xenoN (DARWIN) [7]. DARWIN aims to detect DM directly by DM scatterings off a target material.

Due to the detector characteristics required for a direct DM detection, such as the very low background, DM detectors also allow searching for other rare events, for example related to neutrino physics. Neutrinos are standard model (SM) particles and were first discovered in 1956 [14]. Even though fundamental knowledge about their nature and interactions was gained since then, many central questions like the absolute neutrino mass scale and their mass ordering remain open and could possibly be explored by DM detectors.

This chapter summarizes the theoretical backgrounds, which are important to understand the investigations presented in this thesis. DM evidence, the WIMP as one very well-motivated hypothetical DM candidate, and its direct detection are introduced in section 2.1. In section 2.2 an overview is given about neutrinos, double beta decays as one possibility to explore the neutrino nature, as well as astrophysical neutrino interactions in DM detectors.

## 2.1 Dark matter

Based on several astrophysical observations, we nowadays know that the majority of the Universe is dark. The standard model of cosmology ($\Lambda$CDM), supported by the most recent measurements of the Planck satellite [1], predict that baryonic matter only accounts for 4.9% of the energy content in the Universe; dark energy and DM contribute to 68.7% and 26.4%, respectively.

### 2.1.1 Evidence

A detailed overview of the various pieces of DM evidence based on its gravitational interaction with luminous matter is, e.g., given in [15]. In this section some of the most prominent hints are summarized.

In 1933 Fritz Zwicky was among the first suggesting the existence of DM while studying the Coma cluster, a cluster of galaxies, which is more than 300 million light-years away from the Earth. He determined the cluster's mass by measuring the galaxy velocities through the Doppler effect and applying the virial theorem to calculate the cluster's gravitational potential. A significant difference was observed when comparing this result to the cluster mass calculated via the total luminosity. He interpreted the discrepancy as being caused by a new kind of matter, which does not interact electromagnetically and hence, he called it "dunkle Materie" (dark matter) [13].

For many years Zwicky's work did not get much scientific attention until new evidence for DM emerged: in 1978 Vera Rubin and collaborators studied the rotation curves of spiral galaxies [16]. Since most of the mass within spiral galaxies was considered to be located at its core, the velocity distribution $v$ is assumed to follow Newton's gravitational law

$$v(r) \propto r^{-1/2} \ , \tag{2.1}$$

where $r$ denotes the radial distance from the center of the galaxy. In contrast to the expected behavior, the experimental data showed a constant or even slightly increasing velocity for higher radii, shown in figure 2.1 (a) for NGC 6503. In the 1980s these findings were confirmed using precise measurements of the 21 cm line of neutral hydrogen gas, which extends well beyond the visible disk [17]. As an explanation the "DM halo" was introduced, with a density profile scaling with $\rho \propto r^{-2}$ (included in figure 2.1 (a)). It is considered to expand well beyond the luminous matter and to dominate the matter content of the galaxy's outer regions.

Other strong DM evidence came from studying the galaxy cluster 1E 0657-56, known as the Bullet Cluster [19], which was formed by two clusters traversing themselves, shown in figure 2.1 (b). The gaseous components of these two clusters behaved as a particle fluid and their interacting gas caused X-ray emission. The measurements of these X-rays allowed tracing the baryonic matter distribution (color image in figure 2.1 (b)). A discrepancy was found when comparing this spatial distribution to the mass distribution obtained by gravitational lensing (green lines). Gravitational lensing, predicted by Einstein's general theory of relativity [20], describes the distortion of light from distant objects by massive objects in the foreground. This difference can be explained by two kinds of matter and the separation of interacting (baryonic) gas and non-interacting DM and stars. Due to the DM halos traversing each other undisturbed, limits on the DM self-interaction cross-section were set [21]. Similar results were reported for other clusters such as Abell 1689 [22] or Abell 2744 [23]. In general, the findings by gravitational lensing deliver one of the best evidences for the nature of DM: they cannot be explained by a modification of the gravitational law, such as the MOND theory [24].

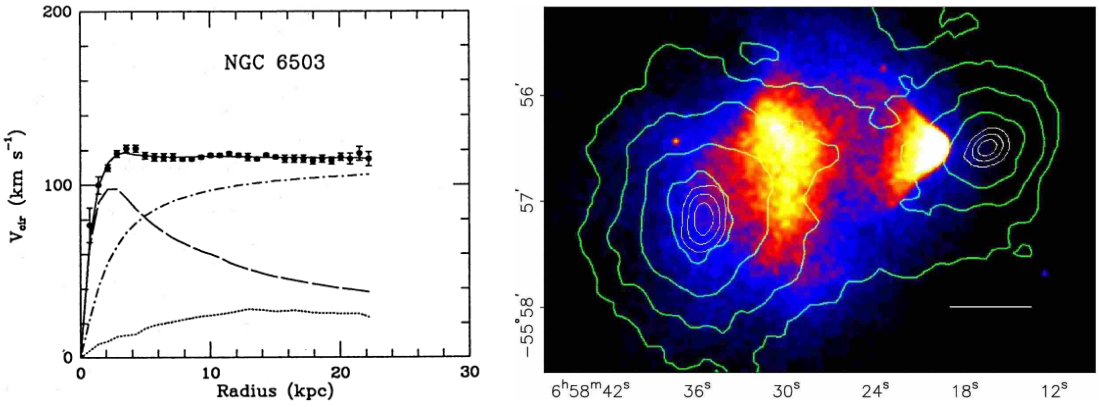


(a) (b)

**Figure 2.1:** Evidence for DM from rotation velocities of spiral galaxies and gravitational lensing. (a) shows the radius-dependent rotation velocity (solid line, measurements), which can be attributed to the effects from the galaxy's stellar disk (dashed line), gas (dotted line), and DM halo (dash-dotted line). (b) presents the discrepancy of the mass distributions within the Bullet Cluster inferred via X-ray measurements (color scale) and gravitational lensing (green lines). Figures from [18] and [19].

Currently, the most accurate values for the Universe's energy densities are obtained by analyzing the electromagnetic radiation originating from the early Universe: the cosmic microwave background (CMB), which was first observed in 1965 [25]. After the Universe cooled down to approximately 3000 K, it became optically transparent since neutral hydrogen atoms could form. The nearly ideal black body spectrum created at this time can still be observed today and has been red-shifted due to the Universe's cool-down to $\sim 2.7\,\mathrm{K}$ [26]. Its tiny temperature anisotropies at the $\mathcal{O}(10^{-5})$ level are explained by density fluctuations in the early Universe. The corresponding power spectrum depends on the angular scale and is shown in figure 2.2, where the most recent Planck satellite measurements are presented. By applying the six-parameter ΛCDM model, the data can be very well described and yields precise information on the Universe's density, which is the sum of the constituents $\Omega_b$ (baryonic matter), $\Omega_{\mathrm{CDM}}$ (cold DM), and $\Omega_\Lambda$ (vacuum energy). The baryonic and DM contributions were estimated to [1]

$$\Omega_b = 0.0493 \pm 0.0006 \tag{2.2}$$

$$\Omega_{\mathrm{CDM}} = 0.264 \pm 0.004 \ , \tag{2.3}$$

indicating that DM is 5.4 times more abundant than baryonic matter.

### 2.1.2 Weakly interacting massive particles

Even though the existence of DM is well-motivated by its gravitational evidence at different mass scales, its nature and properties remain mostly unknown, which makes the non-gravitational DM detection difficult. DM is assumed to be of particle nature. Accordingly, a variety of theoretical models and corresponding detection possibilities are pursued. Since the mass range arising from theoretical models spans

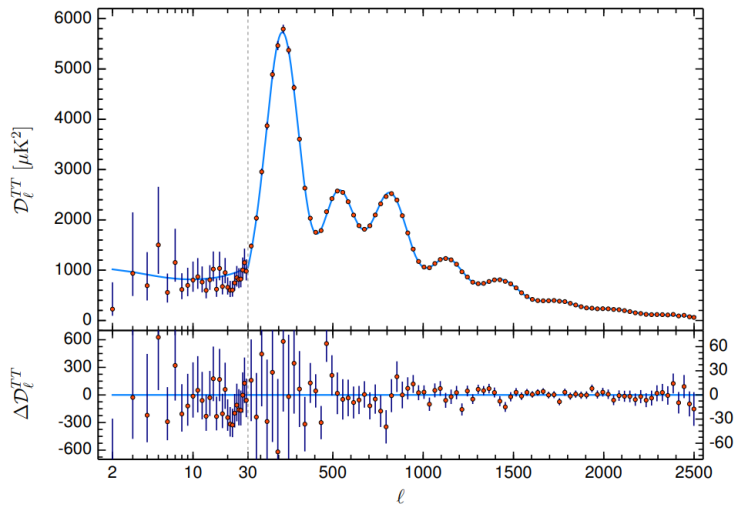


**Figure 2.2:** Multipole expansion of the power spectrum of the CMB temperature anisotropies as measured by the Planck satellite (red points). The blue line shows the six-parameter ΛCDM model yielding precise information on the composition of the energy density of the Universe. The residuals between the data points and the fit function are shown in the bottom panel. Figure from [1].

from $10^{-21}$ eV to $10^{18}$ GeV [27, 2] with a various number of DM candidates, we will focus in the following on the most important candidate for the work presented here: the weakly interacting massive particle (WIMP). A comprehensive and detailed overview of other DM candidates is for example presented in [28].

The gravitational evidence summarized in section 2.1.1 allows concluding on several commonly assumed DM particle properties. Firstly, as indicated by its name, it is expected to be dark, i.e., it does not interact electromagnetically or strongly with luminous matter; otherwise, photons would be emitted and DM would fall into galactic centers due to their energy loss. Secondly, DM must be stable since its gravitational effects are still observed today. Alternatively, its lifetime must be long (at least 160 Gyr [29]) compared to the age of the Universe. Thirdly, it is non-baryonic, as shown by the CMB or the gravitational lensing effects. Lastly, DM is assumed to be cold, i.e., slowly moving, to explain the observed large-scale structures in the Universe and the total amount of DM, which could not be explained by assuming hot DM instead.

The WIMP, which denotes a generic class of hypothetical DM candidates with masses ranging from 1 GeV to several TeV [30], fulfills the listed requirements. WIMPs are rather model-independent DM candidates and naturally arise in various beyond the SM theories, which were initially not intended to explain DM. Examples are the supersymmetric theories whose lightest particle, the neutralino, could be associated with the WIMP [31]. Other theories, like universal extra dimensions, are shortly summarized in [30].

WIMPs are considered to be relics of the early Universe, similar to baryonic matter. Their assumed production mechanism is known as the *thermal freeze-out* and is illustrated in figure 2.3. Shortly after the Big Bang, WIMPs' annihilation and production rates were equal, causing the WIMP to be in equilibrium with the thermal plasma. As the Universe expanded and cooled down, WIMPs started to decouple from the other particles and annihilated, causing a rapid drop in their number density. This process continued until the WIMP annihilation rate $\Gamma_{\text{ann}}$ fell below the Hubble rate $H$, which led to a freeze-out of the WIMPs [2]. From that point on, the DM density was only affected by the further expansion of the Universe, assuming the WIMP to be a stable particle.

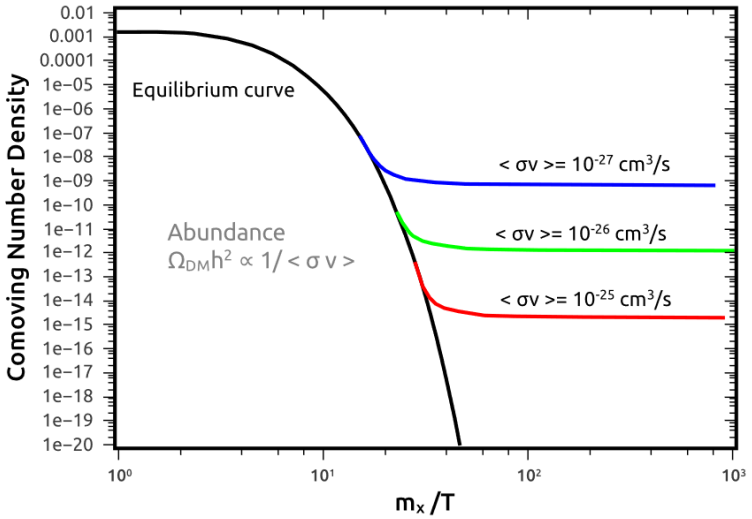


**Figure 2.3:** Comoving (i.e., with the expanding Universe) DM number density depending on $m_\chi/T$, which is proportional to the time after the Big Bang. $T$ and $m_\chi$ denote the freeze-out temperature and WIMP mass, respectively. In black, the thermal equilibrium curve is shown. The three different freeze-out scenarios with varying DM thermally averaged total annihilation cross-sections $\langle\sigma v\rangle$ are marked in blue/green/red and lead to different relic DM abundances today. Figure from [32].

As indicated by figure 2.3, the freeze-out time depends on $\Gamma_{\text{ann}} \propto \langle\sigma_{\text{ann}} v\rangle$, where the latter describes the thermally averaged total annihilation cross-section. When assuming weak-scale cross-sections of $\langle\sigma_{\text{ann}} v\rangle = 10^{-26}\text{cm}^3/\text{s}$ (marked in green) and employing the Boltzmann equation, a relic DM density of $\Omega_{\text{CDM}} \sim 0.3$ is calculated [33]. The fact that this calculated DM density assuming electroweak scale cross-sections agrees with the DM density obtained by Planck measurements (shown in section 2.1.1) is called the *WIMP miracle*. The expected signal rates fall into the sensitivity of current or planned detectors, causing strong experimental interest. The following section will thus introduce several methods of how to detect DM WIMPs.

### 2.1.3 WIMP detection methods

DM detection experiments are divided into three classes, as presented in figure 2.4, depending on their detection strategy: DM production at colliders, DM indirect detection, and DM direct detection.

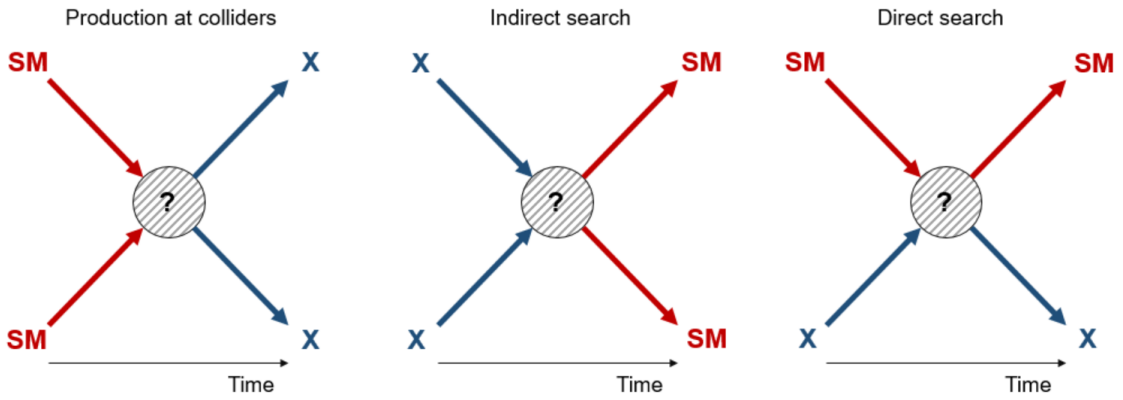


**Figure 2.4:** The three experiment classes for detecting DM: production at colliders (left), indirect search (center), and direct search (right). At colliders, the production of DM particles $\chi$ by two SM particles would result in missing energy and momentum carried away by the very weakly interacting DM particles. Indirect detection experiments search for signals from DM annihilation. Direct searches look for DM particles depositing energy by scattering off a target material.

#### Production at colliders

DM particles could be produced at high-energy colliders like the LHC [34], as shown in figure 2.4 (left). Due to the expected tiny interaction cross-section of DM with luminous matter and its stability of the order of the lifetime of the Universe, the produced pair of WIMPs is assumed to leave the detector without any interactions. Thus, event signatures with a large amount of missing energy and momentum and a single particle/jet from initial/final state radiation are searched for (mono-X searches).

Observing DM at colliders yields many advantages, such as not being influenced by astrophysical backgrounds, not suffering from astrophysical uncertainties, or the possibility of probing lower DM masses than with direct detection experiments. However, it also carries several challenges. These include the model-dependent search or the fact that an invisible particle carrying away energy and momentum does not necessarily correspond to DM. An overview of several considered models for collider searches can be found in [35]. For an experimental overview, which is consistent with standard model expectations so far, we refer to [36].

#### Indirect search

DM could also be detected indirectly by its self-annihilation products emitted from DM-rich astrophysical objects, compare to figure 2.4 (center). Possible detection channels are the annihilation of a WIMP pair $\chi\bar{\chi}$ into $\gamma\gamma$, $\gamma Z$, $\gamma H$, $W^-W^+$, or

$ZZ$, with some of these products further decaying into $e^-e^+$, $p\bar{p}$, $\gamma$-rays, and neutrinos [30]. While charged particles like electrons and protons will be deflected, $\gamma$-rays and neutrinos will not lose the information of their origin while traveling from the source to the observer. However, photons might get absorbed by the interstellar medium. The DM annihilation rate increases proportionally with the square of the DM density. Thus, one of the most favored sources for indirect detection is the center of galaxies, where the DM halo is assumed to be the densest, such as the center of the Milky Way. Since large astronomical objects could gravitationally capture DM as they lose energy by scattering off the object's nuclei, an excess of WIMPs might also appear, e.g., in the Sun [30]. In addition to its annihilation, DM could also decay generating (anti-)particles, $\gamma$-rays, or neutrinos, with the decay rate growing linearly with the DM density [37].

One of the major difficulties in indirect DM searches comes from backgrounds of astrophysical origin, which might mimic DM signals: the positron excess measured by PAMELA [38] and AMS-02 [39] cannot only be explained by DM but also by an emission spectrum of pulsars or cosmic rays colliding with the interstellar medium, producing positrons as secondary particles [40]. Besides charged particles, several experiments are looking for $\gamma$-rays as DM signature, either by atmospheric Cherenkov telescopes like HESS [41], MAGIC [42], or VERITAS [43] or directly with satellite-based detectors like Fermi-LAT [44]. While Cherenkov telescopes are sensitive to $\gamma$-rays in the TeV energy range, Fermi-LAT is capable of detecting $\gamma$-rays with energies of $\mathcal{O}$(MeV - GeV). Experiments such as IceCube [45] or Super-Kamiokande [46] search for DM annihilation into neutrinos. Besides some controversial signals, including the positron excess, the indirect searches saw no clear DM signal as of now. An overview of indirect DM detection is given in [47] and [36].

### Direct search

Extensive experimental efforts are also put into the direct detection of DM, aiming to measure the recoils induced by WIMPs colliding with the target material of Earth-based ultra low-background detectors, illustrated in figure 2.4 (right). In this work only elastic scatterings off target nuclei will be discussed (following the reviews provided in [48, 49, 30]), where nuclear recoil (NR) energies of $\mathcal{O}$(keV) are expected for WIMP masses of $\mathcal{O}(100\,\mathrm{GeV}/c^2)$ [48]. However, direct detection experiments also investigate other DM signatures depending on the assumed model, which are summarized in [30]. This includes processes such as inelastic scatterings off nuclei simultaneously exciting the WIMP or the target nucleus. The latter would result not only in a measurable NR but would also cause a $\gamma$-ray by its prompt deexcitation.

The differential recoil spectrum of WIMPs elastically scattering off target nuclei is given by

$$\frac{dR}{dE_{\mathrm{NR}}} = \frac{\rho_0}{m_A m_\chi} \int_{v_{\mathrm{min}}}^{v_{\mathrm{esc}}} v f(v) \frac{d\sigma}{dE_{\mathrm{NR}}} dv \ , \tag{2.4}$$

where $E_{\mathrm{NR}}$ is the NR energy, $m_A$ the nuclear mass of the target material, $m_\chi$ and $\sigma$ the two main observables describing the DM mass and its scattering cross-section, respectively, $v$ the relative DM velocity, and $\rho_0$ the local DM density. In the standard halo model, the local DM density is typically assumed to be $\rho_0 = 0.3\,\mathrm{GeV}/(c^2\,\mathrm{cm}^3)$ [50]. Modern investigations of the kinematics within the Milky Way support a set of parameters ranging from (0.22 - 0.33) $\mathrm{GeV}/(c^2\,\mathrm{cm}^3)$ [50].

A Maxwell-Boltzmann distribution describes the velocity $v$ of DM particles with a median of $v_0 = 220\,\mathrm{km/s}$ and a cut-off at the escape velocity $v_{\mathrm{esc}} = 544\,\mathrm{km/s}$, which corresponds to the minimum velocity required to escape the gravitational potential of the system [51]. The latter is taken as the upper integration limit in equation (2.4); the lower integration limit describes the minimal velocity of a WIMP required to induce a NR with the energy $E_{\mathrm{NR}}$ and is calculated by

$$v_{\mathrm{min}} = \sqrt{\frac{E_{\mathrm{NR}}\, m_A}{2}\frac{1}{\mu^2}}\ , \tag{2.5}$$

where $\mu = \frac{m_A\, m_\chi}{m_A + m_\chi}$ denotes the reduced WIMP-nucleon mass. In equation (2.4) the velocity distribution $f(v)$ is not given in the galactic but the detector's reference frame, taking into account the Earth orbiting around the Sun with the velocity $v_E$. While in June the Sun's motion $v_\odot$ and the Earth's orbiting $v_E$ are parallel, adding to the highest possible speed relative to WIMPs in the DM halo, $v_\odot$ and $v_E$ point in anti-parallel directions in December. This change of the absolute velocity causes two observational consequences.

Firstly, the number of particles that can produce a detectable NR signal grows with increasing velocity and, thus, is largest in June. This causes the so-called *annual modulation*, which describes a temporal variation of the number of observed DM signal events above a fixed threshold [52]:

$$S(t) = S_0 + S_m \cdot \cos\left(\frac{2\pi(t - t_0)}{T}\right)\ . \tag{2.6}$$

$t_0$ is the phase, $T$ the modulation period of one year, $S_0$ the unmodulated signal, and $S_m$ the modulation amplitude. Due to $v_E/v_\odot \sim 5\%$ [49], $S_m$ is expected to be small compared to the unmodulated signal $S_0$.

Secondly, the Earth's daily rotation allows for a directional DM search since the NRs induced by WIMPs are angular-dependent [53]. Their differential rate written as a function of the scattering angle $\theta$ is given by

$$\frac{dR}{dE_{\mathrm{NR}}\, d\cos\theta} \propto \exp\left(\frac{-2((v_E + v_\odot)\cos\theta - v_{\mathrm{min}})^2}{3v_\odot^2}\right)\ . \tag{2.7}$$

Since the integrated rate of DM events scattering in forward and backward direction differ by one order of magnitude [53] and backgrounds are expected to be uniformly distributed, equation (2.7) could be applied to discriminate WIMP from

background signals. However, most DM detectors cannot reconstruct the signal's track of $\ll 1\,\mathrm{mm}$ [49] to measure the scattering angle $\theta$. They thus cannot apply this powerful discrimination tool.

The WIMP scattering cross-section $\frac{d\sigma}{dE_{\mathrm{NR}}}$ included in equation (2.4) depends on the involved nuclear physics processes, where both spin-dependent (SD) and spin-independent (SI) DM interactions are conceivable. While only unpaired nucleons contribute to the scattering in the former case, the latter assumes an equal contribution from all neutrons and protons. A loss of coherence must be considered since for a high momentum transfer $q$, the WIMP's de Broglie wavelength $\lambda = h/q$ is no longer large compared to the nuclear radius. Thus, the cross-section decreases since only a part of the nucleus participates in the interaction. The form factor $F$ accounts for this loss of coherence. In figure 2.5 its impact for SI interactions is shown, where a WIMP mass of $100\,\mathrm{GeV}/c^2$ and a cross-section of $1 \cdot 10^{-47}\,\mathrm{cm}^2$ are assumed and $F$ is approximated by the Helm parameterization [54]. The influence of different target materials is shown, where a rate suppression due to the Form factor primarily occurs for large nuclei (here xenon) at higher recoil energies.

The differential cross-section $\frac{d\sigma}{dE_{\mathrm{NR}}}$ is thus written as a sum of the SD and SI components, taking into account the different form factors $F_{SD}$ and $F_{SI}$:

$$\frac{d\sigma}{dE_{\mathrm{NR}}} = \frac{m_A}{2\mu^2 v^2} \cdot \left(\sigma_{SI} \cdot F_{SI}^2(E_{\mathrm{NR}}) + \sigma_{SD} \cdot F_{SD}^2(E_{\mathrm{NR}})\right) \quad . \tag{2.8}$$

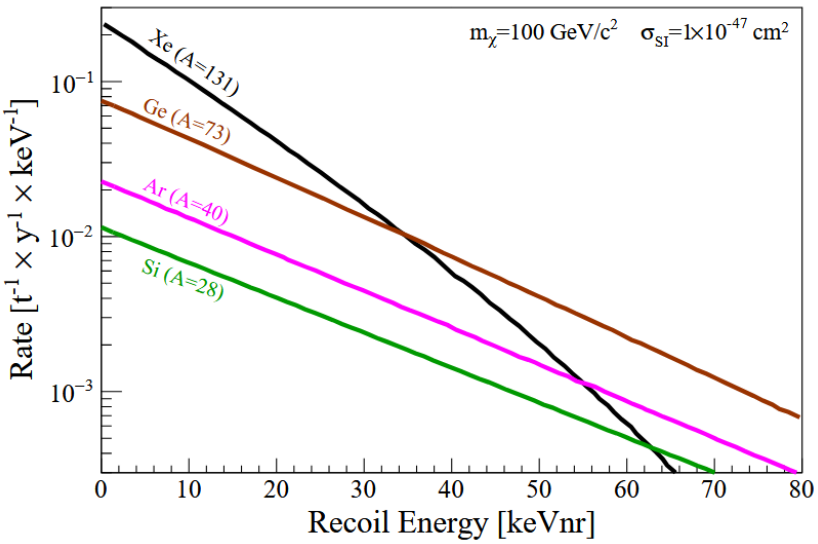


**Figure 2.5:** Differential nuclear recoil spectrum of WIMPs scattering off various target materials. A WIMP mass of $100\,\mathrm{GeV}/\mathrm{c}^2$ and a spin-independent (SI) interaction cross-section of $1 \cdot 10^{-47}\,\mathrm{cm}^2$ are assumed. For lower recoil energies the recoil spectra of heavier target materials dominate due to $\sigma_{SI} \propto A^2$. For higher energies the rate of heavier targets decreases due to their suppression by the form factor, which is caused by the loss of coherence. Figure from [49].

For SI interactions the cross-section $\sigma_{SI}$ is expressed by

$$\sigma_{SI} = \sigma_p \cdot \frac{\mu^2}{\mu_n^2} \cdot \frac{(f_p Z + f_n(A-Z))^2}{f_n^2} \tag{2.9}$$

$$= \sigma_n \cdot \frac{\mu^2}{\mu_n^2} \cdot A^2 \ , \tag{2.10}$$

where $\mu_n$ describes the WIMP-nucleon reduced mass and $f^p$ and $f^n$ the WIMP coupling strengths to protons and neutrons, respectively. In equation (2.10) $f^p = f^n$ is assumed, which results in $\sigma_{SI} \propto A^2$, showing that heavier target nuclei are preferred in direct DM searches. This effect is visualized in figure 2.5, where at lower recoil energies xenon (being the heaviest shown target material) dominates the differential spectrum.

SD cross-sections with the WIMP coupling to unpaired nuclear spins $J$ are given by

$$\sigma_{SD} = \frac{32}{\pi}\mu^2 \cdot G_F^2 \cdot \frac{J+1}{J} \cdot (a_p \cdot \langle S^p \rangle + a_n \cdot \langle S^n \rangle)^2 \ , \tag{2.11}$$

where $G_F$ is the Fermi coupling constant, $a_p$ and $a_n$ the effective proton and neutron couplings, and $\langle S^p \rangle$ and $\langle S^n \rangle$ the model-dependent expectation values of the total spin operators for neutrons and protons, respectively. With the expectation values $\langle S^{p,n} \rangle$ taken from [55], the SD cross-sections of several isotopes are calculated, showing that the most relevant isotopes for SD DM searches are $^{19}$F, $^{129}$Xe, $^{73}$Ge, $^{127}$I, $^{27}$Al, $^{131}$Xe, $^{23}$Na, $^{29}$Si, sorted by their detection strength. $^{19}$F leads to the highest sensitivity to SD DM searches due to its high WIMP-proton coupling.

Various experiments aim to directly detect DM with technologies depending on the different readout channel(s): heat, charge, and light. An overview sketch with the several detection technologies and a selection of experiments relying on them is shown in figure 2.6. For a comprehensive and detailed review of these detectors, their advantages, and results, we refer to [30] and [49]. A few of these techniques are shortly explained in the following.

As shown by figure 3.3 on page 32, which compares SI cross-section sensitivities of several past, current, and next-generation experiments, the most stringent constraints on WIMP masses $> 3\,\mathrm{GeV}/c^2$ stem from experiments using noble liquids as target material - either argon or xenon. Two different types of noble liquid detectors are distinguished: single-phase and dual-phase detectors. Single-phase detectors, which operate spherical noble liquid targets with a $4\pi$ photosensor coverage, solely record the scintillation light generated at the interaction vertex of the particle's primary interaction. With the photon arrival times and the hit pattern on the photosensors, position resolutions of $\mathcal{O}(\mathrm{cm})$ are obtained. Experiments leading this technique are XMASS [57], using a xenon, or DEAP-3600 [58], using an argon target, with argon allowing for background identification using pulse-shape discrimination [59]. In contrast, dual-phase noble liquid detectors exploit scintillation light and ionization charge information using a TPC. TPCs are filled with

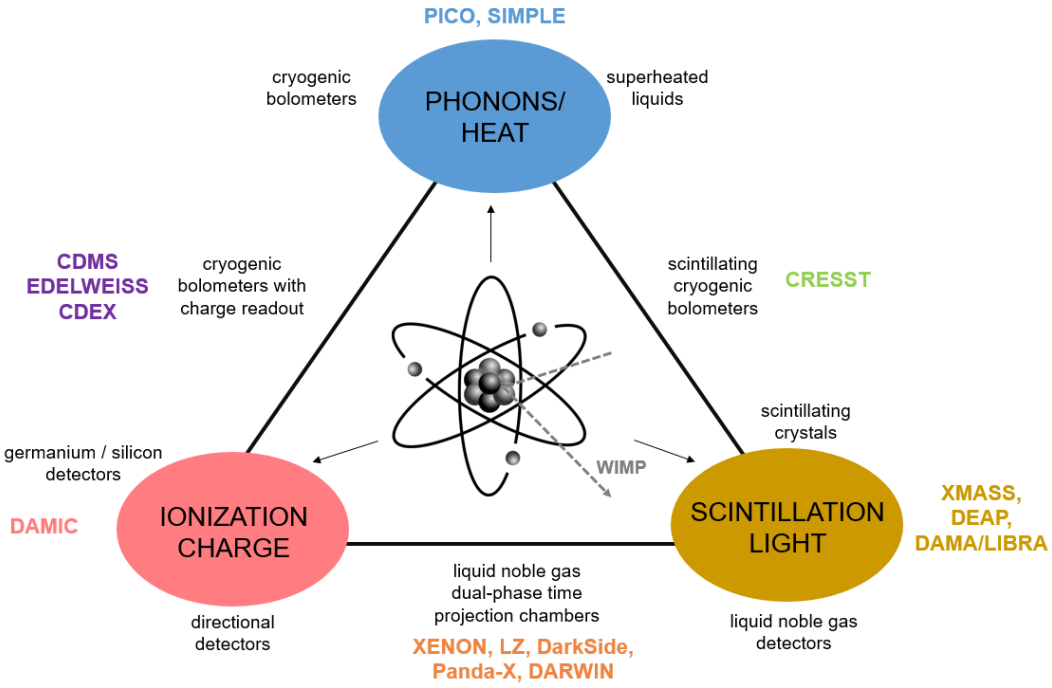


**Figure 2.6:** Possible observables in direct DM searches: heat, charge, and light. Experiments using one or two of these channels and the corresponding technologies are included. Figure based on [30] and [56].

the liquid noble gas plus a small gaseous layer at the top, where the latter enables the additional detection of the charge signal. Details about their functionality are given in chapter 3. Prominent experiments using noble liquid TPCs are XENON1T [3]/XENONnT [4], LUX [60]/LZ [5], PandaX-II [61]/PandaX-4T [6], and DarkSide-50 [62].

Crystalline cryogenic detectors measure heat/phonons from a tiny temperature increase $\Delta T$ induced by the interaction of a particle. These detectors require a low heat capacity and are operated at low temperatures of $\mathcal{O}(\mathrm{mK})$ to achieve good sensitivity. Since most of the energy deposited during a WIMP's interaction is transferred into heat, these detectors can detect lower-mass WIMPs that are incapable of producing detectable scintillation or ionization signals. For WIMP masses $< 2\,\mathrm{keV}/c^2$, crystalline cryogenic detectors thus provide the most stringent cross-section limits. Most of these experiments measure a second readout channel, either scintillation or charge, allowing for an efficient signal/background discrimination, one of their main advantages besides the excellent energy resolution. Exemplary experiments are EDELWEISS [63] or SuperCDMS [64], which measure heat and charge in germanium/silicon, or CRESST-III [65], which measures heat and scintillation light in $CaWO_4$.

Besides these two main groups of experiments leading the SI direct DM search, considerable experimental effort is also put, e.g., in ionization detectors like DAMIC [66]. Due to the small energy required to produce an electron-hole pair, they provide an excellent energy resolution. However, their high electronic noise level hinders

a detector scale-up. Superheated liquids with different chemical compositions are employed in bubble chambers, e.g., by PICO [67]. Since the liquid is kept in a supercritical state just above the boiling point, an energy deposition causes local phase transitions and creates bubbles, which are recorded by a camera. Most targets contain $^{19}$F and thus are very sensitive to SD WIMP interactions. Scintillating crystals are characterized by their simple geometry, stable long-term operation but comparably high intrinsic backgrounds. One of the most prominent experiments utilizing scintillating crystals is DAMA/LIBRA, which claims the observation of the DM annual modulation using NaI(Tl) crystals [68]. However, these findings are in strong tension with results provided by other experiments using the same technology, ANAIS-112 [69] and COSINE-100 [70], and essentially all other direct detection experiments.

## 2.2 Neutrinos

Neutrinos are SM particles produced in various processes such as nuclear reactions in the core of the Sun, beta decays, or during supernovae explosions. The first observation of the three neutrino flavors $\nu_e$, $\nu_\mu$, and $\nu_\tau$ dates back to 1956 by the Cowan-Reines experiment [14], 1962 by G. Danby et al. [71], and 2001 by the DONUT experiment [72], respectively. Since then, fundamental knowledge about the neutrino nature has been gained: neutrinos are spin $\frac{1}{2}$ leptons, they do not carry an electrical charge and interact only weakly with matter. Even though their absolute masses have not yet been measured, neutrinos must have a non-zero mass due to the observation of neutrino oscillations. These oscillations, which modify the neutrino flavor, were first predicted by B. Pontecorvo in 1958 [73] and discovered in 1998 by Super-Kamiokande studying high-energy atmospheric $\nu_\mu$ [74]. In the following years other experiments like SNO also reported flavor oscillations of other neutrino types [75]. This explained the solar neutrino problem, known since the 1960s due to solar $\nu_e$ measurements of the Homestake experiment [76].

To calculate the oscillation probability, the neutrino flavor states $\nu_\alpha$ are expressed by a quantum mechanical superposition of three mass eigenstates $|\nu_i\rangle$ and the Pontecorvo-Maki-Nakagawa-Sakata (PMNS) neutrino mixing matrix:

$$|\nu_\alpha\rangle = \sum_{i=1}^{3} U_{\alpha i} \, |\nu_i\rangle \ , \tag{2.12}$$

where $U_{\alpha i}$ are the elements of the PMNS matrix. Since the resulting probability is a function of the differences of the squared neutrino masses, oscillation experiments do not provide measurements of absolute masses. Instead, they show by the existence of neutrino oscillations that at least two mass eigenstates have non-zero values. The two independent mass differences $\Delta m^2_{\text{sol}} = \Delta m^2_{21}$ and $\Delta m^2_{\text{atm}} = \Delta m^2_{31}$ obtained by measuring solar and atmospheric neutrino oscillations, respectively, are [77]:

$$\Delta m^2_{\text{sol}} \approx 7.5 \cdot 10^{-5} \, \text{eV}^2 \tag{2.13}$$

$$|\Delta m^2_{\text{atm}}| \approx 2.5 \cdot 10^{-3} \, \text{eV}^2 \ . \tag{2.14}$$

While $\Delta m^2_{\text{sol}}$ is positive, showing that $m_1 < m_2$, the sign of $\Delta m^2_{\text{atm}}$ is unknown, resulting in two different possible neutrino mass ordering scenarios:

$$\begin{aligned} &\text{normal ordering (NO):} \; m_1 < m_2 \ll m_3 \\ &\text{inverted ordering (IO):} \; m_3 \ll m_1 < m_2 \; . \end{aligned}$$

These two scenarios are shown in figure 2.7. Each horizontal bar represents a mass eigenstate with the different neutrino flavors $\nu_e$, $\nu_\mu$, and $\nu_\tau$ marked in red, blue, and green, respectively. One of the primary goals of current neutrino experiments is to distinguish between these two neutrino ordering scenarios and measure the absolute neutrino masses. A more detailed overview of the most updated results on neutrino oscillation measurements, including the angles $\theta_{12}$, $\theta_{13}$, $\theta_{23}$, and the charge parity (CP) violating phase $\delta$ of the PMNS matrix, is presented in [77].

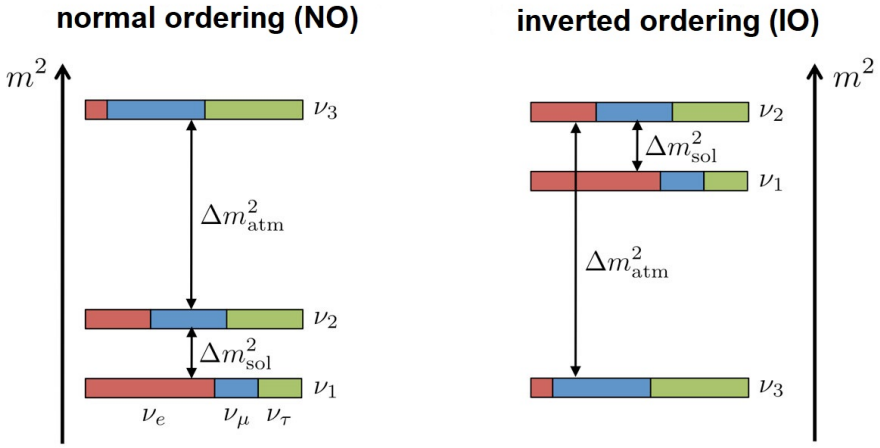


**Figure 2.7:** The neutrino mass ordering scenarios: normal ordering (NO) and inverted ordering (IO). Each horizontal bar presents a neutrino mass eigenstate and the colors red, blue, and green indicate the contributions from the neutrino flavors $\nu_e$, $\nu_\mu$, and $\nu_\tau$, respectively. Figure from [78].

In the following, we explain how liquid xenon-based DM detectors can address open questions about the neutrino nature and for example could give access to the neutrino masses. On the one hand, this includes searches for hypothetical second-order weak decays, the $0\nu\beta\beta$ decay of $^{136}$Xe and $0\nu$ECEC of $^{124}$Xe, presented in section 2.2.1. On the other hand, one can search for the interaction of astrophysical neutrinos in Earth-based detectors, explained in section 2.2.2.

### 2.2.1 Second-order weak decays

The two-neutrino double beta decay ($2\nu\beta\beta$) of $^{136}$Xe and the two-neutrino double electron capture ($2\nu$ECEC) of $^{124}$Xe are rare second-order decay processes. In the $2\nu\beta\beta$ two neutrons are converted into two protons, including the emission of two anti-neutrinos:

$$2\nu\beta\beta : (A, Z) \rightarrow (A, Z+2) + 2e^- + 2\bar{\nu_e} \; , \tag{2.15}$$

while two protons are converted into two neutrons in the $2\nu$ECEC, including the emission of two neutrinos:

$$2\nu\text{ECEC} : 2e^- + (Z, A) \rightarrow (Z-2, A)^{**} + 2\nu_e \ , \tag{2.16}$$

where $A$ is the mass number, $Z$ the atomic number, and each asterisk denotes a vacancy in the atomic shell. Both $2\nu\beta\beta$ and $2\nu$ECEC were already detected for several isotopes, including the mentioned xenon isotopes [79, 80]. In the following, unless explicitly stated otherwise, the expression $\beta$ decay always refers to a $\beta^-$ decay.

Since neutrinos could be Majorana fermions [81], the neutrinoless decays $0\nu\beta\beta$ and $0\nu$ECEC are conceivable but have not yet been detected:

$$0\nu\beta\beta : (A, Z) \rightarrow (A, Z+2) + 2e^- \tag{2.17}$$

$$0\nu\text{ECEC} : 2e^- + (Z, A) \rightarrow (Z-2, A)^{**} + \text{excitation} \ . \tag{2.18}$$

Observing such processes would require lepton number violation and therefore requires an extension of the SM. Instead of a four-component Dirac spinor, the neutrinos would be two-component Majorana particles with no electric charge and no lepton number; for details we refer to [82] and [83], which describe an effective Lagrangian approach. Important information about the effective neutrino Majorana mass

$$\langle m_{\beta\beta} \rangle = |\sum_i U_{ei}^2 m_i| \tag{2.19}$$

would be obtained by detecting $0\nu\beta\beta$ or $0\nu$ECEC. $\langle m_{\beta\beta} \rangle$ describes a superposition of the neutrino mass eigenstates scaled by the corresponding entries $U_{ei}$ of the neutrino mixing matrix and gives insight into the absolute neutrino masses.

In the following, the two mentioned second-order decays are explained in more detail and their experimental signature for both the two-neutrino and neutrinoless processes are presented.

### Double beta decay

Since the $2\nu\beta\beta$ is highly suppressed by a factor of $\sim 10^{21}$ [84] compared to the simple $\beta$ decay, $2\nu\beta\beta$ can only be experimentally observed if the simple $\beta$ decay is energetically forbidden, as visualized in figure 2.8 (a). Based on the Bethe-Weizsäcker formula, the masses of nuclei with the same atomic mass number $A$ are represented as quadratic functions, which depend on the atomic number $Z$. For even mass numbers $A$ (either even-even or odd-odd nuclei) this splits into two parabolas with the odd-odd nuclei shifted towards higher masses due to the pairing term. Since a $\beta$ decay of an even-even nucleus must lead to the energetically lower odd-odd nucleus, simple $\beta$ decays might be forbidden, as marked in red in figure 2.8 (a). Instead, if the even-even nucleus is not the most stable isobar of the mass parabola, a $2\nu\beta\beta$ can occur. The isotopes for which a $2\nu\beta\beta$ has already been observed are listed with their corresponding $Q$ values in table 2.1.

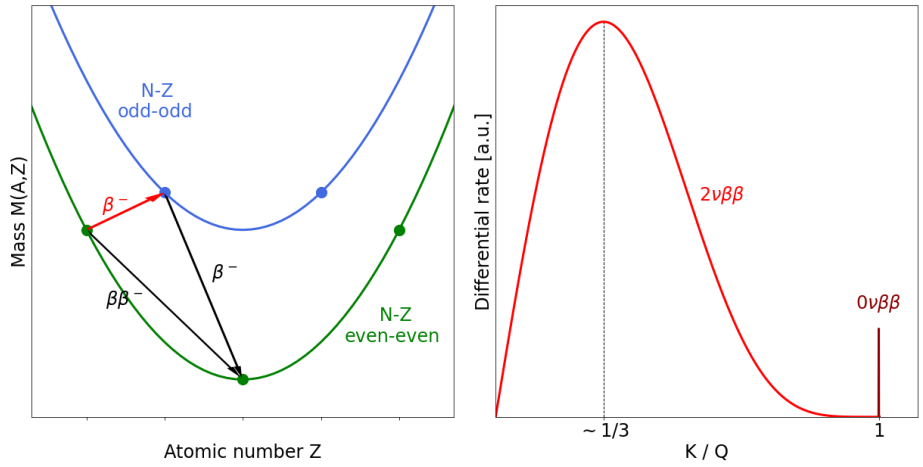


(a) (b)

**Figure 2.8:** (a) The nuclear mass $M$, depending on the atomic number $Z$, splits into two parabolas for nuclei with even mass number due to the pairing term of the Bethe-Weizsäcker formula. In red the energetically forbidden $\beta^-$ decay is marked. (b) Experimental signature of $2\nu\beta\beta$ (red) and the hypothetical $0\nu\beta\beta$ (dark red) from the kinetic energy $K$ deposited by the produced electrons. Since no energy is carried away by neutrinos in the $0\nu\beta\beta$ case, a sharp peak at the $Q$ value is expected, which will be smeared by the detector resolution. For visualization purposes the $0\nu\beta\beta$ rate is enlarged to an arbitrary scale.

The decay rate of $2\nu\beta\beta$, which corresponds to the inverse of its half-life $T^{2\nu}_{1/2}$, is calculated by

$$\frac{1}{T^{2\nu}_{1/2}} = G^{2\nu}|M^{2\nu}|^2 \ , \tag{2.20}$$

where $G^{2\nu}$ denotes the phase space factor and $M^{2\nu}$ the nuclear matrix element. Similarly, the decay rate of the hypothetical neutrinoless mode is determined by

$$\frac{1}{T^{0\nu}_{1/2}} = \frac{\langle m_{\beta\beta}\rangle^2}{m_e^2} G^{0\nu}|M^{0\nu}|^2 \ , \tag{2.21}$$

where $m_e$ is the electron mass. This equation shows that limits on the $0\nu\beta\beta$ half-life can be directly translated into exclusion limits on the effective neutrino Majorana mass $\langle m_{\beta\beta}\rangle$. The largest source of uncertainty stems from the theoretically not precisely predicted nuclear matrix element $M^{0\nu}$, which depends on the underlying theoretical model. A review of several approaches such as the interacting boson model, interacting shell model, or quasiparticle random phase approximation, together with their nuclear matrix element differences, can be found in [85].

Experimentally, $2\nu\beta\beta$ and $0\nu\beta\beta$ decays are distinguished by the sum of the electrons' kinetic energy $K$ deposited in the detector, as presented in figure 2.8 (b). In the $2\nu\beta\beta$, a fraction of the energy is carried away by neutrinos, which results in a continuous spectrum of $K$ with a maximum at $\sim 1/3$ of the decay's $Q$ value. In contrast, the electrons carry all the energy in $0\nu\beta\beta$ processes, which results in a monoenergetic peak at $Q_{\beta\beta}$, smeared only by the detector resolution.

**Table 2.1:** Isotopes undergoing double beta decay sorted by mass number with their $Q$ values and experimental neutrinoless $\tilde{T}^{0\nu}_{1/2}$ limits (90% C.L.). To compare the different results, the corresponding effective neutrino Majorana mass $\langle m_{\beta\beta} \rangle$ is included. $Q$ values from [86] and [87].

| **Isotope** | **Q value** [MeV] | $\tilde{\mathbf{T}}^{\mathbf{0\nu}}_{\mathbf{1/2}}$ [$\mathbf{10^{25}}$ **yr**] | $\langle \mathbf{m}_{\beta\beta} \rangle$ [**eV**] | **Ref.** |
|---|---|---|---|---|
| $^{48}$Ca | 4.263 | $> 5.8 \cdot 10^{-3}$ | $< (3.5 - 22)$ | [88] |
| $^{76}$Ge | 2.039 | $> 8.0$ | $< (0.12 - 0.26)$ | [89] |
| $^{82}$Se | 2.998 | $> 3.6 \cdot 10^{-2}$ | $< (0.89 - 2.43)$ | [90] |
| $^{96}$Zr | 3.348 | $> 9.2 \cdot 10^{-4}$ | $< (7.2 - 19.5)$ | [91] |
| $^{100}$Mo | 3.035 | $> 1.1 \cdot 10^{-1}$ | $< (0.33 - 0.62)$ | [92] |
| $^{116}$Cd | 2.813 | $> 2.2 \cdot 10^{-2}$ | $< (1.0 - 1.7)$ | [93] |
| $^{130}$Te | 2.527 | $> 3.2$ | $< (0.075 - 0.350)$ | [94] |
| $^{136}$Xe | 2.458 | $> 10.7$ | $< (0.061 - 0.165)$ | [95] |
| $^{150}$Nd | 3.371 | $> 2.0 \cdot 10^{-3}$ | $< (1.6 - 5.3)$ | [96] |

As listed in table 2.1, various experiments already set half-life exclusion limits for the $0\nu\beta\beta$ of several isotopes. For the calculation of such limits, the figure-of-merit estimator, proposed in [97], is commonly used. It describes the detector's capacity to maximize the $0\nu\beta\beta$ signal while minimizing the background and is defined as the decay's half-life. For a 90% confidence level (C.L.), it is given by [98]

$$\tilde{T}^{0\nu}_{1/2} = \ln 2 \, \frac{\varepsilon \cdot N_{\beta\beta} \cdot t}{1.64 \cdot n_B} \ , \tag{2.22}$$

where $\varepsilon$ is the signal detection efficiency, $N_{\beta\beta}$ the number of nuclei possibly decaying via $0\nu\beta\beta$, $t$ the measurement time, and $n_B$ the maximum number of events hidden by background fluctuations. Assuming a Poissonian distribution (valid for a non-zero background experiment) and the background scaling with the mass $M$ of the source, $n_B$ can be rewritten as $n_B = \sqrt{N_B} = \sqrt{b \cdot \Delta E \cdot t \cdot M}$. $N_B$ describes the number of background events, $\Delta E$ the width of the energy region of interest (ROI), and $b$ the background rate. Furthermore, $N_{\beta\beta} = \alpha \cdot f_{\mathrm{ROI}} \cdot N_A \cdot M/A$, where $\alpha$ denotes the abundance of the $0\nu\beta\beta$ candidate, $f_{\mathrm{ROI}}$ the fraction of the signal covered by the energy ROI, $A$ the molar mass of the decaying nucleus, and $N_A$ the Avogadro number. Inserting the expressions for $n_B$ and $N_{\beta\beta}$ in equation (2.22) results in

$$\tilde{T}^{0\nu}_{1/2} = \ln 2 \, \frac{\varepsilon \cdot \alpha \cdot f_{\mathrm{ROI}} \cdot N_A}{1.64 \cdot A} \sqrt{\frac{M \cdot t}{\Delta E \cdot b}} \ . \tag{2.23}$$

It shows that the highest half-life sensitivities can be achieved by a low-background, large-exposure, and high-energy resolution experiment. Isotopic enrichment further improves the half-life sensitivity, as applied by the EXO-200 experiment [99] and essentially any other dedicated $0\nu\beta\beta$ experiment.

An overview of the most recent $\tilde{T}^{0\nu}_{1/2}$ half-life limits for various $0\nu\beta\beta$ candidates is shown in table 2.1, ranging from $\mathcal{O}(10^{21}\,\mathrm{yr})$ to $\mathcal{O}(10^{26}\,\mathrm{yr})$. In order to compare the results of the different isotopes, the corresponding effective neutrino Majorana

masses are included as well. Table 2.1 shows that the best results stem from $^{76}$Ge and $^{136}$Xe experiments, where KamLAND-Zen provides the most stringent limits of $\langle m_{\beta\beta} \rangle < (61 - 165)\,\text{meV}$. This mass exclusion is visualized in figure 2.9, where the parameter space of $\langle m_{\beta\beta} \rangle$ vs. the mass of the lightest neutrino is shown together with the $2\sigma$ regions of the NO and IO neutrino scenarios. Planck and KATRIN additionally exclude masses $m_{\text{min}} > 0.1\,\text{eV}$ of the lightest neutrino. Next-generation $0\nu\beta\beta$ experiments will reach sensitivities covering the inverted ordering parameter space (marked in yellow) and thus might allow concluding on one neutrino ordering scenario. Examples are the future experiments LEGEND-1000 and nEXO, where the former uses $^{76}$Ge and the latter $^{136}$Xe as $\beta\beta$ isotope. LEGEND-1000 is designed to reach a $3\sigma$ discovery sensitivity of $\tilde{T}^{0\nu}_{1/2} = 1.2 \cdot 10^{28}\,\text{yr}$ translating to $\langle m_{\beta\beta} \rangle < (10 - 20)\,\text{meV}$ [100]. nEXO aims for $\tilde{T}^{0\nu}_{1/2} = 5.7 \cdot 10^{27}\,\text{yr}$ and $\langle m_{\beta\beta} \rangle < (7.3 - 22.3)\,\text{meV}$ [101].

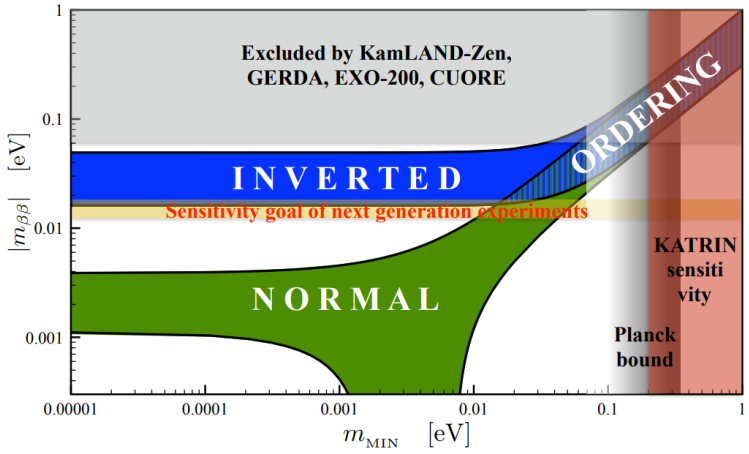


**Figure 2.9:** Effective neutrino Majorana mass $\langle m_{\beta\beta} \rangle$ plotted vs. the mass of the lightest neutrino. The blue/green area marks the $2\sigma$ regions of the inverted/normal neutrino ordering scenario as obtained from neutrino oscillations. Planck and KATRIN exclude lightest neutrino masses of $m_{\text{min}} > 0.1\,\text{eV}$; $0\nu\beta\beta$ experiments exclude effective neutrino masses $\langle m_{\beta\beta} \rangle > 60\,\text{meV}$. Next-generation $0\nu\beta\beta$ experiments will reach sensitivities beyond the inverted ordering scale, marked in yellow. Figure from [102].

### Double electron capture

Similar to the $\beta^-\beta^-$ decays and the forbidden simple $\beta^-$ decay visualized in figure 2.8 (a), the proton-rich right side of the mass parabola also includes energetically forbidden EC or $\beta^+$ decays, where two simultaneous transitions are allowed instead. This includes $2\nu$ECEC, $2\nu\beta^+EC$, and $2\nu\beta^+\beta^+$, with the first decay being discussed in more detail in the following. With their hypothetical neutrinoless modes, similar conclusions on the neutrino nature as for $0\nu\beta^-\beta^-$ decays could be drawn.

The $2\nu$ECEC, as described by equation (2.16), has already been measured for several isotopes, including $^{124}$Xe (first observed by XENON1T [80]), which will be introduced in more detail in the following: The two captured electrons stem in

76.6% of the cases [103] from the innermost K-shell, causing the vacancies of the daughter atom to be filled subsequently by higher-order shell electrons. Since neutrinos carry away most energy in this two-neutrino decay, the resulting cascade of X-rays and Auger electrons constitute the only experimentally accessible signature. They cause an energy deposition of $E_{2K} = (64.457 \pm 0.012)\,\mathrm{keV}$ [104]. For the hypothetical $0\nu$ECEC transition, however, the energy has to be transferred to a matching excited state of the daughter nucleus since no neutrinos are produced. The subsequent $\gamma$ emission with the total excitation energy $E_{\mathrm{exc}}$ occurs in addition to the Auger electrons and X-rays emitted during filling the K-shell vacancies. In this decay mode the total $Q$ value energy is deposited within the detector. For $^{124}$Xe, with the decay scheme shown in figure 2.10, this adds up to an energy of $Q = (2856.73 \pm 0.12)\,\mathrm{keV}$ [104]. Due to the energy mismatch of

$$\Delta E = Q - E_{2K} - E_{\mathrm{exc}} = (1.86 \pm 0.15)\,\mathrm{keV} \tag{2.24}$$

between the available energy and the excited state of the daughter nucleus $^{124}$Te [104], the $0\nu$ECEC of $^{124}$Xe is suppressed by a resonance factor $R$ [105]:

$$R = \frac{m_e\, c^2\, \Gamma}{(\Delta E)^2 + \Gamma^2/4} = 2.92 \pm 0.47 \ , \tag{2.25}$$

where $m_e$ is the electron mass and $\Gamma = 0.0198\,\mathrm{keV}$ [106] the two-hole width. This factor $R$ has to be considered when translating the half-life exclusion limit of $0\nu$ECEC to exclusions on the effective neutrino Majorana mass:

$$\frac{1}{T^{0\nu}_{1/2}} = \frac{\langle m_{\beta\beta}\rangle^2}{m_e^2} G^{0\nu} |M^{0\nu}|^2 R \ . \tag{2.26}$$

Further information on the resonance factor and the $0\nu$ECEC nuclear matrix element predictions can be found in [105].

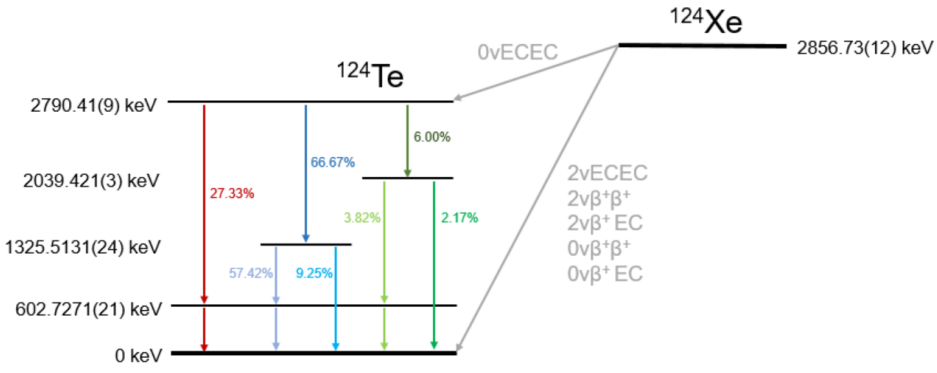


**Figure 2.10:** $^{124}$Xe decay scheme including the hypothetical neutrinoless modes $0\nu$ECEC, $0\nu\beta^+\beta^+$, and $0\nu\beta^+$EC. Data from [107].

### 2.2.2 Astrophysical neutrinos

Multi-tonne DM detectors also allow gaining knowledge about the sources of astrophysical neutrinos: solar, atmospheric, and supernova neutrinos. Solar neutrinos are discussed in more detail in the following since their rate is several orders of magnitude higher than that of atmospheric and supernova neutrinos, for which we refer to [108] and [109]. Multi-tonne DM detectors with their high target mass, ultra-low background environment and very low thresholds are very well equipped for their observation, even though neutrinos only weakly interact with luminous matter.

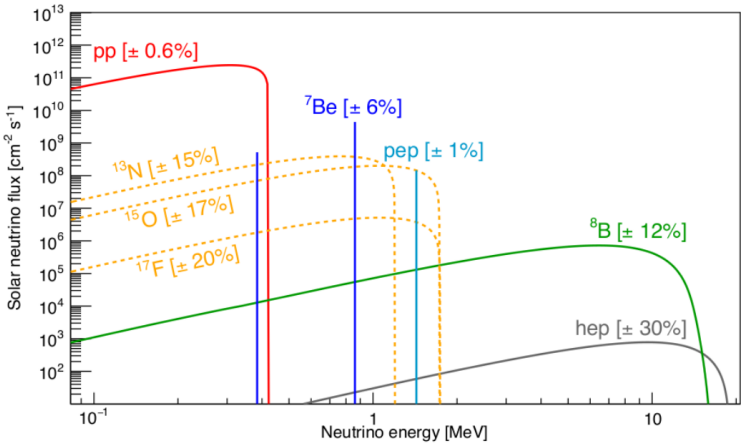


**Figure 2.11:** Solar neutrino fluxes per neutrino source as fraction of the neutrino energy. The relative flux uncertainties are given in brackets. Figure from [110].

A variety of neutrinos with different rates and energies are emitted by the Sun. They are produced in one of the several hydrogen-burning steps, the Sun's energy production mechanism. This includes the *pp* chain, which accounts for $\sim 99\%$ of the Sun's released energy, and the carbon–nitrogen–oxygen (CNO) cycle, which contributes the remaining 1% [110]. For the *pp* chain, this includes *pp*, $^{8}$B, and *hep* neutrinos with their characteristic energy spectra presented in figure 2.11, as well as the monoenergetic $^{7}$Be (2 lines) and *pep* neutrinos. The neutrinos emitted within the CNO cycle stem from $\beta^{+}$ decays of $^{13}$N, $^{15}$O, and $^{17}$F. Their energy spectra are also included in figure 2.11.

The experimental signature of astrophysical neutrinos in Earth-based DM detectors depends on their type of interaction. Solar neutrinos with energies at the MeV scale can either scatter elastically with the electrons of the detection medium, causing an electronic recoil (ER), or by coherent elastic neutrino-nucleus scattering (CE$\nu$NS), causing a nuclear recoil (NR). The corresponding cross-sections of these two interaction types are strongly energy-dependent and vary by several orders of magnitude. Since only part of the neutrino's kinetic energy is deposited within these scattering processes, the resulting recoil spectrum ranges up to the neutrino's characteristic $Q$ value. Their differential recoil rate $\frac{dR}{dE_r}$ is calculated by

$$\frac{dR^{\mathrm{ER}}}{dE_r} = N_e \sum_j \int P_{ej} \frac{d\Phi}{dE_\nu} \frac{d\sigma_j}{dE_r} dE_\nu \ , \tag{2.27}$$

assuming an elastic ER. $N_e$ describes the number of target electrons, $P_{ej}$ the probability of $\nu_e$ oscillating to lepton flavor $j$, $\frac{d\Phi}{dE_\nu}$ the spectral flux, and $\frac{d\sigma_j}{dE_r}$ the differential cross-section. Similarly, the NR rate for CE$\nu$NS is determined by

$$\frac{dR^{\mathrm{NR}}}{dE_r} = N_n \int_{E_{\mathrm{min}}}^{\infty} \frac{d\Phi}{dE_\nu} \frac{d\sigma}{dE_r} dE_\nu \ , \tag{2.28}$$

where $N_n$ denotes the number of target nucleons and $E_{\mathrm{min}} = \sqrt{ME_r/2}$ the minimal neutrino energy required for a given recoil energy $E_r$ and nucleus mass $M$. Even though CE$\nu$NS has not yet been detected for astrophysical neutrinos, this process is predicted by the SM and was first observed by COHERENT in 2017 using a CsI[Na] scintillation crystal exposed to a high flux of neutrinos produced at the Spallation Neutron Source at Oak Ridge National Laboratory [111].

Elastic electron scatterings of solar neutrinos, in contrast, were already observed by a variety of experiments using water, heavy water, and liquid scintillator targets: Borexino measured *pp* [112], *pep* [113], $^7$Be [114], CNO [110], and $^8$B [115] neutrinos. However, other experiments like SNO [116], SNO+ [117], KamLAND [118], and Super-Kamiokande [119] also showed their capability of detecting solar neutrinos. Current- and next-generation multi-tonne DM detectors will reach sensitivities, which will also allow for their detection. These measurements can be used to draw further conclusions on electroweak and oscillation parameters such as the $\nu_e$ survival probability $P_{ee}$ or to obtain important information about the solar abundance problem [120].

# Chapter 3

# The DARWIN project

The noble gas xenon is widely used as a detection medium in astroparticle and particle physics due to its excellent scintillation and ionization properties. It will be employed by the future DARWIN experiment, which plans to operate a dual-phase xenon TPC with a 40 t LXe target to search for WIMPs scattering off xenon nuclei [7]. Due to the irreducible background from CE$\nu$NS, the so-called *neutrino floor* [8], and DARWIN's expected excellent sensitivity of detecting these neutrino interactions, it is also referred to as the *ultimate* DM detector. A DARWIN-size xenon TPC, characterized by its very low background, low energy threshold, large target mass, and good energy resolution, will also provide the possibility for further physics objectives, such as the detection of the $0\nu\beta\beta$ of $^{136}$Xe or elastic $\nu$-electron scattering of solar neutrinos. These objectives are described in more detail in the following chapter, which serves as a basis for both main chapters of this thesis: the investigations of DARWIN's science channels and the characterization of the small-scale hermetic TPC. First, xenon as target material, its particle interaction processes, and the working principle of a TPC are introduced in section 3.1. The DARWIN observatory with its various science channels and expected backgrounds is presented in section 3.2. The detector's start of data taking is planned in 2027 and its design is not finalized yet, but the baseline assumptions are shown.

Dual-phase xenon TPCs have extensively evolved during the last 20 years, as demonstrated by DARWIN's predecessors within the XENON Dark Matter Project [121, 122, 123, 3, 4]. The XENON10 experiment started in 2006 at the Laboratori Nazionali del Gran Sasso (LNGS), an underground laboratory with $\sim$ 3600 meter water-equivalent (m.w.e.) rock overburden. This experiment location was also chosen for all successive detectors. With its 15 kg xenon target and 59 d of data, XENON10 successfully demonstrated the detector technology's functionality and reached SI WIMP-nucleon cross-sections of down to $4.5 \cdot 10^{-44}\,\mathrm{cm}^2$ for WIMP masses of $30\,\mathrm{GeV}/c^2$ [122] in 2008. Similar exclusion limits were reported by ZEPLIN-III in 2012 [124] with cross-sections down to $4.8 \cdot 10^{-44}\,\mathrm{cm}^2$ for $50\,\mathrm{GeV}/c^2$ WIMPs. With an improved background reduction by a factor of 100 compared to XENON10 and an increased exposure of $48\,\mathrm{kg} \times \mathrm{yr}$, the XENON100 detector excluded SI WIMP-nucleon cross-sections with a minimum of $1.1 \cdot 10^{-45}\,\mathrm{cm}^2$ at $50\,\mathrm{GeV}/c^2$ in 2016 [123], which was further improved to $1.1 \cdot 10^{-46}\,\mathrm{cm}^2$ at $50\,\mathrm{GeV}/c^2$ by LUX in

2017 [60]. In 2018, XENON1T provided the currently world-best cross-sections limits of $4.1 \cdot 10^{-47}\,\mathrm{cm}^2$ at $30\,\mathrm{GeV}/c^2$ with an exposure of $1.0\,\mathrm{t} \times \mathrm{yr}$ [3]. In a preprint, PandaX-4T claims an improved limit of $3.3 \cdot 10^{-47}\,\mathrm{cm}^2$ at $30\,\mathrm{GeV}/c^2$ [6]. XENONnT, the updated and enlarged version of XENON1T, is currently recording data and is expected to reach SI cross-sections of down to $1.4 \cdot 10^{-48}\,\mathrm{cm}^2$ for $50\,\mathrm{GeV}/c^2$ WIMP masses after a $20\,\mathrm{t} \times \mathrm{yr}$ exposure [4].

Besides its excellent sensitivity for the DM search, XENON1T observed the $2\nu$ECEC of $^{124}$Xe, yielding the longest ever directly measured half-life of $(1.8 \pm 0.5_{\mathrm{stat}} \pm 0.1_{\mathrm{sys}}) \cdot 10^{22}\,\mathrm{yr}$ [80]. This finding serves as a basis for the investigations described in section 4.5 of DARWIN's sensitivity to the hypothetical neutrinoless mode. Furthermore, it showcases the great possibility of rare event searches beyond DM utilizing LXe TPCs.

## 3.1 Particle detection with liquid xenon

In the following section the target material xenon is introduced and its several advantageous properties are listed. After a detailed explanation of particle interaction processes in LXe, causing particularly scintillation and ionization signals, the working principle of a TPC is presented. Thereby, the signal formation and its readout, as well as possible background reductions are discussed.

### 3.1.1 Liquid xenon properties and particle interactions

Xenon is the fifth and heaviest noble gas with stable isotopes. Its high atomic mass of $131\,\mathrm{g/mol}$ [9] enhances SI WIMP-nucleus cross-sections due to the sensitivity's proportionality to $A^2$, see equation (2.10). Compared to the noble gas argon, also commonly used in astroparticle physics, xenon shows an $\sim 10$ times higher cross-section for these DM interactions.

Xenon contains several isotopes, listed in table 3.1 with their natural abundance and nuclear spin [9, 125]. This includes $^{129}$Xe and $^{131}$Xe with unpaired spins, allowing the search for SD DM interactions. Additionally, the non-stable isotopes $^{124}$Xe and $^{136}$Xe open the possibility for rare event searches beyond the DM detection: $^{124}$Xe decays via $2\nu$ECEC with a half-life of $1.8 \cdot 10^{22}\,\mathrm{yr}$ [80] and $^{136}$Xe via $2\nu\beta\beta$ and a half-life of $2.1 \cdot 10^{21}\,\mathrm{yr}$ [126]. Details about DARWIN's sensitivity to the hypothetical neutrinoless processes are presented in sections 4.4 and 4.5.

LXe's density of $2.95\,\mathrm{g/cm}^3$ at its boiling point of $165\,\mathrm{K}$ and atmospheric pressure [125] implies a high stopping power. This self-shielding ability allows the reduction of external backgrounds, like penetrating $\gamma$ particles or neutrons, by cutting events near the detector walls, called *fiducialization*. E.g., a $2.5\,\mathrm{MeV}$ $\gamma$, a typical background in the $0\nu\beta\beta$ search introduced later, shows a mean free path of $\mathcal{O}(10\,\mathrm{cm})$ in LXe [127]. Additionally, xenon's high density allows the construction of compact detectors.

**Table 3.1:** Natural xenon isotopes and their properties. $^{129}$Xe and $^{131}$Xe enable SD DM searches, $^{124}$Xe and $^{136}$Xe allow for rare event searches beyond DM interactions. Data from [9, 125].

| Isotope | Abundance [%] | Nuclear Spin (I) |
|---|---|---|
| $^{124}$Xe | 0.09 | 0 |
| $^{126}$Xe | 0.09 | 0 |
| $^{128}$Xe | 1.92 | 0 |
| $^{129}$Xe | 26.44 | 1/2 |
| $^{130}$Xe | 4.08 | 0 |
| $^{131}$Xe | 21.18 | 3/2 |
| $^{132}$Xe | 26.89 | 0 |
| $^{134}$Xe | 10.44 | 0 |
| $^{136}$Xe | 8.87 | 0 |

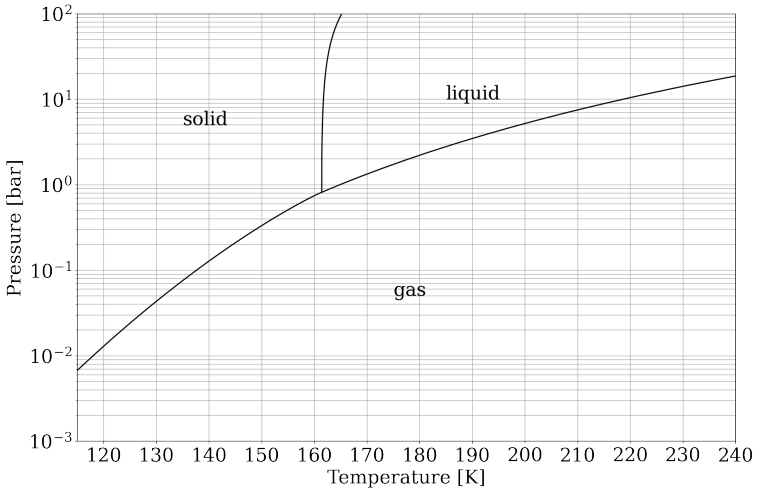


**Figure 3.1:** Xenon phase diagram with its triple point at $T = 161.4\,\mathrm{K}$ and $p = 0.82\,\mathrm{bar}$. LXe TPCs are typically operated at $\sim 2\,\mathrm{bar}$ and $\sim 175\,\mathrm{K}$. Data from [128].

Xenon liquefaction temperatures and the corresponding pressures are presented in the phase diagram of figure 3.1. Xenon boils at temperatures above 160 K, relatively high compared to other cryogenic fluids. This allows cooling mechanisms based on liquid nitrogen ($LN_2$) as applied for the XeBRA platform, introduced in chapter 5. Typically, LXe TPCs are operated at $\sim 2\,\mathrm{bar}$, which leads to temperatures of $\sim 175\,\mathrm{K}$.

Xenon has excellent scintillation and ionization properties and is transparent to its scintillation light at 175 nm [129]. The dissimilar scintillation and ionization yields for different kinds of recoils, ER (interaction with xenon shell electrons) and NR (interactions with xenon nuclei), enables their discrimination [125]. Last-generation experiments typically reached ER event discrimination efficiencies of $> 99.5\%$ at 50% NR acceptance [130, 61, 131].

Particle interactions with xenon, either with its nucleus or electrons, produce heat, scintillation light, and ionization charge, with the number of generated quanta depending on the transferred energy. TPCs, as utilized, e.g., by DARWIN,

XENON [121], or LZ [5], only exploit the information from excitation (Xe*) and ionization ($Xe^+$). Since ERs and NRs differ in the fraction of energy transferred to the three channels heat, charge, and light, they show different signal strengths in LXe TPCs. While ERs produce negligible heat, the fraction of atomic motion for low-energy NRs is significant. The quenching factor $L$, describing the fraction of energy left for ionization and scintillation processes, is energy- and target material-dependent [49] and has to be taken into account when comparing energy spectra of ER and NR interactions.

In the following the reactions after the initial xenon excitation and ionization causing the release of xenon's characteristic scintillation light are explained. The produced excited xenon atoms Xe*, the *excitons*, collide with neighboring xenon atoms and combine to excited dimers $Xe_2$*, the *excimers*:

$$Xe^* + Xe \rightarrow Xe_2^* \ . \tag{3.1}$$

During the decays of these excimers with a half-life of $(3.1 \pm 0.7)$ ns and $(24 \pm 1)$ ns [132] corresponding to the decay of the spin-singlet and spin-triplet states, respectively, the xenon-characteristic scintillation light is released:

$$Xe_2^* \rightarrow 2\ Xe + h\nu \ . \tag{3.2}$$

Its wavelength of around 175 nm [133] in the vacuum ultra-violet (VUV) range corresponds to a photon energy of 7 eV. In principle, the singlet and triplet states could be utilized for particle discrimination since their ratio depends on the type of recoil. Due to their half-lives of $\mathcal{O}$(ns), this technique is rather exploited in argon-based detectors. E.g., DEAP-3600 shows excellent *pulse shape discriminations* with an ER rejection power of $\sim 3 \cdot 10^8$ for NR acceptances of $> 90\%$ [134] due to the argon triplet state's half-life of approximately 1600 ns [135], more than two orders of magnitude longer than the singlet state's half-life. Consequently, the scintillation light signals in argon are much longer than in xenon-based detectors.

Since xenon is not only excited but also ionized by particle interactions, free electrons are generated. They can be drifted away from the interaction point by means of an electric field, allowing the generated $Xe^+$ ions to form $Xe_2^+$ molecules with neighboring atoms:

$$Xe^+ + Xe \rightarrow Xe_2^+ \ . \tag{3.3}$$

These molecules can recombine with the electrons, where the recombination probability decreases with an increased electric field and lower electron-ion density. By recombining excited xenon atoms are generated, and via the production of an excimer, VUV photons are released:

$$Xe_2^+ + e^- \rightarrow Xe^{**} + Xe \tag{3.4}$$

$$Xe^{**} \rightarrow Xe^* + \text{heat} \tag{3.5}$$

$$Xe^* + Xe \rightarrow Xe_2^* \tag{3.6}$$

$$Xe_2^* \rightarrow 2\ Xe + h\nu \ . \tag{3.7}$$

The liberated electrons, which are not captured by $Xe^+$ ions and therefore do not cause this series of reactions, generate an additional signal in TPCs, discussed in the next section.

In high-excitation densities *bi-excitonic quenching* has to be taken into account. This process describes the collision of two excitons, which produce an electron-ion pair as well as a xenon atom:

$$Xe^* + Xe^* \rightarrow Xe + Xe^+ + e^- \quad . \tag{3.8}$$

Here, only one VUV $\gamma$ is released, lowering the number of produced photons by one compared to the reactions shown above. In [136] this effect is considered to be the main mechanism responsible for the low scintillation yields of NRs.

One of xenon's most essential properties, the transparency to its own scintillation light, is presented in equations (3.2) and (3.7): the VUV photons are not released by the atoms but by the excimers. Due to their different energy level configurations, the photons emitted by the excimers are not absorbed by the xenon atoms.

### 3.1.2 Working principle of a time projection chamber

The working principle of a dual-phase time projection chamber (TPC) is depicted in figure 3.2. A LXe phase makes up most of the detector's volume and serves as a target for DM or other rare interaction processes. At the top and bottom of the cylindrical TPC, photosensors are placed for the light readout. The most common TPC photosensor is a photomultiplier tube (PMT). PMTs are also chosen for DARWIN's baseline design as presented in section 3.2.2, used for the sensitivity studies in chapter 4, and are implemented in the small-scale hermetic TPC characterized in chapter 5. Alternatives like a silicon photomultiplier (SiPM) are mentioned in section 3.2.2.

As described in section 3.1.1, a particle interacting with the xenon target produces VUV light due to excitation and electron-ion pairs due to ionization. The prompt scintillation light, the *S1 signal*, is detected by the PMTs on the top and bottom of the TPC. Since the ionization electrons might recombine with the xenon ions, the signal is further strengthened. Its signal size depends on the geometrical light collection efficiency (LCE), describing the probability of photons traveling from the interaction point to the PMT's photocathode, the quantum efficiency (QE), the chance of releasing a photoelectron (PE) at the photocathode, and the collection efficiency (CE), the PE's probability of being collected and further accelerated.

The electrons liberated in the initial interaction are drifted upwards by an electric field $E_{\text{drift}}$. This drift field is applied between a negatively biased cathode at the bottom of the TPC and a grounded gate electrode located a few millimeters below the LXe surface. The region between these two electrodes is referred to as the *active/sensitive volume* or *xenon target*. After the transit through the gate electrode, which is optimized for transparency (e.g., an optical transparency

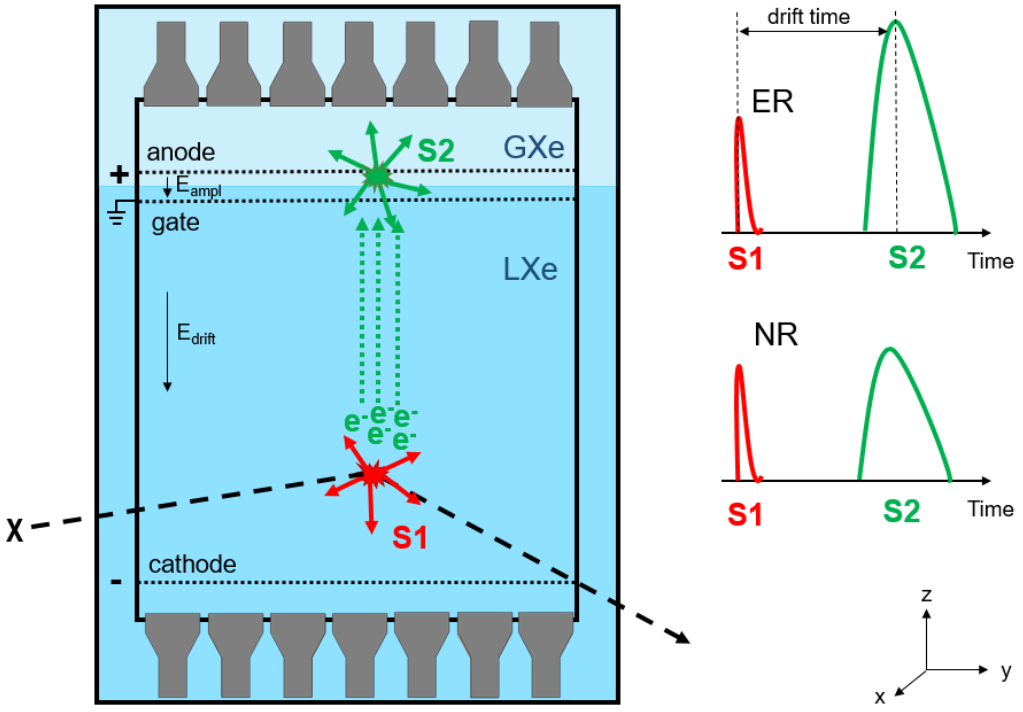


**Figure 3.2:** Working principle of a dual-phase xenon TPC: an interacting particle X excites the xenon target, leading to the prompt S1 signal, and also ionizes it, causing a delayed, charge-proportional S2 signal. Both signals are detected by photosensors installed at the top and bottom of the TPC. The three-dimensional interaction position is determined by the drift time ($z$) and the top photosensor's hit pattern ($x$-$y$). The charge to light ratio S2/S1 allows the recoil type identification, which is expected to be higher for ERs than for NRs.

of $\sim 96\%$ is reached in XENONnT [4]), the drifted electrons reach the liquid-gas interface. There they are extracted to the xenon gas phase by a second stronger electric field, the amplification field $E_{\text{ampl}}$. The extraction efficiency depends on the field strength between the gate and the positively biased anode electrode in the gaseous xenon (GXe), which are typically installed a few millimeters apart from each other. For electric fields of $E_{\text{ampl, GXe}} = 10\,\text{kV/cm}$ in the gas phase, 100% efficiency is achieved [125]. During the electrons' further acceleration in the gas, their collisions with xenon atoms lead to xenon's excitation and, therefore, the generation of VUV photons. The produced light detected by the photosensors, the *S2 signal*, is proportional to the number of extracted electrons and expressed by [125]:

$$N_\gamma = \alpha\, N_{e^-}\, (E_{\text{ampl, GXe}}/p - \beta)\, p\, d \ , \tag{3.9}$$

where $p$ is the gas pressure, $d$ the gas gap thickness between the phase boundary and the anode, $\alpha$ the amplification factor, and $\beta$ the threshold of the reduced field for electroluminescence.

The advantage of utilizing a TPC is its two-signal response, which allows for the reconstruction of the interaction position in all three dimensions: the $z$ position is calculated by the time difference between the S1 and S2 signals, the *drift time*,

and the $x$-$y$ location is derived from the top photosensors' S2 hit pattern. This allows background reduction near the detector boundaries by fiducializing the target volume. For DARWIN drift times of up to $\mathcal{O}(2\,\mathrm{ms})$ are expected, whereas the small-scale HUsXe shows drift times of up to $\mathcal{O}(40\,\mu\mathrm{s})$. Their position reconstruction resolution is, e.g., affected by xenon-intrinsic effects such as diffusion [137, 138] or the S2 signal strength. For DARWIN a position resolution of $\sigma_{xy} = \sigma_z = 10\,\mathrm{mm}$ is assumed for ER energies of $> 2\,\mathrm{MeV}$ [10].

Furthermore, the position reconstruction allows the discrimination between *single scatter (SS)* and *multiple scatter (MS)* events. Due to the WIMPs' and neutrinos' tiny interaction cross-sections, these particles are not expected to scatter twice within the TPC target. Since a significant fraction of background-induced photons and neutrons generate MS events, SS/MS discrimination allows further background mitigation. For position interaction differences larger than the position resolution, an event signature with several S2 signals and one S1 signal is seen. The S1 caused by the individual interactions overlap due to the photons traveling with the speed of light.

The S1 and S2 signals are used to calculate the deposited energy (excluding the part transferred by heat), called the *combined energy scale (CES)* [139, 140]:

$$E = W \cdot (n_\gamma + n_{e^-}) = W \cdot \left( \frac{S1}{g_1} + \frac{S2}{g_2} \right) \quad . \tag{3.10}$$

$W$ is the average energy to generate a quantum, $n_\gamma$ the number of produced scintillation photons, and $n_{e^-}$ the number of produced electrons. The detector-inherent gains $g1$ and $g2$ describe the photon detection efficiency and the effective charge gain, respectively. As indicated by the right side of equation (3.10), the CES exploits the anti-correlation of the S1 and S2 signals, which is both drift field- and energy-dependent.

## 3.2 The DARWIN observatory

In the following section the next-generation LXe-based ultimate DM detector DARWIN [7] is introduced. Besides a short overview of its science channels and expected backgrounds, the detector geometry is discussed. However, DARWIN's design is not finalized yet, and several of its systems are still subject to active R&D efforts.

### 3.2.1 Physics objectives

A comprehensive and detailed overview of the rich science portfolio addressed by a next-generation multi-tonne LXe detector such as DARWIN is given in [141]. This section summarizes the physics objectives and sensitivities for a 40 t DARWIN detector, including DM, neutrino, and nuclear physics.

DARWIN's main science goal, the direct detection of WIMP-nucleus interactions, is expected to yield SI WIMP-nucleon cross-sections sensitivities of down to $2.5 \cdot 10^{-49}\,\mathrm{cm}^2$ for WIMP masses of $40\,\mathrm{GeV}/c^2$ [7] (90% C.L.), as shown in figure 3.3. Such cross-sections cover most of the experimentally accessible parameter space, which is limited by the neutrino floor [8], describing the irreducible CE$\nu$NS background. Compared to the current limits set by XENON1T and PandaX-4T, DARWIN's sensitivity improves by two orders of magnitude. An improvement by a factor of $\sim 10$ is expected compared to experiments currently taking data such as XENONnT or LZ. The underlying study presented in [142] assumes a 50 t/40 t/30 t total/active/fiducial mass, respectively, and an exposure of $200\,\mathrm{t} \times \mathrm{yr}$. For the discrimination of ER and NR signals, where the latter type of interaction is expected for WIMPs, a 99.98% ER rejection at 30% NR acceptance is assumed. Such a discrimination power was already shown by ZEPLIN-III [143]. The considered backgrounds expected for DARWIN are listed in section 3.2.3.

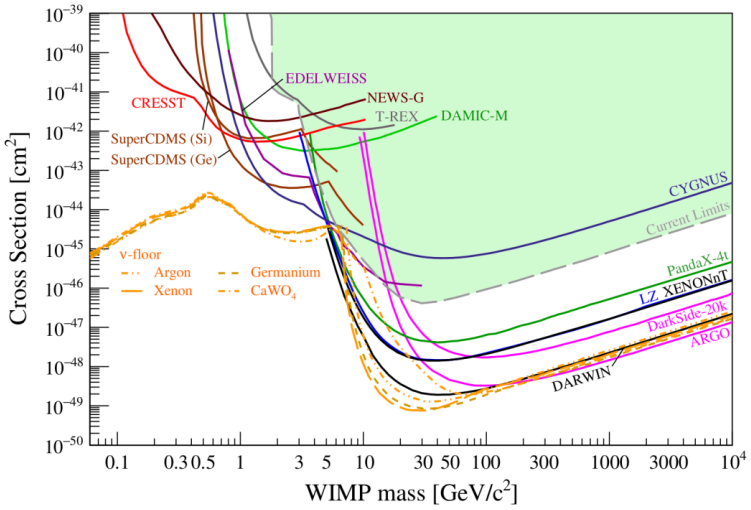


**Figure 3.3:** Spin-independent WIMP-nucleon scattering sensitivities for various past-, current-, and next-generation experiments. In orange the irreducible neutrino background caused by CE$\nu$NS is shown for different target materials. DARWIN, as the ultimate LXe-based DM detector, aims to reach sensitivities down to the neutrino floor with a $200\,\mathrm{t} \times \mathrm{yr}$ exposure. Figure from [2].

For the SD WIMP-neutron sensitivity, exploiting the non-zero spin of the $^{129}$Xe and $^{131}$Xe nuclei, sensitivities down to $2 \cdot 10^{-44}\,\mathrm{cm}^2$ at WIMP masses of $50\,\mathrm{GeV}/c^2$ (90% C.L.) are predicted [142]. For a large mass range, these cross-sections are complementary to the sensitivity of the 14 TeV center-of-mass energy LHC [144]. Besides WIMPs also other particles such as solar axions and axion-like particles (ALP) are possible DM candidates. DARWIN searches for them through the inverse Primakoff [145] and axio-electric effects [146], which cause low-energy signatures. Assuming a $200\,\mathrm{t} \times \mathrm{yr}$ exposure, DARWIN is expected to exclude solar axion-electron couplings of $g_{Ae}^{\mathrm{solar}} > 1 \cdot 10^{-12}$ in a mass range of $10^{-5} < m_A < 1\,\mathrm{keV/c^2}$ (90% C.L.) [7]. Compared to XENON100, this yields a sensitivity improvement of about a factor 4 [147]. With the same exposure, the sensitivity to ALPs is expected to improve the XENON100 result by two orders of magnitude, excluding ALP-electron couplings of $g_e^{\mathrm{ALP}} > 2 \cdot 10^{-14}$ in a mass range of $1 < m_A < 40\,\mathrm{keV}/c^2$ [7] (90% C.L.).

In addition to DARWIN's excellent sensitivity to DM interactions, it can also probe the possible Majorana nature of neutrinos and the neutrino hierarchy, compare to section 2.2. One possibility for such an investigation is the search for the $0\nu\beta\beta$, a hypothetical lepton number-violating process. The unstable xenon isotope $^{136}$Xe, with its natural abundance of 8.9% [125], constitutes an excellent candidate. Its two-neutrino mode $2\nu\beta\beta$ was first measured by EXO-200 [79], with an improved half-life of $(2.165 \pm 0.016_{\text{stat}} \pm 0.059_{\text{sys}}) \cdot 10^{21}$ yr reported in [126]. DARWIN's projected half-life sensitivity to $^{136}$Xe's $0\nu\beta\beta$ of $2.4 \cdot 10^{27}$ yr (90% C.L.) as published in [10] is competitive to dedicated $0\nu\beta\beta$ experiments with enriched xenon targets. A further opportunity to investigate the Majorana nature of neutrinos is through the $0\nu$ECEC of $^{124}$Xe. $^{124}$Xe has a natural abundance of 0.09% [125] and the two-neutrino process $2\nu$ECEC was detected by XENON1T [80]. For DARWIN a half-life sensitivity to $0\nu$ECEC of $\mathcal{O}(10^{26}\,\text{yr})$ is projected.

DARWIN is expected to measure five different solar neutrino components through elastic $\nu$-electron scatterings, namely *pp*, $^{7}$Be, $^{13}$N, $^{15}$O and *pep* neutrinos. Their detection opens the possibility for new insights into the Sun's energy production. High-statistics measurements of *pp* neutrinos can also be used to calculate the electron-neutrino survival probability $P_{ee}$ in a not yet measured neutrino energy range. Further details can be found in [11].

Neutrinos of all flavors are emitted during core-collapse supernovae and can be detected via CE$\nu$NS in DARWIN, where the calculated neutrino energy can be used to constrain the energy of the explosion. DARWIN will be sensitive to supernova bursts up to 65 kpc from the Earth with $> 5\sigma$ significance [109]. Additionally, atmospheric neutrinos are expected to cause CE$\nu$NS. A study presenting their detection for next-generation xenon experiments is given in [108], suggesting that a $500\,\text{t} \times \text{yr}$ exposure is needed for a $5\sigma$ detection of these neutrinos.

Several of the mentioned physics objectives are addressed in the presented thesis: section 4.3 reports on an updated NR background for the WIMP search, which provides essential feedback for realizing the DARWIN detector. The sensitivities to the hypothetical processes $0\nu\beta\beta$ of $^{136}$Xe and $0\nu$ECEC of $^{124}$Xe are derived in sections 4.4 and 4.5. DARWIN's expected measurements of different solar neutrino types are shortly summarized in section 4.6.

### 3.2.2 DARWIN baseline design

DARWIN's R&D phase is ongoing and its technical and conceptual design is not finalized yet. However, its current baseline geometry is described in the following. This geometry is used in the presented work for both the science channel sensitivities reported in chapter 4, as well as the expected radon concentration when assuming a hermetic DARWIN TPC in chapter 5.

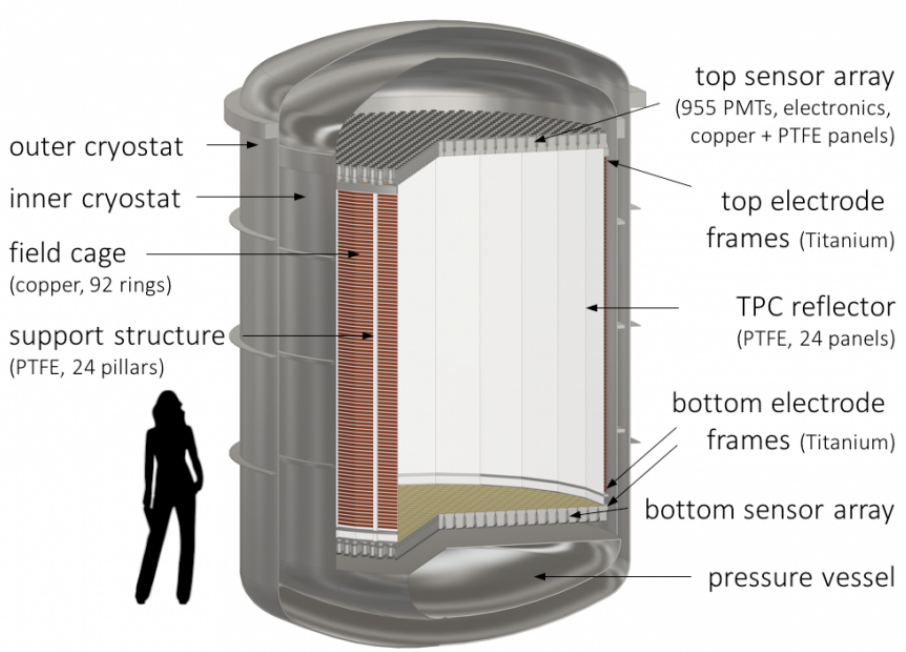


**Figure 3.4:** DARWIN baseline design sketch. The TPC (ø 2.6m × 2.6 m) consisting of the shown components accommodates 40 t LXe and is enclosed within a double-walled titanium cryostat.

A sketch of the DARWIN geometry is shown in figure 3.4. Its dual-phase xenon TPC contains a 40 t LXe target in a ø 2.6m × 2.6 m cylinder and is housed in a double-walled cryostat made of high-purity titanium. To minimize the cryostat material, torispherical domes and stiffening rings are included. Additionally, a pressurizable vessel is placed at the inner cryostat's floor to replace the unused xenon there. 10 t of xenon are used as a passive shielding between the TPC and the cryostat.

Due to its high reflectance > 97% [148] for 175 nm [133] VUV scintillation light, PTFE sheets of 3 mm thickness build the TPC walls. Additionally, PTFE pillars support the TPC structure and hold copper rings. These copper *field shaping electrodes* are installed at equal distances between the gate and cathode electrodes, connected by resistors, and ensure a uniform drift field. The electrodes' design is still under investigation; in the baseline design they are supported by titanium frames. On the one hand, these electrodes need to be highly transparent, and, on the other hand, electrostatic or gravitational sagging needs to be avoided. To investigate electrode designs, the DARWIN full-diameter detector test platform PANCAKE was built by the Freiburg Astroparticle Physics group. The Zurich group operates the full-drift length DARWIN demonstrator Xenoscope [149] for investigating, e.g., the required high electron lifetimes for drifts over several meters.

Photosensors recording the scintillation and ionization signals are placed at the top and bottom of the TPC together with their copper support structure and PTFE reflector disk. In the shown geometry, 1910 Hamamatsu R11410 3-inch PMTs [150] are assumed, the same type of photosensors as implemented in the

LZ and XENON1T/XENONnT TPCs, and the hermetic TPC presented in chapter 5. Other investigated sensors under general consideration are, e.g., SiPMs [151], ABALONE photosensors [152] or liquid hole multipliers [153].

The double-walled cryostat containing the TPC will be installed in a large tank filled with gadolinium-doped water. Its exact dimensions depend on the experiment's location and the corresponding cosmogenic backgrounds. A dedicated study showing the impact of different water tank sizes placed in the halls of LNGS is conducted and discussed within this work (see section 4.3). It constitutes an essential input for the choice of the laboratory and the water tank geometry. The tank will be equipped with photosensors and can be operated as a water Cherenkov muon veto. Additionally, the inner-most region around the outer cryostat will act as a separated veto system, the neutron veto, and is also instrumented with photosensors. This veto reduces the neutron backgrounds since low-energy neutrons originating from detector material impurities have a high chance of being captured by the dissolved gadolinium after an energy deposition in the TPC. Gadolinium is used since the neutron capture cross-sections of the isotopes $^{155}$Gd and $^{157}$Gd, with natural abundances of $(14.80 \pm 0.12)\%$ and $(15.65 \pm 0.02)\%$ [9], respectively, are high: $^{157}$Gd has the largest thermal neutron capture cross-section among all stable isotopes of $(2.15 \pm 0.05) \cdot 10^5$ b, $^{155}$Gd has a cross-section of $(5.17 \pm 0.18) \cdot 10^4$ b [154]. The de-excitation of the produced excited states of $^{156}$Gd and $^{158}$Gd cause $\gamma$-ray cascades with total energies of 8.5 MeV and 7.9 MeV [155], respectively, detected by the photosensors of the veto. A neutron veto simulation study for XENONnT yields an 85% radiogenic neutron background reduction [156]; a similar design is envisaged for DARWIN.

### 3.2.3 Background expectations

DARWIN's ultimate DM sensitivity requires the background at low energies to be dominated by irreducible neutrino-induced events. For ER backgrounds *pp* and $^7$Be are the most significant sources, as shown in figure 3.5 (a), where two hypothetical WIMP spectra for different interaction cross-sections and masses are presented along with the neutrino signatures. The $2\nu\beta\beta$ background, non-avoidable for non-depleted xenon targets, is also included but has a negligible impact on the WIMP sensitivity for low energies. Figure 3.5 (b) depicts the irreducible NR background from CE$\nu$NS of several neutrino sources in addition to possible WIMP signatures. At low energies the spectrum is dominated by $^8$B neutrino recoils; in the higher energy range atmospheric neutrinos dominate.

To be dominated by these irreducible neutrino backgrounds, several other sources have to be minimized. This can be achieved by the background reduction techniques presented in section 3.1.2 or by additional veto systems such as the muon and neutron veto, explained in section 3.2.2. A short overview of these minimizable backgrounds is given in the following and is further discussed in chapter 4. Xenon-intrinsic and external backgrounds are listed separately, as the former cannot be reduced by target fiducialization.

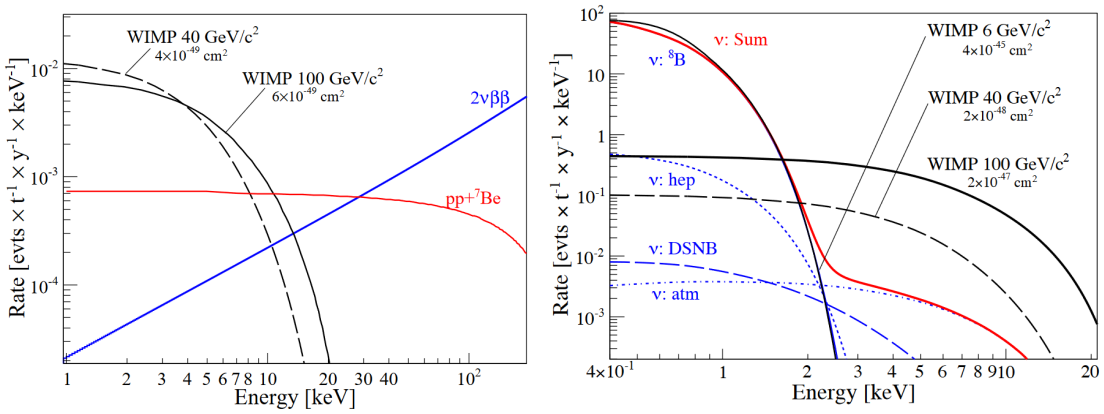


**Figure 3.5:** WIMP spectra together with irreducible ER and NR $\nu$-induced backgrounds. A 99.98% ER/NR discrimination with 30% NR acceptance is assumed. In (a) possible WIMP recoil spectra, *pp*, and $^{7}$Be neutrinos, as well as the background from $2\nu\beta\beta$ of $^{136}$Xe are shown. In (b) the hypothetical WIMP signals are compared to CE$\nu$NS backgrounds, namely $^{8}$B, *hep*, atmospheric, and diffuse supernova (DSN) neutrinos. Figures from [7].

External ER backgrounds are induced by the long-lived primordial radionuclides contained in all detector materials. Typical contaminations are the decay chains of $^{238}$U, $^{232}$Th, $^{235}$U, as well as the nuclides $^{60}$Co, $^{137}$Cs, and $^{40}$K. Additionally, $^{44}$Ti is produced by cosmogenic activation at sea level within the cryostat material. Due to xenon's high stopping power for $\alpha$ and $\beta$ decays, their main backgrounds are caused by $\gamma$-rays. All materials are screened by high-purity germanium detectors, such as GeMSE [157], Gator [158], or GeMPI [159], and selected accordingly to build a detector.

Xenon-intrinsic ER backgrounds stem from unstable noble gas isotopes contained in the LXe target decaying via $\beta$ and $\gamma$ emission. While low-energy monoenergetic depositions at 64.3 keV, 36.7 keV, and 9.8 keV are expected for the $2\nu$ECEC of $^{124}$Xe [80], a continuous spectrum up to the $Q$ value of 2.458 MeV is assumed for the $2\nu\beta\beta$ of $^{136}$Xe [160, 87]. $^{137}$Xe is produced by the capture of a thermalized muon-induced neutron by $^{136}$Xe [161] and undergoes $\beta^-$ decay. Additionally, $^{85}$Kr and $^{222}$Rn contaminate the xenon target. The former is present from the xenon production process, the extraction from the atmosphere. Cryogenic distillation columns allow the reduction of $^{85}$Kr to the $^{\text{nat}}$Kr/Xe $< 0.03$ ppt level [162], well below the DARWIN expectations [142]. $^{222}$Rn is permanently produced as part of the $^{238}$U chain; it is constantly emanated from all detector surfaces. DARWIN aims to reach a challenging radon concentration of 0.1 $\mu$Bq/kg [7]. For that, the second part of this thesis investigates a hermetic TPC as one possible radon reduction technique.

External NR backgrounds are caused by radiogenic and cosmogenic neutrons. Radiogenic neutrons originate from detector material impurities with energies of up to several MeV either by $(\alpha, n)$ reactions or spontaneous fission. While the highest $(\alpha, n)$ yields stem from materials composed of light atoms like PTFE (the high

Coulomb barrier of heavy nuclei suppresses these processes), spontaneous fission is mainly caused by heavy nuclei. Cosmogenic neutrons are generated by muons that penetrate the rock overburden of the experiment and interact with the rock and concrete surrounding the detector. In case these neutrons are produced within the detector, they are considered negligible since the "mother" muon will be tagged by the muon veto with a very high efficiency [163]. The impact of cosmogenic neutrons depends on the laboratory depth and the size of the shield. For LNGS cosmogenic neutrons show mean energies of about 270 GeV [164].

# Chapter 4

# DARWIN's science channels

Several physics objectives of DARWIN's rich science portfolio are studied in this chapter. This includes WIMP DM, the neutrinoless double beta decay ($0\nu\beta\beta$) of $^{136}$Xe and neutrinoless double electron capture ($0\nu$ECEC) of $^{124}$Xe, as well as elastic scattering of solar neutrinos off atomic electrons. GEANT4-based MC simulations were conducted to model backgrounds as well as signals, assuming the DARWIN detector design as presented in section 3.2.2.

In section 4.1 the MC framework is introduced. It consists of the GEANT4 detector and particle interaction model, as well as the steps for data production, processing, selection, and weighting. The radio-purity assumptions, which directly impact the science reach, are explained in section 4.2. Besides discussing the assumed activities of the detector materials, an optimization study for the cryostat material and geometry is presented. The WIMP science case is discussed in section 4.3. In contrast to the subsequent studies, the results presented there do not aim to yield a detection sensitivity but determine required inputs for designing and constructing the DARWIN detector. DARWIN's expected sensitivity to the $0\nu\beta\beta$ of $^{136}$Xe is calculated in section 4.4, which was published in [10], with this work contributing to the background modeling. Section 4.5 examines the sensitivity to the $0\nu$ECEC of $^{124}$Xe, following the master's thesis of M. Rajado Nunes da Silva [165], supervised in the scope of this work. Finally, DARWIN's sensitivity to elastic $\nu$-electron interactions of solar neutrinos is presented in section 4.6, showing that DARWIN is able to detect five different solar neutrino components. The study was published in [11] and this work contributed by the material background model.

## 4.1 Monte Carlo framework

MC simulations form the basis of detector sensitivity predictions and allow the optimization of the detector design in terms of geometry and material selection. In DARWIN's current R&D phase, such simulations are important since they recommend improvements, which are required to reach specific science goals. In this section the MC framework and the analysis steps are presented: after introducing the GEANT4 toolkit and the DARWIN code in section 4.1.1, the data production and treatment as used for all following investigations are explained in section 4.1.2.

### 4.1.1 Geant4 detector model

The GEANT4 toolkit [166, 167] is widely used in high-energy, astroparticle, and nuclear physics to simulate particle tracks through matter. In this work the versions *10.3-patch03* and *10.7-patch02* were used. The DARWIN GEANT4 simulation code is jointly used by the collaboration, and its development followed the XENON1T simulation package [168]. According to pre-defined physics lists, primary particles, which are started in a defined volume or point, interact with the detector materials. The information about their tracks, energy depositions, produced secondary particles, and many further details are stored in output files and analyzed afterward. In the presented work, the energy depositions are not translated to the TPC-specific S1 and S2 signals (see section 3.1.2) since the detector design is not yet final. Instead, all investigations are based on the "MC-true" deposited energy directly provided by the GEANT4 simulation output.

For visualization purposes, pre-defined GEANT4 features allow the three-dimensional imaging of the implemented detector geometry. However, a more robust and detailed measure utilizing low computing power is the simulation of so-called *geantinos*. These virtual particles do not interact with matter and instead only undertake transportation processes. Such lightweight simulations allow the detailed review of the implemented detector geometry and are used in the following.

The implemented DARWIN detector geometry is based on the baseline design presented in section 3.2.2. Its $r$-$z$ projection obtained by simulating geantinos is shown in figure 4.1. The included materials are listed in table 4.1, together with their corresponding masses. The LXe between the gate and cathode defines the *sensitive detector*: all energy depositions in this volume are saved to the GEANT4 output file. Since the GEANT4 detector design is kept rather simple, details such as the liquid level control, cables, resistors between the copper field shaping electrodes, or temperature sensors are not included. Due to their small masses, these components do not significantly change the background rate and thus the conclusions of this chapter.

The double-walled titanium cryostat housing the TPC is placed in a water tank, shielding against environmental backgrounds and acting as a muon veto system. Due to an assumed gadolinium-doping of 0.2%, it also serves as a neutron veto system, which operates in the innermost region of the tank. It records the neutron captures by $^{155}$Gd or $^{157}$Gd near the cryostat with a 1 m distance to its walls and thus provides a neutron tagging capability. The exact dimensions of the water tank are still unknown and depend on several factors, such as the laboratory depth and the corresponding rock overburden. Assuming the depth of LNGS, the tank's impact on the cosmogenic neutron background rate is investigated in section 4.3, where different geometries were considered (see figure 4.9 (b) on page 56). For both veto systems, the muon and neutron veto, no detailed geometry (such as photosensor placement) is implemented in the GEANT4 code. Instead, the gadolinium-doped water is set as a sensitive detector for the corresponding studies. Further information on the functionality of the neutron veto system is given in the following sections.

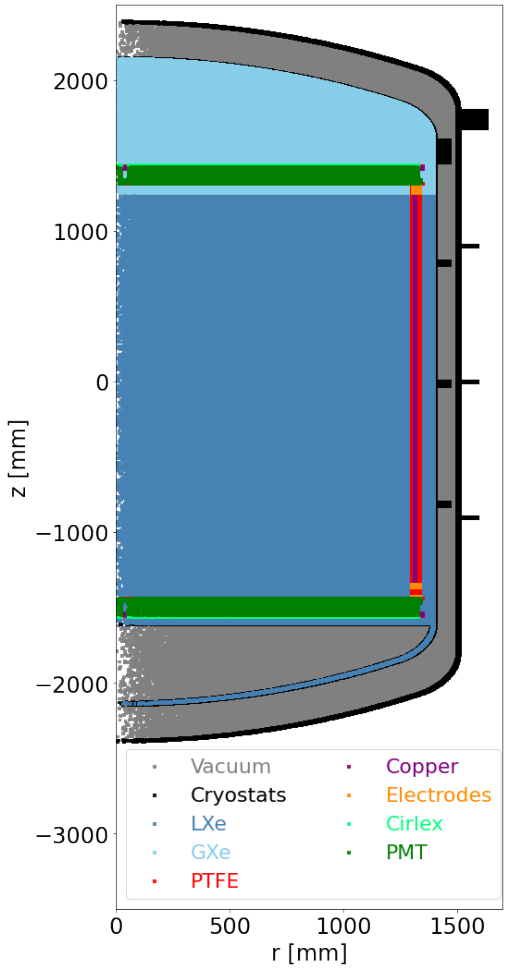


**Figure 4.1:** DARWIN detector geometry as implemented in GEANT4.

**Table 4.1:** Masses of the detector components as implemented in GEANT4.

| Detector component | Mass |
|---|---|
| *Titanium* | |
| Outer cryostat | 3.0 t |
| Inner cryostat | 2.1 t |
| Bottom pressure vessel | 0.4 t |
| Electrode support frames | 120 kg |
| *Xenon* | |
| LXe sensitive target | 39.3 t |
| LXe buffer | 9.0 t |
| LXe around pressure vessel | 270 kg |
| GXe | 30 kg |
| *PTFE* | |
| Reflectors | 216 kg |
| Support pillars | 84 kg |
| *Copper* | |
| Field shaping electrodes | 680 kg |
| Photosensor support | 520 kg |
| *PMT (composite: Kovar, quartz, ceramics, stainless steel)* | |
| 1910 3-inch PMTs | 363 kg |
| *Cirlex* | |
| PMT bases | 5.7 kg |

### 4.1.2 Data production and treatment

The background simulation procedure is described in the following. It is split into the data production, processing, selection, and weighting (for the translation of events to background rates) steps, which require different treatments depending on the simulated background source. In this work, ER sources from materials, including the xenon itself, radiogenic NR backgrounds, and cosmogenic NR backgrounds were simulated using the DARWIN GEANT4 simulation code.

#### Data production

ER backgrounds from materials are mainly caused by the decays of the unstable isotopes $^{238}$U, $^{232}$Th, $^{235}$U, $^{60}$Co, $^{137}$Cs, $^{40}$K, and $^{44}$Ti. For the background simulations, these isotopes are randomly placed in the material of interest. The DARWIN GEANT4 code then automatically simulates their decays with isotropic emission of the created $\gamma$-rays, and saves (among other information) any energy depositions in the LXe target. Every new isotope that is produced in the decay series is stored as a separate event if its half-life is $> 10$ ns. This time cut primarily impacts the $^{60}$Co

simulations since the excited states of its daughter nucleus $^{60}$Ni show half-lives of $\mathcal{O}$(ps) [9], which cannot be time-resolved in the DARWIN TPC. The number of simulated events $N_{\text{gen}}$ is specified at the beginning of each simulation.

Radiogenic neutrons, produced by $(\alpha, n)$ reactions or spontaneous fission in detector materials, show isotope- and material-dependent energy spectra and production rates. Figure 4.2 (a) exemplarily shows the neutron spectra of the five separately treated decay chains releasing radiogenic neutrons in titanium: $^{238}$U, $^{226}$Ra, $^{235}$U, $^{232}$Th, and $^{228}$Th. Both, the $^{238}$U and $^{232}$Th decay chains are split due to the very long half-lives in the first parts of the decay series, possibly resulting in a radioactive disequilibrium, as shown in table 4.3 on page 46. For each material and isotope, the corresponding neutron spectrum is taken as a simulation input, obtained by available calculations utilizing the SOURCES-4A software [169, 170]. Again, at the beginning of every simulation the number of events is specified, and the neutrons with the corresponding kinetic energy input spectrum are randomly started in the material of interest. The xenon target and the neutron veto are set as sensitive detectors recording energy depositions, which allows for background rejection due to coincident neutron captures.

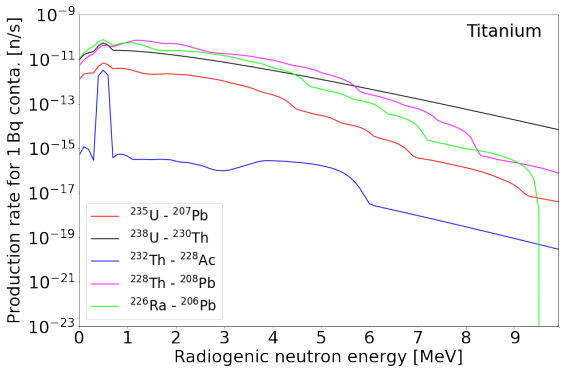


(a) Energy spectra of radiogenic neutrons.

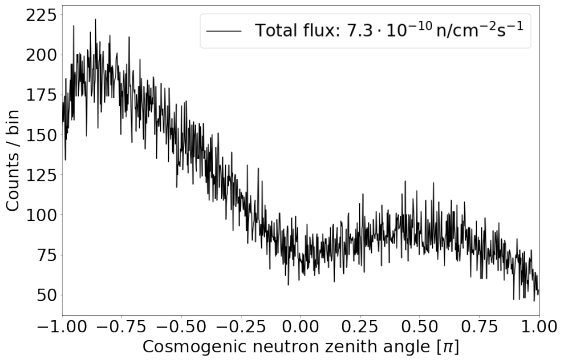


(b) Angular spectrum of cosmogenic neutrons.

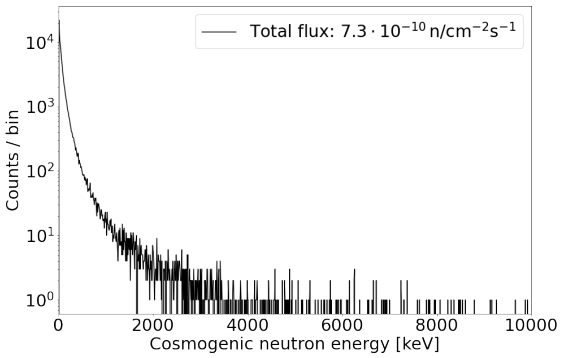


(c) Energy spectrum of cosmogenic neutrons.

**Figure 4.2:** MC simulation input spectra of cosmogenic and radiogenic neutrons: (a) shows the energy spectra of radiogenic neutrons from five decay chains releasing neutrons in titanium. Data from [170]. (b) and (c) describe the angular and energy spectra of cosmogenic neutrons, respectively, as simulated by [171], assuming the rock overburden of LNGS, leading to a total neutron flux of $7.3 \cdot 10^{-10}\,(\text{cm}^2\,\text{s})^{-1}$.

Cosmogenic neutrons are induced by muons and are generated in the rock and concrete surrounding the detector with a laboratory-dependent rate, energy spectrum, and angular spectrum. Previous simulations from [171] provide this rate and the spectra, shown in figure 4.2 (b) and (c), assuming that the detector is placed at LNGS. Using these inputs, neutrons with a specific kinetic energy and momentum direction are started on a sphere surrounding the water tank and propagated towards the TPC. Similar to radiogenic neutron simulations, both the TPC and the neutron veto volumes are set as sensitive detectors to record subsequent energy depositions. Cosmogenic neutrons induced in detector materials are not considered in this study since the muon is tagged with a high efficiency of $> 98\%$ [171] in the muon veto; it thus results in an irrelevant background contribution.

### Data processing

The GEANT4 simulations are followed by an event-by-event processing, accounting for the detector's ability to distinguish single scatter (SS) and multiple scatter (MS) event signatures. Using the density-based clustering algorithm DBSCAN [172], all small energy depositions of $\mathcal{O}(100\,\mathrm{eV})$ in the LXe target are grouped. An energy deposition is considered a new cluster if any other deposition of the event has a larger physical distance than a chosen separation distance $\varepsilon$. A sketch illustrating this clustering for the $0\nu\beta\beta$ study is given in figure 4.17 on page 66. Since a meaningful threshold value $\varepsilon$ depends on different parameters in the physical detector, such as the chosen photosensors and their granularity (not yet decided for the DARWIN detector), different separation thresholds were used in the following investigations. If not further specified, a default value of $\varepsilon = 15\,\mathrm{mm}$ was applied.

### Data selection

Since neutron simulations require a more complex data selection, e.g., due to the additional veto system, ER and NR event selection criteria are presented separately. These criteria include a SS tagging since most science channels (here: WIMPs, $0\nu\beta\beta$, solar neutrinos) are expected to cause a SS event topology. The hypothetical $0\nu$ECEC constitutes an exception since its emission of a $\gamma$-ray cascade would result in a MS signature. Its event selection is separately discussed in section 4.5.

Neutrons do not only cause elastic NR but also inelastic processes, such as the excitation of $^{129}$Xe with a prompt ($T_{1/2} = 0.97\,\mathrm{ns}$) gamma emission of $\sim 40\,\mathrm{keV}$ [9], which causes an ER. Thus, the clusters obtained by the data processing code are first categorized in ER- and NR-like clusters. A cluster is classified as NR type if the initial energy deposition was caused by an elastic hadronic process and involves xenon atoms in the energy deposition; any other group is referred to as ER cluster. Using Noble Element Simulation Technique (NEST), a software package based on data from liquid xenon experiments describing detector response models [173, 174], the energy contained in both types of clusters is translated to generated quanta, particularly electrons. It is assumed that a cluster must contain at least 7 electrons to be detected (considering an electron lifetime of $\mathcal{O}(10\,\mathrm{ms})$ and thus on average $> 5$ electrons surviving the drift and producing the S2 signal) and it must contain

at least 20% of the energy of the event's leading cluster. If an event contains exactly one separately detectable NR cluster, it is used for further analysis (*SS cut*). The event is discriminated if the simulated neutron is captured by a gadolinium nucleus in the neutron veto system within 150 $\mu$s after the SS in the TPC (*neutron veto cut*). The surviving events, which are convoluted with a Gaussian function with $\sigma_{x,y} = \sigma_z = 10\,\text{mm}$ to account for the detector's finite position resolution, must be contained in an ellipsoidal fiducial volume, defined by

$$\left(\frac{r}{r_{\text{max}}}\right)^n + \left(\frac{z + z_{\text{shift}}}{z_{\text{max}}}\right)^n < 1 \tag{4.1}$$

for further background reduction (*fiducial volume cut*). The parameters $r_{\text{max}}$ and $2 \cdot z_{\text{max}}$ define the maximal radius and height of the selected volume, respectively; the additional parameter $z_{\text{shift}}$ accounts for the reduced shielding power in the xenon gas phase and allows shifting the volume downwards. The optimum fiducial volume parameters depend on the science case. Finally, the energy ROI is selected (*energy cut*). It corresponds to [5,40] keV for the WIMP search. Since WIMPs are expected to induce a recoil spectrum and not a monoenergetic signature, no additional energy smearing to account for the detector's finite energy resolution is applied since its impact is rather small.

For the ER event selection, events are checked for the presence of several detectable clusters; if yes, the event is rejected (*SS cut*). Furthermore, a *fiducial volume cut* is applied, the MC-true energy convoluted with a Gaussian function to account for the detector resolution and the energy ROI is selected according to the investigated science channel (*energy cut*).

### Data weighting

Finally, the number of selected simulated background events $N_{\text{selec}}$ is translated to a background rate $R$. For detector material simulations, i.e., radiogenic neutrons and ER backgrounds, the effective lifetime $T_{\text{eff}}$ of the simulation is calculated by

$$T_{\text{eff}} = \frac{N_{\text{gen}}}{m_C \cdot A_C} \ , \tag{4.2}$$

where $N_{\text{gen}}$ is the number of simulated decay chains/neutrons (*mother isotopes*) and $m_C$ and $A_C$ are the mass and activity of the simulated detector component, respectively. GEANT4's event splitting explained above must be considered for $N_{\text{gen}}$, resulting in a mismatch between the number of stored events and the number of simulated mother isotopes. $N_{\text{gen}}$ is obtained from the MC truth information stored in the GEANT4 output file. For radiogenic neutron simulations, equation (4.2) additionally has to be divided by the material- and isotope-dependent neutron production rate, which is obtained by SOURCES-4A calculations (shown in table 4.2) with a systematic uncertainty of 17% [156]. The masses of the various detector components are listed in table 4.1 and their assumed activities are specified in table 4.3. For cosmogenic neutron simulations, the effective lifetime of the simulation is calculated by the ratio of the number of simulated neutrons $N_{\text{gen}}$ and the expected number of cosmogenic neutrons per unit time $n_{\text{cosm}}$:

$$T_{\text{eff}} = \frac{N_{\text{gen}}}{n_{\text{cosm}}} = \frac{N_{\text{gen}}}{A \cdot n_{\text{cosm,LNGS}}} \ . \tag{4.3}$$

$A$ is the surface of the sphere surrounding the water tank from where the cosmogenic neutrons are initially started and $n_{\text{cosm,LNGS}}$ the neutron rate at LNGS of $7.3 \cdot 10^{-10}\,(\text{cm}^2\,\text{s})^{-1}$ [171].

Taking the effective simulation lifetime $T_{\text{eff}}$, the background rate $R$, given in units of $(\text{t}\,\text{yr}\,\text{keV})^{-1}$, is calculated by

$$R = \frac{N_{\text{selec}}}{m_{\text{FV}} \cdot T_{\text{eff}} \cdot \Delta E} \ , \tag{4.4}$$

where $N_{\text{selec}}$ describes the number of selected events, $m_{\text{FV}}$ the mass of the selected fiducial volume and $\Delta E$ the energy range of interest.

**Table 4.2:** Neutron production rates of materials typically used in LXe TPCs, given in units of 1 Bq and for a contamination of 1 Bq. PTFE and ceramics show the highest production rates. Data from [170].

| **Material** | $^{238}$**U** | $^{226}$**Ra** | $^{235}$**U** | $^{232}$**Th** | $^{228}$**Th** |
|---|---|---|---|---|---|
| **Titanium** | $1.2 \cdot 10^{-6}$ | $2.0 \cdot 10^{-6}$ | $3.3 \cdot 10^{-6}$ | $3.8 \cdot 10^{-8}$ | $7.7 \cdot 10^{-6}$ |
| **Stainless steel** | $1.1 \cdot 10^{-6}$ | $3.1 \cdot 10^{-7}$ | $4.1 \cdot 10^{-7}$ | $1.8 \cdot 10^{-9}$ | $2.0 \cdot 10^{-6}$ |
| **PTFE** | $7.4 \cdot 10^{-6}$ | $5.5 \cdot 10^{-5}$ | $1.3 \cdot 10^{-4}$ | $7.3 \cdot 10^{-7}$ | $1.0 \cdot 10^{-4}$ |
| **Copper** | $1.1 \cdot 10^{-6}$ | $2.5 \cdot 10^{-8}$ | $3.3 \cdot 10^{-8}$ | $3.0 \cdot 10^{-11}$ | $3.6 \cdot 10^{-7}$ |
| **Quartz** | $1.2 \cdot 10^{-6}$ | $8.8 \cdot 10^{-7}$ | $1.9 \cdot 10^{-6}$ | $6.8 \cdot 10^{-9}$ | $1.9 \cdot 10^{-6}$ |
| **Kovar** | $1.1 \cdot 10^{-6}$ | $1.2 \cdot 10^{-7}$ | $1.3 \cdot 10^{-7}$ | $3.0 \cdot 10^{-11}$ | $1.0 \cdot 10^{-6}$ |
| **Ceramics** | $1.2 \cdot 10^{-6}$ | $6.0 \cdot 10^{-6}$ | $1.3 \cdot 10^{-5}$ | $9.2 \cdot 10^{-9}$ | $1.4 \cdot 10^{-5}$ |
| **Cirlex** | $1.3 \cdot 10^{-6}$ | $3.5 \cdot 10^{-6}$ | $2.2 \cdot 10^{-6}$ | $4.1 \cdot 10^{-8}$ | $2.4 \cdot 10^{-6}$ |

## 4.2 Radio-purity and design considerations

The material-induced background rate highly depends on the contamination level of the construction materials. The following section thus discusses the material activities assumed in this work. Additionally, a cryostat background study is presented, which compares eight different material and geometry scenarios in terms of the expected ER and NR background rates. The cryostat option yielding the lowest background rate was assumed for all subsequent studies.

### 4.2.1 Material activities

The specific activities assumed in this work were taken from previously measured materials and are thus considered to be conservative. An intense material screening campaign and a more radio-pure production allows improving their contamination level. Mostly, these activities are from XENON1T measurements [175, 168] but also from LZ [176] and EXO-200 [99]. The activities are listed in table 4.3. The table includes the specific activity of $^{44}$Ti, which is produced by cosmogenic activation [177].

**Table 4.3:** Specific activities of materials often used in LXe TPCs and assumed for this work. Activities are taken from [175] and [168] (XENON), [176] (LZ), and [99] (EXO-200). The cosmogenic activation of $^{44}$Ti is from [177].

| Material | Unit | $^{238}$U | $^{226}$Ra | $^{235}$U | $^{232}$Th | $^{228}$Th | $^{137}$Cs | $^{60}$Co | $^{40}$K | $^{44}$Ti | Ref. |
|---|---|---|---|---|---|---|---|---|---|---|---|
| **Titanium** | mBq/kg | $< 1.6$ | $< 0.09$ | - | $0.28 \pm 0.03$ | $0.23 \pm 0.02$ | - | $< 0.02$ | $< 0.54$ | $< 1.16$ | LZ |
| **Stainless steel** | mBq/kg | $2.4 \pm 0.7$ | $< 0.64$ | $< 2.0$ | $0.21 \pm 0.06$ | $< 0.36$ | $< 0.64$ | $9.7 \pm 0.8$ | $< 2.7$ | $< 0.15$ | XENON1T |
| **PTFE** | mBq/kg | $< 0.25$ | $< 0.12$ | $< 0.087$ | $< 0.041$ | $< 0.065$ | $0.17 \pm 0.03$ | $< 0.027$ | $< 0.343$ | - | XENON1T |
| | mBq/kg | $< 0.005$ | - | - | $< 0.0014$ | - | $0.057 \pm 0.006$ | - | - | - | EXO-200 |
| **Copper** | mBq/kg | $< 1$ | $< 0.035$ | $< 0.18$ | $< 0.033$ | $< 0.026$ | $< 0.033$ | $< 0.019$ | $0.4 \pm 0.1$ | - | XENON1T |
| **PMT total** | mBq/PMT | $8 \pm 2$ | $0.5 \pm 0.1$ | $0.36 \pm 0.08$ | $0.5 \pm 0.1$ | $0.50 \pm 0.06$ | $< 0.18$ | $0.71 \pm 0.03$ | $13 \pm 2$ | - | XENON1T |
| **PMT window (quartz)** | mBq/PMT | $< 1.2$ | $0.065 \pm 0.007$ | $< 0.024$ | $< 0.029$ | $< 0.025$ | $< 0.0068$ | $< 0.0067$ | $< 0.015$ | - | XENON1T |
| **PMT stain. st.** | mBq/PMT | $0.26 \pm 0.08$ | $< 0.065$ | $0.011 \pm 0.004$ | $< 0.039$ | $< 0.05$ | $< 0.019$ | $0.080 \pm 0.007$ | $< 0.16$ | - | XENON1T |
| **PMT body (Kovar)** | mBq/PMT | $< 0.14$ | $< 0.31$ | $< 0.0064$ | $< 0.049$ | $< 0.37$ | $< 0.12$ | $0.32 \pm 0.03$ | $< 1.1$ | - | XENON1T |
| **PMT stem (ceramics)** | mBq/PMT | $2.4 \pm 0.4$ | $0.26 \pm 0.02$ | $0.11 \pm 0.02$ | $0.23 \pm 0.03$ | $0.11 \pm 0.02$ | $< 0.022$ | $< 0.018$ | $1.1 \pm 0.2$ | - | XENON1T |
| **Cirlex** | mBq/PMT | $0.82 \pm 0.03$ | $0.32 \pm 0.02$ | $0.71 \pm 0.16$ | $0.20 \pm 0.03$ | $0.153 \pm 0.013$ | $< 0.0098$ | $< 0.0052$ | $0.36 \pm 0.08$ | - | XENON1T |

In the following analyses, upper detection limits were conservatively treated as measurements. If no specific contamination for the second parts of the $^{238}$U and $^{232}$Th chains, i.e., the $^{226}$Ra and $^{228}$Th activity, is given, equilibrium within the decay chain was assumed, which is also considered to be conservative. Missing $^{235}$U measurements were replaced by scaled $^{238}$U activities using the natural abundance ratio $\rho_r = \rho_{U235}/\rho_{U238}$ of the uranium isotopes. From the decay law, it is known that $A_{235} = \lambda_{U235} \cdot N_{U235}$. Applying the relative abundance $\rho_r$ allows the estimation of $^{235}$U's activity:

$$A_{U235} = \frac{\ln 2 \cdot N_{U235}}{T_{1/2,U235}} = \frac{\ln 2 \cdot N_{U238} \cdot \rho_r}{T_{1/2,U235}} = \frac{A_{U238} \cdot T_{1/2,U238} \cdot \rho_r}{T_{1/2,U235}} \ , \tag{4.5}$$

where $N_{U235}$ and $N_{U238}$ are the number of $^{235}$U and $^{238}$U atoms, respectively, and $T_{1/2,U235}$ and $T_{1/2,U238}$ the half-lives.

Note that two different PTFE material purities are listed in table 4.3. Their resulting background rates are compared in the following sections. Both the total PMT activity and the activity of the single PMT materials, including quartz, Kovar, stainless steel, and ceramics, are given. While for ER studies one joint PMT simulation was conducted and translated to background rates using the PMT's total activity, NR simulations require the material-dependent neutron energy spectrum as input. Thus, separate simulations for each photosensor material are necessary.

### 4.2.2 Optimization of the cryostat material and geometry

Besides the xenon target and the water tank, the double-walled cryostat is DARWIN's detector component with the largest mass. Since the expected background rate scales linearly with the mass, indicated by equations (4.2) and (4.4), the minimally required amount of material was calculated in engineering studies done at Nikhef [178]. These studies were based on the following assumptions:

- The outer cryostat supports its weight with no additional load from the inner cryostat. It has to stand a maximal pressure of 2.5 bar on the outside and a minimum pressure of 0 bar on the inside. In its cylindrical part, the outer cryostat has dimensions of ø 3.0 m × 3.5 m.
- The inner cryostat supports its weights plus 40 t of LXe. It is suspended from the top with a maximal pressure of 3.5 bar on the inside and a minimum pressure of 0 bar on the outside, where temperatures of −110°C are considered. In its cylindrical part, the inner cryostat has dimensions of ø 2.8 m × 3.5 m.

For simplification, only the cylinders without flanges were considered for both cryostats. Assuming two possibilities of failure, elastic buckling (structural failure) and non-elastic yielding (material failure), wall thicknesses yielding a safety factor of 3 were calculated. The safety factor describes the ratio of maximum strength to intended load. Two different materials, stainless steel and titanium, and a varying number of hoop stiffening rings to minimize the wall thickness were considered, resulting in eight different cryostat designs: a cryostat made of stainless steel and a

cryostat made of titanium, each with 0-3 hoop stiffeners. A follow-up study conducted in 2021, which included a much higher level of detail (e.g., the torispherical domes of the cryostats), resulted in slightly increased wall thicknesses but overall confirmed the previous result from [178]. The earlier cryostat scenarios were taken as an input for the following study, which determines the expected ER and NR cryostat background rates.

The different cryostat geometries were implemented in the DARWIN GEANT4 code. The four titanium options are exemplarily shown in figure 4.3, where the LXe target, the volume between the cathode and gate electrodes, is marked in red. The wall thicknesses and masses of the eight geometry options are listed in table 4.4, showing that titanium causes lower cryostat weights. While this lighter weight already indicates lower background rates, detailed background simulations are required since titanium and stainless steel have different contamination levels and neutron production rates, as listed in table 4.3 and table 4.2. Additionally, it is possible that the hoop stiffening rings lead to local accumulations of background events, showing the need to compare the geometries with a varying number of hoop stiffening rings.

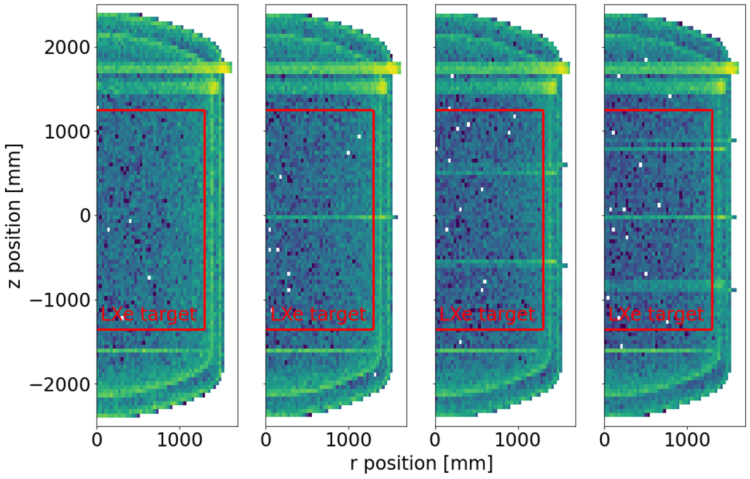


**Figure 4.3:** Geantino visualization of the different titanium cryostat geometries with a varying number of hoop stiffening rings as implemented in the DARWIN GEANT4 model. The red volume marks the LXe target.

**Table 4.4:** Material- and geometry-dependent double-walled cryostat masses and wall thicknesses of the outer/inner cryostat as implemented in the DARWIN GEANT4 model.

| Material | 0 hoop rings | 1 hoop ring | 2 hoop rings | 3 hoop rings |
|---|---|---|---|---|
| **Titanium** | 8100 kg (18.5/12.5) mm | 6528 kg (14.0/9.5) mm | 5954 kg (12.0/8.5) mm | 5508 kg (10.5/7.5) mm |
| **Stainless steel** | 12380 kg (15.5/10.5) mm | 10012 kg (11.5/8.0) mm | 9026 kg (10.0/6.5) mm | 8615 kg (9.0/6.0) mm |

Following the procedure described in section 4.1.2, both ER and NR simulation data were generated, processed, selected, and weighted. The outcome is separately discussed for ER and NR backgrounds, based on SS events within a 30 t fiducial volume.

### ER background simulations

For each cryostat scenario and isotope, $10^8$ primary events were simulated, corresponding to an effective simulation lifetime of several weeks. The exact lifetime depends on the cryostat mass and the simulated isotope. Such lifetimes provide sufficient statistics due to the high ER background rates. The 30 t fiducial volume was optimized by choosing its parameters $z_{\text{max}}$, $r_{\text{max}}$, $z_{\text{shift}}$, and $n$ to contain the lowest possible background. This optimization was conducted for each cryostat scenario separately. To account for the finite detector resolution, the SS event energies were smeared following the energy resolution of XENON1T, defined by

$$\frac{\sigma_E}{E} = \frac{a}{\sqrt{E}} + b \ , \tag{4.6}$$

where $a = (0.317 \pm 0.007)\,\sqrt{\text{keV}}$ and $b = 0.0015 \pm 0.0002$ [179]. The resulting background is exemplarily presented in figure 4.4, which directly compares the spectra of a stainless steel (a) and titanium double-walled cryostat (b), each with 3 hoop stiffening rings.

In figure 4.4 (a), the isotope $^{60}$Co dominates the background spectrum over a wide recoil energy range due to its high contamination in stainless steel, as evident in table 4.3. For higher energies, e.g., the $0\nu\beta\beta$ ROI around 2.5 MeV, the main background is caused by the $^{228}$Th and $^{226}$Ra decays and their daughters, the late parts of the $^{232}$Th and $^{238}$U decay chains, respectively. Note that a quasi ER background-free condition is achieved for recoil energies $< 100$ keV, which includes the WIMP ROI at $\sim [1, 11]$ keV. Firstly, this is caused by the target volume fiducialization excluding $\beta$ contributions, as well as low-energy photons due to their small penetration depths [127]; secondly, by the SS cut excluding Compton-scattering photons generating multiple low-energy depositions within the target.

The titanium cryostat background is dominated by the cosmogenically activated $^{44}$Ti for energies $< 1.2$ MeV, as shown in figure 4.4 (b). This background will slowly decrease during the detector operation due to its placement under a rock overburden and $^{44}$Ti's half-life of 60 yr [9]. For higher recoil energies, the background rate is again dominated by the $^{228}$Th- and $^{226}$Ra-induced decays.

To compare the eight considered cryostat scenarios, their total background spectra are shown in figure 4.5. Over the entire recoil energy range of up to 3 MeV, a titanium cryostat yields lower background rates than a stainless steel cryostat. ER physics objectives covering the energy range $< 1.5$ MeV, such as elastic electron scattering of solar neutrinos, profit from the lower titanium rates, which are approximately one order of magnitude lower than the stainless steel rates. Furthermore, figure 4.5 indicates that the more hoop stiffeners are included to minimize the wall

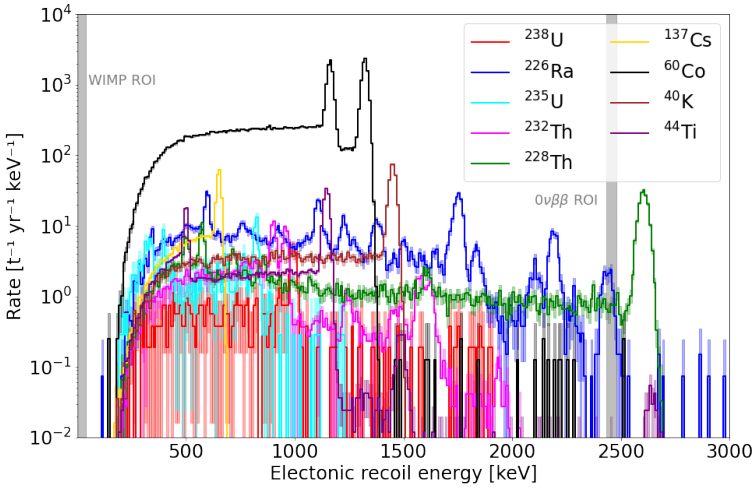


(a) Stainless steel cryostat.

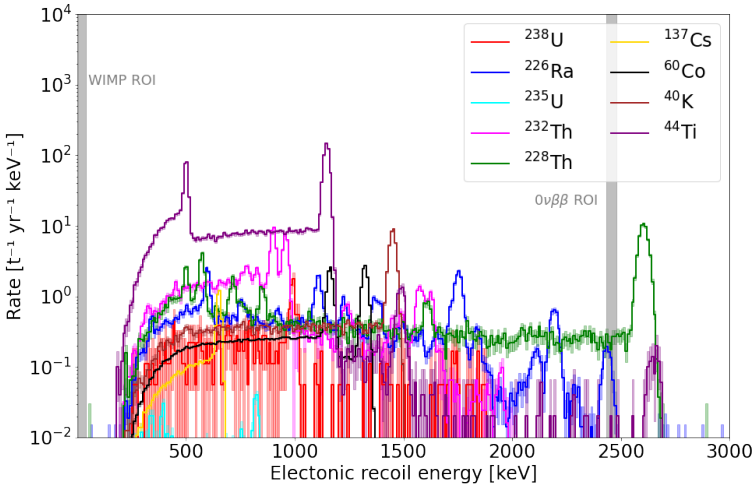


(b) Titanium cryostat.

**Figure 4.4:** ER background spectra from various radioactive contaminations inside realistic stainless steel and titanium cryostats, each with 3 hoop stiffening rings. A 30 t fiducial volume and a single scatter cut were applied. While the stainless steel cryostat is dominated by $^{60}$Co-induced background, the cosmogenically activated $^{44}$Ti dominates the titanium cryostat spectrum. Bands indicate the $1\sigma$ uncertainty range. The WIMP and $0\nu\beta\beta$ energy ROI are marked in grey.

thickness, the less background is induced: the titanium cryostat with 0 hoop stiffening rings causes a 35% higher background rate than the titanium cryostat with 3 hoop stiffening rings. Note that these results, favoring a titanium cryostat with 3 hoop stiffening rings, directly depend on the activities listed in table 4.3.

### NR background simulations

For each cryostat geometry and isotope, $10^7$ radiogenic neutrons were simulated, corresponding to an effective simulation time of several thousands of years. Such long simulation times were required to provide sufficient statistics for accurate predictions. Similar to the ER analysis, the 30 t fiducial volume was optimized separately

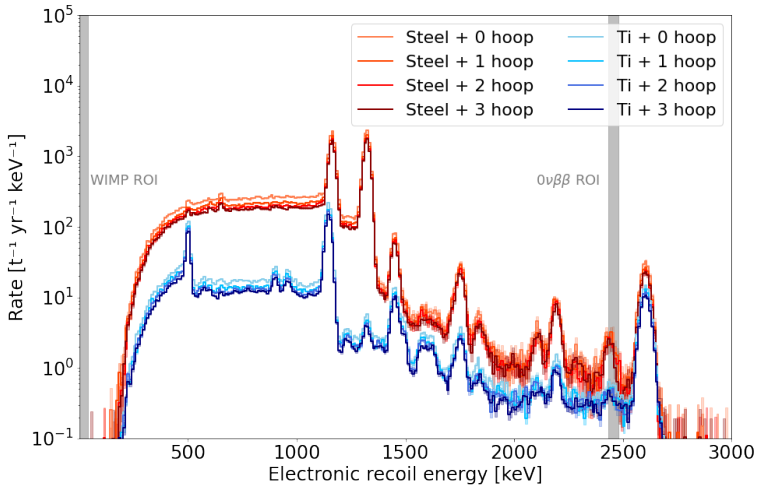


**Figure 4.5:** Comparison of combined ER background spectra of different cryostat geometries and materials after applying a 30 t fiducial volume and a single scatter cut. Over the entire energy range up to 3 MeV, titanium cryostats induce background rates of up to one order of magnitude lower than stainless steel cryostats. The implementation of hoop stiffening rings reduces the background rate. Bands indicate the $1\sigma$ uncertainty range. The WIMP and $0\nu\beta\beta$ energy ROI are marked in grey.

per cryostat scenario. Exemplarily, the resulting SS NR background spectra of the stainless steel and titanium cryostats including 3 hoop stiffening rings are shown in figure 4.6.

The background spectra for the stainless steel cryostat (figure 4.6 (a)) are dominated by $^{238}$U-induced backgrounds due to its high abundance in the steel and the high neutron production rate, as shown in table 4.3 and table 4.2. The neutrons caused by the $^{232}$Th contamination have a negligible impact due to the small neutron production rate in stainless steel.

The background spectra for the titanium cryostat presented in figure 4.6 (b) show three main contributors for recoil energies $< 20$ keV: $^{238}$U-, $^{228}$Th-, and $^{232}$Th-induced backgrounds. The prominent recoil spectrum of the latter isotope is caused by the neutron's kinetic energy distribution, shown in figure 4.2 (a).

The total NR backgrounds of the eight different cryostat scenarios under study are presented in figure 4.7. Comparing the best stainless steel and titanium options, the 3 hoop stiffening rings geometries, the stainless steel cryostat yields an $\sim 30\%$ higher background rate in the WIMP ROI of [5-40] keV. The comparison of the varying number of hoop stiffening rings for the titanium cryostat yields a 55% higher background for 0 hoop rings than for 3 rings.

To summarize, the simulations of both background types, ER and NR, predict a lower background rate for a titanium than for a stainless steel cryostat. Implementing hoop stiffening rings to reduce the wall thickness decreases these rates. Out of the investigated cryostat scenarios, the titanium cryostat with 3 hoop stiffening

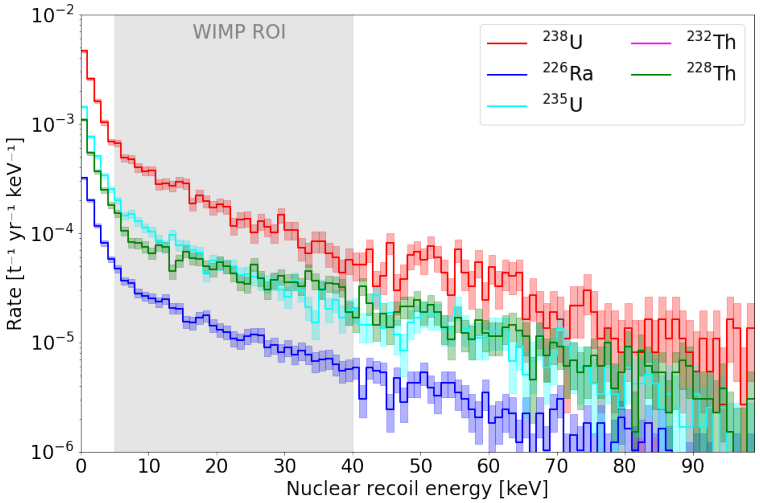


(a) Stainless steel cryostat.

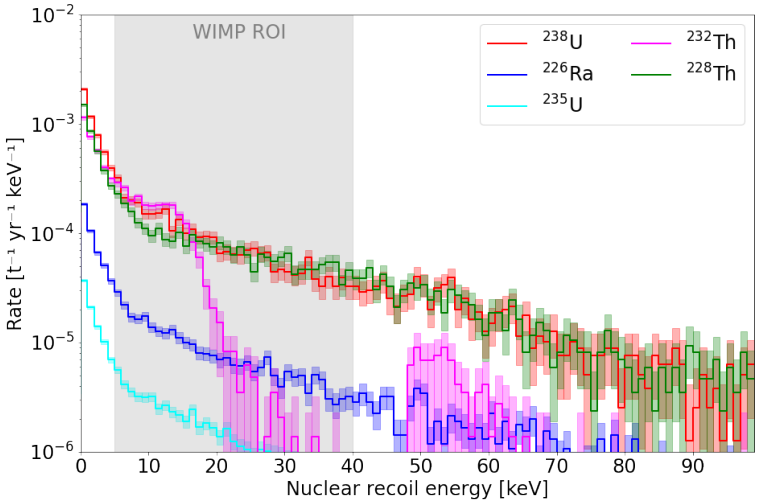


(b) Titanium cryostat.

**Figure 4.6:** NR cryostat background spectra from various radioactive contaminations inside realistic stainless steel and titanium cryostats, each with 3 hoop stiffening rings. A 30 fiducial volume cut and a single scatter cut were applied. The background for the stainless steel cryostat is dominated by $^{238}$U-induced backgrounds, the spectrum for the titanium cryostat by $^{238}$U-, $^{232}$Th-, and $^{228}$U-induced backgrounds. Bands indicate the $1\sigma$ uncertainty range. The WIMP energy ROI is marked in grey.

rings, yielding wall thicknesses of 10.5 mm and 7.5 mm of the outer and inner cryostat, respectively, thus provides the lowest expected background. In particular ER physics channels, such as the solar neutrino detection by elastic electron scattering, profit significantly from this cryostat choice due to the background reduction of approximately one order of magnitude over a wide energy range compared to the best stainless steel option. In the WIMP ROI, this cryostat induces an ER rate of $< 10^{-2}$ events/(t yr keV) before ER/NR discrimination and an NR rate of $\sim 3 \cdot 10^{-4}$ events/(t yr keV), excluding NR acceptance. All following science channels investigations studied in this work, as well as all investigations by the DARWIN collaboration, including the publications [10] and [11], chose this titanium cryostat,

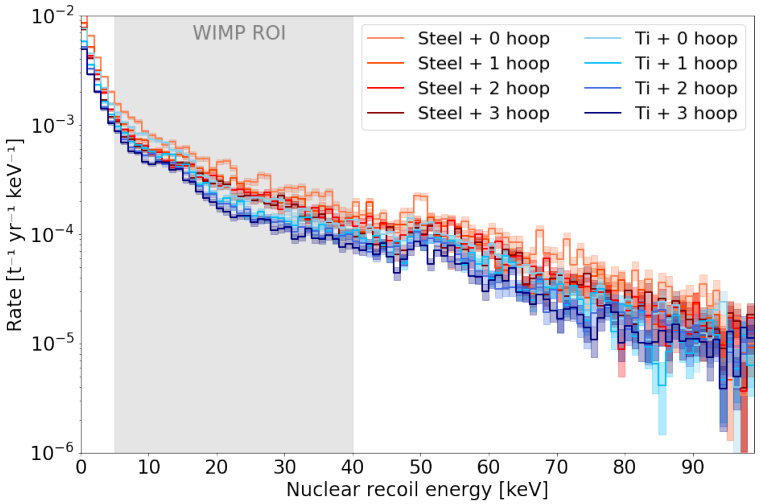


**Figure 4.7:** Comparison of NR background spectra for different cryostat geometries and materials, applying a 30 t fiducial volume and a single scatter cut. A stainless steel cryostat with 3 hoop stiffening rings causes an $\sim 30\%$ higher background rate in the WIMP ROI (marked in grey) than a titanium cryostat with 3 rings. Bands indicate the $1\sigma$ uncertainty range.

which directly affects the yielded sensitivities and thus demonstrates the importance of this study. Furthermore, the results presented here yield valuable inputs for further engineering studies to optimize the cryostat, e.g., by an increased number of hoop stiffening rings to further reduce the wall thickness, and motivate the search for an even less contaminated titanium material than reported in [176], which was assumed in this study.

## 4.3 Nuclear recoil background investigations for the WIMP search

DARWIN's sensitivity to directly detect SI WIMP-nucleus scatterings yields cross-sections down to a few $10^{-49}\,\mathrm{cm}^2$ for WIMP masses of $30\,\mathrm{GeV}/c^2$ [142], see figure 3.3 on page 32. The most detrimental background sources for the search are the ones inducing a nuclear recoil (NR) with signatures being indistinguishable from WIMPs: high-energy solar and atmospheric neutrinos, cosmogenic neutrons, and radiogenic neutrons. While the rate of the former source is fixed by nature, the rates of the latter two are detector- and location-dependent. In the DARWIN WIMP sensitivity study presented in [142], the radiogenic neutron rate was estimated by scaling simulations of the material background of a smaller 18 t LXe target to a 40 t LXe target, assuming the quartz of the photosensors, the PTFE reflectors, and a double-walled copper cryostat as the primary background sources. However, several of these assumptions are now considered as too progressive. The impact of cosmogenic neutrons induced by muons was assumed to be negligible due to the installation of DARWIN inside a water tank, acting as a muon Cherenkov veto, but no proper background simulations confirmed this expectation. Besides these NR backgrounds, also ER sources contribute events relevant for the WIMP search, as shown in figure 3.5 (a) on page 36: *pp* and $^{7}$Be solar neutrinos, as well as the $2\nu\beta\beta$ of $^{136}$Xe.

Assuming a non-depleted xenon target, these sources constitute irreducible backgrounds and, thus, are not further investigated in this section. Other ER sources like $^{85}$Kr, $^{222}$Rn, and the backgrounds induced by materials can be highly avoided by measures discussed in chapter 3 and chapter 5.

The following section aims to verify the NR background for the DARWIN WIMP search through detailed simulations of cosmogenic (section 4.3.2) and radiogenic neutrons (section 4.3.3) using updated and significantly more precise assumptions on material activities and the detector design. Their outcomes are compared to the irreducible NR background rate induced by CE$\nu$NS events, calculated in section 4.3.1. The results are required for identifying the most problematic NR background sources and thus constitute an important input towards the design and construction of the ultimate dark matter detector and for future sensitivity studies.

### 4.3.1 Coherent elastic neutrino-nucleus scattering

The coherent elastic neutrino-nucleus scattering (CE$\nu$NS) rates were determined following the approach presented in [180]. Three types of neutrino sources were considered: atmospheric, diffuse supernova (DSN), and solar neutrinos. For the latter, only $^{8}$B and *hep* neutrinos were included in the calculation due to their higher energies. Other solar neutrinos such as *pp*, $^{7}$Be, or CNO neutrinos do not yield sufficient energy to cause detectable NR signals in LXe detectors [110].

The differential CE$\nu$NS rate was calculated using equation (2.28), repeated here for completeness:

$$\frac{dR}{dE_r} = N_n \int_{E_{\min}}^{\infty} \frac{d\Phi}{dE_\nu} \frac{d\sigma}{dE_r} dE_\nu \ , \tag{4.7}$$

where $N_n$ denotes the number of target nucleons, $E_{\min} = \sqrt{ME_r/2}$ the minimal neutrino energy required for a given recoil energy $E_r$ and nucleus mass $M$, $\frac{d\Phi}{dE_\nu}$ the spectral neutrino flux, and $\frac{d\sigma}{dE_r}$ the differential scattering cross-section. The differential fluxes $\frac{d\Phi}{dE_\nu}$ for solar neutrinos (see figure 2.11 on page 23) were determined using the procedure presented in [11], taking the characteristic $Q$ and $\Phi_0$ values from the most up-to-date solar models [181]. For the fluxes of atmospheric and DSN neutrinos, the approach described in [108] was applied. The differential $\nu$-nucleus scattering cross-sections $\frac{d\sigma}{dE_r}$ were calculated by

$$\frac{d\sigma}{dE_r} = \frac{G_F^2}{4\pi} Q_W^2 M \left(1 - \frac{ME_r}{2E_\nu^2}\right) F(Q^2)^2 \, \Theta\left(\frac{2E_\nu^2}{M + 2E_\nu} - E_r\right) \ , \tag{4.8}$$

where $G_F$ describes the Fermi coupling constant and $Q_W = N - (1 - 4\sin^2\theta_W)Z$ is the weak nuclear charge with the number of neutrons $N$ and protons $Z$. $M$ is the mass of the nucleus, $\Theta$ the Heaviside step function describing the limitation of momentum transfer by kinematics according to the mass of the incoming neutrino, and $F(Q^2)^2$ is the squared Helm form factor (compare to section 2.1.3). For the latter, the average atomic mass of all xenon isotopes is taken, following the approximation in [48].

The resulting rate spectra are shown in figure 4.8 along with three hypothetical WIMP spectra with WIMP masses of $6\,\mathrm{GeV}/c^2$, $10\,\mathrm{GeV}/c^2$, and $100\,\mathrm{GeV}/c^2$, assuming SI WIMP-nucleus scattering cross-sections of $5 \cdot 10^{-45}\,\mathrm{cm}^2$, $5 \cdot 10^{-48}\,\mathrm{cm}^2$, and $5 \cdot 10^{-49}\,\mathrm{cm}^2$, respectively. While the low-energy recoil range is mostly dominated by $^8$B neutrinos, affecting particularly the sensitivity to lower WIMP masses, the background at higher energies primarily stems from atmospheric neutrinos, affecting the sensitivity to higher WIMP masses. Within the approximate WIMP ROI of [5-40] keV, an integrated total CE$\nu$NS rate of $(8.3 \pm 1.6)\,\mathrm{events}/(200\,\mathrm{t} \times \mathrm{yr})$ is expected, assuming 100% NR acceptance.

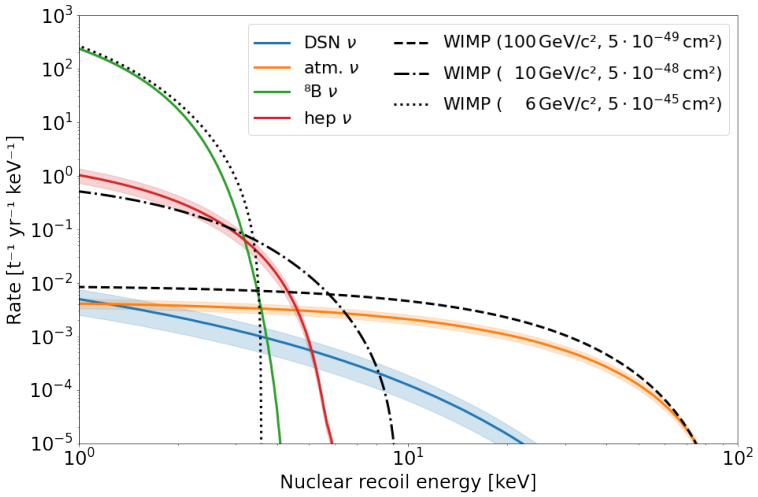


**Figure 4.8:** CE$\nu$NS-induced NR background rates along with three hypothetical WIMP spectra. The low-energy range is dominated by $^8$B neutrinos, the high-energy range by atmospheric neutrinos. The former affects the sensitivity to lower WIMP masses and the latter to higher WIMP masses. The figure assumes 100% NR acceptance and no energy resolution. Bands indicate a $1\sigma$ uncertainty range. WIMP rates calculated with [182].

### 4.3.2 Cosmogenic neutrons

Cosmogenic neutrons are generated in nuclear reactions with energies of up to several GeV by an incoming muon interacting with materials or through muon-induced spallation, negative muon capture, or by secondary particles generated in muon-induced cascades. Their production rate depends on the flux of muons penetrating the rock overburden of the laboratory and the detector shielding. DARWIN's expected rate of NR induced by cosmogenic neutrons was predicted by MC simulations and is presented here, assuming different water tank shields placed at LNGS, where the muon flux was measured to be $(2.6 \pm 0.3) \cdot 10^{-8}\,(\mathrm{cm}^2\,\mathrm{s})^{-1}$ [164] with an average energy of 270 GeV [183].

As inputs for these MC simulations, the energy and angular spectra of muon-induced neutrons produced in the rock and concrete surrounding the laboratory halls at LNGS were used, shown in figure 4.2 (a) and (b). These spectra were taken from [171], where muons following the LNGS-specific energy and angular spectrum were

simulated to generate cosmogenic neutrons in the walls of the laboratory. Due to the known underestimation of the neutron multiplicity by GEANT4, the obtained neutron spectra were scaled to a flux of $7.3 \cdot 10^{-10}\,(\mathrm{cm}^2\mathrm{s})^{-1}$, as reported by additional FLUKA simulations [164]. The study presented in the following is based on pure neutron simulations without considering the preceding "mother" muon or the induced hadronic shower, which might allow tagging the event when these particles cross the detector or the water tank. Thus, the obtained rates must be interpreted as conservative upper values.

Although cosmogenic neutrons are also produced in the detector materials, especially in heavy materials such as the titanium of the cryostat, their induced background is negligible: the probability of generating a SS recoil is fairly small due to accompanying particles created in electromagnetic or hadronic showers, causing a MS event signature. Furthermore, the Cherenkov light produced by a muon crossing the water tank allows tagging such events with an efficiency of $> 98\%$, as simulated by XENON1T [171].

Due to the high energies of cosmogenic neutrons, they are less efficiently shielded by water than photons or radiogenic neutrons originating from the rock and concrete of the laboratory halls. This behavior is shown in figure 4.9 (a), where the fraction of surviving particles depends on the water shield thickness. The simulated $\gamma$ energy spectrum at LNGS was taken from a NaI detector measurement [184], the radiogenic neutron energy spectrum from a SOURCES-4A calculation [170], and the cosmogenic neutron spectrum from figure 4.2 (b).

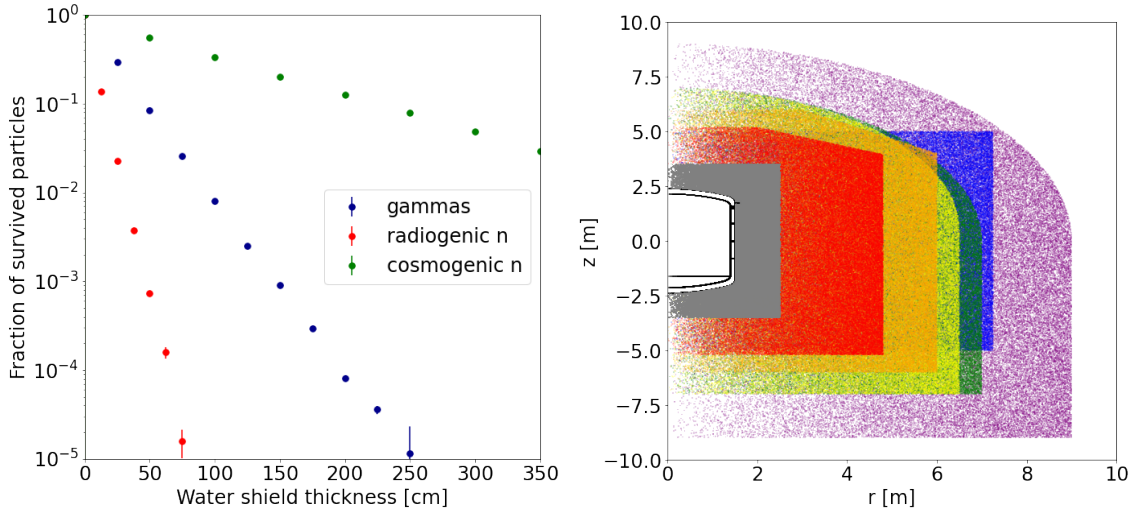


(a) (b)

**Figure 4.9:** (a) Comparison of the shielding efficiencies of a water tank for gammas and radiogenic neutrons originating from the rock/concrete at LNGS and cosmogenic neutrons produced by muons outside the water shield. (b) Geantino visualizations of the investigated water shield geometries. The double-walled DARWIN cryostat is shown in black, surrounded by the neutron veto volume (grey).

According to the procedure described in section 4.1, cosmogenic neutrons corresponding to 715 yr of DARWIN lifetime were simulated, processed, and analyzed to study the impact of the different water tank geometries presented in figure 4.9 (b). Their exact dimensions are given in table 4.5. While most of the tanks fit into Hall B at LNGS, the purple tank describes the larger water tank of the Borexino experiment installed in Hall C. The tank marked in red represents the XENON1T/nT water tank installed in Hall B. In all cases, the water is assumed to be 0.2% gadolinium-doped, allowing for neutron detection in the neutron veto. However, only 20% of all SS NR events were accompanied by a coincident neutron capture event.

The resulting $r^2$-$z$ scatter plots presenting SS NRs with energies $< 100$ keV are shown in figure 4.10: in (a) for the smallest simulated tank (red, XENON1T/nT, ø 9.6 m × 10.4 m) and in (b) for the largest tank (purple, Borexino, ø 18 m × 18 m). The boundaries of a 30 t fiducial volume are marked in red. Note that both plots include data of the same effective simulation time. While for the Borexino tank barely any SS NRs are visible, the XENON1T/nT tank causes a $> 50$ times higher background, which can be reduced only partially by fiducialization. As a consequence of the angular distribution of cosmogenic neutrons presented in figure 4.2 (c), both plots show a slight top-bottom asymmetry.

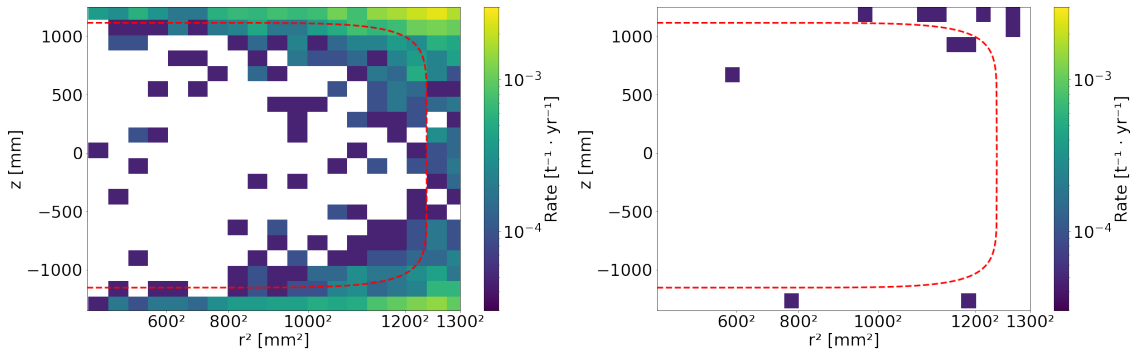


**Figure 4.10:** $r^2$-$z$ projection of the cosmogenic NR background assuming (a) the XENON1T/nT and (b) the Borexino water tank. While the Borexino tank shields most of the cosmogenic neutrons, the XENON1/nT tank leads to a significant cosmogenic neutron background contribution.

The corresponding NR energy spectra of SS events are compared to the irreducible neutrino-induced background in figure 4.11, also including the background spectrum of the ø 12 m × 12 m tank. These spectra show significantly lower rates than the expected CE$\nu$NS rate. However, especially the contribution of the XENON1T/nT tank (ø 9.6 m × 10.4 m) is not negligibly small. A relative comparison of the integrated cosmogenic neutron background rates in the WIMP ROI of [5-40] keV with the irreducible neutrino background is given in table 4.5. Although the results of this study must be interpreted as upper values due to the missing coincidence with the "mother" muon, table 4.5 indicates a minor background contribution of cosmogenic neutrons assuming water tanks larger than ø 12 m × 12 m, which would fit into the Halls A and B at LNGS. A background contribution of $< 6\%$ of the neutrino background is expected for these tanks, corresponding to $< 1$ event/(200 t × yr), as-

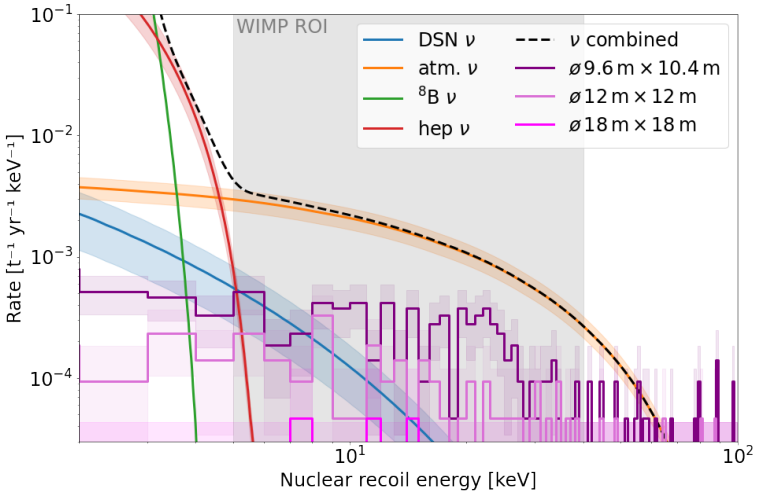


**Figure 4.11:** Differential background rates of cosmogenic neutrons after shielding by different water tanks compared to the irreducible CE$\nu$NS background. A 30 t fiducial volume and a single scatter cut are applied; 100% NR acceptance is assumed. While the contribution assuming the Borexino tank (ø 18 m × 18 m) is negligible, the background assuming the XENON1T/nT shield (ø 9.6 m × 10.4 m) is $\sim$ 17% of the CE$\nu$NS rate.

suming 100% NR acceptance. Considering an even larger water tank of Borexino size would reduce the background rate to a negligible level of $< 1\%$ of the CE$\nu$NS background. This shows that the assumption in [142] to not consider this background in the WIMP sensitivity study was realistic.

**Table 4.5:** Comparison of the cosmogenic single scatter background rates in the WIMP ROI between [5-40] keV for the different water tanks with the irreducible $\nu$ background, assuming a 30 t fiducial volume. The uncertainties are driven by the uncertainties of the expected CE$\nu$NS rate.

| **Tank** | **Size** | **Fraction of $\nu$ background** |
|---|---|---|
| Red (XENON1T/nT) | ø 9.6 m × 10.4 m | $(16.8 \pm 3.6)\%$ |
| Orange | ø 12 m × 12 m | $(5.9 \pm 1.4)\%$ |
| Blue | ø 14.5 m × 10.0 m | $(5.0 \pm 1.2)\%$ |
| Yellow | ø 13 m × 14 m | $(3.4 \pm 0.9)\%$ |
| Green | ø 14 m × 14 m | $(2.6 \pm 0.7)\%$ |
| Purple (Borexino) | ø 18 m × 18 m | $(0.3 \pm 0.2)\%$ |

### 4.3.3 Radiogenic neutrons

Radiogenic neutrons with kinetic energies of several MeV are caused by material contaminations via $(\alpha, n)$ and spontaneous fission reactions. Two types of radiogenic neutrons are distinguished: the neutrons created outside the detector due to contaminations of the rock and concrete surrounding the water tank and the ones created in the detector materials. The former source is negligible due to the efficient shielding by water, as indicated in figure 4.9 (a): every 0.5 m the initial neutron flux

of $9 \cdot 10^{-7}\,(\mathrm{cm}^2\,\mathrm{s})^{-1}$ [171] at LNGS is reduced by one order of magnitude. Consequently, the simulation of radiogenic neutrons presented in the following concentrate on the neutrons created in the detector materials.

In the DARWIN WIMP sensitivity study presented in [142], a radiogenic neutron background rate of $3.8 \cdot 10^{-5}\,\mathrm{events}/(\mathrm{t\,yr\,keV})$ within a 30 t fiducial volume was assumed, corresponding to $\sim 3\%$ of the irreducible CE$\nu$NS background in the WIMP energy ROI of [5-40] keV. The radiogenic neutron study shown here, which includes a much higher level detail and updated assumptions, e.g., on the material activities, yields significantly higher NR background rates (see below). However, a rate of $< 10\%$ of the CE$\nu$NS rate in the WIMP ROI must be reached to be sensitive to SI WIMP-nucleus cross-sections down to $\mathcal{O}(10^{-49}\,\mathrm{cm}^2)$. Thus, options for background reduction are also discussed.

Following the procedure described in section 4.1, $10^6$ radiogenic neutrons were simulated for every material and the isotopes $^{238}$U, $^{226}$Ra, $^{235}$U, $^{232}$Th, and $^{228}$Th. According to equation (4.2), such event numbers correspond to $\mathcal{O}(1000\,\mathrm{yr})$ of effective simulation lifetime, thus providing sufficient statistics. After the SS event selection with a three-dimensional DBSCAN separation threshold of $\varepsilon = 15\,\mathrm{mm}$, the NR rates were reduced to $\sim 65\%$ by the neutron veto due to a coincident neutron capture on gadolinium in the veto volume. The events surviving all cuts were scaled by the neutron production rates in table 4.2 and the assumed specific material activities taken from XENON1T and LZ, as listed in table 4.3.

The $r^2$-$z$ projections of SS NRs of four exemplary detector components (double-walled titanium cryostat, stainless steel electrode support frames, PTFE reflectors and TPC pillars, and Kovar PMT body) are presented in figure 4.12: the contributions of the five decay chains are added for every material and only SS recoils with energies $< 100\,\mathrm{keV}$ are shown. The boundary of a background-optimized 30 t fiducial volume is shown in red. While the Kovar of the PMTs and the electrode support frames mainly induce NRs at the top and bottom of the LXe target, the PTFE and cryostat additionally contribute events along the $r$ direction. Lower rates in the innermost detector region are due to xenon's high stopping power: radiogenic neutrons have mean free paths of $\mathcal{O}(10\,\mathrm{cm})$ and thus can be reduced significantly by fiducialization.

The color scale in figure 4.12 indicates that PTFE and the cryostat induce much higher background rates than the other two studied components. To quantify this difference, the total SS NR energy spectrum of each detector component is shown in figure 4.13, after applying a 30 t fiducial volume cut. In the WIMP ROI (marked grey), the spectra approximately follow an exponential decrease with an increased statistical uncertainty towards higher recoil energies. The highest background rate stems from the titanium cryostat (35.8% of the total radiogenic neutron rate in the WIMP ROI), the PTFE (35.6%), and the PMTs (20.6%), with minor contributions from the Cirlex PMT voltage divider circuits (4.0%), the copper (3.5%), and the electrode support frames (0.5%).

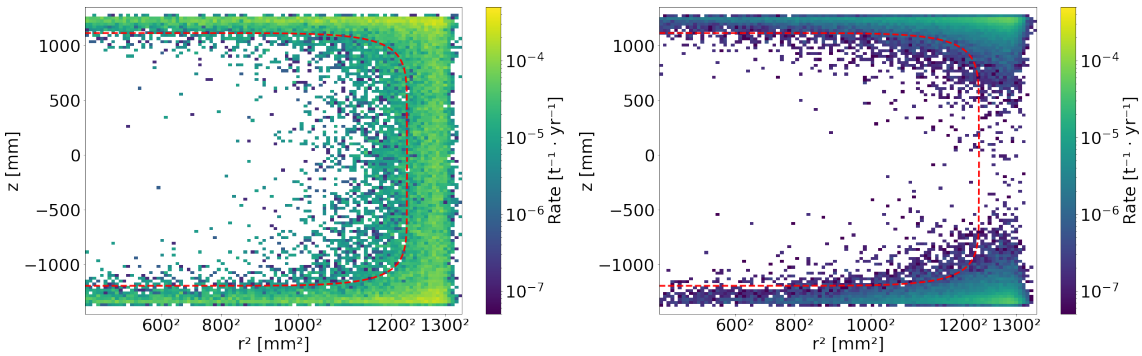


(a) Double-walled titanium cryostat.

(b) Stainless steel electrode support frames.

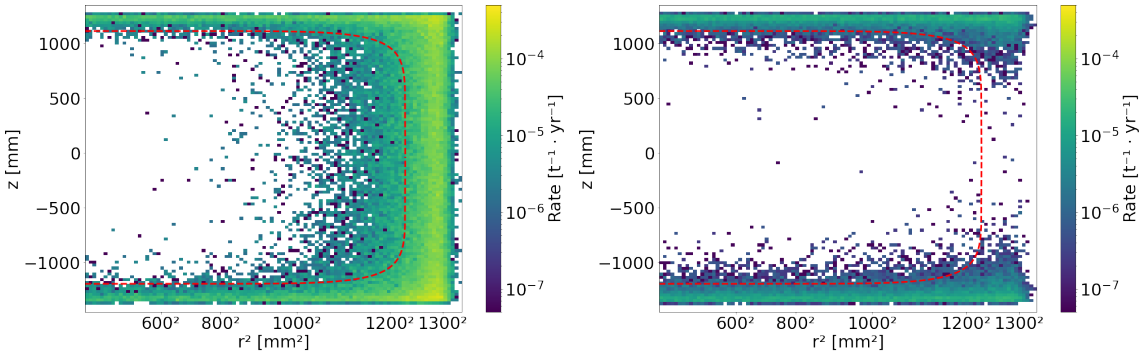


(c) PTFE reflectors and TPC pillars.

(d) Kovar PMT body.

**Figure 4.12:** $r^2$-$z$ projections of SS radiogenic NR background events from different materials. Only SS events with energy depositions $< 100\,\text{keV}$ are shown. The boundary of a 30 t fiducial volume is marked in red. While the PMTs and electrode support frames mainly induce events at the top and bottom of the TPC, the cryostat and PTFE additionally lead to events near the TPC walls and show higher background rates, as indicated by the color scale.

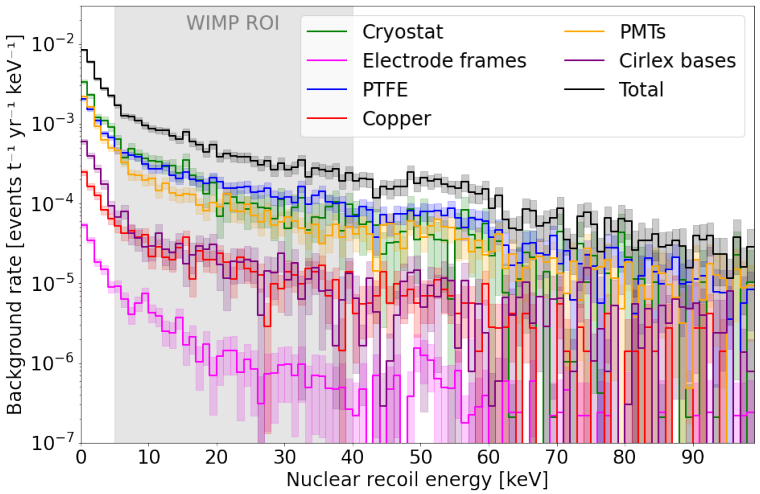


**Figure 4.13:** SS radiogenic NR background spectra assuming a 30 t fiducial volume. The sum spectrum for every material is shown, indicating the cryostat, PTFE, and PMTs as the primary sources of radiogenic neutrons. A typical WIMP energy ROI of [5-40] keV is marked in grey.

The total radiogenic neutron rate (black line in figure 4.13) is compared to the irreducible CE$\nu$NS background in figure 4.14. This total neutron rate is marked as 'baseline scenario', which implies the material activities as identified and used by XENON1T and LZ. The integration of the rate in the WIMP ROI indicates that the radiogenic neutron rate is 51% of the CE$\nu$NS rate, a factor of 17 higher than the background assumed in [142]. Since DARWIN, as the ultimate dark matter detector limited only by irreducible neutrino interactions, requires a minimal background contribution from materials to reach its envisaged WIMP sensitivity, several possibilities of reducing this rate are discussed in the following.

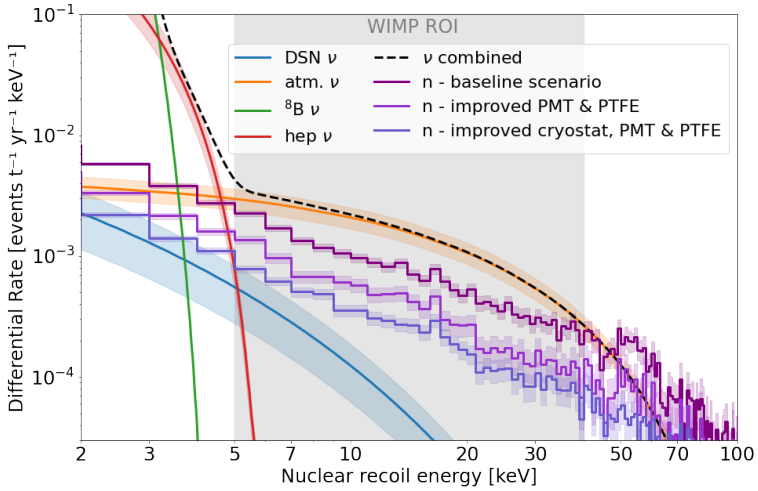


**Figure 4.14:** Comparison of the background rates from irreducible CE$\nu$NS and radiogenic neutrons assuming different material purities. The most progressive assumption with improved cryostat, PMTs, and PTFE materials results in 17% of the CE$\nu$NS rate integrated in the WIMP ROI.

Materials such as PTFE and PMTs could be improved in their contamination levels and geometries. For the PMTs, especially the ceramics of the PMT stem constitutes a significant neutron source due to its high neutron production rate shown in table 4.2. An improved PMT design with a ceramic mass decrease by a factor of 5 was successfully demonstrated in [185]. Assuming these results and the low-background PTFE identified by EXO-200 [99] results in a reduced background spectrum, also shown in figure 4.14 ('improved PMT & PTFE'). It reduces the ratio to the CE$\nu$NS background to 27%. The cryostat would remain by far the largest background source, inducing 70% of the total neutron NR rate. Assuming an improved cryostat background by a factor of 2 further reduces the ratio to the CE$\nu$NS rate to 17%, with the corresponding recoil spectrum also shown in figure 4.14 ('improved cryostat, PMT & PTFE'). This is achievable by either lower titanium material activities or an improved cryostat design. The implementation of more hoop stiffening rings to minimize the wall thickness, as suggested in section 4.2.2, could contribute but does not suffice as a single measure.

MC simulations also allow tracing back the origins of neutrons causing SS NRs in the fiducial volume. This is presented in figure 4.15: (a) shows the origins and corresponding rates for the baseline scenario, (b) shows these results assuming improved PMT, PTFE, and cryostat materials. The color scale indicates, which parts of the

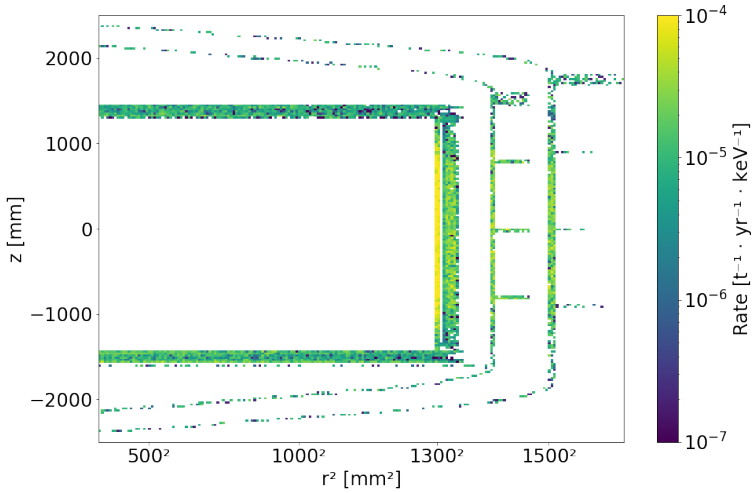


(a) Baseline scenario.

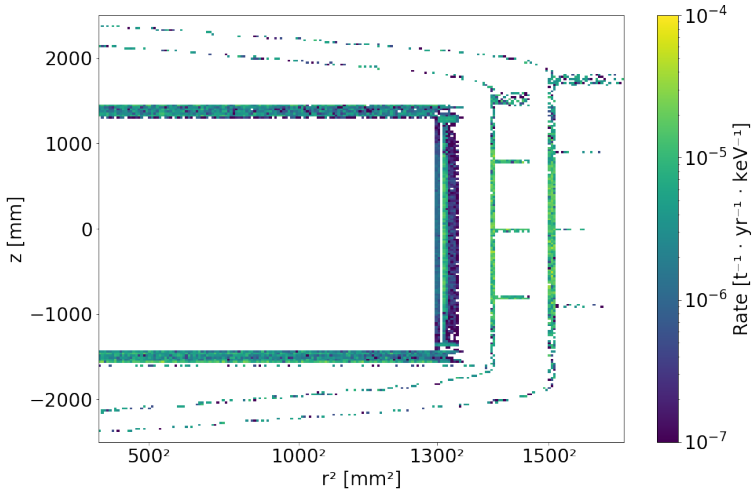


(b) Improved PMT, PTFE, and cryostat.

**Figure 4.15:** Origins of the neutrons causing SS NRs in a 30 t fiducial volume, assuming two different material contamination scenarios. The detector components causing the highest background rates can be identified by the color scale, such as the cryostat walls. Installing the cleanest material samples or reducing the amount of material there allows for background reduction.

materials induce the highest background rates, such as the cryostat walls. Thus, one possibility for background reduction is to install the cleanest materials there or to minimize the required amount of material in these regions.

A veto system could be installed in the non-instrumented LXe volume between the cryostat and the TPC (*LXe veto*). Such a system, which is solely based on the readout of scintillation light, was realized in the XENON100 [186] and LZ [187] detectors to reduce the ER background rate by coincident energy depositions in the veto. An ER energy threshold of $\sim$ 100 keV was achieved in the LXe veto of XENON100, which, however, translates to an $\sim$ 380 keV NR threshold calculated via NEST simulations [173, 174]. This is caused by the lower scintillation yield of NRs. A negligible rate of such high-energy recoils is expected (see figure 4.13),

resulting in a minimal possible NR rate reduction. Moreover, the required implementation of additional veto photosensors, their Cirlex bases, and PTFE reflectors will also contribute to actually increasing the background rate.

Since MS events could falsely be identified as SS events, an improved SS/MS discrimination power serves as a further reduction option. It could be realizable by implementing fine-graved SiPM arrays as light sensors or a $4\pi$ photosensor coverage around the LXe target, resulting in three-dimensional separation thresholds smaller than $\varepsilon = 15\,\text{mm}$. To check its impact on the NR SS rate, the neutron simulation data was clustered assuming a separation threshold of $\varepsilon = 3\,\text{mm}$, which is considered to be the absolute lower limit caused by diffusion. Integrating the expected rates in the WIMP ROI only results in an $\sim 10\%$ decrease compared to the 15 mm scenario. MS events that were falsely identified as SS will be reduced by a factor of $\sim 4$, while true SS events still limit this option for background reduction. Note that the required photosensor installations again induce additional backgrounds, indicating that this approach might be non-profitable. Besides the implementation of additional photosensors, a separation threshold of $\varepsilon = 3\,\text{mm}$ could be obtained by employing a single-phase TPC, discussed in [12], which is also expected to reduce slightly the backgrounds originating from the top photosensor array due to an additional layer of LXe.

The ultima-ratio measure is the background reduction by selecting more stringent fiducial volumes, which directly translates to longer measuring times to achieve a certain exposure. Assuming the improved PTFE, PMTs, and cryostat materials, optimal fiducial volumes containing 28 t, 26 t, and 24 t LXe were defined. The resulting recoil spectra are presented in figure 4.16, which nicely shows the decreasing rate for smaller volumes due to xenon's neutron stopping power. By reducing the fiducial volume from 30 t to 28 t, the background is reduced from 17% to 11% compared to the CE$\nu$NS rate in the WIMP ROI, reaching the envisaged $\mathcal{O}(10\%)$ level. A further volume decrease to 26 t (24 t) results in 7% (4%). The latter result corresponds to a neutron rate of $5.2 \cdot 10^{-5}$ events/(t yr keV) (before applying any finite NR acceptance), comparable to the neutron background assumption of the DARWIN sensitivity study presented in [142].

This study thus shows that sufficiently low radiogenic neutron background rates can be achieved by using ultra-pure materials, which were already identified, by reducing the rate from the titanium cryostat by a factor 2 and by reducing the fiducial volume, which requires to measure 20% longer to reach a given target exposure.

### 4.3.4 Discussion of the WIMP nuclear recoil backgrounds

Motivated by the progressive underlying assumptions in the WIMP sensitivity study in [142] and the input required towards the detector design, DARWIN's expected neutron background was studied in detail in this section. The simulations of cosmogenic neutrons with varying water tank geometries showed that a water shield of at least $\text{ø}12 \times 12\,\text{m}$ water tank is required to push this background contribution

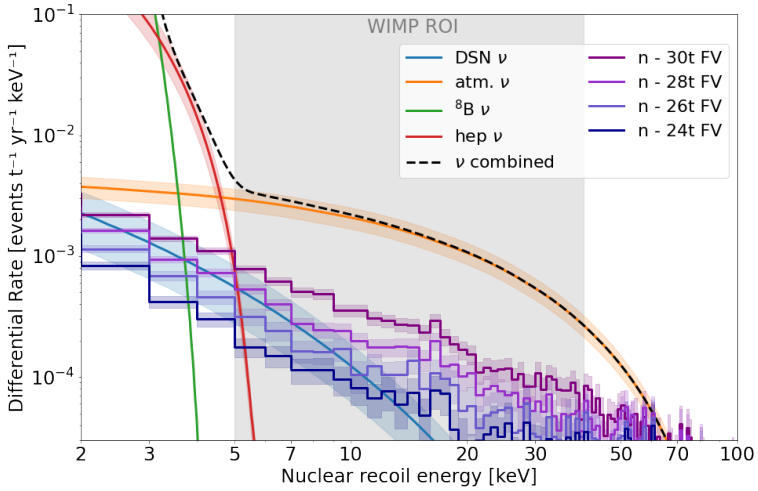


**Figure 4.16:** Comparison of the background rates from the irreducible CE$\nu$NS and radiogenic neutrons assuming different fiducial volumes. A 28 t fiducial volume reduces the neutron background rate to 11% of the CE$\nu$NS rate in the WIMP ROI, a 24 t volume leads to only 4%.

below 6% of the CE$\nu$NS background, assuming LNGS as the experiment's location. The Borexino water tank (ø18 × 18 m) would reduce this rate to a negligible level and thus confirms the general validity of the assumption made in [142] to neglect this background source. Besides the installation of a very large water tank, the cosmogenic neutron background rate could also be decreased by selecting a laboratory with a larger rock overburden. Examples are SURF (4300 m.w.e. [188]) or SNOLAB (6000 m.w.e. [189]) due to their lower muon flux, which would result in an approximate reduction of muon-induced NRs by a factor of 6 and 100, respectively.

Assuming material activities found by the LZ and XENON1T experiments, radiogenic neutrons contribute significantly to the total NR background at the 50% level of the CE$\nu$NS rate. This background contribution is a factor of 17 higher than assumed in [142] and does not allow DARWIN to reach its envisaged WIMP sensitivity. By assuming improved material activities and geometries and more stringent fiducial volume cuts, the radiogenic neutron background rate could be pushed below 10% of the CE$\nu$NS rate. This study shows that the radioactive contaminations in the main materials/components PTFE, PMTs, and in particular the titanium cryostat have to be improved. For each of these materials, studies are currently ongoing. The impact of this background on the WIMP sensitivity is subject of follow-up investigations.

## 4.4 Neutrinoless double beta decay of $^{136}$Xe

DARWIN's primary science goal is the direct detection of WIMPs with expected recoil energies of a few keV$_{\mathrm{NR}}$. However, its low-background environment and good energy resolution also allow competitive searches of physics objectives in the MeV$_{\mathrm{ER}}$ range, such as the neutrinoless double beta decay ($0\nu\beta\beta$) of $^{136}$Xe with a $Q$ value of (2457.83 ± 0.37) keV [87]. This decay is a yet-unobserved process beyond the

SM and its detection would provide crucial information on the neutrino nature (see section 2.2.1). Several detectors have been specifically built to detect the $0\nu\beta\beta$ of $^{136}$Xe; the most stringent limits to date are from EXO-200 [190] and KamLAND-Zen [95]. In contrast to the two mentioned experiments, DARWIN will not be enriched in the double-beta decaying isotope $^{136}$Xe and still is expected to improve the current limits. In this section, a MC-based study predicting DARWIN's half-life sensitivity is presented, which follows the corresponding publication [10]. This thesis contributed to the work by investigating the external backgrounds, developing a background model, and calculating the optimal fiducial volume.

First, the signature of hypothetical $0\nu\beta\beta$ signal events in LXe is studied in section 4.4.1. The relevant backgrounds, both xenon-intrinsic and external, are investigated in section 4.4.2, where the background model is established. Since external backgrounds can be highly reduced by target fiducialization, the optimal fiducial volume is determined by applying a figure-of-merit estimator in section 4.4.3, where DARWIN's sensitivity is presented. All assumptions in this study are based on previously achieved detector performances and thus considered to be rather conservative. The discussion in section 4.4.4 also covers the expected sensitivities of more progressive scenarios, i.e., possible achievements of a detector with a neutrino-dominated background.

### 4.4.1 $0\nu\beta\beta$ signatures in LXe

In contrast to the $2\nu\beta\beta$, in which a fraction of the $Q$ value is carried away undetected by the two generated neutrinos, the energy in a $0\nu\beta\beta$ is completely transferred to the two emitted electrons in the form of kinetic energy. Since these electrons thermalize within $\mathcal{O}$(mm) in LXe - unresolvable by a DARWIN-like detector - the $0\nu\beta\beta$ signal is expected to be a SS event with a signature as presented in figure 2.8 (b) on page 19. However, Bremsstrahlung photons emitted during the electrons' thermalization can travel longer distances without energy depositions: e.g., a 300 keV photon shows a mean free path of $> 15$ mm. This can result in several spatially separated energy depositions and thus lead to a possible MS signature.

Two simulated $0\nu\beta\beta$ events are shown in figure 4.17. While the left plot shows a SS event with the thermalization of the electrons generated back-to-back on a scale of 1-2 mm, the right plot presents a MS event, where a 400 keV photon first Compton scatters $\sim 8$ mm away from the decaying $^{136}$Xe atom and is then absorbed after traveling further $\sim 2$ cm without any energy depositions. The circles indicate the boundaries of the DBSCAN algorithm, which groups the single energy depositions, accounting for the detector's ability to distinguish SS/MS topologies.

The signal acceptance - the fraction of true signal events with a SS topology - was studied by GEANT4 MC simulations of the two emitted electrons for varying DBSCAN separation thresholds $\varepsilon$. The results are presented in figure 4.18. Since the exact energy share between the electrons and their emission angle are unknown, different models were investigated and are shown in the plot. This includes the

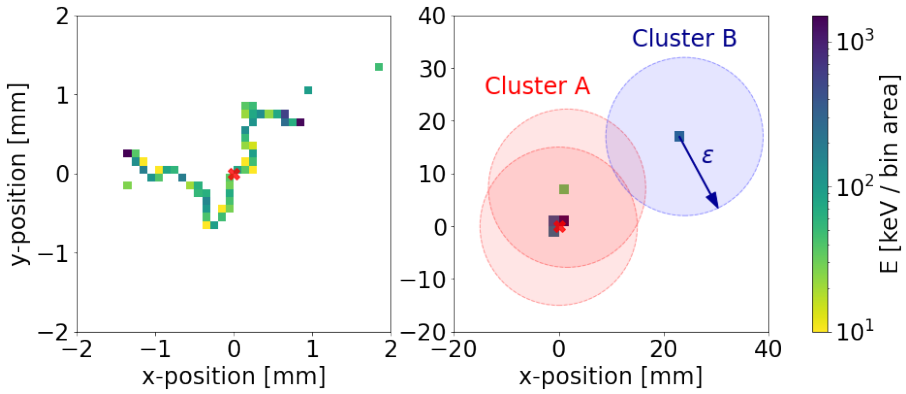


**Figure 4.17:** Energy depositions of two simulated $0\nu\beta\beta$ events in the $x$-$y$ plane. The left figure shows the thermalization track of two electrons with equal kinetic energy, generated back-to-back, leading to a SS event topology as all energy is deposited within a radius of $\sim$ 1.5 mm. The right plot shows a MS event with two reconstructed clusters A and B, caused by the emission of a Bremsstrahlung photon, traveling for $\sim$ 2 cm without interacting with the LXe. The decay position is marked by a red cross. The circles indicate the boundaries of individually resolvable energy depositions assuming a separation threshold of $\varepsilon = 15$ mm. Figure from [10].

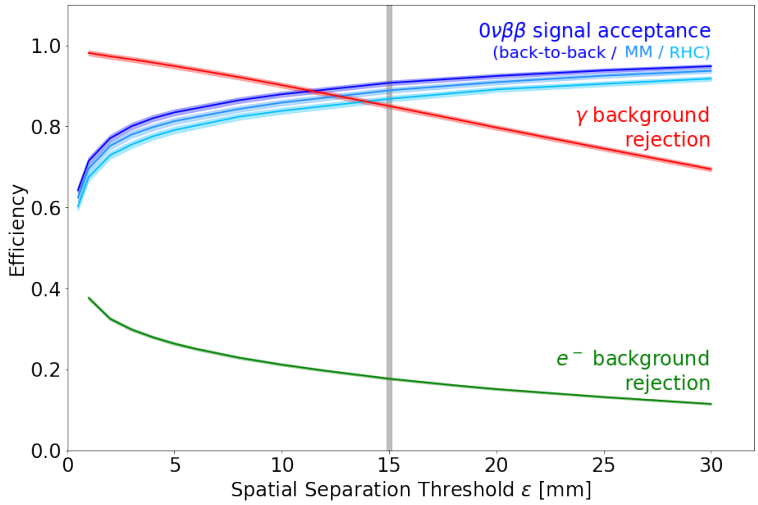


**Figure 4.18:** $0\nu\beta\beta$ signal acceptance and $\gamma/e^-$ background rejection efficiencies for varying cluster separation thresholds $\varepsilon$. The signal acceptance (blue) is shown for three different models for the kinematics of the two electrons: back-to-back, mass-mixing (MM), and right-handed current (RHC) model [191]. For comparison, the background rejections of photons (red) and electrons (green) with $Q_{\beta\beta}$ energies are included. A spatial separation threshold of $\varepsilon = 15$ mm (grey) is applied for the further analysis. Bands indicate the $2\sigma$ uncertainty range. Figure from [10].

"standard" back-to-back electrons with equal kinetic energies but also the MM, and RHC model [191]. They show similar results within $< 5\%$, indicating that the exact model of the $0\nu\beta\beta$ decay only subdominantly influences the expected sensitivity. The MM and RHC model are expected to predict smaller efficiencies than the back-to-back model since their energy asymmetry causes the presence of one electron of higher energy and thus a higher probability of emitting higher-energetic Bremsstrahlung photons.

In this analysis the results for back-to-back electrons were taken, assuming a spatial separation threshold of $\varepsilon = 15\,\text{mm}$, which is expected to be feasible in the DARWIN TPC at recoil energies of around 2.5 MeV. According to figure 4.18, this results in a signal acceptance of 90.4% (the MM and RHC model give acceptances of 88.7% and 86.6%, respectively). Figure 4.18 also includes the efficiency for the background rejections of photons and electrons with $Q_{\beta\beta}$ energy. Both efficiencies improve for lower separation thresholds. For the assumed $\varepsilon = 15\,\text{mm}$, $\gamma$ background events are tagged as MS events and rejected with a probability of 85.1%; electron backgrounds are rejected with an efficiency of 17.7%.

### 4.4.2 Background model

Several background sources contribute events in the $0\nu\beta\beta$ energy ROI, defined as the full width at half maximum (FWHM) of the Gaussian signal peak at $Q_{\beta\beta}$, assuming an energy resolution of 0.8% [179], which corresponds to the [2435-2481] keV interval. There are xenon-intrinsic and external backgrounds, where the former sources are characterized by their homogeneous distribution in the LXe target. The different backgrounds are investigated in the following; for the external backgrounds, which stem from long-lived primordial radionuclides contained in materials, a detailed background model is developed.

#### Intrinsic backgrounds

The double beta-decaying isotope $^{136}$Xe itself contributes to the background via the known $2\nu\beta\beta$. Since its energy deposited within the LXe target follows the differential spectrum presented in figure 2.8 (b) on page 19, its impact strongly depends on the detector's energy resolution. The resolution achieved by XENON1T is described by equation (4.6) with an uncertainty of 0.8% at $Q_{\beta\beta}$ [179]. The overlap of the $2\nu\beta\beta$ spectrum with the $0\nu\beta\beta$ ROI was assessed in detail by calculating the $2\nu\beta\beta$ spectrum using the non-relativistic Primakoff-Rosen approximation for the interaction between nuclei and electrons. It is assumed to be conservative due to the overestimated signal rate around $Q_{\beta\beta}$ [160]. With the measured $2\nu\beta\beta$ half-life of $(2.165 \pm 0.061) \cdot 10^{21}\,\text{yr}$ [126], a background rate of $< 10^{-5}\,\text{events}/(\text{t}\,\text{yr}\,\text{keV})$ at $Q_{\beta\beta}$ is calculated.

Furthermore, the $^{136}$Xe nucleus can be activated by neutron capture, resulting in the $\beta^-$-decaying isotope $^{137}$Xe with a half-life of 3.82 min and a $Q_\beta$ value of 4.17 MeV [9]. It contributes to the $0\nu\beta\beta$ background by naked and $\gamma$-accompanied $\beta$ decays if they are identified as SS events. Even though radiogenic neutrons originating from the detector material can also be captured by $^{136}$Xe, the capture process is dominated by several orders of magnitude by cosmogenic neutrons, primarily those generated and thermalized in the LXe target. Cosmogenic neutrons can also be captured by $^{136}$Xe atoms in the xenon purification loop outside the water shield. However, the induced background can be suppressed by a delayed xenon re-feed after an activity cool down in a shielded environment. Assuming a muon flux of $2.58 \cdot 10^{-8}\,(\text{cm}^2\,\text{s})^{-1}$

at LNGS [164] the $^{137}$Xe production rate is estimated by MC simulations. It results in the production of $(6.9 \pm 0.4)$ atoms/(t yr), which corresponds to a SS background rate of $(1.42 \pm 0.17) \cdot 10^{-3}$ events/(t yr keV) at $Q_{\beta\beta}$.

$^{222}$Rn is permanently emanated from material surfaces due to the presence of $^{238}$U. It is dissolved in the LXe target with an assumed specific activity of 0.1 $\mu$Bq/kg [7]. Among the decay daughters of $^{222}$Rn, only the $\beta^-$ decay of $^{214}$Bi features a sufficiently high Q-value of 3.27 MeV [9] to contribute to the background in the $0\nu\beta\beta$ ROI. It directly decays with no additional $\gamma$ emission to the ground state of $^{214}$Po with a probability of 19.1%, which prevents an efficient background rejection based on the spatial signal topology. However, $^{214}$Po's short half-life of 164 $\mu$s enables a background suppression with an efficiency of 99.8% [192] due to its coincident decay (*BiPo tagging*). $^{214}$Bi decays are studied by MC simulations, taking into account both naked and $\gamma$-accompanied $\beta$ decays, and result in a SS background rate of $(3.09 \pm 0.05) \cdot 10^{-4}$ events/(t yr keV) at $Q_{\beta\beta}$.

Among the various sources of neutrinos, only $^8$B and *hep* solar neutrinos yield sufficient energy for elastic electron scattering with energies in the $0\nu\beta\beta$ ROI. Since the flux of *hep* neutrinos is 3 orders of magnitude lower than the $^8$B flux and atmospheric neutrinos show even lower fluxes, they are considered negligible. Based on current numbers on the solar neutrino fluxes shown in figure 2.11 on page 23 with an $^8$B flux of $\Phi = (5.46 \pm 0.66) \cdot 10^6$ (cm$^2$ s)$^{-1}$ [193], the differential background rate from $^8$B is calculated using equation (2.27). An electron neutrino survival probability of $P_{ee} = 0.50^{+5\%}_{-30\%}$ is assumed, which leads to a background rate of $(2.36^{+0.31}_{-0.76}) \cdot 10^{-4}$ events/(t yr keV) at $Q_{\beta\beta}$.

The background rates of all intrinsic sources are summarized in figure 4.23 (b), where the complete background spectrum (intrinsic and external) around $0\nu\beta\beta$ for a 5 t fiducial volume is presented. For the analytic background model used in section 4.4.3, the $^8$B background is assumed to be flat, the $^{137}$Xe and $^{222}$Rn spectra linearly falling with fit parameters obtained from MC simulations, and the $2\nu\beta\beta$ background as described above with the Primakoff-Rosen approximation. The dominant intrinsic background source are $^{137}$Xe decays, followed by $^{222}$Rn, $^8$B, and the subdominant contribution from $^{136}$Xe. The impact of a different laboratory than LNGS, with a possible lower muon flux and thus lower background contribution from $^{137}$Xe, is discussed in section 4.4.4.

### External backgrounds

Long-lived radionuclides contaminate each detector material. Their decays and the decays of their daughter isotopes induce background events, whose rate are estimated in the following. Most radionuclides of these decay chains do not yield sufficiently high $Q$ values to cause events in the $0\nu\beta\beta$ ROI. The relevant isotopes are $^{214}$Bi, $^{208}$Tl, $^{44}$Sc, and $^{60}$Co. The main contribution of the two former isotopes, parts of the $^{226}$Ra and $^{228}$Th chains, are $\gamma$-rays with energies of 2.45 MeV and 2.61 MeV, respectively. $^{44}$Sc, a daughter of the cosmogenically activated $^{44}$Ti, causes a $\gamma$ emission

at 2.66 MeV. $^{60}$Co could contribute temporally non-resolvable deexcitations of its daughter isotope $^{60}$Ni with energies of 1.17 MeV and 1.33 MeV [9], if both gammas are absorbed at the same location.

Background simulations of these isotopes were generated, processed, and analyzed following the procedure described in section 4.1. An equivalent of at least 100 years of DARWIN run time was generated for each material and isotope. Besides the materials listed in table 4.3, this includes the simulation of the non-instrumented LXe volume, where dissolved $^{222}$Rn can lead to $^{214}$Bi decays, which cannot be discriminated by BiPo tagging. The energy depositions generated by GEANT4 were spatially grouped using the DBSCAN algorithm with a separation threshold of $\varepsilon = 15$ mm, similar to section 4.4.1, to define SS and MS events. A spatial resolution of 10 mm and the energy resolution described by equation (4.6) were applied. Material activities as measured by XENON1T and LZ were assumed to translate MC events to background rates following equation (4.4). The resulting spatial distribution of the total external background is shown in figure 4.19, where only SS events contained in the $0\nu\beta\beta$ ROI are included. In addition, the boundaries of several fiducial volumes are plotted. Each of these volumes is optimized individually to contain the lowest possible background rate for a given fiducial LXe mass. To compensate for the reduced shielding power in the xenon gas phase, they are not located at the vertical center of the instrumented volume but slightly shifted downwards.

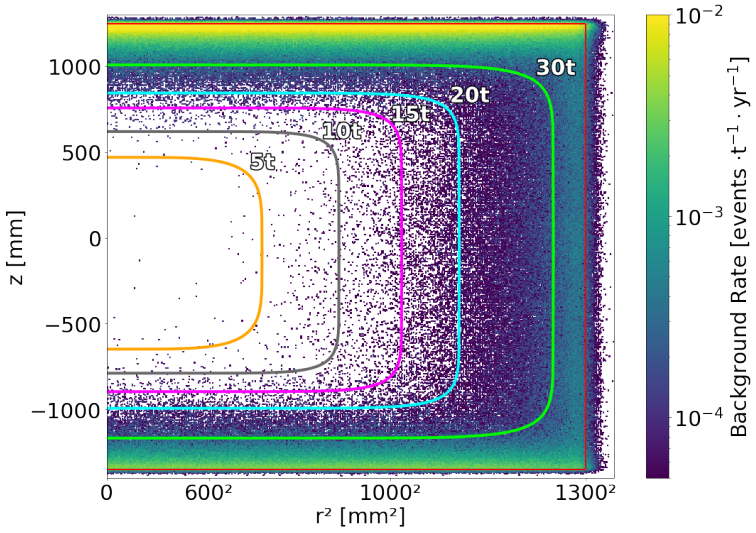


**Figure 4.19:** Spatial distribution of external background events for the $0\nu\beta\beta$ search. The red line indicates the boundaries of the target volume; other colored lines indicate several fiducial volumes containing different LXe target masses.

The relative background contribution of each material in the $0\nu\beta\beta$ ROI for a 20 t fiducial volume is presented in figure 4.20 (a). The titanium, primarily from the double-walled cryostat, and the PMTs with their Cirlex HV dividers contribute background rates of a similar level. This is due to the fiducial volume optimization, which properly balances the events from the PMTs (along $z$) and the cryostat (also along $r$). Figure 4.20 (b) shows the total spectral contribution of each simulated isotope, summed over all materials. The total background in the $0\nu\beta\beta$ ROI is primarily

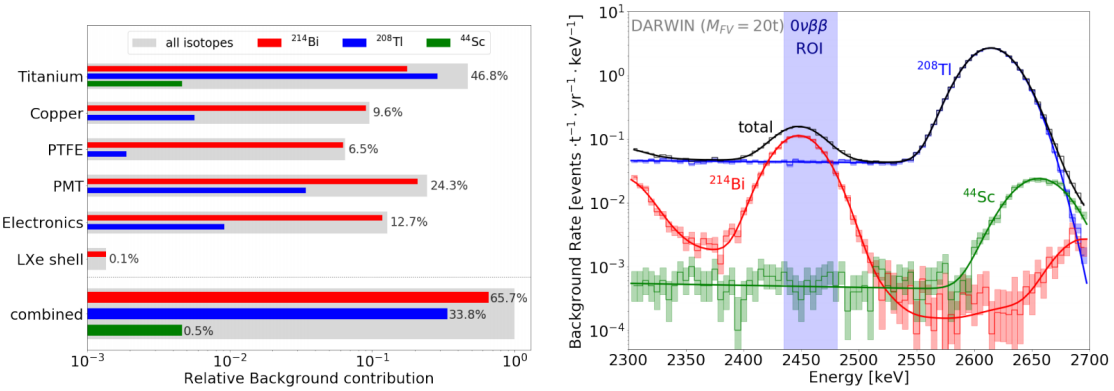


(a) (b)

**Figure 4.20:** Composition of external backgrounds for a 20 t fiducial volume. (a) shows the relative contribution for every material and isotope, indicating that titanium and the PMTs with their high voltage (HV) divider circuits constitute the largest background sources. (b) shows the contribution of the three dominant isotopes $^{208}$Tl, $^{214}$Bi, and $^{44}$Sc summed over all materials, where $^{214}$Bi contributes the most background events in the $0\nu\beta\beta$ ROI.

composed of the $^{214}$Bi absorption peak at 2.45 MeV (red) and the Compton-scattered photons of the 2.61 MeV $^{208}$Tl peak (blue). Their $\alpha$ and $\beta$ contributions are removed by target fiducialization. The latter contribution is dominated by photons undergoing an undetected Compton scatter outside the instrumented LXe followed by an absorption inside the fiducial volume. The $^{44}$Sc and $^{60}$Co rates only contribute negligibly: at $Q_{\beta\beta}$ $^{60}$Co accounts for approximately 0.1% of the background events due to its comparably low material contamination (compare table 4.3) and the low chance of causing a SS topology. It is thus not included in figure 4.20 (b). $^{44}$Sc, which contaminates the titanium material, accounts for less than 1% of the $0\nu\beta\beta$ ROI background through its continuous contribution below the 2.66 MeV full absorption peak (green).

Since the background rates presented above are highly reduced by target fiducialization and for small fiducial volumes these rates have large statistical uncertainties (even though 100 yr of DARWIN run time were simulated), a background model is established in the following. The background rates of larger fiducial volumes with higher statistics are taken to predict the background rates of smaller fiducial volumes, which is expected to predict valid results since the same physics processes take place in all volumes. This background model is used in section 4.4.3 to calculate DARWIN's fiducial volume-dependent sensitivity to the $0\nu\beta\beta$.

Figure 4.20 (b) shows the background model (black) for a 20 t fiducial volume: The isotopes' spectra are modeled by a Gaussian peak plus an exponentially decreasing Compton continuum. The 2.66 MeV full absorption peak of $^{208}$Tl, the 2.61 MeV peak of $^{44}$Sc, and each contribution $> 2$ MeV of $^{214}$Bi were considered. The isotope-specific models are presented for different fiducial volumes in figure 4.21, where the 6 t volume approximation is not shown for $^{214}$Bi and $^{44}$Sc due to a lack of statistics.

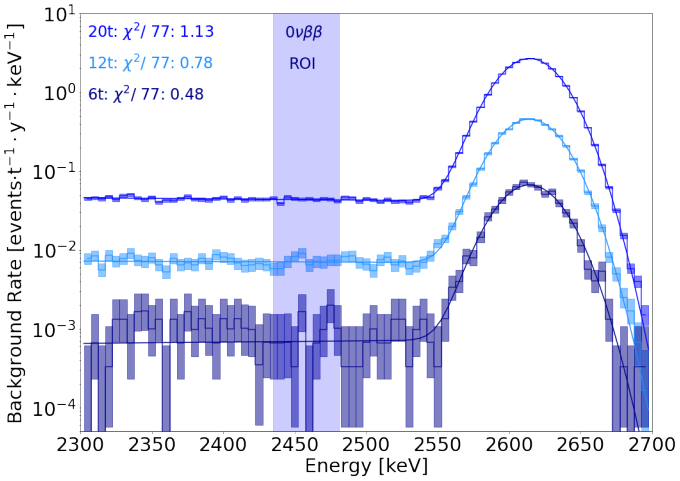


(a) $^{208}$Tl.

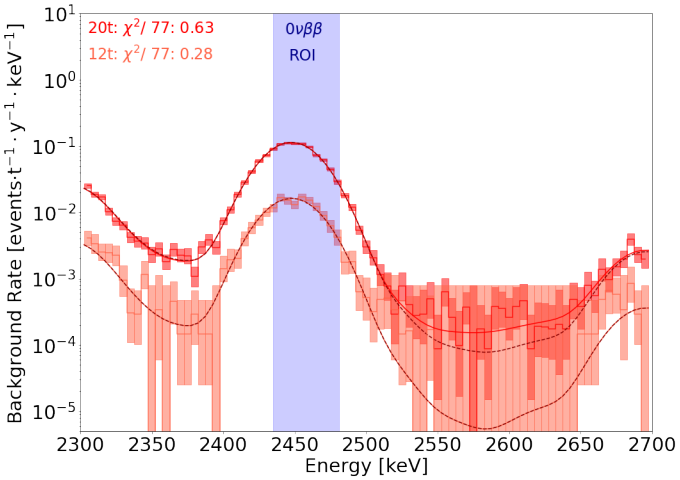


(b) $^{214}$Bi.

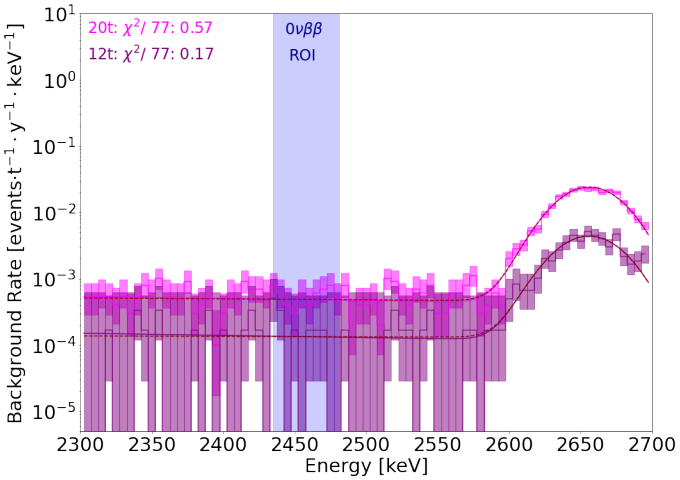


(c) $^{44}$Sc.

**Figure 4.21:** Fits to the simulated background spectra for each isotope and different fiducial volumes. Each absorption peak is modelled by a Gaussian function plus an exponentially decreasing continuum. The corresponding peak intensity, continuum, and slope parameters are extracted to constrain a background model with fewer free parameters for model simplification.

Since the individual widths of the Gaussian peaks are given by the energy resolution defined in equation (4.6), the remaining free model fit parameters (for each isotope) are the peak intensity, the parameter describing the background index of the continuum at $Q_{\beta\beta}$, and the parameter describing the slope of the Compton continuum. In total, this adds up to 9 free parameters for the total background model, which is the sum of the three isotopes.

The slope parameters are in agreement with each other within statistical uncertainties, which is expected due to the similar physics processes. To reduce the number of free parameters from 9 to 7 and simplify the background model, the slopes of the $^{214}$Bi and $^{44}$Sc models were thus fixed to the value obtained by fitting the $^{208}$Tl simulation. The latter provides the highest statistics and is thus considered to be the most accurate choice in smaller fiducial volumes. Fits with both fixed and free slopes are included in figure 4.21. They only show minor deviations with a negligible effect on the $\tilde{\chi}^2$ goodness-of-fit test, where $\tilde{\chi}^2$ describes the $\chi^2$ per degree of freedom.

Similarly, the peak intensity and continuum parameters were constrained to further reduce the number of free parameters and simplify the total background fit. In figure 4.22 (a) the peak intensity factors of the individual isotope fits are presented, showing the same behavior for varying fiducial masses. The mass-dependent scale parameter ratios $^{208}$Tl/$^{44}$Sc and $^{208}$Tl/$^{214}$Bi are shown in figure 4.22 (b). Since a linear function can approximate these ratios, figure 4.22 (b) demonstrates the possibility to also fix the $^{214}$Bi and $^{44}$Sc peak intensity parameters to the $^{208}$Tl simulation. To establish the parameters of these linear functions, fiducial volume mass ranges with sufficient statistics were used: $> 6\,\mathrm{t}$ for $^{214}$Bi and $> 10\,\mathrm{t}$ for $^{44}$Sc. The slight decrease for the former and increase for the latter is attributed to the difference in photon attenuation at the corresponding peak energies.

Figure 4.22 (c) shows the ratio of the continuum parameters. Again, a linear function describes a mass-dependent relation to the $^{208}$Tl value. Since the $^{214}$Bi continuum intensities derived from the individual fit drops towards zero at moderate fiducial volume masses, only data of $> 15\,\mathrm{t}$ fits was taken to establish the fit parameters; for $^{44}$Sc fiducial masses $> 12\,\mathrm{t}$ were considered. Figure 4.22 (d) indicates that $^{208}$Tl's continuum and scale parameter are related, and a power function can describe their ratio. The corresponding fit parameters were verified for fiducial masses of $> 10\,\mathrm{t}$.

To summarize, the relations of the individual fit parameters allow the reduction from initially 9 to 2 free parameters describing the total background spectrum. A summary of the different constraints is given in table 4.6. With the reduced parameter set, global fits on the total material-induced background were performed, as exemplarily shown in figure 4.20 (b) for the 20 t fiducial volume. The $\tilde{\chi}^2$ value was taken to measure the goodness-of-fit (for the 20 t fit: $\tilde{\chi}^2 = 1.0$). It indicates a good agreement between the MC data and the background model, where the latter provides an in total much smaller uncertainty. Based on this established model, the background rates in the energy ROI were derived for several fiducial volumes, used for the sensitivity estimation in the following section.

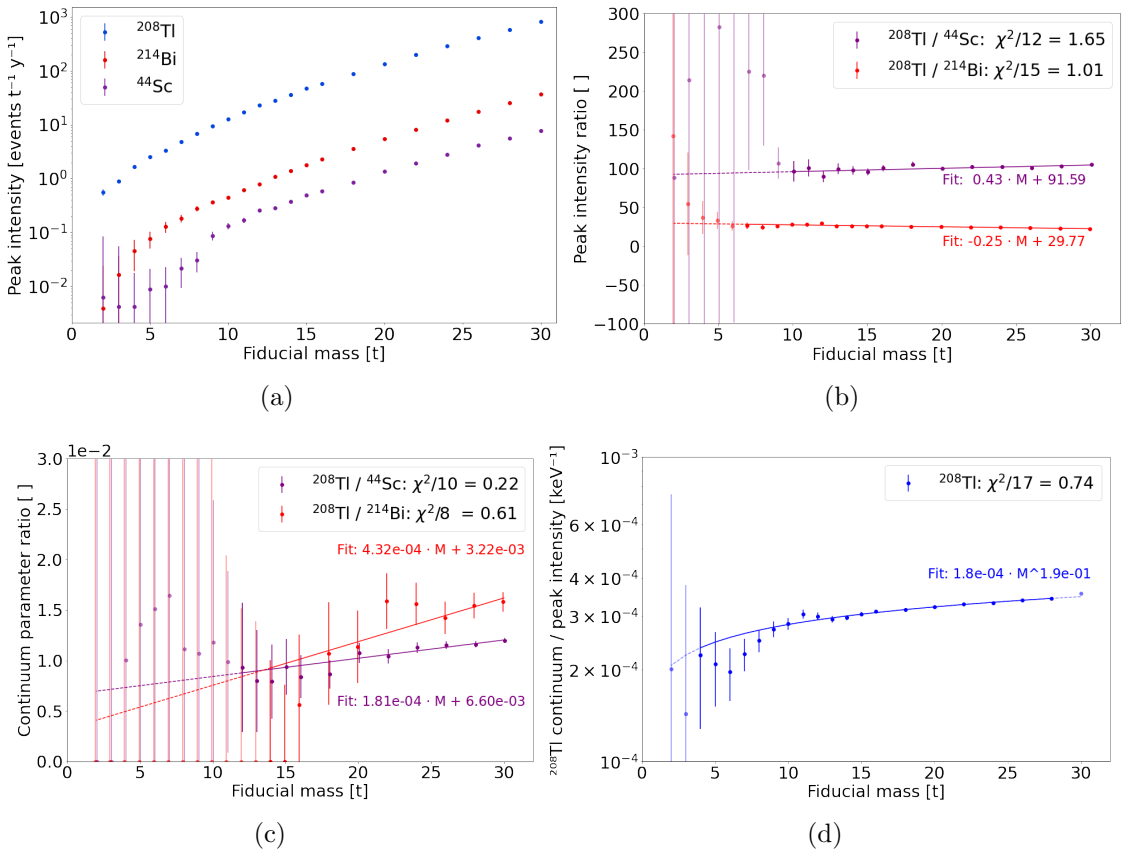


**Figure 4.22:** Relations used to reduce the number of free parameters in the full external background model: (a) indicates the equal scaling of the absorption peak intensity of the three isotopes $^{208}$Tl, $^{214}$Bi, and $^{44}$Sc for varying fiducial masses. (b) Their ratios are described by linear functions. (c) Similarly, the continuum parameters of $^{214}$Bi and $^{44}$Sc can be related to the continuum parameter of $^{208}$Tl. (d) The ratio of the continuum and peak intensity factor of $^{208}$Tl is described by a power function. (a-d) Data of small fiducial masses are not considered for the individual fits due to their high statistical uncertainties. The shown relations reduce the number of free parameters of the external background model to 2, which are fixed by a fit to the MC data.

**Table 4.6:** Parameters used for the fit of the total external background. The only free parameters are the peak intensity and slope of the simulated $^{208}$Tl spectrum.

| Isotope | Peak intensity | Slope | Continuum |
|---|---|---|---|
| $^{208}$Tl | $sc_{^{208}\mathrm{Tl}}$ (free) | $sl_{^{208}\mathrm{Tl}}$ (free) | $c_{^{208}\mathrm{Tl}} = sc_{^{208}\mathrm{Tl}} \cdot (1.8 \cdot 10^{-4} \cdot M^{0.19})$ |
| $^{214}$Bi | $= sc_{^{208}\mathrm{Tl}}/(-0.25 \cdot M + 29.8)$ | $= sl_{^{208}\mathrm{Tl}}$ | $= c_{^{208}\mathrm{Tl}} \cdot (4.3 \cdot 10^{-4} \cdot M + 3.2 \cdot 10^{-3})$ |
| $^{44}$Sc | $= sc_{^{208}\mathrm{Tl}}/(0.43 \cdot M + 91.6)$ | $= sl_{^{208}\mathrm{Tl}}$ | $= c_{^{208}\mathrm{Tl}} \cdot (1.8 \cdot 10^{-4} \cdot M + 6.6 \cdot 10^{-3})$ |

### 4.4.3 Sensitivity

Thanks to the self-shielding ability of the LXe target, the background rate is strongly suppressed by target fiducialization, which is beneficial for the sensitivity to $0\nu\beta\beta$. The background rate depending on the fiducial mass is presented in figure 4.23 (a) and shows the decreasing external background rate for smaller volumes. However,

the fiducialization also minimizes the number of $^{136}$Xe nuclei possible decaying via $0\nu\beta\beta$, which, in turn, worsens the sensitivity. In order to find an optimum between these two trends, an approach using equation (2.23) as figure-of-merit was applied, repeated here for completeness:

$$T^{0\nu}_{1/2} = \ln 2 \frac{\varepsilon \cdot \alpha \cdot f_{\mathrm{ROI}} \cdot N_A}{1.64 \cdot A} \sqrt{\frac{M \cdot t}{\Delta E \cdot b(M)}} \ . \tag{4.9}$$

By inserting the parameters, such as the signal acceptance efficiency $\varepsilon = 90.4\%$ derived in section 4.4.1 or the background index $b(M)$ calculated as the sum of the intrinsic and external backgrounds, the sensitivity to the half-life $T^{0\nu}_{1/2}$ is calculated for every fiducial mass. The results indicate that a 5 t fiducial mass maximizes the sensitivity, reaching a half-life of $T^{0\nu}_{1/2} > 2.0 \cdot 10^{27}$ yr (90% C.L.) after 10 years of DARWIN run time. For this 5 t fiducial volume, the material and intrinsic sources contribute background events at a similar level, as presented by figure 4.23 (a). The corresponding background rates and spectra for every background source are shown in figure 4.23 (b) and table 4.7, which sum up to less than one background event per year in the $0\nu\beta\beta$ ROI. The yellow curve in figure 4.23 (b) corresponds to a hypothetical signal of 0.5 counts/yr, corresponding to a $0\nu\beta\beta$ half-life of $2.0 \cdot 10^{27}$ yr.

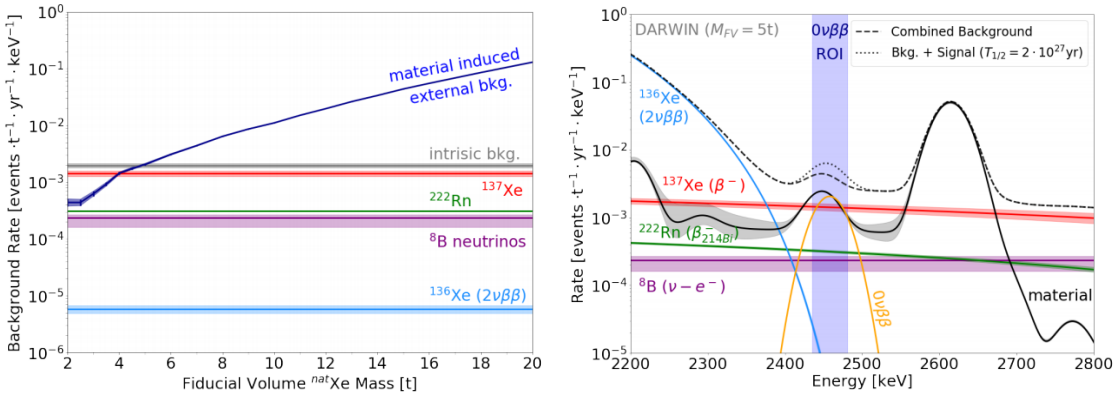


(a) (b)

**Figure 4.23:** (a) The intrinsic and material-induced external background rates in the $0\nu\beta\beta$ ROI depend on the fiducial volume mass. For a 5 t fiducial volume, the external and intrinsic sources contribute a similar amount of background events. (b) Background spectrum around the $0\nu\beta\beta$ ROI assuming a 5 t fiducial volume. The hypothetical $0\nu\beta\beta$ signal (yellow) of 0.5 counts/yr corresponds to a half-life of $T^{0\nu}_{1/2} = 2.0 \cdot 10^{27}$ yr. Bands indicate a $1\sigma$ uncertainty range. Figure from [10].

Since the figure-of-merit estimator does not consider background uncertainties but assumes perfect knowledge of the background rates, a profile-likelihood analysis was performed in [10]. It accounts for the uncertainties presented in table 4.7, obtained from the background model fit, which were treated as nuisance parameters with Gaussian constraining terms in the likelihood. The signal at $Q_{\beta\beta}$ is smeared by the detector energy resolution according to equation (4.6) and scaled by the detection efficiency plus an activity corresponding to $T^{0\nu}_{1/2}$. Assuming 10 yr DARWIN run time and a 5 t fiducial mass, we obtain an exclusion limit of $T^{0\nu}_{1/2} > 2.4 \cdot 10^{27}$ yr (90% C.L.), and a $3\sigma$ discovery potential of $1.1 \cdot 10^{27}$ yr.

**Table 4.7:** Expected background rates in the $0\nu\beta\beta$ ROI, assuming a 5 t fiducial volume mass.

| **Background source** | **Background index [events/(t yr keV)]** | **Rate [events/yr]** | **Rel. uncertainty** |
|---|---|---|---|
| *External backgrounds:* | | | |
| $^{214}$Bi | $1.36 \cdot 10^{-3}$ | 0.313 | ±3.6% |
| $^{208}$Tl | $6.20 \cdot 10^{-4}$ | 0.143 | ±4.9% |
| $^{44}$Sc | $4.64 \cdot 10^{-6}$ | 0.001 | ±15.8% |
| *Intrinsic backgrounds*: | | | |
| $^{8}$B | $2.36 \cdot 10^{-4}$ | 0.054 | +13.9%, −32.2% |
| $^{137}$Xe | $1.42 \cdot 10^{-3}$ | 0.327 | ±12.0% |
| $^{136}$Xe | $5.78 \cdot 10^{-6}$ | 0.001 | +17.0%, −15.2% |
| $^{222}$Rn | $3.09 \cdot 10^{-4}$ | 0.071 | ±1.6% |
| **Total**: | $\mathbf{3.96 \cdot 10^{-3}}$ | **0.910** | **+4.7%, −5.0%** |

### 4.4.4 Discussion

Based on detailed GEANT4 MC background simulations, DARWIN's sensitivity to the $0\nu\beta\beta$ of $^{136}$Xe was predicted, yielding a half-life limit of $T^{0\nu}_{1/2} > 2.4 \cdot 10^{27}$ yr (90% C.L.). This result is considered to be conservative due to the underlying assumptions on the detector performance and detector material purity. For the latter, only activity levels already used in previous or current experiments were assumed. In a more optimistic scenario, which includes the reduction of the ceramic mass in PMTs or alternative photosensors like SiPMs, as well as more radio-pure PTFE and titanium, the material-induced background could be reduced by a factor of 3 or even 5. Reducing the intrinsic backgrounds is also feasible: operating the experiment in a deeper laboratory than LNGS could suppress $^{137}$Xe to a subdominant contribution, reducing the total intrinsic background by a factor of 2. Combined with a higher BiPo tagging efficiency of 99.9% or 99.99%, a factor of 5 or 8, respectively, could be reached. Combining the latter scenario with an assumed external background reduction of factor 5 leads to a solar $^{8}$B neutrino-dominated background.

Furthermore, the $0\nu\beta\beta$ sensitivity could be increased with a smaller spatial separation threshold $\varepsilon$, which could be achieved by a higher photosensor granularity, enabling an improved SS/MS discrimination. Even though the results presented in section 4.4.1 indicate only a minor increase in signal acceptance when reducing this threshold from 15 mm to 3 mm, a sensitivity gain is expected due to the significant background reduction in particular for the external gamma background.

The impact of these measures is presented in figure 4.24, where the $T^{0\nu}_{1/2}$ sensitivity limit is shown dependent on (a) the exposure time and (b) on the mass of the fiducial volume mass. The limits are calculated again using the figure-of-merit estimator and show the most significant increase for a combination of the various possible improvements. For comparison, figure 4.24 (a) also includes the projected sensitivities of several proposed detectors. It indicates that DARWIN will be comparable in its science reach to these dedicated $0\nu\beta\beta$ experiments.

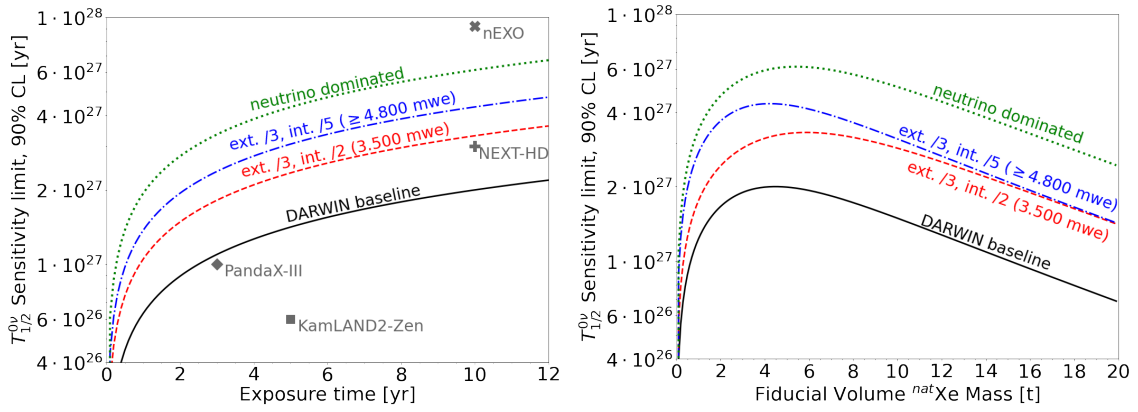


(a) (b)

**Figure 4.24:** The $0\nu\beta\beta$ sensitivity limit of DARWIN at 90% C.L. depends on (a) the exposure time, assuming a 5 t fiducial volume and (b) on the fiducial volume mass, assuming 10 yr run time. The DARWIN baseline performance (black) is compared to possible improved scenarios, which include both the reduction of xenon-intrinsic and external backgrounds and a deeper laboratory. (a) additionally shows the projected sensitivities of several future $0\nu\beta\beta$ detectors, indicating DARWIN's competitiveness to dedicated $0\nu\beta\beta$ experiments. Figures from [10].

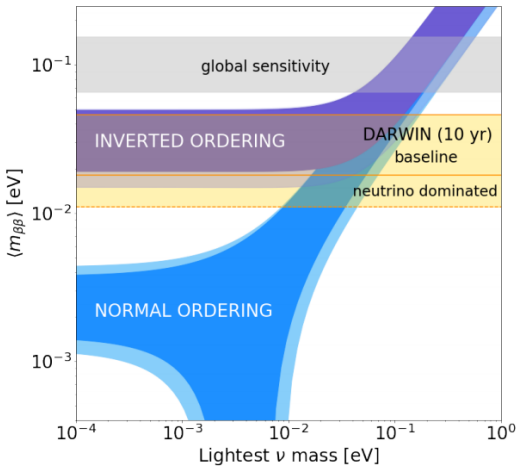


**Figure 4.25:** Effective neutrino Majorana mass $m_{\beta\beta}$ vs. the lightest neutrino mass. DARWIN's expected sensitivity after 10 years run time is shown for the baseline and neutrino-dominated scenario (yellow) and compared to current results (global sensitivity, grey). The neutrino-dominated scenario might allow conclusions on the neutrino mass ordering. The width of the bands correspond to the range of nuclear matrix elements.

Using equation (2.21), DARWIN's $T^{0\nu}_{1/2}$ sensitivity limit is translated to the effective neutrino Majorana mass $m_{\beta\beta}$. For the baseline scenario and 10 yr run time, this results in a $m_{\beta\beta}$ limit of [18-46] meV; for the neutrino-dominated case, the limit is reduced to [11-28] meV. The width of these bands are caused by the range of published nuclear matrix elements. These results are shown in figure 4.25 and compared to the global sensitivity (the most stringent limits up to date, grey) and neutrino ordering scenarios (blue). It shows that the DARWIN dark matter experiment could provide crucial information on the neutrino masses since it could explore the

entire inverted ordering parameter space in the neutrino-dominated background scenario. Consequently, DARWIN will compete with future $0\nu\beta\beta$ projects introduced in section 2.2.1, such as LEGEND1000 or nEXO.

## 4.5 Neutrinoless double electron capture of $^{124}$Xe

DARWIN's sensitivity to the neutrinoless double electron capture ($0\nu$ECEC) of $^{124}$Xe, a yet-unobserved process beyond the SM, is presented in this section. Similarly to the $0\nu\beta\beta$ of $^{136}$Xe, the observation of the $0\nu$ECEC would imply lepton number violation and the existence of Majorana particles. It would thus provide crucial information on the neutrino nature. This section largely follows the master's thesis of M. Rajado Nunes da Silva [165], supervised in the scope of this work, which provided a first sensitivity estimation. A follow-up study currently investigates possible detector and analysis optimizations to improve the obtained half-life sensitivity presented below.

The $0\nu$ECEC is one of the hypothetical second-order weak decays of $^{124}$Xe, briefly introduced in section 2.2.1. Since its $Q$ value of $(2856.73 \pm 0.12)$ keV [105] is close to the $0\nu\beta\beta$ energy ROI of around 2.5 MeV, the $0\nu$ECEC study closely follows the investigation of the $0\nu\beta\beta$ of $^{136}$Xe (see section 4.4) and uses the same background simulations. The main difference between these two channels is given by their signal topology. While for the $0\nu\beta\beta$ of $^{136}$Xe, the signal is expected to be a SS event, the $0\nu$ECEC of $^{124}$Xe would cause a MS event: Auger electrons and X-rays would be emitted when filling the two K-shell vacancies and $\gamma$-rays released by the deexcitation of the daughter isotope $^{124}$Te. While the Auger electrons and X-rays are expected to deposit energy at the decay position, the released photons with energies between 600 keV and 2000 keV (see figure 2.10 on page 22) have mean free paths of $\mathcal{O}(10\,\text{cm})$ [127]. They thus travel some distance from the decay position without depositing energy. The specific $\gamma$ and double K-shell energies define a very characteristic MS signal signature, which can be used to efficiently discriminate background events. The analysis of these scatter energies requires the knowledge of the S2-only energy resolution, which differs from the combined S1-S2 resolution given by equation (4.6), since the S2 signals cannot be matched with their corresponding S1 signals. The S2-only resolution is thus estimated in section 4.5.1, considering its three driving factors: the fluctuations in the electron production, electron survival probability, and photon detection. The resulting resolution is used in section 4.5.2 to establish a signal tagging mechanism. The intrinsic and external background rates are reduced significantly by an event selection based on this signal tagging. The sensitivity to $0\nu$ECEC is estimated in section 4.5.3, where possibilities to further enhance the results are also given and compared to a zero-background experiment.

### 4.5.1 S2-only energy resolution

In a MS event, the S1 signals are detected simultaneously since the photons travel with the speed of light, while the S2 signals can be separated either spatially ($x$-$y$) and/or in time ($z$). This implies that a direct matching of corresponding S1 and S2

signals to obtain the energy from both signals in combination is not possible and the energy estimation of all scatters must be based on the S2 signal only. However, the S2-only energy resolution is significantly worse than the combined S1-S2 resolution. Since typical science objectives of LXe TPCs are expected to induce SS events, no experimental measurement of an S2-only resolution in the MeV range is publically available and is thus estimated in the following.

Using the S2 signal size, the cluster energy $E$ (the energy deposited in one of the multiple scatters) is determined. It proportionally depends on the energy-dependent number $n$ of electrons generated in the recoil, the fraction $P_{\text{surv}}$ of electrons surviving the drift in the TPC and being extracted into the gas phase, and the mean number of detected photons $\bar{A}$:

$$E \propto n(E) \cdot P_{\text{surv}} \cdot \bar{A} \ . \tag{4.10}$$

Extraction fields of $\mathcal{O}(10\,\text{kV/cm})$ are assumed to yield 100% electron extraction efficiency [125]. Assuming that the parameters of equation (4.10) are independent, which is a good first-order assumption, the S2-only energy resolution is given by the individual uncertainties of the parameters:

$$\frac{\sigma_E}{E} = \sqrt{\left(\frac{\sigma_n}{n}\right)^2 + \left(\frac{\sigma_{P_{\text{surv}}}}{P_{\text{surv}}}\right)^2 + \left(\frac{\sigma_{\bar{A}}}{\bar{A}}\right)^2} \ . \tag{4.11}$$

In contrast to $P_{\text{surv}}$ and $\bar{A}$, $\sigma_{P_{\text{surv}}}$ and $\sigma_{\bar{A}}$ are energy-dependent since they follow a Poissonian distribution and thus are driven by the energy-dependent number of electrons. The factors $\frac{\sigma_n}{n}$, $\frac{\sigma_{P_{\text{surv}}}}{P_{\text{surv}}}$, and $\frac{\sigma_{\bar{A}}}{\bar{A}}$, describing the fluctuation in electron production, survival probability, and number of detected photons, respectively, are studied in the following.

### Fluctuation in production

The parameter $\frac{\sigma_n}{n}$, the fluctuation in the electron production for a certain energy deposition, was obtained from NEST simulations [173, 174]: the recoil energy-dependent number of produced electrons was simulated and its average fluctuation calculated. The results are presented in figure 4.26 (a). Three different TPC drift field strengths, 100 V/cm, 250 V/cm, and 500 V/cm, were assumed. Higher drift fields cause smaller fluctuations, explained by less electron-ion recombination. The lower number of generated electrons explains the higher fluctuations at lower recoil energies. At $Q_{\text{ECEC}}$ fluctuations of 5.0%, 3.5%, and 2.8% for drift fields of 100 V/cm, 250 V/cm and 500 V/cm are obtained.

### Fluctuation in survival probability

The fluctuation in survival probability describes the variation of the number of electrons that survive the electron drift across the TPC and reach the liquid-gas interface. This parameter highly depends on the purity of the LXe target since

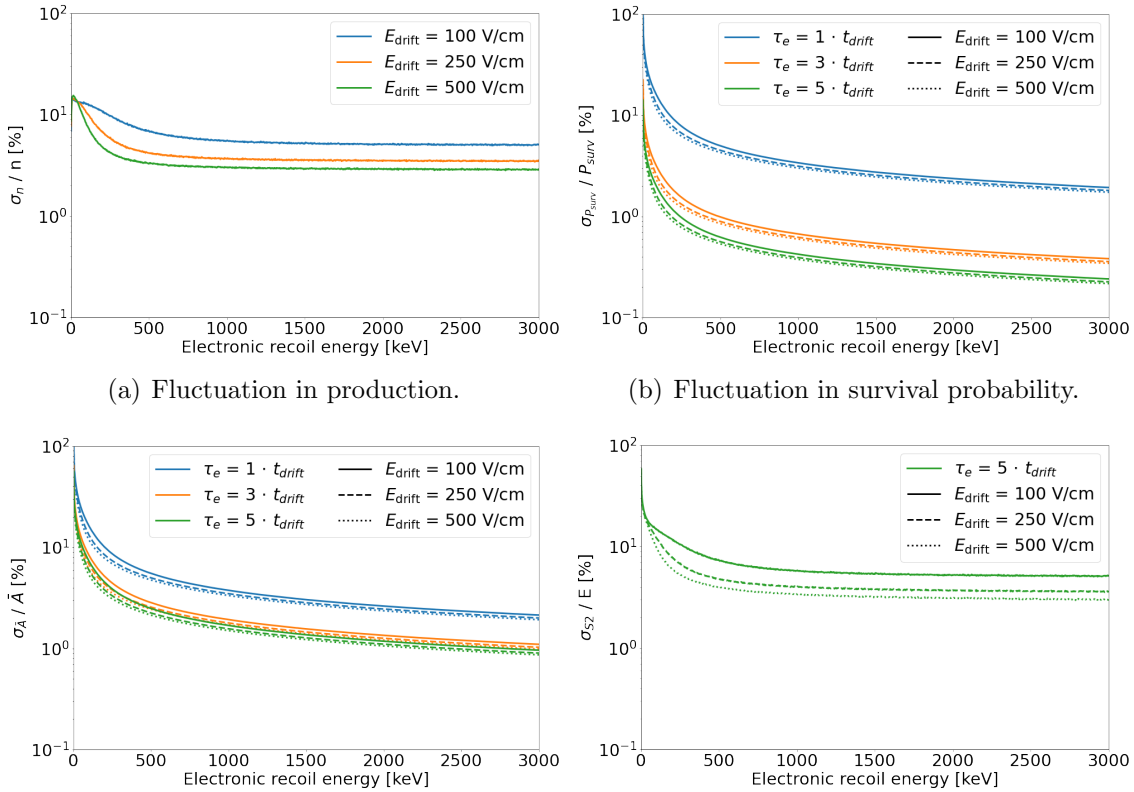


(a) Fluctuation in production.

(b) Fluctuation in survival probability.

(c) Fluctuation photon detection.

(d) Total fluctuation.

**Figure 4.26:** Estimation of the S2-only energy resolution, driven by (a) the fluctuation in electron production, (b) the fluctuation in electron survival probability, and (c) the fluctuation in the number of detected photons. Three drift field strengths (100 V/cm, 250 V/cm, 500 V/cm) and three electron lifetimes ($\tau_e = 1 \cdot \bar{t}_{\text{drift}}$, $\tau_e = 3 \cdot \bar{t}_{\text{drift}}$, $\tau_e = 5 \cdot \bar{t}_{\text{drift}}$) were investigated. As expected, the best results were obtained for higher electron lifetimes and drift fields. The total S2-only resolution, which is dominated by the fluctuation in electron production at $Q_{\text{ECEC}}$, is shown in (d). Data from [165].

electronegative impurities might capture drifting electrons. $\frac{\sigma_{P_{\text{surv}}}}{P_{\text{surv}}}$ follows a Poissonian distribution and is calculated by

$$\frac{\sigma_{P_{\text{surv}}}}{P_{\text{surv}}} = \frac{\sqrt{n_{\text{lost}}}/n}{P_{\text{surv}}} = \frac{\sqrt{P_{\text{lost}} \cdot n}}{P_{\text{surv}} \cdot n} \quad , \tag{4.12}$$

where $n_{\text{lost}}$ describes the number of electrons lost during their drift and $P_{\text{lost}}$ the corresponding probability. Since the number of surviving electrons $n_{\text{surv}} = n - n_{\text{lost}}$ follows a decreasing exponential function, the probabilities $P_{\text{lost}}$ and $P_{\text{surv}}$ can be expressed by

$$P_{\text{surv}} = \frac{n_{\text{surv}}}{n} = e^{-t_{\text{drift}}/\tau_e} \tag{4.13}$$

$$P_{\text{lost}} = 1 - P_{\text{surv}} = 1 - e^{-t_{\text{drift}}/\tau_e} \quad , \tag{4.14}$$

where $t_{\text{drift}}$ describes the drift time and $\tau_e$ the electron lifetime. Using these relations and following equation (4.12), the fluctuation in the survival probability is calculated: the number of produced electrons is extracted from NEST simulations,

assuming different drift field and electron lifetime scenarios. This includes drift fields of 100 V/cm, 250 V/cm, and 500 V/cm and lifetimes of $\tau_e = 1 \cdot \bar{t}_{\text{drift}}$, $\tau_e = 3 \cdot \bar{t}_{\text{drift}}$, and $\tau_e = 5 \cdot \bar{t}_{\text{drift}}$, where $\bar{t}_{\text{drift}}$ describes the average drift time and corresponds to the drift time of electrons produced in the center of the TPC. The results are presented in figure 4.26 (b) and indicate a smaller influence of the drift field compared to the impact of different electron lifetimes. At $Q_{\text{ECEC}}$ and a drift field of 500 V/cm, fluctuations of 1.8%, 0.4%, and 0.2% are obtained for electron lifetimes of $1 \cdot \bar{t}_{\text{drift}}$, $3 \cdot \bar{t}_{\text{drift}}$, and $5 \cdot \bar{t}_{\text{drift}}$, respectively.

**Fluctuation in detected photons**

This parameter corresponds to the variation of photons detected by the photosensors. Photons are created by ionization electrons via proportional scintillation in the gas phase, with numbers following a Poissionian distribution. The more electrons are initially extracted into the gas phase, the lower the expected fluctuation in detected photons, which is calculated by

$$\frac{\sigma_{\bar{A}}}{\bar{A}} = \frac{1}{\sqrt{n_{\text{surv}}}} \cdot \frac{\sigma_{\bar{A}_{SE}}}{\bar{A}_{SE}} \quad , \tag{4.15}$$

where $\bar{A}_{SE}$ describes the S2 yield of a single electron. The factor $\frac{\sigma_{\bar{A}_{SE}}}{\bar{A}_{SE}}$ is extracted from XENON1T data and yields a single electron amplification resolution of $\sim$ 34% [165]. NEST simulation data and assuming electron lifetimes of $\tau_e = 1 \cdot \bar{t}_{\text{drift}}$, $\tau_e = 3 \cdot \bar{t}_{\text{drift}}$, and $\tau_e = 5 \cdot \bar{t}_{\text{drift}}$ were used to determine the number of surviving electrons. Results are presented in figure 4.26 (c) for assumed drift fields of 100 V/cm, 250 V/cm, and 500 V/cm. The field influences the result only as a second-order effect. For a drift field of 500 V/cm and $Q_{\text{ECEC}}$ energy, fluctuations of 2.0%, 1.0%, and 0.9% are obtained for electron lifetimes of $1 \cdot \bar{t}_{\text{drift}}$, $3 \cdot \bar{t}_{\text{drift}}$, and $5 \cdot \bar{t}_{\text{drift}}$, respectively.

The S2-only resolution, which describes the total fluctuation, was calculated using equation (4.11). Figure 4.26 (d) shows the obtained results for an assumed electron lifetime of $5 \cdot \bar{t}_{\text{drift}}$. In the work presented here, this electron lifetime and a drift field of 500 V/cm are assumed. It results in an S2-only resolution of 3.0% at $Q_{\text{ECEC}}$, dominated by the fluctuations in the electron production process. While the electron lifetime might be realistic, considering the lifetime achievements of current experiments [194, 6], the drift field is a rather optimistic assumption.

### 4.5.2 Signal tagging and background reduction

Since the $Q$ value of the $0\nu$ECEC of $^{124}$Xe is close to the $Q$ value of the $0\nu\beta\beta$ of $^{136}$Xe, the background simulations described in section 4.4 could be re-used in this framework with minor modifications: a more progressive SS/MS discrimination power was assumed, described by a DBSCAN cluster separation threshold of $\varepsilon = 5$ mm, which might be feasible in the investigated MeV energy range. The re-analyzed background simulations include the simulations of the material contaminations $^{214}$Bi, $^{208}$Tl, and $^{44}$Sc and of the xenon-intrinsic sources $^{214}$Bi, $^{137}$Xe, as well

as $^{8}$B neutrinos. Even though $^{8}$B solar neutrinos show a negligible probability of scattering more than once in the detector and thus cannot mimic the MS 0$\nu$ECEC signal, Bremsstrahlung photons could be induced by the recoiling electron, which, with their mean free paths of $\mathcal{O}$(cm) [127], could cause a MS event topology. The 2$\nu\beta\beta$ of $^{136}$Xe was not included in this study due to its spectral endpoint at $Q_{\beta\beta}$, well below the $Q_{\mathrm{ECEC}}$.

The differential spectra of the considered backgrounds are shown in figure 4.27 for the external (a) and xenon-intrinsic sources (b). The recoil energies correspond to the total event energies (the sum of all separately detected S2 cluster energies with the corresponding S1 signal) and were thus smeared with the S1-S2 energy resolution given by equation (4.6). A position resolution of $\sigma_{xy} = \sigma_z = 10\,\mathrm{mm}$ was assumed and a 20 t fiducial volume cut was applied to reduce the external background. Figure 4.27 (a) shows that around $Q_{\mathrm{ECEC}}$, the external backgrounds are dominated by $^{208}$Tl. The contribution of $^{44}$Sc is negligible due to its low $Q$ value of 2657 keV [9]. The intrinsic backgrounds, which show significantly lower rates than the external ones, are dominated by $^{214}$Bi and $^{137}$Xe, where a BiPo tagging efficiency of 99.8% [192] was assumed.

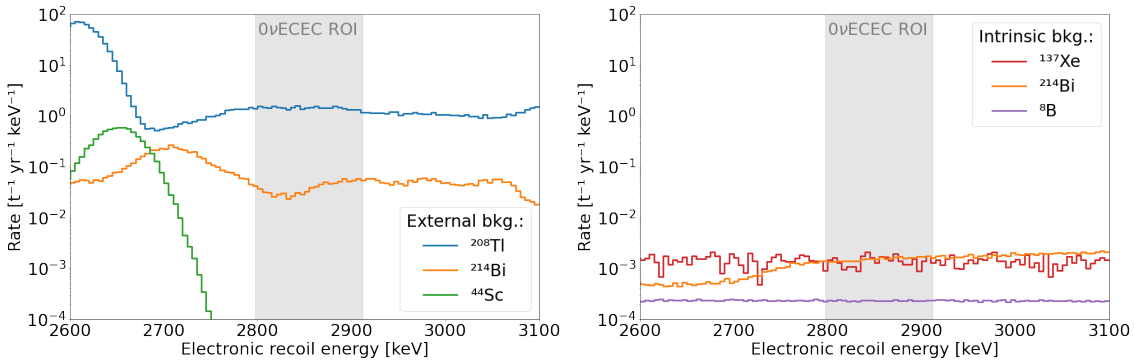


(a) External backgrounds.

(b) Intrinsic backgrounds.

**Figure 4.27:** Differential rates of (a) external (b) and xenon-intrinsic backgrounds around the 0$\nu$ECEC ROI, assuming a 20 t fiducial volume and without a SS cut. SS events contribute $< 10\%$ of the background events. The 0$\nu$ECEC is the range [2798-2912] keV. External backgrounds from $^{208}$Tl dominate the intrinsic backgrounds by three orders of magnitude. Data from [165].

When comparing the total background rate of figure 4.27, which is mainly driven by the $^{208}$Tl contribution, with the corresponding SS-only background shown in figure 4.20 (b) on page 70, a difference of more than one order of magnitude can be seen. This is caused by the high chance of MeV photons to deposit spatially distinguishable energy clusters and thus a MS signature. This demonstrates the high background reduction power of a SS cut, which cannot be applied in this study. However, the MS 0$\nu$ECEC analysis allows for an alternative background reduction technique, which exploits the specific expected cluster energies of the signal. In the following we thus present a 0$\nu$ECEC signal tagging algorithm, which was developed using GEANT4 MC simulations of the expected signal.

Since $0\nu$ECEC is a yet-unobserved process (hypothetical decay scheme shown in figure 2.10 on page 22) and the simulated deexcitation of $^{124}$Te$^*$ by GEANT4 is not accompanied by a release of the double hole energy, the signal simulations could not be conducted straightforwardly: the deexcitation of $^{124}$Te$^*$ was simulated using GEANT4, and the double hole energy of 64.5 keV released in this resonant decay was added afterward at the decay position. This additional energy corresponds to two K-shell captures. Other electron capture possibilities like one K- and one L- or two L-shell captures are forbidden by energy conservation. $10^6$ signal events were simulated following the described procedure. To account for the detector resolution, the clustered events were smeared in energy and position: this includes the total event energy (energy reconstructed from the S1 and several S2 signals) following the combined S1-S2 resolution given by equation (4.6), the cluster energy (energy of S2s) by the S2-only resolution determined in section 4.5.1, and the position assuming $\sigma_{xy} = \sigma_z = 10\,\text{mm}$. Afterward, the obtained cluster energies were compared to the theoretical double K-shell and $\gamma$ energies emitted in the deexcitation of $^{124}$Te$^*$, considering the different deexcitation channels (see figure 2.10).

The following selection criteria have to be passed in order to be classified as a $0\nu$ECEC signal event:

- **Number of clusters $\geq$ 3 and $\leq$ 13**: In every $^{124}$Te$^*$ deexcitation channel, at least 2 photons are emitted, which travel some distance away from the decay position. They are expected to be detected separately. Each photon deposits its energy either in a single cluster or divides it amongst several. Since the double K-shell energy is deposited at the decay position, every signal event thus should contain at least 3 clusters. The upper limit of 13 clusters is implemented to reduce the computing power (growing with $n!$) and causes a minor signal efficiency loss of $< 1\%$.

- **Total event energy contained in the $0\nu$ECEC ROI**: The total event energy must match $Q_{\text{ECEC}}$ within an acceptance range, the $0\nu$ECEC ROI, which is defined as $[Q_{\text{ECEC}} - n_{\text{ROI}} \cdot \sigma_{Q,S1S2}, Q_{\text{ECEC}} + n_{\text{ROI}} \cdot \sigma_{Q,S1S2}]$. $\sigma_{Q,S1S2} = 21.2\,\text{keV}$ describes the combined S1-S2 energy resolution at $Q_{\text{ECEC}}$ and $n_{\text{ROI}}$ the number of standard deviations. $n_{\text{ROI}}$ is a variable and can be chosen freely.

- **One cluster matches the double electron-hole energy of 64.5 keV**: The energy of one cluster must match the double K-shell energy within an acceptance range of $[64.5 - n_{64} \cdot \sigma_{S2,64}, 64.5 + n_{64} \cdot \sigma_{S2,64}]$. $\sigma_{S2,64} = 10.6\,\text{keV}$ describes the S2-only energy resolution at 64.5 keV and $n_{64}$ the number of standard deviations, which can be adjusted freely.

- **Cluster energies match the gamma energies of at least one decay channel**: Except for the 64.5 keV cluster, at least one combination of the cluster energies must agree with the theoretical $\gamma$ deexcitation energies $E_\gamma$ of one deexcitation mode within an acceptance range of $[E_\gamma - n_{E_\gamma} \cdot \sigma_{S2,E_\gamma}, E_\gamma + n_{E_\gamma} \cdot \sigma_{S2,E_\gamma}]$. $\sigma_{S2,E_\gamma}$ describes the S2-only resolution at $E_\gamma$ and $n_{E_\gamma}$ the number of standard deviations, which can again be chosen freely.

These criteria introduce the three free parameters of the signal tagging algorithm: $n_{ROI}$, $n_{64}$, and $n_{E_\gamma}$. Their choices significantly influence the signal acceptance, which increases with these parameters. However, the choice of $n_{ROI}$, $n_{64}$, and $n_{E_\gamma}$ also determines the background reduction power, which, in turn, increases with smaller parameter values. In order to deal with these two contrary trends, a detailed study is required to optimize the parameters in order to yield the best sensitivity on the resonant $0\nu$ECEC process.

A first set of parameters of $n_{ROI} = 2.7$, $n_{64} = 1.4$, and $n_{E_\gamma} = 1$ has been determined in [165], resulting in a signal acceptance of 62% for fiducial volumes $< 30\,\mathrm{t}$. When applying the corresponding event selection criteria to the background simulations, a total background reduction of nearly two orders of magnitude is obtained. Additionally, all events with any clusters less than 10 cm away from the TPC walls were removed, which further reduces the rate by more than one order of magnitude, resulting in a total background reduction by 3 orders of magnitude. The total background rate after applying this tagging algorithm and wall cut is shown in figure 4.28 (a) for different fiducial masses. An event is considered to be contained within the fiducial volume, if its 64.5 keV double electron-hole energy deposition occurred there. The background rates shown in figure 4.28 (a) exponentially decrease with smaller fiducial volumes since the shieldable external sources dominate the total background rate. An exponential function approximating this data is included ('default background').

The background reduction by 3 orders of magnitude is mainly achieved by the efficient discrimination of $^{208}$Tl events. $^{214}$Bi events, in contrast, are only reduced by 1-2 orders of magnitude due to the many excitation levels of $^{214}$Bi, which lead to a higher chance to mimic the MS $0\nu$ECEC signal. Intrinsic backgrounds are reduced only by one order of magnitude and contribute to $\mathcal{O}(10\%)$ at fiducial volume masses of 20 t: while $^{137}$Xe can be reduced to a negligible level due to its accompanying gammas with energies below the $^{124}$Te$^*$ deexcitation gammas, $^8$B Bremsstrahlung photons and $^{214}$Bi decays show a higher probability to mimic the resonant $0\nu$ECEC signal and are reduced by only one order of magnitude. Note again that this background reduction highly depends on the assumed parameters $n_{ROI}$, $n_{64}$, and $n_{E_\gamma}$.

### 4.5.3 Sensitivity and discussion

Using the results of this specific estimate on the signal acceptance and background reduction, DARWIN's sensitivity to the $0\nu$ECEC of $^{124}$Xe was calculated, using the Neyman construction with 90% acceptance intervals [195] and the likelihood-ratio ordering approach following Feldman-Cousins [196]. The result depends on the fiducial volume and is given in figure 4.28 (b), assuming a 10 yr experiment run time: for a fiducial volume of 18 t, the maximal sensitivity is reached, excluding half-lives below $T^{0\nu}_{1/2} = 3.7 \cdot 10^{25}$ yr (90% C.L.).

This sensitivity is considered to be a conservative result due to the underlying conservative assumptions on material contamination and possible improvements on the signal tagging algorithm. The contaminations used for this study assume materials

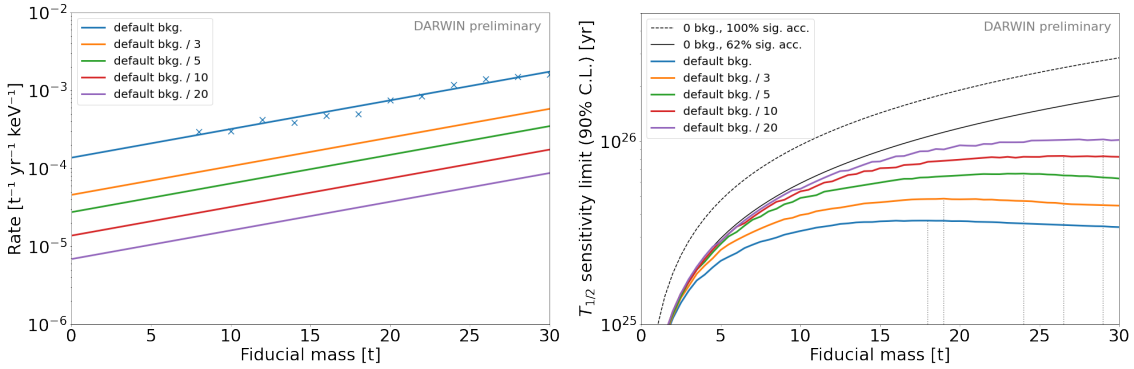


(a) (b)

**Figure 4.28:** (a) Background rate around $Q_{\mathrm{ECEC}}$. The default background marked in blue was taken from a first conservative estimate using specific choices of the tagging algorithm parameters $n_{ROI}$, $n_{64}$, and $n_{E_\gamma}$ (see text), leading to a 62% signal acceptance in fiducial volumes $< 30\,\mathrm{t}$ [165]. Background suppression by a factor of 2, 5, 10, or even 20 might be in reach with measures discussed in the text. (b) Sensitivity to $0\nu$ECEC (90% C.L.) for different background scenarios, assuming 10 yr run time. For comparison, the sensitivities of a zero-background detector with 62% and 100% signal acceptance are included.

identified by XENON1T and LZ, see table 4.3 on page 46. In a more optimistic scenario with more radio-pure PMTs, PTFE and titanium, the external background rate could be reduced by a factor of 3 or even more. When combining this reduced rate with a further optimization of the tagging algorithm and the fiducial volumes (their boundaries were taken from the $0\nu\beta\beta$ study) an improvement of a factor of 5 or even 10 compared to the default background should be feasible. Even though the parameter optimization might yield a lower signal acceptance, a gain in sensitivity is expected due to the significant background reduction. For such low background levels, intrinsic backgrounds would no longer play a subdominant role. Their contribution could be reduced by achieving a higher BiPo tagging efficiency of 99.9% or even 99.99%. Thus, a total background reduction by a factor of 20 could be in reach. However, a further reduction would be limited by the irreducible background from $^{8}$B neutrinos, indicating the cosmogenic limitation of this study.

The background reduction levels motivated above are also included in figure 4.28 (a) and their impact on the sensitivity is shown in figure 4.28 (b). Assuming a background reduction factor of 20, a search in a 29 t fiducial volume would result in a sensitivity of $T^{0\nu}_{1/2} > 1.0 \cdot 10^{26}\,\mathrm{yr}$ (90% C.L., exposure of $290\,\mathrm{t} \times \mathrm{yr}$). The sensitivity of a zero-background experiment with 62% (100%) signal acceptance is also shown, indicating that the present study with its high background suppression yields sensitivities near the optimum. A comparable sensitivity study presented in [105], which assumes a multi-tonne future LXe TPC with zero background and an exposure of $500\,\mathrm{t} \times \mathrm{yr}$ (hard to reach for the 40 t DARWIN detector), yields a sensitivity limit of $T^{0\nu}_{1/2} > 2.4 \cdot 10^{26}\,\mathrm{yr}$ (90% C.L.). However, theoretical models predict $0\nu$ECEC half-lives of several orders of magnitude higher than the discussed results, as calculated in [105]. Such sensitivities are beyond DARWIN's reach due to the low natural abundance of $^{124}$Xe of only 0.09% [125] in a natural xenon target.

## 4.6 Solar neutrinos

DARWIN's sensitivity to detect solar neutrinos via elastic $\nu$-electron scattering is presented in this section. Since the study was mainly done by the corresponding author of [11], the analysis is only summarized briefly. This thesis contributed the material-induced ER background spectra, which are the dominating backgrounds for most energies.

The differential rate of elastic $\nu$-electron scattering is calculated following equation (2.27), repeated here for completeness:

$$\frac{dR}{dE_r} = N_e \sum_j \int P_{ej} \frac{d\Phi}{dE_\nu} \frac{d\sigma_j}{dE_r} dE_\nu \ , \tag{4.16}$$

where $N_e$ is the number of electrons per tonne of xenon, $P_{ej}$ the probability of $\nu_e$ to oscillate to lepton flavor $j$, $\frac{d\Phi}{dE_\nu}$ the neutrino flux, and $\frac{d\sigma_j}{dE_r}$ are the differential cross-sections. The sum is over all three neutrino flavors $j$. While the spectra of $^7$Be ($Q = 862\,\text{keV}$ and $384\,\text{keV}$) and *pep* ($Q = 1442\,\text{keV}$) neutrinos are monoenergetic, the spectra of the *pp* ($Q = 420\,\text{keV}$), $^{13}$N ($Q = 1200\,\text{keV}$), and $^{15}$O ($Q = 1732\,\text{keV}$) neutrinos follow a $\beta$ spectrum, see figure 2.11 on page 23. Details about the assumed solar neutrino fluxes and survival probabilities are given in [11], following the high-metallicity solar model [181, 197]. The differential cross-sections $\frac{d\sigma_j}{dE_r}$ are calculated according to [198, 199]:

$$\frac{d\sigma_j}{dE_r} = \frac{2G_F^2 m_e}{\pi} \left[ g_L^2 + g_R^2 \left(1 - \frac{E_r}{E_\nu}\right)^2 - g_L g_R \frac{m_e E_r}{E_\nu^2} \right] \ , \tag{4.17}$$

where $g_L$ and $g_R$ denote the left- and right-handed coupling parameters, $m_e$ the electron mass, and $G_F$ the Fermi coupling constant.

The differential recoil spectra of the various solar neutrino types, calculated using equation (4.16), are shown in figure 4.29 along with the background rates induced by the detector materials and the xenon-intrinsic background sources radon, krypton, $^{136}$Xe, and $^{124}$Xe. The material-induced background model was derived within this work: the unstable isotopes/decay chains $^{238}$U, $^{226}$Ra, $^{232}$Th, $^{228}$Th, $^{235}$U, $^{137}$Cs, $^{40}$K, $^{60}$Co, and $^{44}$Ti contained in the detector materials were simulated with a lifetime-equivalent of 10 yr, following the description provided in section 4.1. The GEANT4 energy depositions were spatially grouped with a DBSCAN separation threshold of $\varepsilon = 15\,\text{mm}$. Previously measured material activities published by XENON1T and LZ were assumed (see table 4.3), and a SS cut and 30 t fiducial volume cut were applied for background reduction. For the xenon-intrinsic backgrounds, the DARWIN design goals for the radon concentration ($0.1\,\mu\text{Bq/kg}$) and krypton concentration (2 ppq) were assumed. The background from the $2\nu$ECEC of $^{124}$Xe was calculated following [80], assuming a natural abundance of 0.09% [125]; it leads to monoenergetic peaks at 64.3 keV, 36.7 keV, and 9.8 keV, which correspond to the double K-shell, K- and L-shell, and double L-shell energy. The $^{136}$Xe and $^{137}$Xe

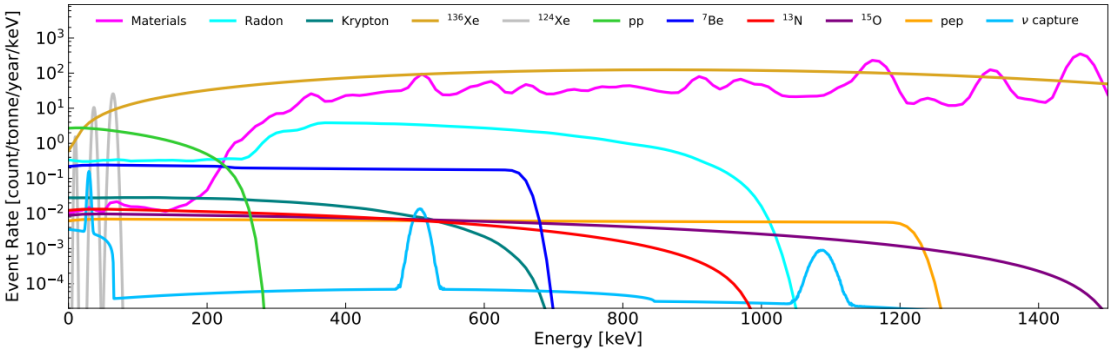


**Figure 4.29:** ER spectra of different solar neutrinos and the considered backgrounds. The neutrino fluxes assume the high-metallicity solar models [181, 197]. A 30 t fiducial volume cut was applied to reduce the material background. At lowest energies *pp* neutrinos dominate the spectrum. Figure from [11].

background rates were taken from the $0\nu\beta\beta$ study described in section 4.4. These backgrounds could be avoided by isotopically depleting the target at the cost of the $^{136}$Xe $0\nu\beta\beta$ science case. The energy resolution of equation (4.6) was applied to both the neutrino and background-induced spectra.

Figure 4.29 shows that *pp* neutrinos constitute the most prominent spectral component in the low-energy range $< 200$ keV with an integrated rate of 365 events/(t yr), followed by $^{7}$Be neutrinos with 141 events/(t yr). Lower rates of $\mathcal{O}(10)$ events/(t yr) are expected for $^{13}$N, $^{15}$O, and *pep* neutrinos. Other neutrinos such as $^{17}$F, $^{8}$B, and *hep* are not shown in figure 4.29 due to their negligible rates. The spectrum from possible neutrino captures on $^{131}$Xe, which is the only isotope with a sufficiently low $Q$ value for this type of charged-current interaction, is included: the two peaks at higher recoil energies are caused by the capture of $^{7}$Be and *pep* neutrinos; the feature $< 50$ keV is from $e^-$ captures and the captures of *pp* and $^{7}$Be neutrinos of the low-energy branch.

With the 11 background and signal components presented in figure 4.29, a multivariate spectral fit is set up for energies of up to 3 MeV. By running toy experiments, the expected $1\sigma$ uncertainty of the neutrino flux measurements is calculated for exposures of [1-1000] t × yr. Figure 4.30 (a) shows the resulting relative flux uncertainties, where the solid lines represents a natural xenon target and the dashed lines a target depleted in $^{136}$Xe by two orders of magnitude. With an exposure of 1 t × yr and a natural xenon target, DARWIN will already be able to reach the $\mathcal{O}(10\%)$ precision on the *pp* flux achieved by Borexino [200] and improves to a 0.15% precision with an exposure of 300 t × yr, which corresponds to 10 yr of DARWIN operation assuming 100% uptime. The $^{7}$Be neutrino flux is expected to be measured to a 1% precision with the same run time. The $^{13}$N and $^{15}$O neutrinos will be attainable in a natural xenon target at $> 3\sigma$ significance with exposures of 100 t × yr and 200 t × yr, respectively. Furthermore, DARWIN is sensitive to *pep* neutrinos and neutrino captures by exposures of 60 t × yr and 200 t × yr, respectively, assuming a depleted xenon target.

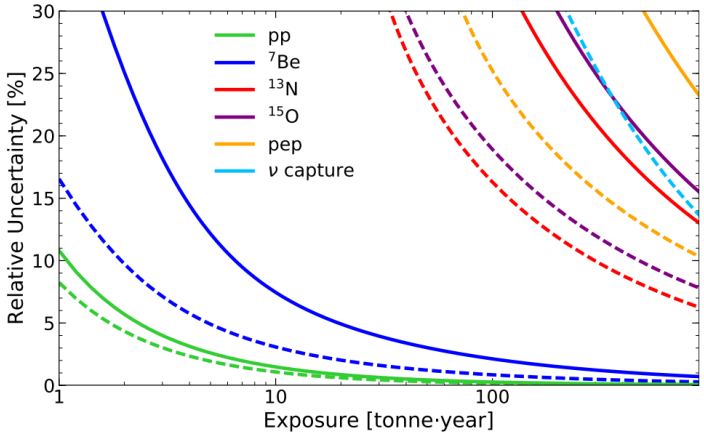


(a)

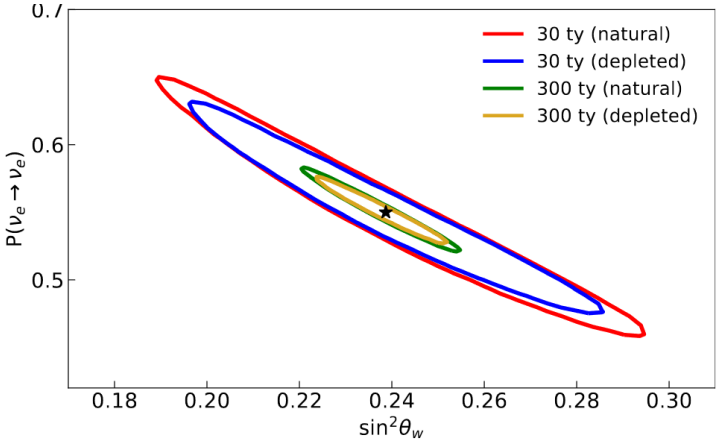


(b)

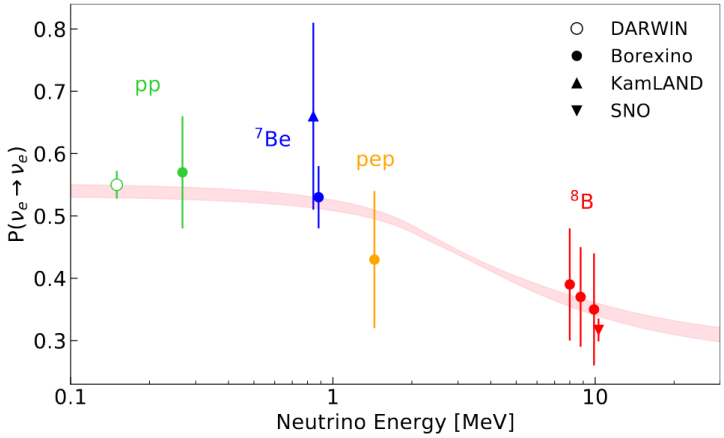


(c)

**Figure 4.30:** (a) Precision to measure the different solar neutrino fluxes (assuming the high-metallicity solar model). Solid (dashed) lines correspond to the relative uncertainties assuming a natural (depleted) LXe target. (b) and (c) $P_{ee}$ and $\sin^2\theta_w$ predictions in a non-explored neutrino energy range: (b) shows the $1\sigma$ confidence regions for two exposures and a natural/depleted LXe target, (c) compares the expected uncertainty on $P_{ee}$ from a measurement of the *pp* neutrino spectrum with the results from KamLAND, SNO, and Borexino. The pink band indicates the MSW-LMA solution [197]. Figures from [11].

With the precise measurement of the *pp* neutrino spectrum, the electroweak mixing angle $\sin^2\theta_w$ and the $\nu_e$ survival probability $P_{ee}$ can be calculated since both directly affect the measured recoil spectrum. Their $1\sigma$ confidence regions are also determined by toy experiments. The results are shown in figure 4.30 (b) for two different exposures and a natural/depleted target: assuming a natural xenon target and a $300\,\mathrm{t}\times\mathrm{yr}$ exposure, uncertainties of 5.1% and 4.0% can be achieved for $\sin^2\theta_w$ and $P_{ee}$, respectively. A measurement with DARWIN would be the first one in this energy region. The $P_{ee}$ sensitivity is compared to other experiments in figure 4.30 (c) and shows a precision improvement by one order of magnitude compared to the value reported by Borexino, again in an energy region, where no measurement exists at the moment.

# Chapter 5

# Hermetic TPC characterization and $^{222}$Rn predictions for DARWIN

As the ultimate dark matter detector, DARWIN aims to reach SI WIMP-nucleon scattering sensitivities down to the irreducible neutrino floor [7, 8]. Several backgrounds have to be minimized to achieve this challenging goal and to maximize the sensitivity to other science channels. This chapter concentrates on reducing the most challenging ER background source: the decays of $^{222}$Rn daughters. As already assumed in the sensitivity studies presented in chapter 4, DARWIN plans to reach a radon concentration of 0.1 $\mu$Bq/kg. For comparison, the last-generation experiment XENON1T measured a radon concentration of 4.5 $\mu$Bq/kg [201], whereas its successor XENONnT aims at a contamination as low as 1.0 $\mu$Bq/kg [4]. The planned reduction of one order of magnitude from XENONnT to DARWIN requires new approaches and improvements of successfully applied radon mitigation techniques.

The following chapter describes the concept of a hermetic TPC as one possibility for radon reduction. Its goal is to mitigate the radon-induced ER background by minimizing the surface area in direct contact with the active xenon target since radon is constantly emanated from all surfaces. This leads to a separation of the xenon contained in the TPC and the surrounding xenon. A hermetic TPC was designed, built, and operated at a small scale in the Freiburg Astroparticle Physics lab.

In section 5.1 the $^{222}$Rn background and several radon reduction techniques are introduced. The concept of a hermetic TPC is explained and compared to other ongoing R&D studies. The Hermetically Used Xenon TPC (HUsXe) detector, built within the scope of this work, and the cryogenic detector test platform Xenon-Based Research Apparatus (XeBRA) are presented in section 5.2. In section 5.3 details about the operation of HUsXe and its stability are given. Section 5.4 concentrates on the TPC characterization, including measurements of LXe properties. Finally, the *hermeticity*, the tightness of the detector, is investigated in section 5.5. The derived hermeticity is transferred to a potentially hermetic DARWIN TPC and its impact on the radon concentration is predicted.

## 5.1 $^{222}$Rn background and reduction techniques

One of the most detrimental background sources in the search for WIMPs is $^{222}$Rn, a decay product of $^{226}$Ra. It is part of the $^{238}$U chain, which is contained primordially in all detector materials. Due to the disequilibrium within the uranium decay series described in chapter 4, only the second part of the chain containing $^{226}$Ra and $^{222}$Rn is discussed in the following. $^{222}$Rn is permanently emanated from surfaces and homogeneously mixes with the xenon target due to its half-life of 3.8 d [9]. It thus forms one of the xenon-intrinsic backgrounds. As a noble gas, radon cannot be removed from the xenon by hot getters in the same way as electronegative contaminations ($O_2$, $H_2O$, hydrocarbons).

In figure 5.1 the $^{226}$Ra decay chain is illustrated. The $\beta^-$ decay of $^{214}$Pb to $^{214}$Bi represents the most problematic background as it decays with a $Q$ value of 1019 keV and a branching ratio of 9% without any other radiation, which could be tagged to reject the event [9]. These *naked beta decays* with energies of up to 1 MeV form ER background events relevant for the WIMP search or the solar neutrino detection. In contrast, the $\beta^-$ decay of $^{214}$Bi to $^{214}$Po can be discriminated with high efficiency of $\mathcal{O}(99\%)$ [202] due to the subsequent $\alpha$ decay of $^{214}$Po with a half-life of 164 $\mu$s, which causes a coincident decay signature (*BiPo tagging*). Due to $^{210}$Pb's half-life of approximately 22 yr [9], the $\beta^-$ decays in the second half of the radon decay chain do not contribute to the total ER background. Furthermore, the $\alpha$ decays in the decay chain are monoenergetic, easy to tag, and far outside any science channels ROI due to their decay energies of $> 4.5$ MeV [9].

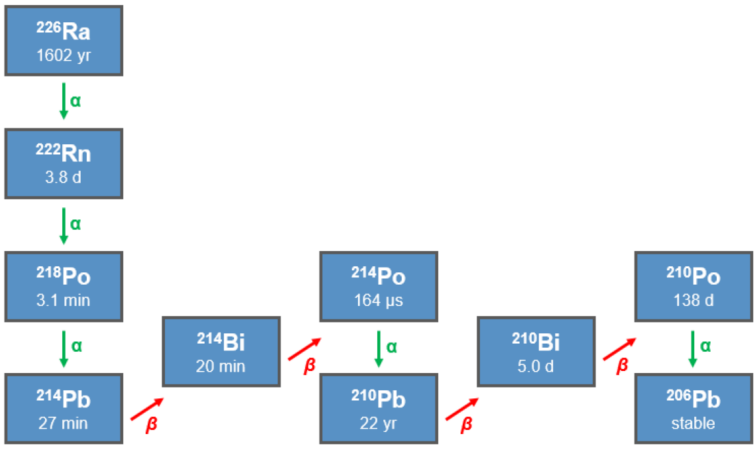


**Figure 5.1:** $^{226}$Ra decay chain. The most critical background stems from the $\beta$ decay of $^{214}$Pb to $^{214}$Bi. Data from [9].

Also $^{220}$Rn, a decay product of $^{224}$Ra within the $^{232}$Th chain, is emanated from surfaces. It similarly features naked $\beta^-$ decays of $^{212}$Pb to $^{212}$Bi and $^{212}$Bi to $^{212}$Po, leading to non-taggable ER background events. However, the difference in the natural abundance of the two radon isotopes and the much shorter half-life of $^{220}$Rn of 56 s [9] causes a by far lower $^{220}$Rn level. Additionally, cleaning for example PTFE surfaces is much more efficient for $^{220}$Rn than for $^{222}$Rn daughters [203]. XENON1T

measured that the activity of $^{220}$Rn in its LXe target is only approximately 0.3% of the $^{222}$Rn contamination [4]. Considering the different branching ratios of the isotope's naked $\beta$ decays, only 1% of the background events originating from the $^{222}$Rn decay chain are expected for the $^{220}$Rn chain. Therefore, we will refer in the following only to the dominating radon isotope $^{222}$Rn. However, it is clear that the reduction techniques discussed below also apply for $^{220}$Rn.

Various techniques are employed to minimize and avoid radon contaminations in LXe detectors and only a combination of several of those will allow reaching DARWIN's challenging radon concentration goal of 0.1 $\mu$Bq/kg: **Selecting materials** with low $^{226}$Ra contamination leads to lower radon emanation and, therefore, lower radon activity within the xenon target. The activities of several materials typically installed in dual-phase xenon TPCs are listed in table 4.3 on page 46, screened by high-purity germanium detectors. **Surface coating** stops the emanated $^{222}$Rn from the bulk material in the coating layer instead of being released to the xenon. It is currently under investigation which coating materials can be used not to affect the low-background TPC performance and which coating techniques (such as physical or chemical vapor deposition) lead to the best results [204]. Removing radon from xenon gas is possible through an **activated charcoal trap** or **cryogenic distillation**. The former technique has, e.g., been investigated by the XMASS collaboration [205]; further exemplary studies are shown in [206] and [207]. $^{222}$Rn cryogenic distillation columns were developed in the last years, e.g., by XENON100 [208]. They make use of the difference in vapor pressure between radon and xenon. Results from XENON100 demonstrate a radon reduction factor of $> 27$ at 90% C.L. [208]. A further possibility to reduce radon is changing the detector design; the **hermetic TPC** is an example and is introduced in the following section.

### 5.1.1 Concept of the hermetic TPC

A hermetic TPC separates the sensitive xenon volume, the *inner xenon volume*, from radon-emitting components mounted outside the TPC, as sketched in figure 5.2. Examples for those components are the inner cryostat, parts of the photosensors, their read-out electronics, the copper field shaping electrodes, cables, as well as feedthroughs and pipes. Since the surfaces of those detector components are only in contact with the *outer xenon volume*, the xenon between the cryostat and TPC walls, the radon emanated from these elements is hindered from entering the hermetically sealed TPC.

This concept is promising for DARWIN: in its baseline design, the surfaces surrounding the active target material add up to approximately 10 m$^2$, while the surfaces within the whole inner cryostat measure more than 100 m$^2$ with the most contaminated materials mounted outside the TPC. Even though a significant radon reduction is expected due to these surface separations, calculating a precise reduction factor is difficult since additional sub-systems like the purification or cryogenic system connected to the sensitive xenon have to be considered. Often, they emanate more radon than the TPC and cryostat elements [201]. We thus refrain from giving

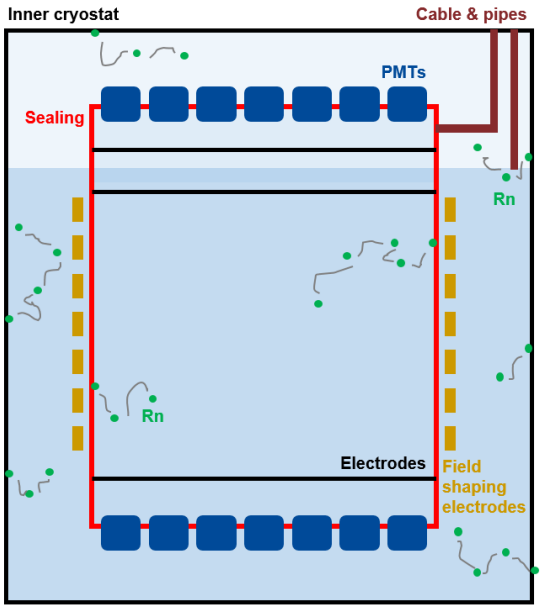


**Figure 5.2:** Concept of the hermetic TPC: the xenon target is separated from elements mounted outside the TPC, such as cables, pipes, or field shaping electrodes. Thus, the radon emanated in the outer xenon volume is hindered from entering the TPC. This is expected to reduce the radon activity in the xenon target significantly since the most contaminated materials are mounted outside the TPC, where larger surfaces additionally lead to more radon emanation.

a precise estimate of the expected radon reduction when applying the concept of a hermetic TPC since the detailed arrangement of the systems is still in the designing phase.

Besides radon minimization, a hermetic TPC could reduce the detector's energy threshold, which is typically limited by single- or few-electron backgrounds, directly impacting the sensitivity for low WIMP masses [209]. Photoionization on metal surfaces and impurities in LXe are assumed to be the reason for the electron emission [210, 211]. For the latter, a sealed TPC is promising since, firstly, most of the contaminations stem from outgassing materials mounted outside the TPC; secondly, the purification is more efficient when cleaning the smaller xenon target only. However, this work does not explore the minimization of single-electron backgrounds but instead concentrates on conclusions for DARWIN's radon activity.

The construction and operation of a hermetic TPC impose many challenges, first of all its sealing concept. Before presenting the HUsXe detector, a short summary of other small-scale detectors dealing with the sealed TPC topic is given: At the Kamioka Observatory, a quartz chamber TPC was developed with a ø 48 mm × 58 mm LXe target [212], sketched in figure 5.3 (a). Quartz and PTFE are the TPC's primary materials; the latter is chosen because of its high reflectance for VUV light [148]. Quartz, which mainly separates the xenon from PTFE, is installed due to its 90% LXe scintillation light transparency [212] and its low concentration of $^{226}$Ra, leading to a low $^{222}$Rn emanation rate. Its 9 eV bandgap avoids secondary electron emission since the xenon scintillation photon energy is only 7 eV. Inter-

actions within the xenon target are recorded by two HAMAMATSU R10789 PMTs. Due to the usage of only one gas system for the inner and outer xenon volume and the implemented holes to feed LXe into the inner volume, the described TPC is not yet considered a hermetic detector. The developers use this prototype to test quartz chambers and plan to build a hermetic TPC in future studies. Exemplary results are the successful operation for $> 200$ h without TPC charge-up, which is an important result since quartz, an insulator, accumulates charges, and the estimation of the single electron S2 yield of $(16.5 \pm 0.5)$ PE.

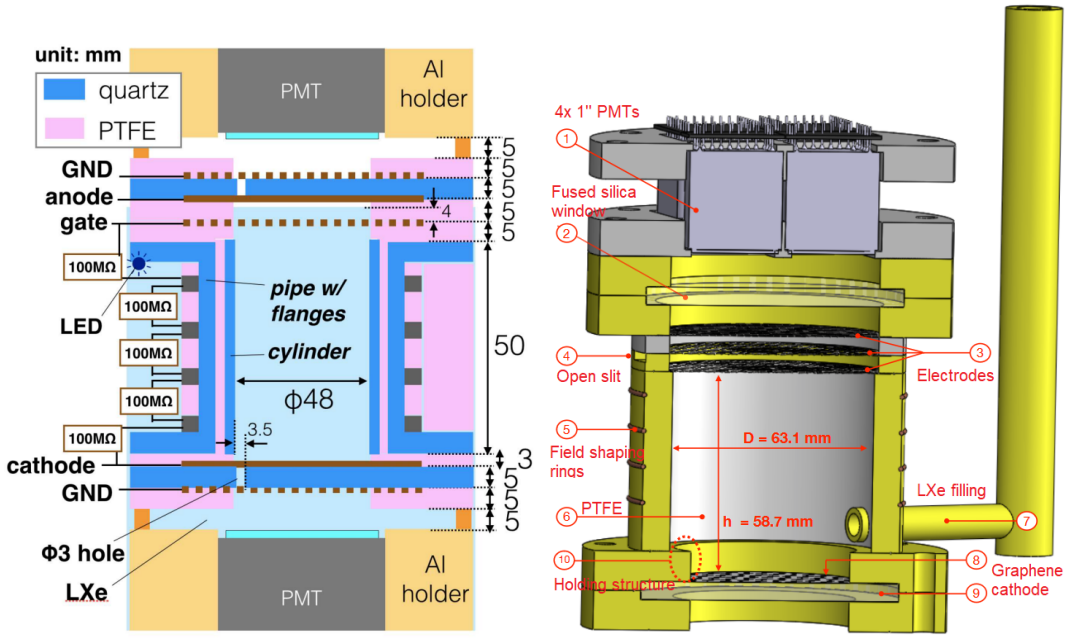


(a) Quartz chamber TPC. (b) Acrylic chamber TPC.

**Figure 5.3:** Sketches of the recently developed TPC prototypes for hermetic TPC studies at Kamioka Observatory (a) and University of San Diego (b). Figures from [212] and [211].

Another TPC prototype was developed at the University of San Diego: a semi-hermetic acrylic chamber with a ø 63 mm × 59 mm target volume [211], sketched in figure 5.3 (b). A thin PTFE layer covers the walls of the acrylic chamber for VUV light reflectance. Two quartz windows are included at the top and bottom of the chamber to separate the inner LXe from the outside volume; the bottom one is graphene-coated and serves as the cathode. The other TPC electrodes are made of stainless steel. Four HAMAMATSU R8520 PMTs are placed on top of the chamber for signal detection. The hermetic TPC design allows the purified xenon to be directly filled into the target volume. An open slit controls its liquid level. The overflowing xenon dripping into the outer xenon volume is pumped out for purification and re-condensed into the xenon target. Since only one gas system is used for the xenon supply and purification for the inner and outer xenon volume, and the slit connects the xenon target with the xenon buffer volume, this TPC is also not considered to be a hermetically sealed TPC. The developers plan further improvements on this in the following works, whereas this study mainly concentrated on single-electron

backgrounds. Exemplary results are the single-electron rate calculation for varying xenon purity levels and the PE emission probability of graphene being lower than that of stainless steel.

Both TPC prototypes presented above concentrated on the single-electron background reduction using semi-sealed detectors; radon minimization studies are only planned for later investigations. In contrast, the TPC developed in this work entirely concentrates on radon mitigation. Therefore, two independent gas systems were set up to individually treat the separated xenon volumes, which is to date a unique technique in the LXe community. It ensures the possibility of detailed investigations of the TPC hermeticity and allows concluding on the $^{222}$Rn reduction level when applying the hermetic TPC concept to the DARWIN detector.

## 5.2 The HUsXe detector at the XeBRA platform

The small-scale hermetic TPC Hermetically Used Xenon TPC (HUsXe) was designed and developed within this work and is presented in detail in the following. It was operated at the cryogenic xenon test platform XeBRA, which is also described.

### 5.2.1 HUsXe - the small-scale hermetic TPC

The hermetic TPC HUsXe is a sealed dual-phase xenon TPC with a cylindrical xenon target of ø 56 mm × 75 mm, housing 550 g LXe. Figure 5.4 (a) and (b) show a CAD drawing and photograph of the detector and depict the several components. To avoid dust and dirt, the apparatus was assembled in a class ISO-6 cleanroom, and cleaned with de-ionized water and ethanol.

The cylindrical TPC, mostly made of PTFE parts, is enclosed at the top and bottom by two Hamamatsu 3-inch R11410-21 PMTs [150] for photon detection. The bottom PMT is contained in an aluminum filler, reducing the amount of xenon required to fill the detector. The PMTs have a QE of 32% for wavelengths of 175 nm [129] and a CE of 95% [213]. Their signals are read out by a 100 MHz Caen digitizer via Cirlex-based voltage divider circuits and PTFE coaxial cables (RG196).

The drift and amplification fields are generated by three etched meshes made of 0.15 mm thick stainless steel foil with 3 mm hexagonal openings. Their optical transparency is calculated to be 90% each. While the gate and cathode electrodes are aligned, the anode mesh is shifted by half a hexagonal opening for more homogeneous field lines within the amplification region. The anode is installed 5 mm above the gate electrode, defined as $z = 0$, while the gate is placed 75 mm above the cathode mesh. The meshes are in electrical contact with their stainless steel support rings embedded in the PTFE chamber and are connected to a voltage supply. The drift field must be uniform to avoid charge losses by guiding electrons into the TPC walls. Thus, copper rings are installed at equal distances and connected via 50 MΩ resistors between the cathode and gate electrode frames. The rings are held by PTFE pillars which support the entire TPC structure. Since three stainless steel

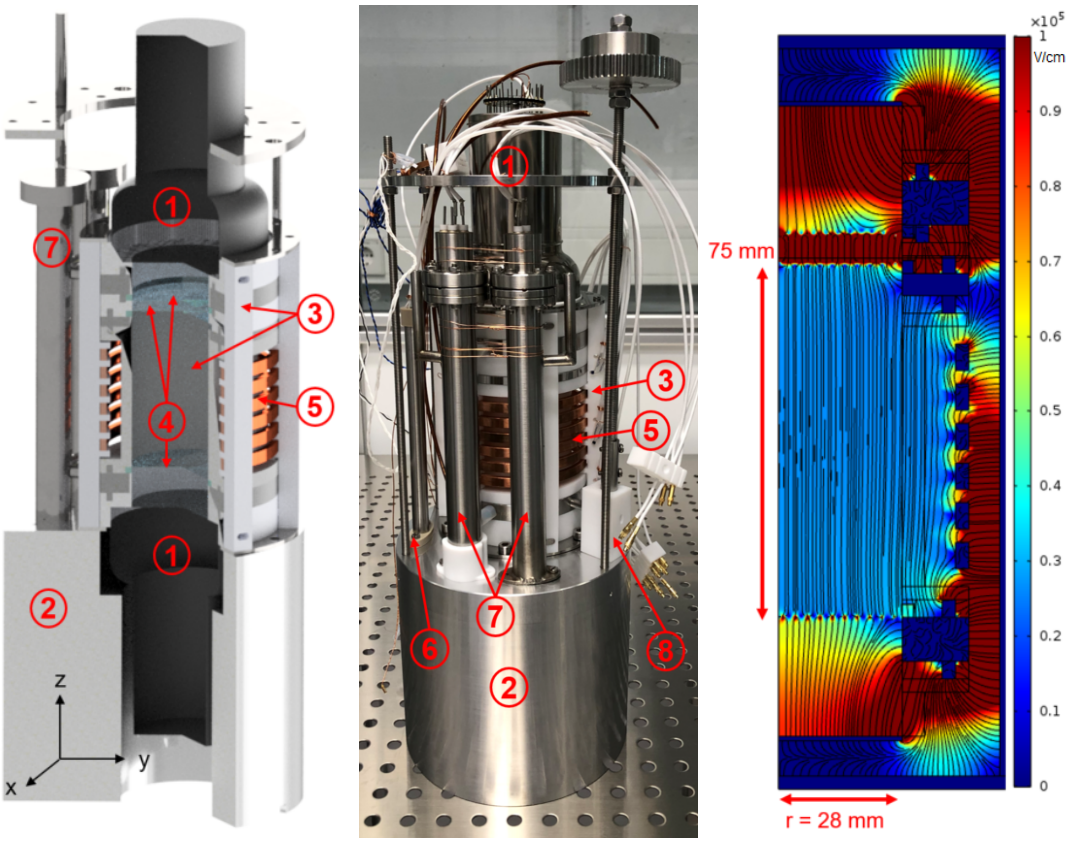


(a) (b) (c)

**Figure 5.4:** CAD drawing, photograph, and electric field simulations of HUsXe. (a) and (b) show the detector components: (1) PMTs, (2) aluminum filler, (3) PTFE reflectors/pillars, (4) cathode, gate, anode electrodes, (5) field shaping electrodes, (6) levelmeter, (7) stainless steel vessels containing a weir/levelmeter, (8) LXe valve. (c) Field simulations indicate a uniform drift field except in the region close to the gate support frame.

support rings are part of the TPC cylinder, electric field simulations using COMSOL Multiphysics® [214] were done. The outcome, presented in figure 5.4 (c), shows the corresponding field strengths and lines. Besides the region around the gate support ring, which can be cut in the analysis, the field lines and strengths indicate a homogeneous electron drift field with minor details acceptable for the scope of this work.

A sketch presenting the xenon supply is shown in figure 5.8 (b) on page 102, where two different installations are compared. PTFE pipes are added in the electrode support frames of the cathode and anode to fill the purified LXe directly into the instrumentation volume. On the opposite side, further pipes connect the anode and cathode frames with two stainless steel vessels, allowing to measure the inner LXe level without mounting any sensors in the sensitive volume: one vessel contains a levelmeter, the other one a weir with its upper edge defining the desired liquid level. A valve connecting the two separated LXe volumes is also included to avoid pressure build-ups, referred to as the *LXe valve/connection valve*. A 90-degree rotation opens and closes the valve. It is controllable from the outside via gears, rods, and a motion feedthrough [215].

To monitor the system's stability while in operation, several temperature Pt100 and pressure sensors are included. Two capacitive levelmeters record the height of the LXe level within the xenon target and the outer xenon volume. The former is contained in one of the SS vessels, as described above; the latter is mounted outside the TPC on top of the aluminum filler. Both levelmeters consist of two concentric stainless steel pipes with different radii, supported by polyetheretherketone (PEEK) components. Their capacitances indicate the LXe level due to the difference in permittivity between LXe ($\varepsilon_{r,\mathrm{LXe}} = 1.96$) and GXe ($\varepsilon_{r,\mathrm{GXe}} = 1.00$) [216]:

$$C = 2\pi\varepsilon_0\varepsilon_{r,\mathrm{LXe}}\frac{d}{\ln(r_2/r_1)} + 2\pi\varepsilon_0\varepsilon_{r,\mathrm{GXe}}\frac{l-d}{\ln(r_2/r_1)} \ , \tag{5.1}$$

where $r_1$ and $r_2$ are the pipe radii, $l$ the length of the levelmeter, and $d$ the LXe level height. For both levelmeters, a 1 mm LXe height increase corresponds to a capacitance change of 0.13 pF.

To decouple the two xenon volumes and achieve hermeticity, the TPC is sealed using the concept of cryofitting, exploiting the different thermal shrinkages of the TPC materials PTFE and stainless steel. While PTFE has a thermal expansion coefficient of $\sim 130 \cdot 10^{-6}\,\mathrm{K}^{-1}$, stainless steel shows a $> 10$ times smaller value of $\sim 10 \cdot 10^{-6\,-1}$ [217]. PTFE and stainless steel components that tightly fit at room temperature make a sealing connection once cooled to LXe temperatures of $-100$°C, induced by an acting force due to PTFE's larger shrinkage. Figure 5.5 visualizes the cryofitting of the electrode support frames with the PTFE and stainless steel parts marked in light grey and dark grey, respectively. When cooling the apparatus to LXe temperatures, the surfaces marked in red are pressed with a force of $\sim 400$ N against the stainless steel components, assuming a PTFE compressive yield strength of 23.5 MPa [218]. All electrode support frames, the two PMTs, the xenon supply pipes, the LXe valve, and the stainless steel vessels are sealed by exploiting this concept. In several pre-tests using cold nitrogen gas to reach temperatures of about $-100$°C, the cryofitting concept was validated. These tests indicated that no vacuum-tight seals could be achieved: a leakage rate of $4 \cdot 10^{-2}$ mbar l/s for a PTFE test chamber containing one PMT and one electrode support frame was measured. Such a leakage flow translates to water-tightness and corresponds to the flow through a hole with a diameter of 0.01 mm [219].

### 5.2.2 The XeBRA detector test platform

XeBRA is a versatile cryogenic detector test platform, shown in figure 5.6, which allows studying novel detector concepts based on LXe. Examples are a single-phase TPC with secondary scintillations in LXe in strong electric fields close to very thin electrode wires of $\mathcal{O}(10\,\mu\mathrm{m})$ [220, 221], and the hermetic TPC concept presented here. A detailed description of XeBRA is given in [222].

The double-walled cryostat contains the core of the platform: the LXe detector to be tested, i.e., HUsXe in our case. An insulation vacuum of $\mathcal{O}(10^{-3}\,\mathrm{mbar})$ is kept between the inner and outer cryostat, and 10 layers of super-insulating Mylar

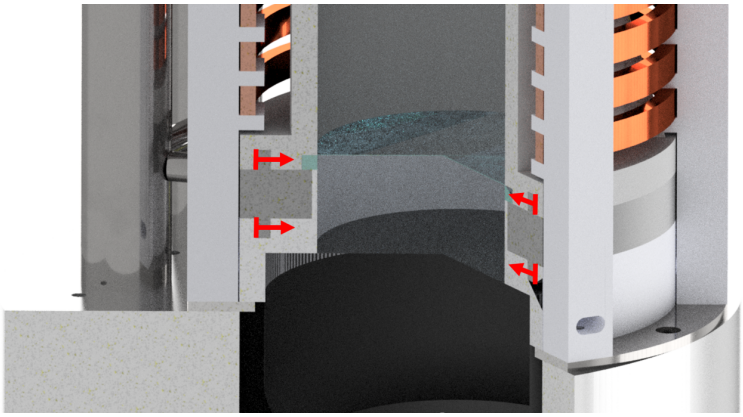

**Figure 5.5:** TPC sealing by cryofitting: PTFE (light grey) shows a $> 10$ times larger thermal expansion coefficient than stainless steel (dark grey). When cooling the detector from room to cryogenic LXe temperature, the surface marked in red is pressed against the stainless steel component and make a sealing connection, indicated by the red arrows. All electrode support frames, PMTs, pipes, the LXe valve, and stainless steel vessels were sealed by this technique.

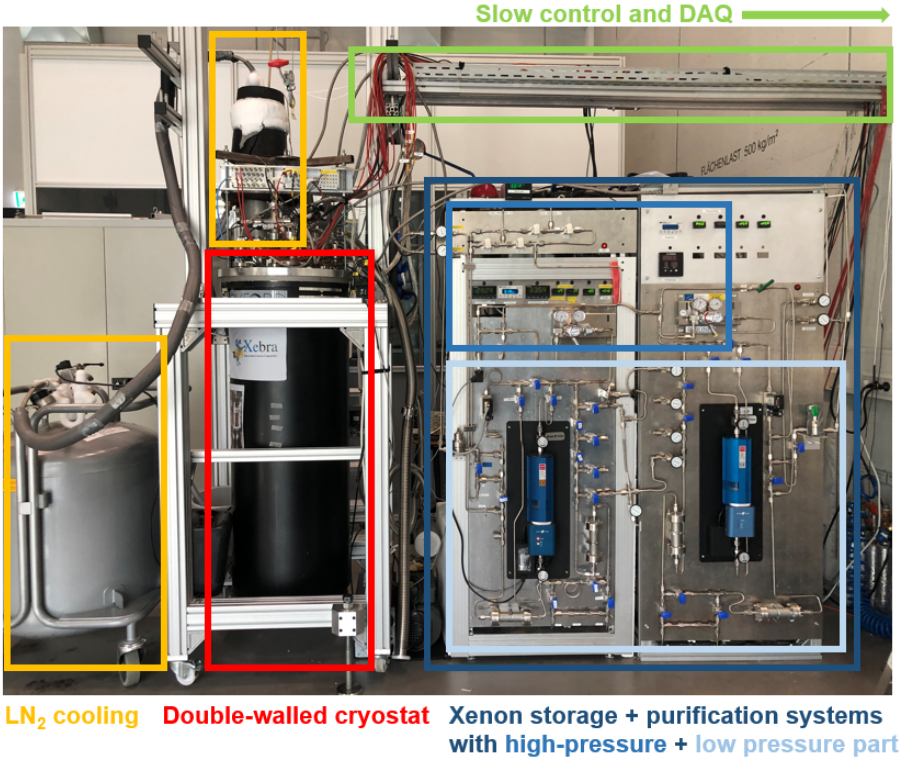


**Figure 5.6:** The XeBRA cryogenic detector test platform: the 200 l $LN_2$ dewar for cooling, the double-walled cryostat containing the TPC with the open flask $LN_2$ dewar on top, and two gas systems for xenon gas supply and purification by hot getters, split into high-pressure and low-pressure parts. The data acquisition (DAQ) and slow control servers are installed next to the setup.

foil are installed to minimize the heat input via radiation. The outer cryostat, with its volume of $\sim 1\,\mathrm{m}^3$, is made of aluminum and contains several ports on its top flange. Three of them serve as connections to the inner cryostat volume. All TPC cables, LXe in- and outlet pipes, a heat exchanger to avoid thermal losses in the xenon purification process, and the rod needed to open and close the LXe valve by the motion feedthrough are routed via these parts. The inner cryostat is a ø 15 cm × 39 cm long stainless steel cylinder with an extension of ø 25 cm × 8 cm on the top to provide sufficient space for cables. All components of the inner cryostat are standard CF sealed [223] and are leak checked by a Helium leak tester down to leak rates of $\mathcal{O}(10^{-8}\,\mathrm{mbar}\cdot\mathrm{l/s})$.

$LN_2$ is used to cool the xenon gas. It is supplied by a movable 200 l dewar connected to an open flask dewar on top of the outer cryostat. It gets re-filled with 2.5 kg of $LN_2$ approximately every 1.5 hours, suggesting a heat load of 170 W. The open flask dewar is connected to a ring-shaped $LN_2$ buffer volume inside the outer cryostat, which is thermally coupled by conductive paste and thick copper wires to a copper coldfinger reaching the inner cryostat volume. Heaters are installed to heat up the coldfinger from $LN_2$ to LXe temperatures, regulated by a cryogenic controlling device (Cryocon Model 22C [224]). GXe filled to the inner cryostat condenses at the coldfinger and forms LXe droplets collected by a funnel and guided to the xenon target volume. During HUsXe's operation the inner sensitive xenon volume was cooled using the described mechanism by installing a tight cap around the coldfinger to separate the xenon volumes; the outer xenon volume was only indirectly cooled by thermal contact to the inner LXe volume. $LN_2$ is also used to recuperate the xenon gas to the xenon storage bottles. The xenon gas bottles are immersed in $LN_2$, resulting in a pressure difference between the TPC and the gas system that drives the xenon flow towards the bottles.

Two gas systems are connected to the inner cryostat to independently provide the xenon volumes with xenon gas and ensure separate purification and recuperation. One gas system was already built during the initial installation of the test platform [222], while the second gas system was constructed within the scope of this work. After its installation, it was heated to remove contaminations such as water from its surfaces, checked for leaks down to rates of $\mathcal{O}(10^{-8}\mathrm{mbar}\cdot\mathrm{l/s})$, and evacuated. The diagram presenting the gas systems' components is shown in figure 5.7: the system is divided into a high-pressure part connected to the aluminum bottles for xenon storage, and a low-pressure part connected to the inner cryostat volume. This separation is necessary since, e.g., the membrane pumps driving the xenon gas purification flow can only withstand pressures of up to 5 bar [225], while the xenon gas bottles are filled with up to 50 bar. During the initial xenon filling, this pressure difference is handled by pressure reducers [226]. The entire system is built from 1/4-inch Swagelok® VCR components [227] and sealed using nickel and copper gaskets. The VCR components are arranged such that different gas routes can be selected depending on the operational mode. Both low-pressure systems contain a hot getter for xenon purification, operating at up to 5 standard liters per minute (SLM) with

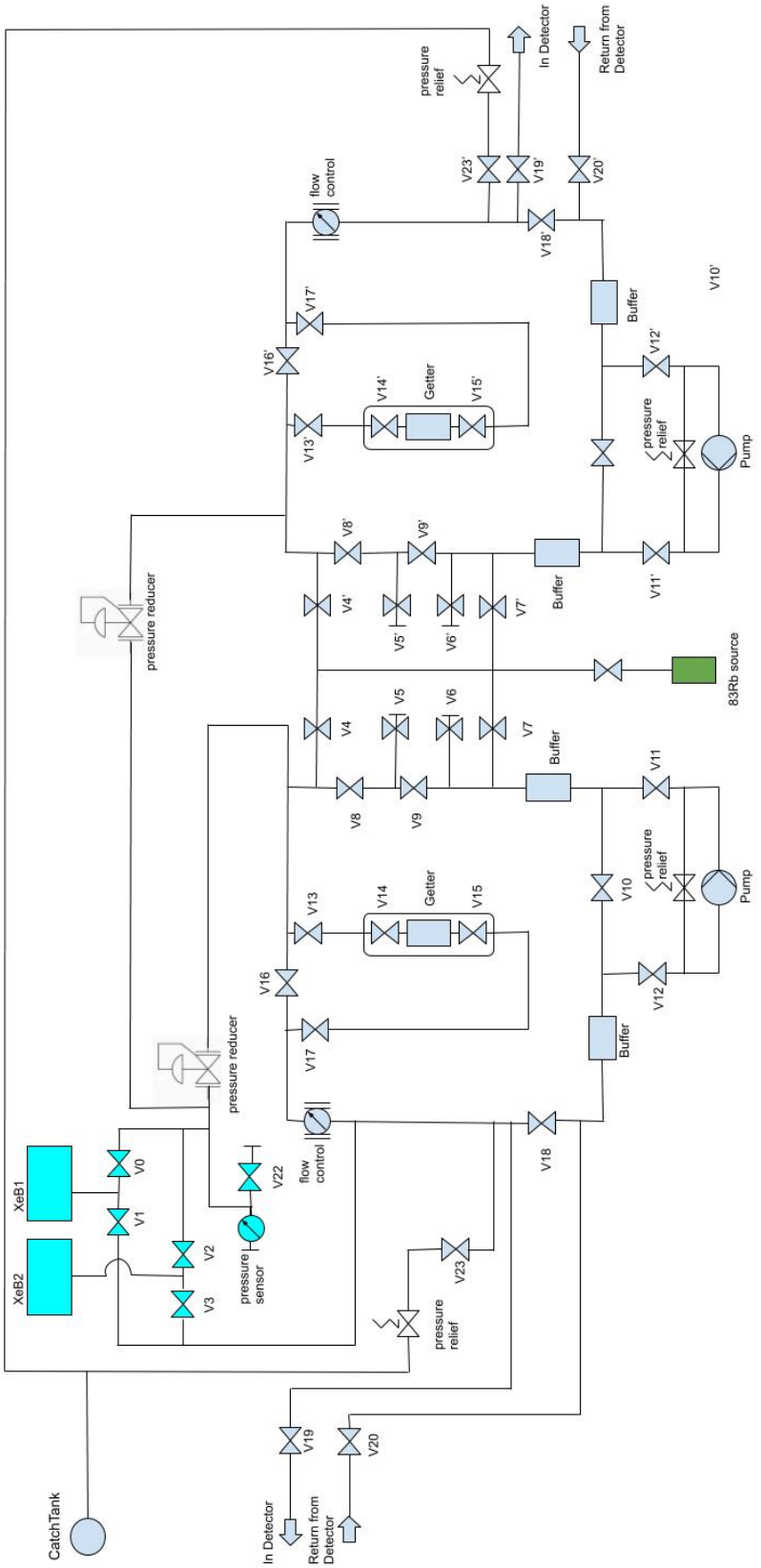


**Figure 5.7:** Sketch of the entire xenon gas system. It allows filling the detector with xenon, and to purify and calibrate the inner and outer LXe volumes independently. The part shown left of the $^{83}$Rb calibration source (green) was already built during the initial installation of the XeBRA platform, the right section in the scope of this work. Turquoise components label the high pressure system connected with the xenon storage bottles; low pressure parts are shown in light blue.

efficiencies depending on the xenon flow [228]. Electronegative impurities in the xenon gas are bound to the getter's heated zirconium surface and consequently removed from the gas. Membrane pumps pull xenon gas out of the cryostat and push it through the purification loop [225], with the purification speed regulated by flow controllers [229]. As a safety measure, pressure relief valves connect the gas systems to a catch tank, to which the xenon is released in case of a pressure build-up in the TPC. Both relief valves were calibrated to open at a xenon pressure of 2.5 bar. An $^{83}$Rb source emitting the short-lived $^{83m}$Kr for detector calibration is installed between the two low-pressure gas systems, allowing for flushing both separated xenon volumes independently. Further details about the source are given in section 5.4.2.

During detector operation all operational parameters, such as pressures, temperatures, and levelmeter capacities, are monitored by the versatile and lightweight slow control system, consisting of the programs *Doberman* and *Pinscher* [230, 231]. The system was initially developed in [232] and further improved in [233]. Doberman communicates with the sensors while Pinscher processes and interprets the data. Different alarm types can be set, e.g., simple threshold alarms. In an emergency such as a lack of cooling power due to missing $LN_2$, an alarm is issued and distributed via SMS and emails. The collected sensor data is permanently stored in a database and visualized on a web page. Exemplary slow control plots describing the stability of HUsXe's operation are presented in section 5.3.

Two separate units provide the HV: the electrodes are biased by the Caen N1470 [234] and the PMTs by the Caen SY5527 [235]. The PMT data acquisition system for digitization and storage is a lightweight version of the DAQ system of the XENON collaboration. The PMT signals are digitized by an 8-channel Caen V1724 digitizer, featuring an analog-to-digital converter (ADC) with a 100 MHz sampling rate and a 14-bit resolution [236]. Its firmware allows a channel-independent readout without a global trigger. Besides the self-trigger option used to acquire data, the ADC also allows the usage of an external trigger, applied during PMT gain calibrations using a pulsed LED. The data is stored on the server using the *redax* software, and the packages *strax* and *straxbra* process the recorded data [237, 238]. Starting from the raw waveforms, straxbra hierarchically processes the data. After the initial identification of peaks in the data stream, S1 and S2 signals are identified and grouped as events if they appear within a pre-defined time window. Plugins allow extracting additional information such as the $z$ position calculated using the drift time. A more detailed description is given in section 5.4 and in [239].

## 5.3 Detector operation

The HUsXe TPC was operated in three run periods with hardware optimizations in between. Each run lasted for several weeks, with the first taking place between July and September 2020, the second between November and December 2020, and the last run between April and June 2021. Details on the different runs and their corresponding objectives, as well as a report on the detector's stability are given in the following.

### 5.3.1 Measurement campaigns

Before every measurement campaign (*run*), the detector was assembled in the ISO-6 cleanroom to prevent contamination by dust and dirt. During the detector installation, the TPC was leveled by laser distance measurements and highly sensitive spirit levels. The detector installation and cryostat closing were followed by an evacuation of 2-3 days to reach pressures of $\mathcal{O}(10^{-6})$ mbar inside the inner cryostat; the vacuum insulation between the two cryostats was kept at $\mathcal{O}(10^{-3})$ mbar. Afterward, the cooling and xenon filling operation started, where the TPC pressure was kept below 2 bar to prevent damages. After filling the detector with xenon, the PMT gains were extracted and equalized by adjusting the PMT HV. In addition, measurements using the calibration source $^{83m}$Kr were recorded, described in detail in section 5.4 and section 5.5. At the end of the detector run, the xenon was recovered by freezing the xenon storage bottles as described in section 5.2.2. Several heaters were used to vaporize the LXe inside the cryostat.

#### Run 1

The main goal of the first run was to take data for the TPC characterization and check on the system's stability. This is why most of the TPC characterization data presented in section 5.4 was recorded during this period.

One of the primary outcomes of the first detector test campaign was the need to change the gas routing. During this period, the xenon target volume was not directly cooled by the copper coldfinger as in the final detector version (the one described in section 5.2.2); instead, the outer xenon volume was connected to and cooled by the coldfinger. In figure 5.8, the gas pipe routing for (a) run 1 and (b) run 2 and 3 are shown. In run 1 the inner volume was supposed to be cooled by the surrounding outer xenon volume, with the primary heat conductor being the stainless steel electrode frames due to their high thermal conductivity. The purified LXe was foreseen to be pushed into the TPC at anode level. Since the gas filled to the xenon target was not cooled efficiently and therefore not liquefied, this caused instabilities of the LXe level as recorded by the levelmeter. The same purified xenon was again pulled out of the system into the purification loop, rendering xenon target cleaning impossible. As a consequence, the insufficient electron lifetime prohibited reliable S2 measurements.

An additional explanation of the recorded liquid level instabilities could have been the size of the weir. When switching on the pump of the gas purification system, it sucks the xenon out of this container. If its volume is too small, not only LXe from inside the weir but additionally GXe is sucked out, reducing the pressure inside the TPC and further causing a liquid level change according to the xenon phase diagram. This behavior is exemplarily shown in figure 5.9, with a LXe level decrease by several tenths of pF, corresponding to several millimeters, recorded at the time of the start of the circulation pump.

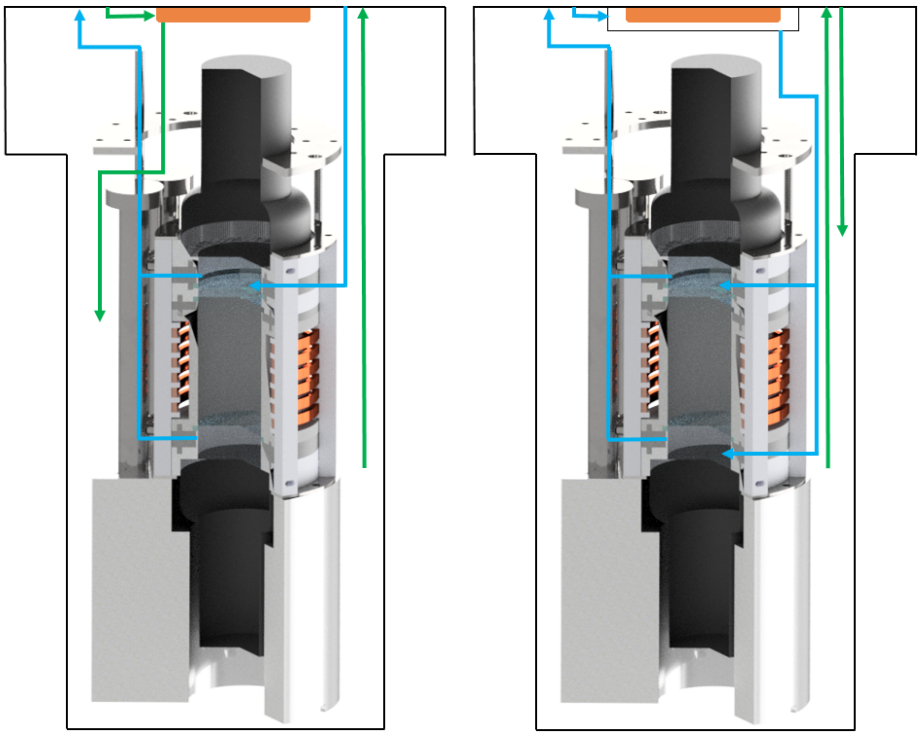

(a) (b)

**Figure 5.8:** Gas routing used in (a) run period 1 and (b) in run period 2 and 3. Only the version (b) allowed for hermetic TPC operation. Blue (green) lines indicate the gas routing of the inner (outer) xenon volume.

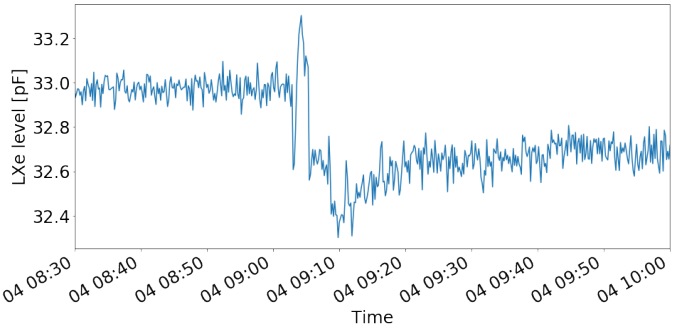


**Figure 5.9:** LXe level change when turning on the circulation pump during run 1. The capacity change of several tenths of pF corresponds to a LXe level change of several millimeters. Possibly, not only LXe was sucked out of the weir but additionally GXe, reducing the TPC pressure and therefore influencing the liquid level.

To overcome these problems and to be able to check the TPC's functionality, the LXe valve was opened, the xenon volumes connected, and gas lines swapped such that the purified xenon was pushed to the outer volume in contact with the copper coldfinger and sucked out from the inner volume's weir. The resulting directional flow of the xenon allowed for xenon target purification and reliable data taking but at cost of hermeticity.

### Run 2

The second run aimed to solve the unstable liquid level and purity problems, and the gas routing was changed to the final version depicted in figure 5.8 (b). Additionally, a hole at the bottom of the weir connecting the two xenon volumes was included, allowing a limited LXe flow between the two volumes to avoid the behavior described in figure 5.9. This coupling, however, connected inner and outer volume (working against the intended hermeticity goal) and caused a situation where minor pressure differences led to significant changes in the liquid level, even when only operating one of the purification systems. Exemplary pressure and LXe level data are presented in figure 5.10, where capillary effects in the weir might have caused the shown behavior. Due to the inability to achieve a stable liquid level, the run was ended prematurely and not used for further analysis.

Nevertheless, essential knowledge about the cooling mechanism was gained. Despite only cooling the xenon target directly, accounting for approximately 15% of the xenon contained in the cryostat, a reliable cooling was detected for the outer xenon volume. This outcome indicates that most heat load is caused by conduction through the metal parts connecting the inner cryostat with the laboratory environment.

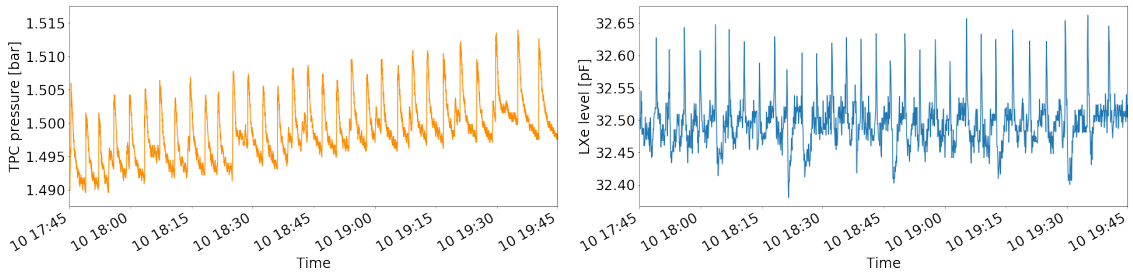


(a) (b)

**Figure 5.10:** Pressure (a) and liquid level (b) instabilities obtained during run 2. Approximately every 3 min the pressure and LXe level increased, the latter corresponding to up to 2-3 mm level changes. The behavior could be due to capillary effects caused by the intended guided LXe flow between the two xenon volumes.

### Run 3

For the third detector run, the TPC design was changed back to the first run version without the intentional connection of the two xenon volumes. The gas routing remained, as shown in figure 5.8 (b). An enlarged weir was included to avoid emptying it upon the start of the circulation pump. The result was a stable liquid level when operating the gas purification system of the inner xenon volume. Adding the purification system for the outer volume caused liquid instabilities; more details are shown in section 5.3.2. The data acquired during this run mainly concentrated on hermeticity measurements, described in more detail in section 5.5.

### 5.3.2 Detector stability

The HUsXe TPC and XeBRA platform are equipped with several sensors recording the system's status, read out by the slow control system described in section 5.2.2. Several slow control plots recorded during run 3 are shown in the following.

#### Cooling mechanism and temperature stability

The XeBRA platform uses $LN_2$ to cool the xenon to liquid temperatures. Despite the temperature difference of nearly 100 K between $LN_2$ and LXe (depending on the pressure, see figure 3.1), the cooling mechanism produces very stable temperature conditions within the TPC. Plots picturing exemplary 24 h behaviors of several sensors are shown in figure 5.11, demonstrating the stable detector conditions.

Figure 5.11 (a) presents the $LN_2$ level inside the open flask dewar, recorded by a capacitive levelmeter with the same working principle as the TPC LXe levelmeters explained in section 5.2.1. The slow control data show a continuous $LN_2$ consumption and a periodical refill every 1.5 h. Every refill consumes approximately 2.5 kg of nitrogen, requiring a nitrogen reservoir tank refill every third day. As a safety measure, alarm boundaries are set on the levelmeter readings. The small plateau visible at around 155 pF is due to one of the levelmeter's calibration rings. These rings made of PTFE with a height of a few millimeters are included between the levelmeter's pipes and allow translating the LXe level height from pF to mm.

The temperatures measured at the copper coldfinger are shown in figure 5.11 (b). The data points in light red are from the temperature sensor mounted at the top side of the copper block within the insulation vacuum volume; the darker red markers are from the bottom side of the coldfinger in contact with the GXe in the inner cryostat. The temperature difference between these two is caused by the heat input of the purified, only partially liquefied xenon being filled into the TPC. Depending on the speed of the purification system regulated by a flow controller, the coldfinger's temperature offset changes. Accordingly, the power required to increase the coldfinger temperature by a heater changes. Its 24 hours evolution is shown in figure 5.11 (c), regulated by the cryocontroller described in section 5.2.2. The $y$ axis of the plot shows the fraction of the controller's 50 W maximum heating power needed to maintain the setpoint temperature. The setpoint was chosen to be 166 K at the top side of the coldfinger, which provides much more stable conditions than controlling the bottom coldfinger temperature. Alarm boundaries were set on both temperatures and on the consumed heating power.

The corresponding LXe temperature outside the TPC is shown in figure 5.11 (d), presenting readings of three Pt100 sensors mounted at different heights along the TPC cylinder. Similar to the temperatures presented in figure 5.11 (c), no fluctuations can be noticed, showing the excellent cryogenic stability of the system. The offset between the three different readings is caused by the heat input of the warm, purified xenon gas entering the TPC at the top of the cryostat. Thus, the higher the sensor is mounted, the larger the temperature it measures.

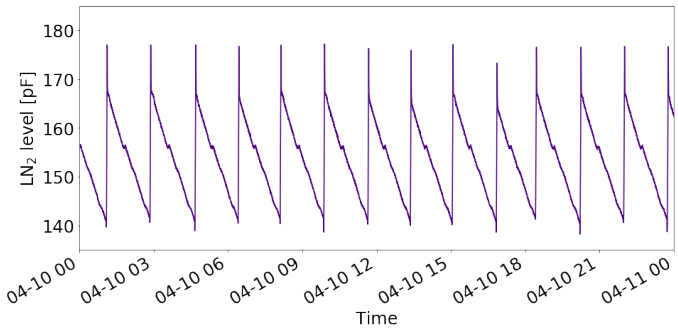


(a) Open flask nitrogen level.

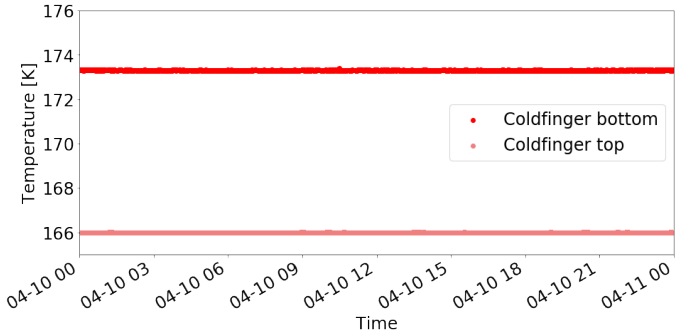


(b) Coldfinger temperatures.

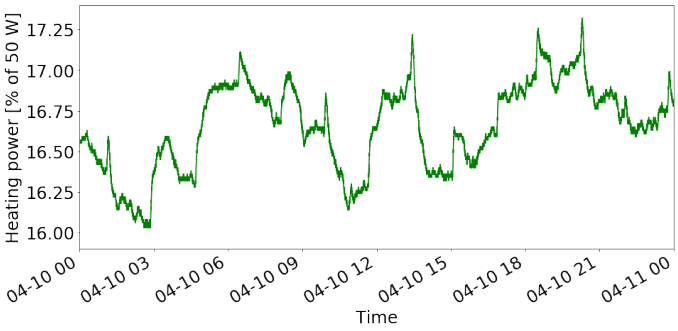


(c) Heating power of the cryogenic controller.

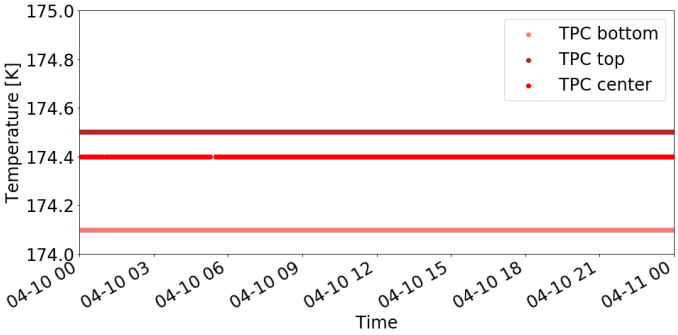


(d) LXe temperatures along TPC.

**Figure 5.11:** Slow control plots showing the platform's cooling mechanism over an exemplary time period of 24 hours without external disturbances. Interpretations are given in the text.

### Liquid level and pressure stability

The HUsXe detector is the only LXe dual-phase TPC to date operated with two separated gas systems. Therefore, particular attention was paid to obtain a stable liquid level with both purification systems in operation. This is challenging since the TPC is not perfectly hermetic, indicated by the cryofitting pre-test. This leads to mass exchanges driven by pressure differences, which are expected due to cooling one of the xenon volumes indirectly. The relevant data was recorded during run 3, in which the xenon target was coupled to the copper coldfinger and hence directly cooled.

In this discussion we compare two different detector configurations: firstly, only the purification system of the inner xenon volume in operation and secondly, operating both purification systems. Figure 5.12 shows two exemplary one-hour measurements of the TPC's liquid level and pressure when operating the detector in these scenarios. Stable conditions were observed while having one purification system online (a), while small periodical fluctuations in pressure and liquid level occurred when turning on the second setup as well (b). The change on the pressure scale from (a) to (b) is caused by a higher heat input due to the increased xenon purification flow by switching on the second gas system.

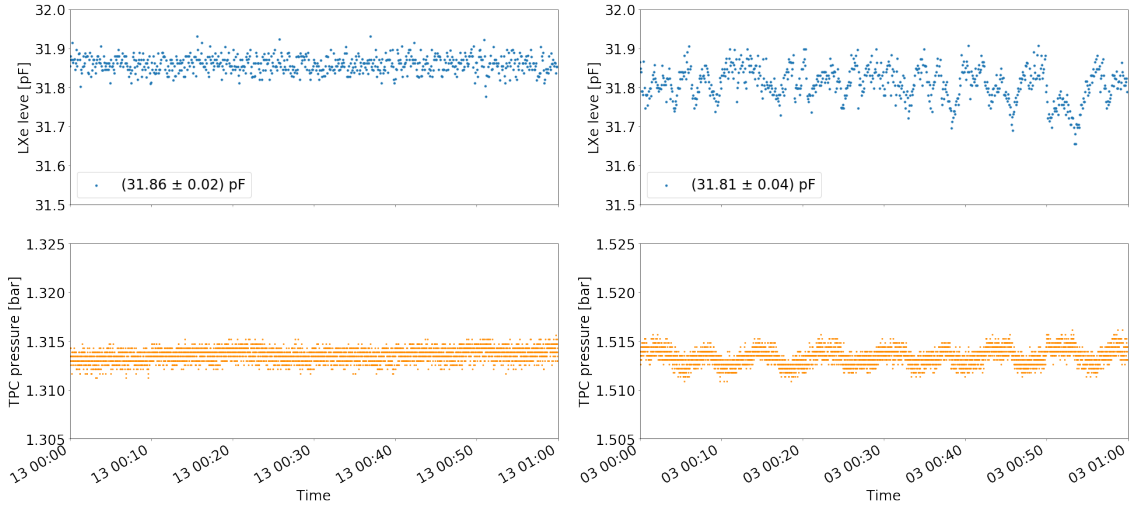


(a) One gas system online.

(b) Two gas systems online.

**Figure 5.12:** TPC levelmeter and pressure measurements during an exemplary one-hour time period. (a) only purification system of inner xenon volume in operation at 1 SLM, (b) purification systems of both volumes in operation with an additional 0.4 SLM purification speed for the outer xenon volume. The additional purification of the outer xenon volume causes pressure and, thus, LXe level instabilities, hindering reliable data acquisition.

To quantify the difference between figure 5.12 (a) and figure 5.12 (b), the mean and standard deviation of the levelmeter measurements are calculated and included in the diagrams. For (a), the one-hour measurement is described by $(31.86 \pm 0.02)$ pF, and the fluctuations between the maximum and minimum measured value remained

within $\Delta C_{\mathrm{max}} = 0.15\,\mathrm{pF}$. Data fluctuations of this size were also observed in levelmeter measurements when only being filled with GXe at the beginning of the detector run, pointing towards an intrinsic readout noise of the device. In comparison, (b) shows a liquid level of $(31.81 \pm 0.04)\,\mathrm{pF}$ and $\Delta C_{\mathrm{max}} = 0.25\,\mathrm{pF}$, much larger than the expected readout noise. Thus, this fluctuation is considered as real liquid level change, which translates into liquid level changes of up to 2 mm. Considering the 5 mm gap between anode and gate, where only 2.5 mm are filled by xenon gas and constitute the amplification region, it gets clear that the S2 generation suffers noticeably by simultaneously operating two gas systems. The data recorded by the PMTs shows this behavior by a washout of the S2 population in peak width and area. In addition to the TPC levelmeter and PMT data, the described findings are supported by the levelmeter measuring the liquid level in the outer xenon volume. It shows the same behavior as the TPC levelmeter and confirms the unwanted coupling of the two xenon volumes.

Several attempts to reduce the liquid level fluctuations were carried out, such as changing the speed of the outer volume's purification system. Plots showing one-hour measurements of the TPC's liquid level for several set purification flows are shown in figure 5.13; the xenon target purification speed was always kept at 1 SLM. Unfortunately, no improvements can be noticed, and especially figure 5.13 (d) shows even higher fluctuations than the data recorded in (a)-(c).

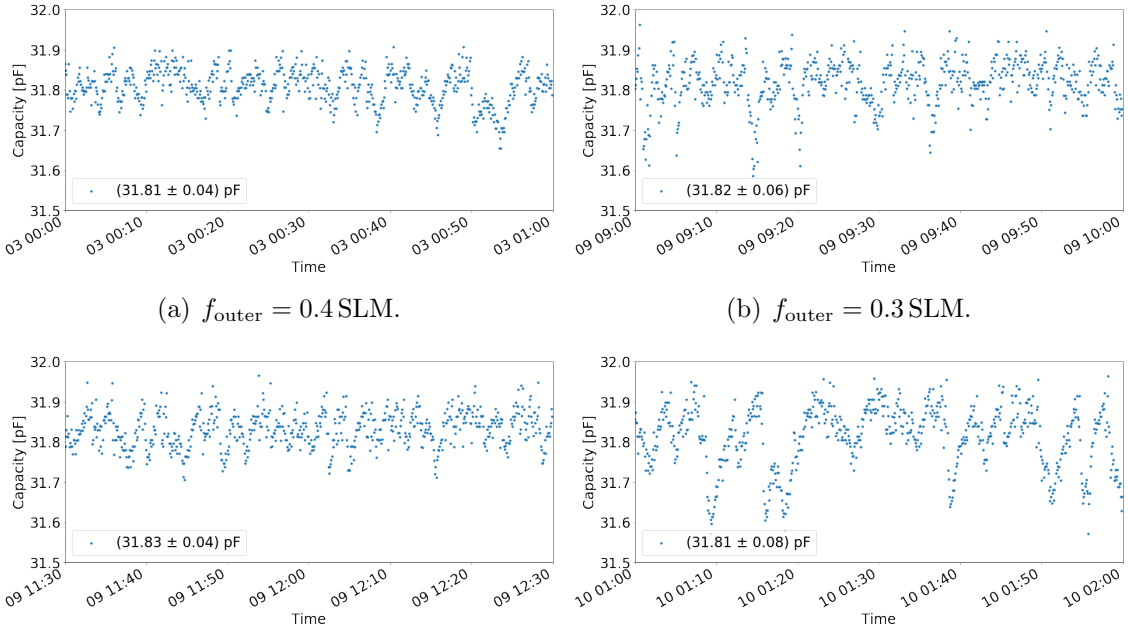


(a) $f_{\mathrm{outer}} = 0.4\,\mathrm{SLM}$. (b) $f_{\mathrm{outer}} = 0.3\,\mathrm{SLM}$.

(c) $f_{\mathrm{outer}} = 0.2\,\mathrm{SLM}$. (d) $f_{\mathrm{outer}} = 0.1\,\mathrm{SLM}$.

**Figure 5.13:** TPC levelmeter data of one-hour time periods, each time with a xenon target purification flow of 1 SLM and a variable cleaning speed $f_{\mathrm{outer}}$ of the outer gas system. None of these attempts could reduce the LXe level instabilities to a negligible level, shown by capacity changes of several tenths of pF, corresponding to a level change of several millimeters.

Additionally, it was examined whether the gas system's flow controller caused the inconstancies by feeding a non-stable amount of xenon to the TPC, resulting in pressure and liquid level changes. Needle and bellow valves mounted at both sides of the flow controller (compare figure 5.7) were used to control the xenon flow without the controlling device. However, also in these configurations no stable conditions were found.

These difficulties during the operation with two gas systems did not hinder the further TPC analysis. Great detector stabilities were obtained while purifying the inner xenon target only and allowed good S2 data-taking campaigns. These measurements are investigated and discussed in the following sections 5.4 and 5.5. Regarding the operation of two systems, the main conclusion is the need to reduce liquid level fluctuations. Future studies could obtain this by either hermetically sealing the detector or by implementing an additional cooling coldfinger. The former solution might only be possible by exploiting another sealing technique, ensuring that the two volumes are fully decoupled; the latter might overcome the observed pressure fluctuations even if the TPC is not hermetically sealed. However, the most promising attempt seems to be the combination of both.

## 5.4 TPC characterization

The HUsXe detector is not only meant to be a hermetic detector but, of course, must be a full-functional dual-phase xenon TPC. Many technical design considerations like the electrode implementation or liquid level control were decided accordingly. In order to check on the TPC's functionality, the following section is dedicated to its characterization. After fundamental studies such as PMT gain calibrations and the identification of $^{83m}$Kr calibration events, the analysis concentrates on determining detector performance parameters, scintillation and ionization yields, and LXe properties. The results on the latter two topics are compared to those of other small- and large-scale experiments.

### 5.4.1 PMT gain calibrations

The combination of signals from different PMTs requires accurate knowledge of their gain, which describes the mean multiplication factor of a single PE released from the PMT's photocathode, accelerated, and multiplied by the PMT's dynode structure. During all three HUsXe runs, gain calibration data was acquired regularly. Additionally, a sweep through different PMT voltages was done at the beginning of each run in order to obtain the HV settings for similar gains of both photosensors. Although a gain correction is foreseen in the analysis, equal gains are important when using the same digitizer threshold for all PMT channels as done at the XeBRA platform.

Blue LEDs are used for the calibration since the Hamamatsu R11410-21 PMTs are not only sensitive in the xenon scintillation light region of around 175 nm [133] but also to wavelengths of up to 650 nm [150]. Two LEDs are fixed at the holding

structure outside the TPC and emit light around 460 nm. A small fraction of their light output is measured by the PMTs due to PTFE's light transmission probability of a few percent [240]. An external pulse generator (RIGOL DG1022 [241]) controls the LED's intensity and pulse rate; at low output voltages only a few photons are detected. Once the voltage pulse driving the LED is generated, the device also triggers the digitizer, which starts a measurement lasting 1.1 $\mu$s, consisting of 110 samples of 10 ns length each. Figure 5.14 shows 20 exemplary waveforms recorded during a PMT calibration run with the signals appearing at $\sim$ 80 ADC units. For a proper calibration measurement only $\sim$ 10% of all waveforms should contain a signal. Thus, the LED voltage is a critical parameter: setting a excessively low voltage leads to no photon emission, while an excessively high voltage causes the emission of several photons, rendering the identification of a single PE amplification difficult.

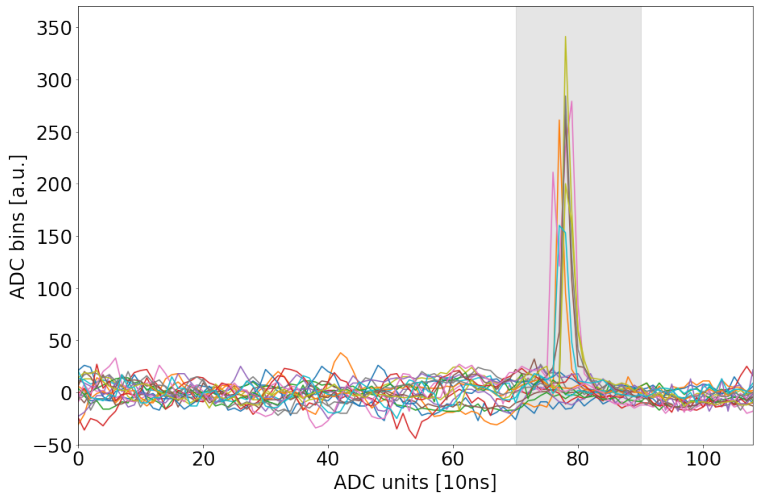


**Figure 5.14:** 20 waveforms recorded during a PMT calibration run. To properly identify single PE amplification, only $\sim$ 10% of the waveforms should contain a signal. Accordingly, a too high LED voltage was set for the shown measurement. The shadowed region indicates the signal integration window.

In the following two different gain extraction approaches are described: the first one is based on a fit of the PMT response spectrum, the second uses a statistical approach. Both methods are applied for HUsXe's PMT calibrations, and their results are compared and discussed.

### Spectral fit approach

For this approach, signals within a pre-defined time window are integrated for each waveform individually. E.g., the range of [70, 90] ADC units was set for the waveforms shown in figure 5.14, as indicated by the grey region. The resulting integral describes the amplified charge induced by the PE(s) initially released from the photocathode; multiplying with the factor $F$ converts to the number of electrons causing the recorded signal:

$$F = \frac{r}{f \cdot Z \cdot q \cdot A} \ , \tag{5.2}$$

where $r = \frac{2.25\,\mathrm{V}}{2^{14}\,\mathrm{bit}}$ represents the ADC resolution, $f = 100\,\mathrm{MHz}$ the sampling frequency, $Z = 50\,\Omega$ the input impedance, $q$ the electron charge, and $A = 10$ the amplification factor of the electronic amplification stage used to distinguish from the amplification in the PMT itself. Histogramming the integrated signals results in plots such as shown in figure 5.15, presenting a typical PMT spectrum.

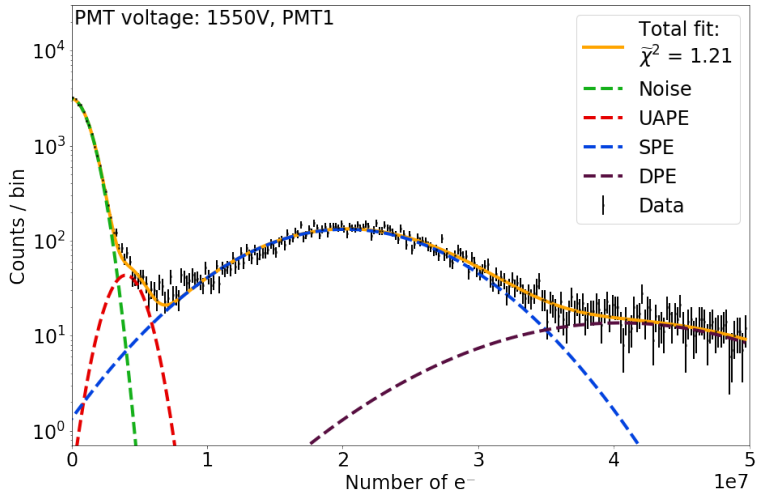


**Figure 5.15:** Exemplary gain calibration spectrum of a R11410 PMT, applying −1550 V bias voltage to the HV divider. The noise contribution is shown in green, the red curve visualizes under-amplified (UA) PE, and the blue curve the single photoelectron (SPE) response followed by higher-order peaks. The PMT gain is extracted from the Gaussian fit parameter $\mu_{SPE}$ of the spectrum.

Several contributions describe the photosensor's response: electronic noise centered around $x = 0$, SPE, double photoelectron (DPE), triple photoelectron (TPE), and higher-order peaks, as well as a contribution from UA PEs. The latter is caused by PEs bypassing the first dynode stage, resulting in less amplified signals. A Gaussian fit well describes each component. Hence, the overall spectral fit consists of a sum of Gaussians with

$$\mu_{iPE} = i \cdot \mu_{SPE} \tag{5.3}$$

$$\sigma_{iPE} = \sqrt{i}\,\sigma_{SPE}\ , \tag{5.4}$$

where $i$ describes the order of the peak. The extracted fit value $\mu_{SPE} = \mu_{1PE}$ represents the PMT gain.

To equalize the PMT bias voltages, measurements with varying voltages were recorded. The data labeled with 'fit' in figure 5.16 (a) shows the resulting amplification factors for both PMTs; 'PMT0' refers to the bottom PMT and 'PMT1' to the top photosensor. The plot nicely shows the expected exponential increase in gain for higher voltages due to the higher acceleration of the electrons between the dynode stages, leading to higher charge multiplication. Additionally, the difference between the two PMTs makes clear why PMT calibrations are so crucial. The shown PMT gain difference is caused by minor geometrical variations inside the PMTs (which

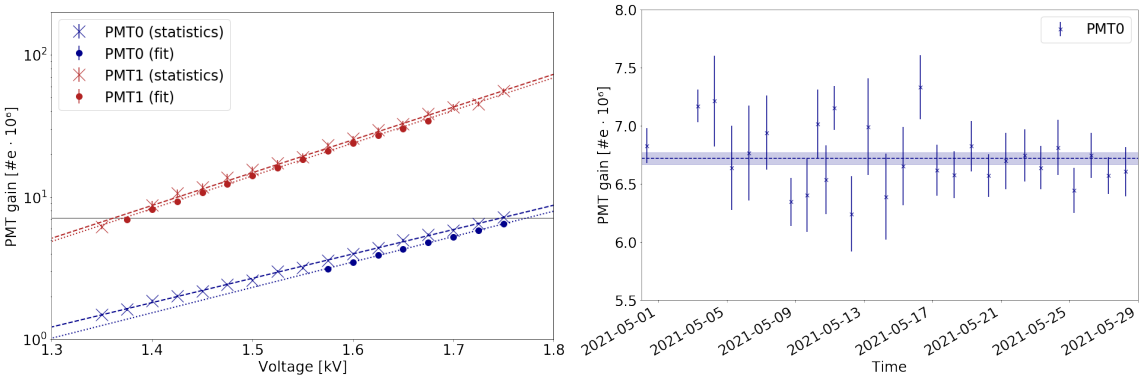


(a) (b)

**Figure 5.16:** (a) The PMT gains depend on the applied bias voltages and slightly on the method for gain estimation. To equalize the gains of the two PMTs, a voltage of 1750 V and 1375 V for PMT0 (bottom PMT) and PMT1 (top PMT) was selected, indicated by the grey solid line. (b) Gain evolution of the bottom PMT over a one-month period. The corresponding mean, as well as standard deviation, are included in the plot, indicating the photosensor's stability.

are all hand-made) and, as a second-order effect, by the operational temperature deviations within the cryostat. While the top PMT is operated in GXe, the bottom PMT is surrounded by LXe, resulting in temperature differences of several Kelvin.

### Statistical approach

Conventional PMT calibration methods such as the approach described above rely on fitting the PMT response spectrum. These methods induce difficulties at low PMT voltages due to an overlap of noise, UA components, and SPE or even higher-order peaks. This is also why no gains for the bottom PMT gains are shown for the fit method for voltages $< 1575$ V in figure 5.16 (a). An alternative statistical approach was suggested in [242], where an accurate model of the electron cascade processes within the dynode chain is described. This includes photons passing the cathode and directly striking the first dynode or skipping dynode stages. Such trajectories can account for up to 20% of the SPE spectrum; ignoring or wrongly modeling these contributions thus leads to incorrect PMT gains. The shape of UA components depends on the PMT and photocathode type and is not known a priori, rendering it difficult for the spectral fit to estimate their contribution accurately. The statistical method works over a wide range of light intensity, making it suitable especially for larger detectors with many sensors and no uniform LED light illumination.

For the details about the mathematical derivation, we refer to [242] but briefly introduce its main ideas. The first two central moments of the SPE response are used to calculate the PMT gain, for which the first two moments of the total and background distribution are needed. Since these two contributions are assumed to be independent, their moments are additive and the mean of the total charge $E[T]$ is calculated by:

$$E[T] = E[S] + E[B] \ , \tag{5.5}$$

where $E[S]$ represents the mean of the signal and $E[B]$ the mean of the background distribution. The signal charge distribution can be written as the sum over the signal charge distributions $S_p$ caused by $p$ PE and the probability $L(p)$ of producing $p$ PEs in a single laser pulse:

$$S = \sum_p S_p \, L(p) \ . \tag{5.6}$$

The PMT response is expected to be linear and, therefore, the multi-PE distribution $S_p$ is expressed by $S_p = S_1^p$. Since its mean $E[S_1^p] = p \cdot E[S_1]$, the mean of the total charge distribution is calculated by:

$$E[S] = E[S_1] \cdot E[L] \ . \tag{5.7}$$

Plugging this relation in equation (5.5) allows the determination of the first two central moments of the SPE response, the PMT gain:

$$E[S_1] = \frac{E[T] - E[B]}{E[L]} \ . \tag{5.8}$$

The PMT gains calculated using this method are also shown in figure 5.16 (a). In the analysis PMT calibration runs with different LED light intensities were compared. Low light intensities result in significant gain uncertainties but agree with the results of higher-intensity measurements, as assumed in [242]. A further expectation is the clearly visible underestimation of PMT gains using the spectral fit method due to an underestimate of UA components.

In general, the discrepancies between the two gain estimation methods are not problematic if the same approach is used during the entire detector operation run. Due to the higher flexibility for changing light intensities, the statistical approach was chosen for this work. Nevertheless, at the beginning of each run period, the spectral fit method was also used to cross-check the results of the statistical approach. In order to monitor the gain stability of the photosensors over a run period of several weeks, PMT calibrations were conducted regularly. For unmodified operational conditions such as temperature and voltage, the amplification factor is assumed to remain constant. Exemplary results are shown in figure 5.16 (b), where the bottom PMT's gain evolution for run 3 is presented. It shows the expected stable photosensor performance with a mean deviation of 4%. The varying size of the error bars is due to changing LED light intensities. The measured PMT gains were stored in a database and provide the conversion of recorded signals into PE, required for the further analysis.

### 5.4.2 Selection of krypton events

The efficient and reliable identification of calibration events is of central importance for the TPC characterization and the investigations on the detector's hermeticity. $^{83m}$Kr is a common LXe calibration source [243, 244]; its mother isotope $^{83}$Rb, contained in a standard VCR component, is installed between the two low-pressure gas

systems of the XeBRA platform, see figure 5.7. By opening valve V4 or V4', $^{83}$Rb's decay product $^{83m}$Kr is flushed into one of the separated xenon volumes, while the $^{83}$Rb is contained in zeolite beads and retained by a $\mu$m-filter. Since $^{83m}$Kr is a noble gas, it is not filtered out of the xenon gas by the hot getters.

The decay scheme of $^{83}$Rb is shown in figure 5.17. $^{83}$Rb decays via two metastable states to the stable isotope $^{83}$Kr. The first transition to $^{83m}$Kr is caused by electron capture; the two following deexcitations primarily occur through the emission of internal conversion electrons with energies of 32.1 keV and 9.4 keV. $^{83m}$Kr is an excellent LXe calibration source thanks to its homogeneous mixing with xenon allowing for event position calibrations (compare sections 5.4.4 and 5.4.5), its easy identification due to its delayed coincidence signature, its decay time of 1.83 h, which ensures no long-lived krypton contamination of the xenon target, and the energies of the decay in the low-energy range.

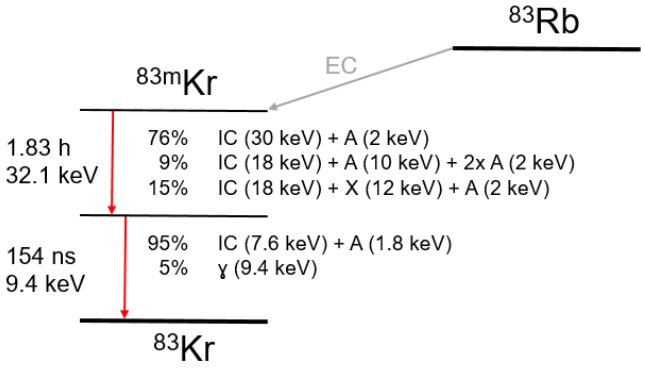


**Figure 5.17:** Decay scheme of $^{83}$Rb. Data from [245].

In the following, the $^{83m}$Kr tagging algorithm is presented. Event selection criteria are listed and explained, which take both the S1 and S2 information to separate signals from background events. During the development of these criteria, it was shown that a tagging mechanism based only on S1 signals also selects krypton events well. This algorithm was primarily used for measurements with small electron lifetimes leading to no or only small recorded S2 signals. Since the data described in this work was acquired after several days of xenon target purification, causing high electron lifetimes, the following krypton selection algorithm concentrates on events containing both S1 and S2 signals.

The digitized waveforms, such as an event recorded during a krypton run, are processed by straxbra (compare section 5.2.2), which identifies the peaks in the waveform. Based on their integrated area and width (the time range containing the 50% central area) they are identified as S1- or S2-like peaks. S1s are expected to have a maximal width of 150 ns; S2s are expected to have a minimum width of 200 ns and a minimum area of 10 PE, where the latter cut reduces noise contributions such as single-electron signals. The S2's width is much broader than the S1 width due to the

production of the secondary scintillation signal in the xenon gas phase. Straxbra's peak finding algorithm is only able to split peaks with time differences $> 200$ ns into two; otherwise, the signal is treated as one peak. For $^{83m}$Kr delayed coincidence signals with delay times $> 200$ ns, the light yield (LY) and charge yield (CY) of the 9.4 keV line are minimally affected by the previous transition, the 32.1 keV decay. This assumption is based on drift field-dependent scintillation signal investigations in [246] and simulation predictions using NEST [173, 174]. The following criteria are now applied to select krypton events. Straxbra's plugins provide the required parameters.

- **Number of peaks $\geq$ 3:** In principle, an $^{83m}$Kr event should contain two S1 and two S2 signals corresponding to the 32.1 keV and 9.4 keV decays. Depending on the detector's resolution, affected for example by diffusion, and the peak identification efficiency, not all four peaks might be visible: the two S2 signals often overlap and cause the absence of krypton's typical S2 double-peak structure [239]. Thus, the number of peaks was chosen to be $\geq 3$ with at least two S1 and one S2 signal. Due to the above-mentioned peak splitting method with zero efficiency for time differences $< 200$ ns, the 'two S1 peaks' condition drastically impacts the krypton event identification efficiency. Since the metastable state's half-life is 154 ns, excluding events with delay times $< 200$ ns rejects 72% of all krypton decays. Compared to this, all further applied cuts show minimal efficiency losses. Nevertheless, this loss does not impact the following analysis as long there is sufficient statistics, since the main goal of the krypton tagging is to identify a clean calibration data set.

- **S1 area $>$ 20 PE:** A 20 PE cut on the second-largest S1 signal is applied to reduce noise. Since the 9.4 keV decay shows signals of approximately $(50 \pm 10)$ PE (compare section 5.4.4), this cut causes minimal efficiency losses of $< 1\%$. No condition exploiting the approximate 3:1 ratio of the krypton S1 signals is used. The reasons are the relatively poor energy resolution of small-scale dual-phase xenon detectors and the two decays' different CY and LY due to different decay energies.

- **S1 order cut**: Since the first of the two coincident krypton decays releases more energy, the most prominent S1 peak has to appear before the second-largest S1 signal within one waveform.

- **S2 area $>$ 500 PE**: Similar to the S1 area cut, an S2 noise cut is implemented, excluding events with the largest S2 area $< 500$ PE. Since krypton S2 signals are detected with approximately $(6000 \pm 2000)$ PE (compare section 5.4.5), this cut also only causes minor efficiency losses of $< 1\%$.

- **z cut**: Depending on the analysis goal, it might be useful to introduce a $z$ cut, with the $z$ position being calculated using the electron's drift time and the drift field strength (compare section 5.4.3). Cuts excluding events occurring 1 cm below the gate or 1 cm above the cathode electrodes reduce background events such as interactions in the xenon gas. An additional $x$-$y$ cut is not possible for the HUsXe detector, which is instrumented with only one top PMT.

Two exemplary waveforms surviving the described cuts are shown in figure 5.18. The characteristic S1 double-peak structure is visible, with the S1 signals labeled blue. The S2 signals are shown in green: for both waveforms (a) and (b), they are identified as one overlapping S2 peak.

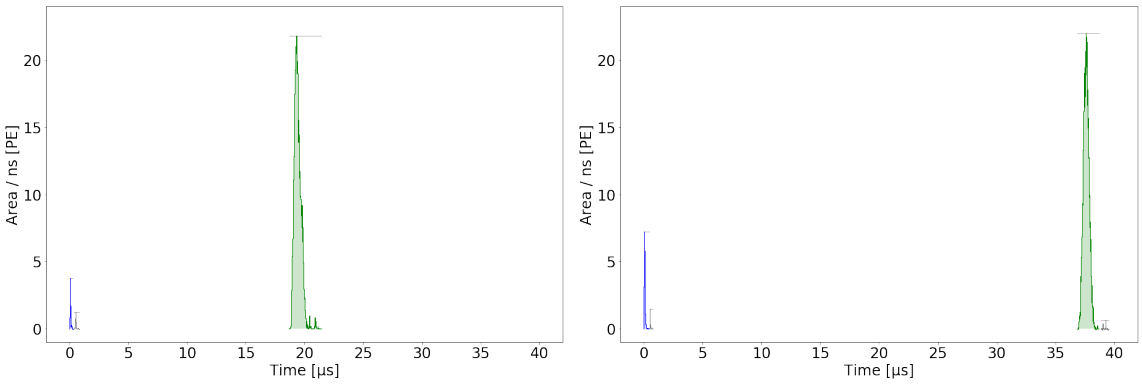


(a) (b)

**Figure 5.18:** Two exemplary waveforms after applying the krypton selection criteria showing different drift times. For the S1 peaks, the double-peak structure is clearly visible (blue). The corresponding S2 signals overlap and lead to only one S2 peak (green).

In figure 5.19 (a), the peaks contained in the selected krypton events are histogrammed based on their area and width. The typical $^{83m}$Kr populations are visible: at smaller widths, the two contributions correspond to the S1 signals. The group at larger area belongs to the 32.1 keV decay since its higher energy deposition releases more prompt scintillation photons. Accordingly, the 9.4 keV S1s appear at lower areas. For larger widths one population corresponding to the S2 signals is seen. Most waveforms contain overlapping S2 signals, leading to only one S2 population with a total energy-equivalent of 41.5 keV.

A further cross-check to verify that the krypton tagging algorithm works properly can be performed by histogramming the S1s' time difference, as presented in figure 5.19 (b). An exponential fit approximates the data; the extracted half-life agrees with the literature value of 154.4 ns [9]. The first 300 ns are excluded from the fit due to straxbra's peak splitting efficiency. The small structure at around 500 ns is seen in many measurements and could be caused by PMT afterpulses due to helium contamination [213].

### 5.4.3 LXe properties

With homogeneously distributed krypton atoms in the LXe target, HUsXe provides the possibility to study intrinsic LXe properties. In the following, results on drift field-dependent electron drift velocities and on longitudinal diffusion constants are presented.

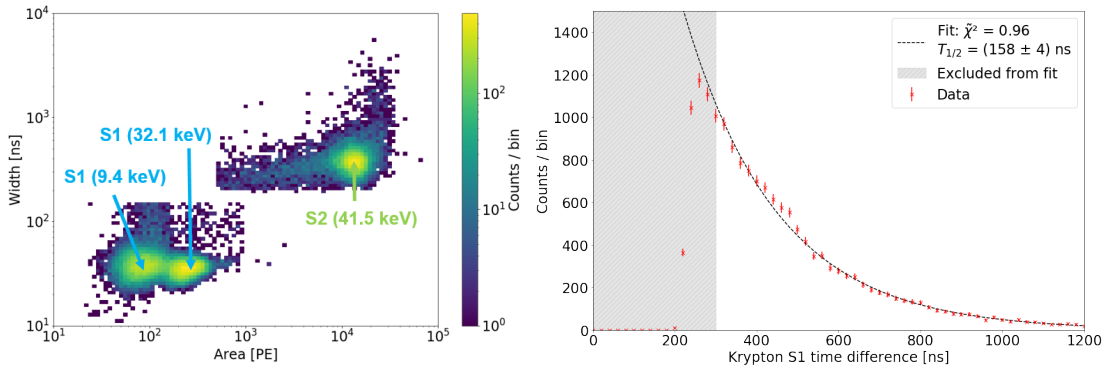


(a) (b)

**Figure 5.19:** (a) Histogram of the peaks contained in krypton-tagged waveforms. The two populations at smaller widths correspond to the 9.4 keV and 32.1 keV S1 signals, respectively. The S2 signal from the 41.5 keV sum peak is visible at larger area and width. (b) Histogram of the time difference of the krypton S1 peaks. The turn-on function is due to the efficiency of the peak splitting algorithm. The decay spectrum follows the expected exponential function with the extracted half-life agreeing with the literature value.

### Electron drift velocity

To convert an event's drift time to its corresponding $z$ position, the data processing package straxbra uses electron drift velocities measured by the XENON Collaboration [247]. The verification of these measurements is the aim of the following study; however, the results also constitute valuable input for the LXe community.

The electron drift velocity primarily depends on the TPC's drift field and via second-order effects on other operational parameters, such as temperature and pressure. It is calculated using the TPC dimensions and the difference in drift time between events occurring at the gate's and the cathode's $z$ position:

$$v_{\text{drift}} = \frac{\Delta z}{\Delta t} = \frac{z_{\text{cat}} - z_{\text{gat}}}{t_{\text{cat}} - t_{\text{gat}}} \ . \tag{5.9}$$

For the $\Delta z$ determination, the thermal contraction of PTFE is taken into account since the TPC is mainly built by PTFE parts, causing an absolute shrinkage of its length by 1.1 mm when being cooled from room temperature to −100°C. The drift time of events originating at the gate and cathode is derived in detail in the following and is shown in figure 5.20. Since the average motion of the drifting electron cloud is the crucial parameter, the S2 time being used is defined by the S2's 50% area quantile. Even though an increased signal width is expected for events occurring closer to the cathode caused by diffusion, the exact definition of the S2 time negligibly influences the final result. The single-electron scintillation width also does not impact the drift velocity calculation since it is a constant value and therefore subtracted in equation (5.9)'s denominator.

The drift time determination of events occurring at the cathode $t_{\text{cat}}$ is exemplarily illustrated in figure 5.20 (a), presenting $^{83\text{m}}$Kr events dependent on their drift time.

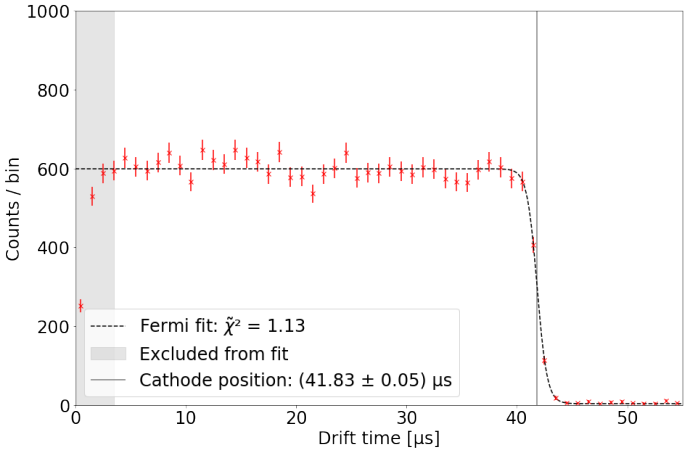


(a) Cathode drift time determination.

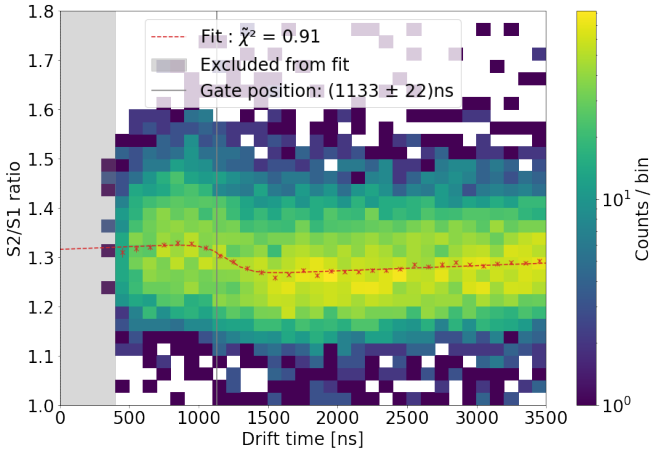


(b) Gate drift time determination.

**Figure 5.20:** Drift time determination of events occurring at (a) the cathode height using the maximum drift time and (b) the gate utilizing the change in S2/S1 ratio due to changing electric fields. The data is described by Fermi functions and the electrodes' positions are calculated based on knowledge from COMSOL electric field simulations.

A steep fall-off at approximately 42 $\mu$s is observed, indicating the edge of the sensitive xenon target at the cathode. To determine the cathode's exact position, a Fermi function is used to describe the data. Motivated by electric field simulations with COMSOL, the turn-over point at 50% height $f_{50\%}$ of the fit function is defined as the cathode's drift time $t_{\text{cat}}$. A systematic uncertainty of $f_{75\%} - f_{50\%}$ is considered in addition to the statistical uncertainty extracted from the fit. For small drift fields, the steep fall-off is smeared out and therefore causes the systematic uncertainties to dominate the statistical ones.

For the drift time determination of events from the gate, the S2/S1 ratio is examined, as shown in figure 5.20 (b). Due to the field strength difference below and above the gate, different electron and photon yields cause different signal ratios. A Fermi function describes the fall-off observed at around 1250 ns. The additional linear slope is caused by the usage of non-corrected S1 and S2 signals and their

position-dependent signal strengths (compare sections 5.4.4 and 5.4.5). The field leakage between drift and amplification field was studied with COMSOL simulations, indicating the gate level at 90% of the Fermi function $f_{90\%}$ .

Measurements with varying drift fields and fixed amplification field are analyzed to extract $t_{\mathrm{cat}}$ and $t_{\mathrm{gat}}$. The resulting electron drift velocities are shown in figure 5.21, together with the results reported by other experiments. No HUsXe results below drift fields of 300 V/cm were calculated due to difficulties extracting $t_{\mathrm{cat}}$, caused by non-converging fits. The HUsXe measurements follow the trend of the XENON results [248, 249, 247] and those from HeXe [250]. The power function approximating the XENON1T results (dashed) used by straxbra agrees with the drift velocity measurements obtained here. However, it differs noticeably from other measurements for drift fields below 100 V/cm. Large deviations can be seen when comparing the HUsXe results to those of other experiments. These differences might be due to varying operational parameters: The Xurich-II detector yields relatively low velocities in the drift field range of the HUsXe measurements and was operated at 184 K [251]. In contrast, the measurements by Miller et al. were taken at temperatures of 163 K and show higher results [252]. HUsXe was operated at temperatures around 173 K and yields drift velocities between the results of the two mentioned experiments. This indicates the non-negligible influence of the xenon temperature, and therefore, most of the experiments rely on drift velocity measurements taken with their own detector.

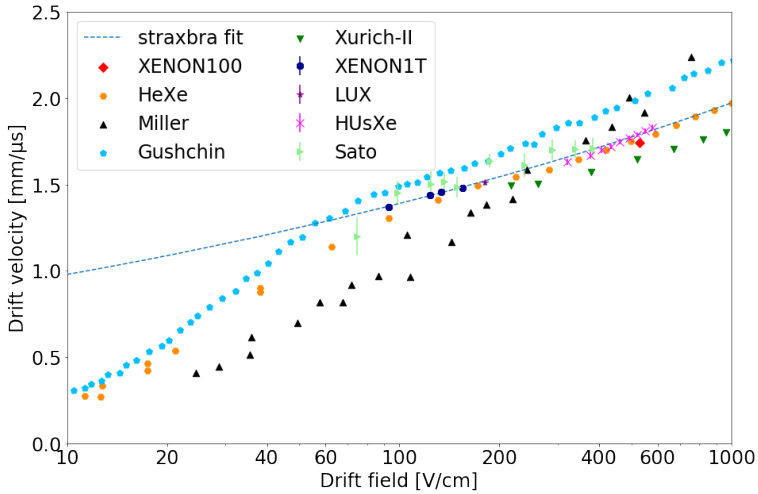


**Figure 5.21:** Electron drift velocity measurements of the HUsXe TPC along with data from other experiments: Sato [212], Xurich-II [251], Gushchin [253], Miller [252], HeXe [250], LUX [131], XENON100 [248, 249], XENON1T [247].

### Longitudinal diffusion

For LXe TPCs, the reconstruction of the event position is one of the central techniques to reduce background interactions by fiducilization and SS vs. MS rejection. The position resolution is intrinsically limited by diffusion, broadening the initially

point-likish electron cloud during the drift to a normal distribution with the transversal and longitudinal diffusion coefficients. Measurements of the transversal diffusion constant depending on the drift field strength are for example presented in [137] and [138]. Since the transversal diffusion only influences the S2 signal by second-order effects, in contrast to the longitudinal diffusion, and due to the non-existing $x$-$y$ resolution, it is difficult to study in LXe TPCs such as HUsXe. We thus focus on longitudinal diffusion.

Due to Brownian motion a point-like electron cloud is broadened during its drift with the standard deviation $\sigma_t$ [254]:

$$\sigma_t = \sqrt{\frac{2D_L t}{v_{\text{drift}}} + \sigma_0^2} \ , \tag{5.10}$$

where $D_L$ represents the longitudinal diffusion constant, $v_{\text{drift}}$ the mean drift velocity, and $t$ the mean drift time. $\sigma_0$ is interpreted as the S2 width for zero drift time caused by the time electrons emit light within the gas gap [255]. It is estimated using the width of single-electron signals. To have a robust measure of the S2 width, the standard deviation $\sigma_t$ is replaced by $\sigma_{t,50\%}$, which describes the time between the moments when 25% and 75% of the signal's charge have arrived:

$$\sigma_{t,50\%} = \sqrt{\frac{3.64 D_L t}{v_{\text{drift}}^2} + w_0^2} \ , \tag{5.11}$$

where $w_0 = 1.82\sigma_0$. This relation between the drift time $v_{\text{drift}}$ and the S2 width $\sigma_{t,50\%}$ is used to describe HUsXe data and extract the longitudinal diffusion constant $D_L$. An example measurement is shown in figure 5.22: $^{83\text{m}}$Kr data is histogrammed depending on its S2 width and the measured drift time. As expected, the longer the drift time, the larger the S2 width. The data in each drift time slice is approximated by a Gaussian; its mean and standard deviation are included in the figure. Due to edge effects, events with high and low drift times are excluded from the analysis. The extracted Gaussian means are approximated by equation (5.11), where the drift velocity results presented above are used. From the fit parameters, the diffusion constant $D_L$ is extracted.

This procedure is repeated for several data sets with varying drift field strengths. The results are shown in figure 5.23, which also shows the measurements reported by other experiments. The HUsXe measurements nicely agree with the XENON10 and XENON100 results. However, the HUsXe data point at 530 V/cm differs from the other HUsXe results, which might have been induced by a changed noise level, which was only recorded for this one specific measurement. Similar to the discussion of the drift velocity measurements of various experiments, a large spread of results is observed. Since the determination of $D_L$ relies on the drift velocity results as indicated by equation (5.11), the disagreements presented by figure 5.21 are reproduced and amplified.

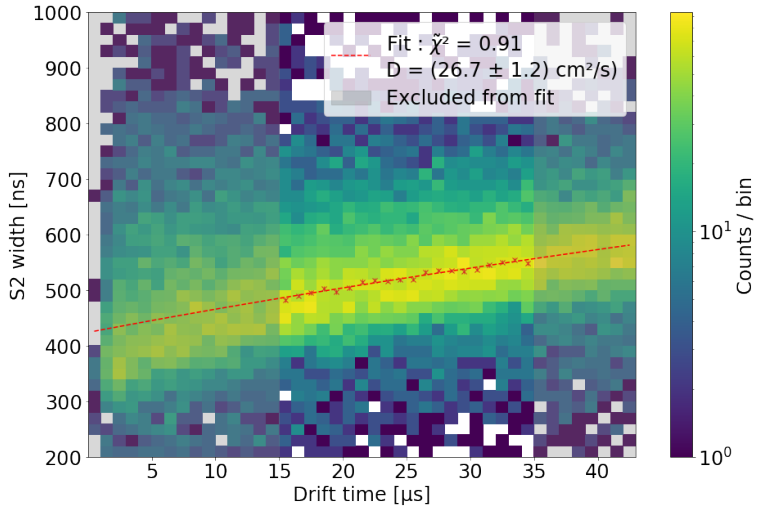


**Figure 5.22:** Exemplary diffusion constant determination. The longitudinal diffusion constant is extracted from the fit parameters of equation (5.11) describing the S2 width dependence on the drift time.

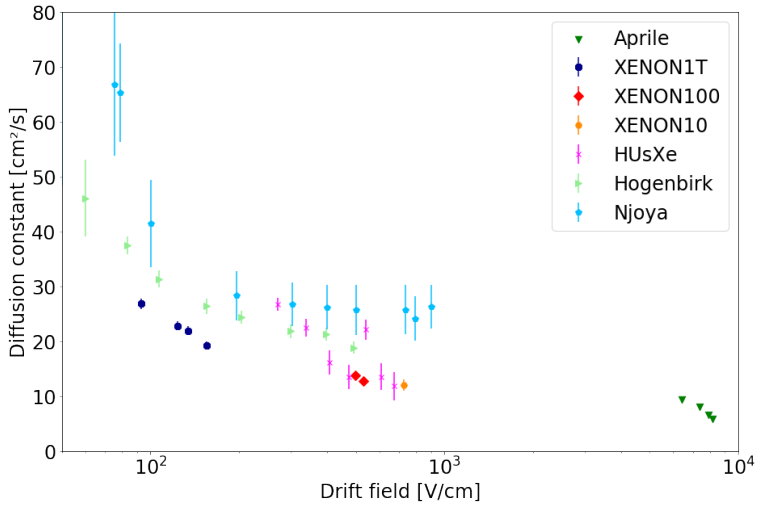


**Figure 5.23:** Longitudinal diffusion constant measurements of the HUsXe TPC along with data from other experiments: Aprile [125], Hogenbirk [255], Njoya [256], XENON1T [247], XENON100 [248, 249], XENON10 [254].

### 5.4.4 S1-only TPC characterization

The prompt scintillation light emitted from the interaction point is measured by the PMTs at the top and bottom of the HUsXe TPC cylinder. Several effects influence the photon detection efficiency and lead to position-dependent S1 signal strengths: Some photons get absorbed by the electrode meshes, which show a geometrical transparency of 90% each. The finite PTFE reflectance of $> 97\%$ [148] for VUV light further causes a signal attenuation, notably relevant for interaction points with small solid angles covered by the bottom PMT. Event positions near the gate suffer from total reflections at the LXe surface, which lead to longer photon travel paths and thus includes more reflections at the TPC walls. As a second-order effect due to the small size of the TPC, photons might get absorbed due to LXe's absorption length

of $\mathcal{O}(50\,\mathrm{m})$ [4] and Rayleigh scattering length of $\mathcal{O}(35\,\mathrm{cm})$ [257]. Inhomogeneities of the drift field leading to a different fraction of electron-ion recombination and therefore also influencing the S1 signal size are expected to be negligible based on the COMSOL simulation results shown in figure 5.4 (c).

In the following, the S1 signal strength depending on the $z$ interaction position and its correction are presented. No $x$-$y$ position correction can be applied since the HUsXe TPC with just one top PMT cannot resolve events within the horizontal plane. However, its influence is expected to be relatively small [220]. The S1 correction is not based on optical photon simulations; instead, the data-driven S1 size is normalized to an arbitrarily selected reference point: the center of the xenon target at $z = -37.5\,\mathrm{mm}$. Since different experiments might correct for different reference points, interpretations of the total corrected S1 size have to be done carefully.

The $z$-dependent S1 size is shown in figure 5.24 (a). $^{83\mathrm{m}}$Kr events are selected as explained in section 5.4.2, and the S1 signal of the 32.1 keV decay is histogrammed depending on the $z$ position and its area. The plot shows that the closer the interaction point to the gate, the smaller the S1 signal, as expected and explained above. This can be translated to the LCE (second $y$ axis), which is defined as the ratio of photons hitting the photocathode $N_{\mathrm{phcath}}$ and the number of generated photons $N_{\mathrm{gen}}$ in the xenon target, including these emitted after recombination (compare section 3.1.1). Taking into account the photosensor-specific response parameters QE and CE, the LCE can also be expressed as the ratio of detected and generated photons:

$$LCE = \frac{N_{\mathrm{phcath}}}{N_{\mathrm{gen}}} = \frac{N_{\mathrm{det}}}{N_{\mathrm{gen}}} \cdot \frac{1}{QE \cdot CE} \quad . \tag{5.12}$$

A QE of 32.5% and a CE of 95% are assumed here [129, 213]. The number of initially released photons from $^{83\mathrm{m}}$Kr interactions are obtained by NEST simulations [173, 174] for a LXe density of $2.9\,\mathrm{g/cm^3}$, a temperature-dependent value [216]. Knowing the amount of generated photons within the interaction, the $y$ axis of figure 5.24 (a) is converted into the LCE by applying equation (5.12). Events occurring near the cathode show LCEs of $\sim 40\%$; in contrast, photons produced near the gate hit the PMTs' photocathode with only an $\sim 20\%$ probability due to the effects explained above. For the measurement presented in figure 5.24, an average LCE of 29.6% is calculated. A comparable result of 29.5% was obtained by another small-scale TPC of similar dimensions, also operated at the XeBRA platform [258]. While HUsXe features a higher photosensor-active area due to its full coverage at the top and bottom of the TPC cylinder, the other detector has fewer massive stainless steel components and a better aspect ratio. A superior LCE is, e.g., expected for XENONnT as predicted by optical simulations [4]: an average LCE of 36% is calculated, ranging from its maximum of 50% above the cathode to its minimum of 25% below the gate. Note that large-scale TPCs such as the XENONnT detector are optimized to yield the best-possible LCE by higher electrode transparencies and polished PTFE surfaces; in contrast, the focus of the HUsXe detector is its tightness and radon reduction properties.

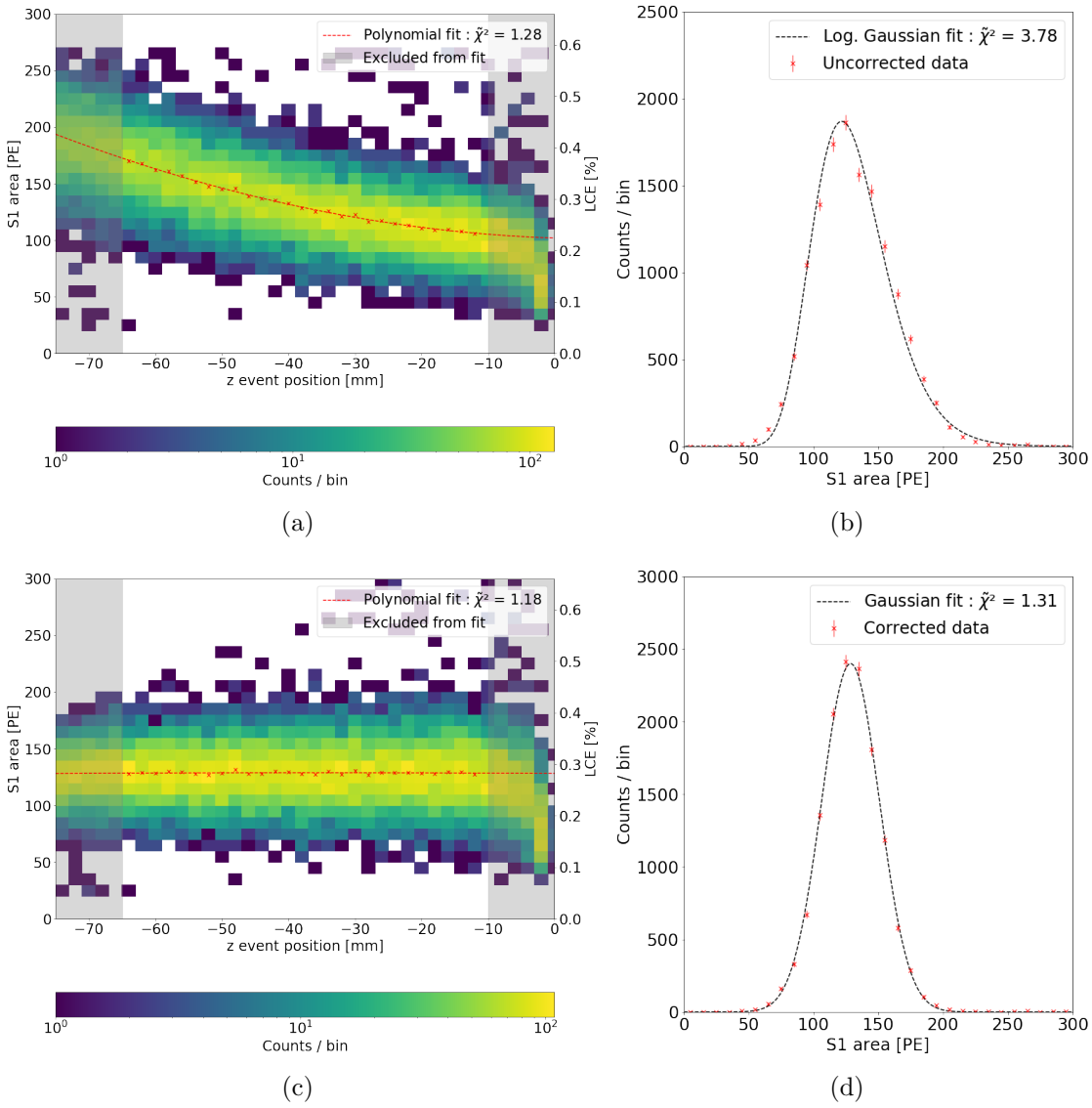


**Figure 5.24:** S1 correction: (a) shows the uncorrected S1 area of the 32.1 keV $^{83m}$Kr decay dependent on the $z$ position, (b) the corresponding S1 area histogram for events occurring at $z$ positions $\in [-65, -10]$ mm, modeled by a logarithmic Gaussian function. Equivalent descriptions for corrected data in (c) with the corresponding corrected S1 area modeled by a Gaussian function in (d).

The interactions occurring within the lowest or highest 1 cm of the xenon target are excluded from the further analysis due to edge effects. This provides a cleaner data set, which still contains sufficient statistics. It excludes, e.g., events originating above the gate, where lower S1 areas are expected due to less electron-ion recombination caused by the higher electric field. Considering the innermost events at $z$ positions between $[-65, -10]$ mm, a difference in the S1 area of $\sim 1.5$ is noticeable. This deviation indicates the need for an S1 correction. Therefore, the data within each $z$ slice of figure 5.24 (a) is fitted by a Gaussian function. Its mean and error on the mean extracted from the fit are included in the plot and a second-order poly-

nomial approximates the extracted data points. The corrected S1 signal $cS1$, with the reference point $z = -37.5\,\text{mm}$, is calculated as:

$$cS1(z) = \frac{S1(z)}{az^2 + bz + c} \cdot S1(z = -37.5\,\text{mm}) \ , \tag{5.13}$$

where the fit parameters $a$, $b$, and $c$ depend on the drift field strength due to its influence on the fraction of electron-ion recombination. The corrected data is shown in figure 5.24 (c).

To further describe the influence of the S1 correction, the distributions of the S1 and cS1 signals are shown in figure 5.24 (b) and figure 5.24 (d), both times only including data for $z \in$ [-65,-10] mm. While a logarithmic Gaussian function roughly describes the S1 area, the cS1 area distribution is nicely approximated by a Gaussian fit. This causes a resolution improvement from $\sim 22\%$ of the uncorrected data in figure 5.24 (b) to $\sim 16\%$ in figure 5.24 (d).

Measurements with different drift fields were S1-corrected using a correction function obtained for the corresponding drift field. The resulting cS1 data is used for field- and energy-dependent LY studies. A field-dependence is expected due to fewer electron-ion recombination for higher fields on the cost of S1 signal size. In figure 5.25 (a), the results for both krypton lines are presented.

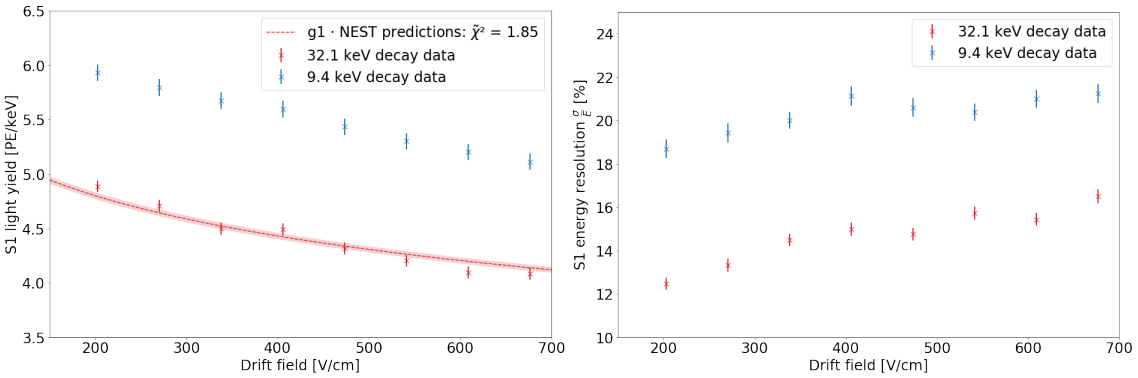


(a) S1 LY (b) S1 energy resolution

**Figure 5.25:** cS1 comparison of the 32 keV and 9 keV $^{83m}$Kr decay: (a) separately shows the LY per drift field, (b) the corresponding cS1 energy resolutions.

The overall trend shown in figure 5.25 (a) is as expected: the higher the drift field, the less recombination occurs, leading to smaller S1 signals. The shift between the 32.1 keV and 9.4 keV data points is due to the LY's dependence on the interaction energy, leading to a different amount of produced photons per keV. Drift field-dependent NEST predictions for the LY of the 32.1 keV signal are scaled to the measured 32.1 keV LY results and included in the plot. The scaling factor describes the detector-dependent $g1$ parameter, the photon detection efficiency. In principle, a $g1$ parameter could also be extracted from the measurement shown in figure 5.24 via the second y-axis describing the LCE, which includes the factor $N_{\text{det}}/N_{\text{gen}} = g1$,

see equation (5.12). Nevertheless, the value presented here is expected to be more precise since it is based on several measurements. Since the LY of the second 9.4 keV krypton line depends on the time difference to the first $^{83m}$Kr deexcitation [246], the $g1$ determination is only reported for the first krypton decay (32.1 keV) and yields

$$g1 = (0.093 \pm 0.001)\frac{\mathrm{PE}}{\gamma} \ . \tag{5.14}$$

This $g1$ value based on NEST predictions is compared to the data-driven result in section 5.4.6. Even though this parameter cannot be cross-checked by the results of other detectors, a comparison of different $g1$ parameters is shown in table 5.1 on page 129.

Figure 5.25 (b) presents the S1 energy resolution for varying drift fields and both krypton decays. A higher LY is obtained at lower drift fields since more PEs are generated. As a conclusion of the central limit theorem, this causes a better energy resolution. The conclusion of the central limit theorem also applies to the difference between the 9.4 keV and 32.1 keV resolution.

### 5.4.5 S2-only TPC characterization

Similar to the S1 size, the S2 signal strength depends on the interaction position. The two main effects influencing the corresponding PMT response are the finite electron lifetime, caused by absorption of drifting electrons, and inhomogeneities of the amplification field. The electron lifetime reduces secondary scintillation due to fewer electrons reaching the liquid-gas interface from interaction points deeper in the TPC; inhomogeneities in the amplification field are caused by a slightly tilted TPC as well as electrostatic sagging of the TPC electrodes and result in $x$-$y$ dependent S2 signal strengths due to the non-uniform gas gap thickness. Experiments with the ability to resolve events in the $x$-$y$ plane correct for inhomogeneities in the amplification region using data-driven models. Different gas gaps due to TPC tilt can be avoided by a detector leveling study based on PMT responses and levelmeter data, exemplarily shown in [220]. Since HUsXe was mainly built to demonstrate a hermetic TPC operation, only one PMT was included per photosensor array and space limitations excluded the implementation of more levelmeters. Therefore, no $x$-$y$ plane corrections can be made; however, the TPC was leveled as well as possible during installation, see section 5.3.1. Consequently, this subsection concentrates on the electron lifetime corrections, which depend on the $z$ interaction position.

Homogeneously distributed krypton events provide the data for the S2 correction. Due to the inability to split the S2 signals of the delayed coincident krypton decays, a total deposited energy of 41.5 keV is considered. The area of the combined S2 peak is used for the analysis and thus, S2 yield comparisons between the two $^{83m}$Kr decays are not possible.

The $z$-dependent S2 size is shown in figure 5.26 (a) with a data selection as described in section 5.4.2. The electron loss during the drift is indicated by decreasing

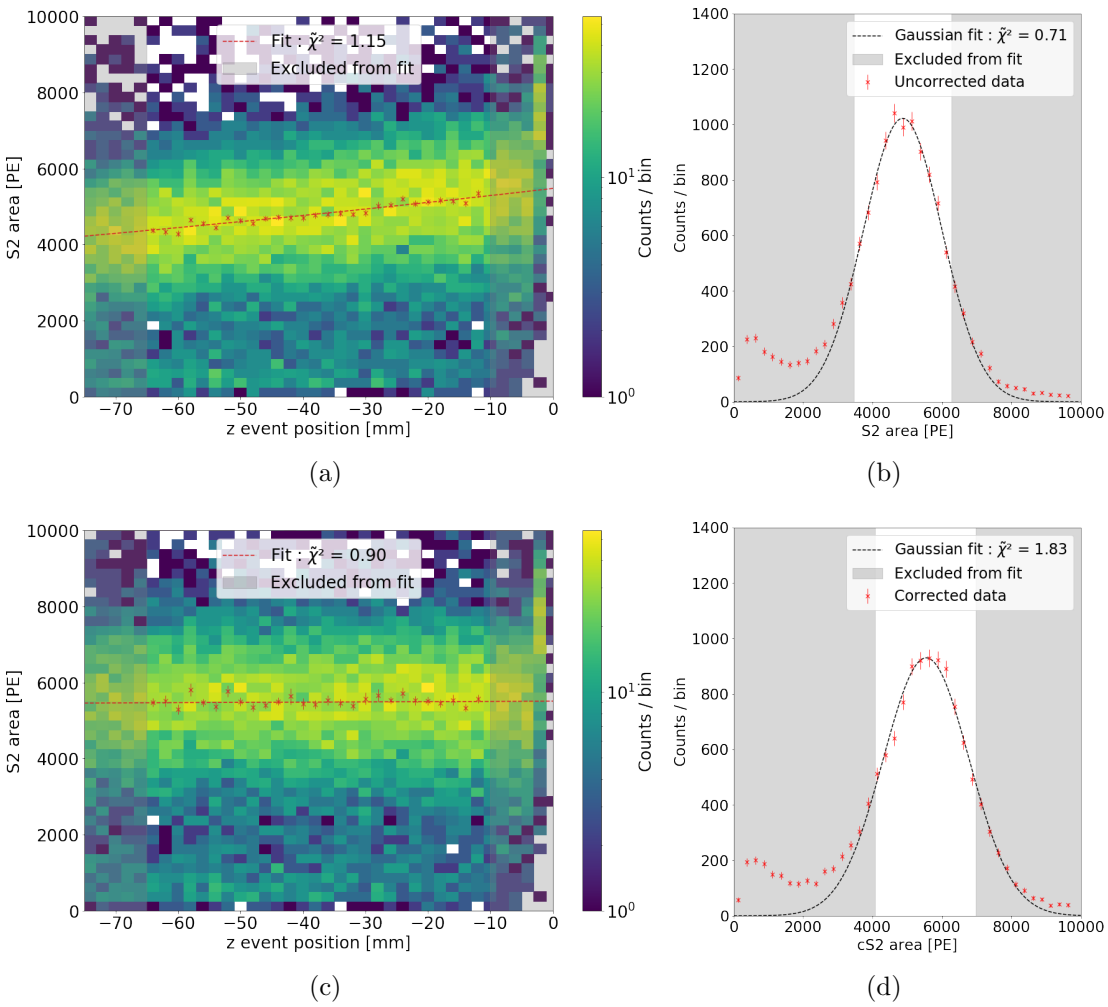


**Figure 5.26:** S2 correction: (a) shows the uncorrected S2 area of the 41.5 keV $^{83m}$Kr sum signal vs. the $z$ position with an electron lifetime of $\tau = (154 \pm 7)\,\mu$s, (b) the corresponding S2 area histogram for events occurring at $z$ positions $\in [-65, -10]$ mm, modeled by a Gaussian function. (c) and (d): equivalent description for corrected data. All four plots show noise signals at small S2 areas, which might have been caused by electron losses due to non-homogeneous field lines near the gate electrode.

S2 signals the deeper the event occurred in the TPC. Additionally, many noise signals are shown at small S2 areas for all $z$ coordinates. Charge losses due to the non-homogeneous field lines near the gate might cause these events (compare figure 5.4 (c)). As before, interactions 1 cm above the cathode and 1 cm below the gate are excluded for the further analysis to avoid edge effects, e.g., caused by events occurring above the gate. A Gaussian function approximates each $z$ slice and its mean and the error on the mean are included in figure 5.26 (a). Due to the noise contribution, only the central part of the peak was used for the fit. An exponential function describes the overall $z$ dependence of the S2 signal, also shown in the diagram. From its decay constant, the electron lifetime is extracted by dividing by the drift field-dependent electron drift velocity $v_{\text{drift}}$ (compare section 5.4.3). In this particular run, a lifetime of $\tau = (154 \pm 7)\,\mu$s, corresponding to $\sim 4$ times the maximal drift time, was achieved.

To correct the S2 signal for electron lifetime losses, the S2 area is calculated for no-electron losses at the gate level. Therefore, the corrected S2 signal $cS2$ with the reference point $z = 0$ is determined by:

$$cS2(z) = \frac{S2(z)}{a \cdot \exp\left(\frac{1}{\tau \cdot v_{\text{drift}}} z\right)} \cdot S2(z = 0\,\text{mm}) \ , \tag{5.15}$$

where $a$ is a fit parameter, $v_{\text{drift}}$ the drift velocity, and $\tau$ the decay constant. The correction outcome is shown in figure 5.26 (c). The included linear fit indicates that $z$ and cS2 data are not correlated anymore. Figure 5.26 (b) and (d) show the histograms of the S2 and cS2 data selected for $z$ coordinates $\in [-65, -10]$ mm with a Gaussian approximation, where only data within the central part of the peak are used. Comparing the means of the two Gaussian approximations results in a higher mean value for the corrected data. In contrast to the S1 correction described above, no S2 resolution improvement can be reached here. This indicates that the width of the S2 distribution is mainly driven by other $z$-independent effects, such as an $x$-$y$ dependence caused by a tilted TPC.

In general, the electron lifetimes achieved with the HUsXe detector range up to 300 $\mu$s, several times the maximum drift length, due to the permanent purification by the hot getters. Such values are more than sufficient. Experiments like XENONnT or PandaX-4T with TPC lengths of $\sim$ 1.5 m have achieved electron lifetimes of several ms [194, 6]; for DARWIN lifetimes $\mathcal{O}$(10 ms) are aimed for.

Varying drift field measurements are utilized to explore the S2 signal's dependence on the applied field. The S2 yield is calculated by dividing the mean of the corrected cS2 data by the energy of 41.5 keV; the corresponding results are shown in figure 5.27 (a). The ratio $\sigma/\mu$ describes the S2 energy resolution and is presented in figure 5.27 (b). Figure 5.27 (a) shows the expected behavior already explained in detail in section 5.4.4: the higher the drift field, the less electron-ion recombination takes place and the higher the S2 signal, nicely showing the S1-S2 anti-correlation. NEST electron yield predictions, scaled by the parameter $g2$, are also included in the figure. Due to the dependence of the second S2 yield on the time $\Delta t$ between the two $^{83\text{m}}$Kr decays and straxbra's finite peak splitting efficiency reported in section 5.4.2, only decay times $>$ 200 ns were simulated. The detector-inherent parameter $g2$ describes the charge amplification and was determined to be:

$$g2 = (6.7 \pm 0.4)\frac{\text{PE}}{e^-} \ . \tag{5.16}$$

An electron extraction efficiency from the liquid into the gas phase of 100% [125] is expected here due to the voltage difference of $\Delta U_{A-G} = 4$ kV between gate and anode for all discussed measurements. This corresponds to an electric field strength in the gas of $E_{\text{GXe}} > 10$ kV/cm, assuming the setpoint liquid level precisely between the two electrodes. The extraction efficiency decreases to 95% for lower liquid levels and thus has a minor impact on the $g2$ calculation. The discrepancies between the data points and the fit function ($\tilde{\chi}^2 = 4.05$) indicate imperfect modeling of HUsXe's detector response by NEST or a systematic bias between the measurements. This

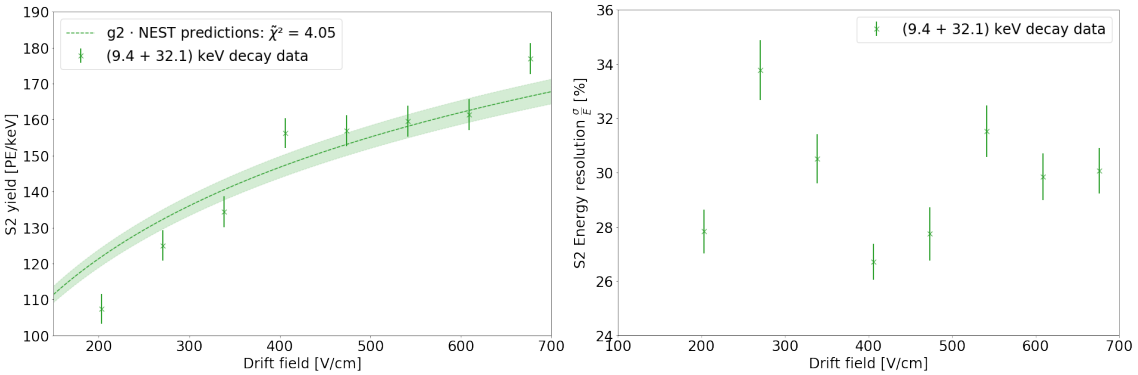


(a) S2 LY. (b) S2 energy resolution.

**Figure 5.27:** Drift field dependency of S2 signals using the 41.5 keV $^{83m}$Kr decay: (a) LY per drift field, (b) the corresponding S2 energy resolutions.

shows the weak point of this method: the $g2$ determination entirely depends on NEST predictions. Therefore, we report in the following section 5.4.6 on a purely data-driven detector parameter extraction, where we also show a comparison to $g2$ parameters obtained by other experiments.

For the energy resolution shown in figure 5.27 (b), one would assume a better resolution for higher drift fields since more quanta are included in the signal generation process; the data hints towards this expectation. The shown S2 resolutions are much worse than the resolutions calculated in section 5.4.4 for the S1-only characterization. In general, the S2 energy resolution depends on three factors: fluctuations in production, electron survival probability, and effective gain amplification. The former two aspects are assumed to be negligible due to xenon's small Fano factor [259] and the achieved high electron lifetimes. In contrast, significant amplification fluctuations are possible, e.g., by a TPC tilt causing different gas gap thicknesses. Due to HUsXe's inability to reconstruct $x$-$y$ positions, no correction can be applied here; this is expected to influence the S2 resolution, as described in [220]. An S2 resolution dominated by amplification fluctuations would also explain the absence of resolution improvements for larger drift fields, as mentioned before (compare figure 5.26 (b) and (d)).

### 5.4.6 Combined S1-S2 TPC characterization

A detector's energy resolution is one of its most essential characteristics to separate background and signals events in a search for line signals. For example, DARWIN's sensitivity calculation for the $0\nu\beta\beta$ of $^{136}$Xe presented in 4.4 is based on assuming an $\sim 0.8\%$ energy resolution at its $Q$ value of $\sim 2.5$ MeV. For worse resolutions, the sensitivity would suffer due to more $2\nu\beta\beta$ events being reconstructed in the $0\nu\beta\beta$ ROI [10]. The assumed energy resolution is taken from XENON1T measurements using various calibration sources, with a measured $\sigma_E/E$ value of 41.5 keV $^{83m}$Kr events of $\sim 5\%$ [179]. Such resolutions are achieved by exploiting the anti-correlation of the S1 and S2 signals, expressing the CES, introduced in section 3.1.2:

$$E = W \cdot (n_\gamma + n_e) = W \cdot \left( \frac{cS1}{g1} + \frac{cS2}{g2} \right) \quad , \tag{5.17}$$

where $W = (13.7 \pm 0.2)\,\mathrm{eV}$ [260] is the average energy needed to produce quanta, either scintillation photons or ionization electrons. For the ongoing discussion about the correctness of the $W$ value, we refer to [261] and [262]. When reformulating equation (5.17) to

$$\frac{cS_2}{E} = -\frac{cS_1}{E} \cdot \frac{g_2}{g_1} + \frac{g_2}{W} \quad , \tag{5.18}$$

it gets clear that the detector-inherent gains $g1$ and $g2$ can be directly determined by the $y$ intersect and the slope of the cS1-cS2 anti-correlation, without the need to use NEST predictions as applied for the S1- and S2-only characterization in the previous sections. Utilizing the S1 and S2 yields of different monoenergetic calibration sources is one possibility to obtain the parameters $g1$ and $g2$. However, in this work only $^{83\mathrm{m}}$Kr signals are available. Therefore, the drift field-dependent S1 and S2 yields are exploited [251], as shown in figure 5.28. Due to the difficulty of splitting krypton S2 peaks, the following investigation is based on a combination of the two krypton S1 signals and their summed S2 signal, corresponding to a total deposited energy of 41.5 keV.

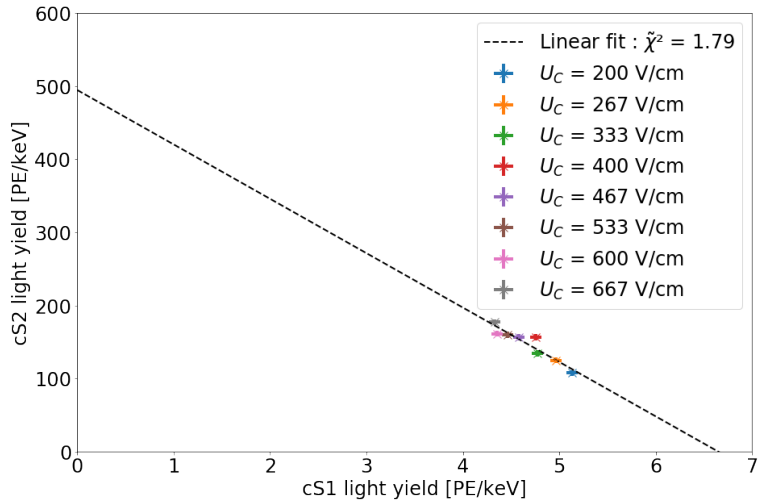


**Figure 5.28:** Anti-correlation of the S1 and S2 signals for drift fields between (200 - 700) V/cm. The detector-specific gains $g1$ and $g2$ describing the photon detection efficiency and charge amplification factor, respectively, are extracted from the linear fit fuction.

The anti-correlated S1 and S2 yields presented in figure 5.25 and figure 5.27 are summarized in figure 5.28, with the yields of the two S1 signals being combined. The detector gains are extracted from a linear fit following equation (5.18):

$$g1 = (0.089 \pm 0.004)\,\frac{\mathrm{PE}}{\gamma} \tag{5.19}$$

$$g2 = (7.1 \pm 0.7)\,\frac{\mathrm{PE}}{e^-} \quad . \tag{5.20}$$

Comparing the gains obtained from the S1-only $g1 = (0.093 \pm 0.001)\,\frac{\mathrm{PE}}{\gamma}$ and S2-only $g2 = (6.7 \pm 0.4)\,\frac{\mathrm{PE}}{e^-}$ detector characterization yields good agreements, indicating that the HUsXe results are in accordance with the findings of other experiments used for the NEST model. Nevertheless, it is noticeable that the parameter extraction based on the combined S1-S2 data results in larger uncertainties, especially for $g2$. This is due to the linear fit's long extrapolation to the $y$ intersect, which determines $g2/W$. In order to compare the HUsXe-inherent parameters, table 5.1 presents the $g1$ and $g2$ gains of other experiments; the higher these two parameters, the better the detector's functionality. HUsXe, which was not built to maximize $g1$ and $g2$, shows results being roughly comparable with XeBRA [220] and the values reported by Hogenbirk et al. [255]. However, experiments like XURICH-II [251] report much higher gains and indicate the possibility of optimizing the detector.

**Table 5.1:** Comparison of the detector-inherent gains $g1$ and $g2$. The HUsXe results are roughly comparable with the gains reported by XeBRA and Hogenbirk.

| **Experiment** | ***g1*** **[PE/$\gamma$]** | ***g2*** **[PE/e$^-$]** | **Reference** |
|---|---|---|---|
| XENON10 | $0.060 \pm 0.001$ | $13.51 \pm 0.03$ | [260] |
| XENON100 | $0.055 \pm 0.002$ | $8.09 \pm 0.39$ | [263] |
| XENON1T | $0.1442 \pm 0.0003$ | $11.52 \pm 0.05$ | [247] |
| LUX | $0.115 \pm 0.005$ | $12.1 \pm 0.9$ | [264] |
| XURICH-II | $0.191 \pm 0.006$ | $24.4 \pm 0.4$ | [251] |
| XeBRA | $0.122 \pm 0.002$ | $5.49 \pm 0.05$ | [220] |
| Hogenbirk et al. | $0.102 \pm 0.003$ | $5.01 \pm 0.13$ | [255] |
| HUsXe | $0.089 \pm 0.004$ | $7.1 \pm 0.7$ | this work |

With the detector-inherent gains $g1$ and $g2$ (results of the data-driven parameter estimation are applied in the following), the absolute scintillation $LY_{\mathrm{abs}}$ and ionization $CY_{\mathrm{abs}}$ yields can be calculated:

$$LY_{\mathrm{abs}} = \frac{cS1}{g1 \cdot E} \tag{5.21}$$

$$CY_{\mathrm{abs}} = \frac{cS2}{g2 \cdot E}\ , \tag{5.22}$$

where $E = 41.5\,\mathrm{keV}$ is the $^{83\mathrm{m}}$Kr-specific energy. $LY_{\mathrm{abs}}$ and $CY_{\mathrm{abs}}$ are xenon-specific numbers, which should not depend on a specific detector but only on the applied drift field. HUsXe's results are shown and compared with other LXe TPCs in figure 5.29: both the absolute ionization and the absolute scintillation yield agree with other xenon experiments. This is not unexpected since the detector gain comparison between the NEST- and data-based methods already implied a good agreement with other detectors, as explained above. Nevertheless, it shows that HUsXe's results could be valuable input for expanding the database of the NEST model.

The $g1$ and $g2$ parameters are also used to calculate the CES, which is expected to improve the energy resolution compared to the S1- and S2-only resolution. The combined energy is calculated according to equation (5.17) and shown in figure 5.30.

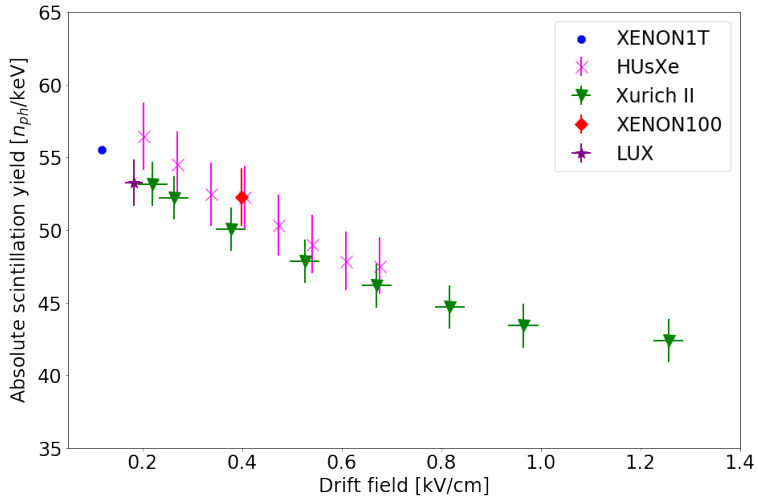


(a) Absolute scintillation yield.

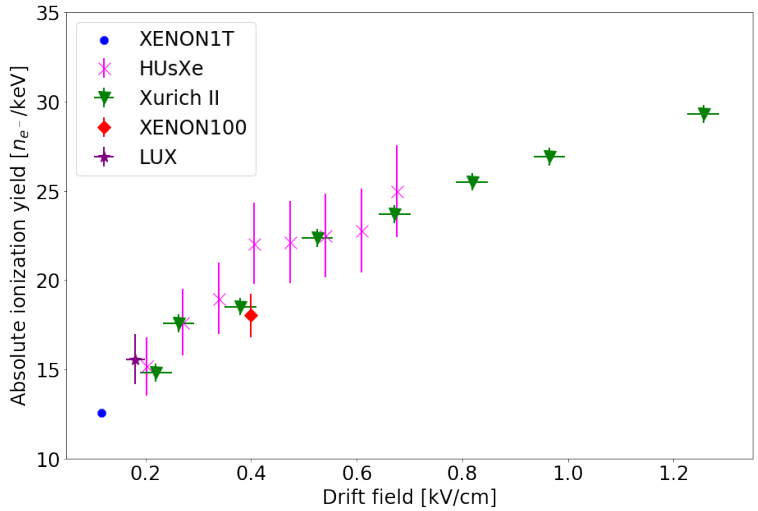


(b) Absolute ionization yield.

**Figure 5.29:** Absolute scintillation (a) and ionization yields (b) as a function of the drift field for the 41.5 keV energy deposition of both delayed $^{83m}$Kr decays. Data is shown from XENON1T [265], XENON100 [263], LUX [266] and XURICH-II [251] for comparison. The HUsXe data agrees well with the other measurements.

There the S1 and S2 data are included as well. The light blue curve approximates the S1-S2 combined energy with a large $1\sigma$ uncertainty band due to the significant detector gain uncertainties. The CES' mean value agrees with the expected krypton energy of 41.5 keV, indicating the successful $g1$ and $g2$ determination. However, the resolution did not improve by exploiting the scintillation-ionization anti-correlation. This is probably due to the very smeared out S2 distribution and, accordingly, a small information gain by combining its knowledge with the S1 signals. The S2 resolution suffers from the impossibility to apply $x$-$y$ corrections as discussed in section 5.4.5 and a low charge amplification gain $g2$. This affects the attainable resolution for HUsXe to 14%, much lower than the resolution of 5% obtained with XENON1T.

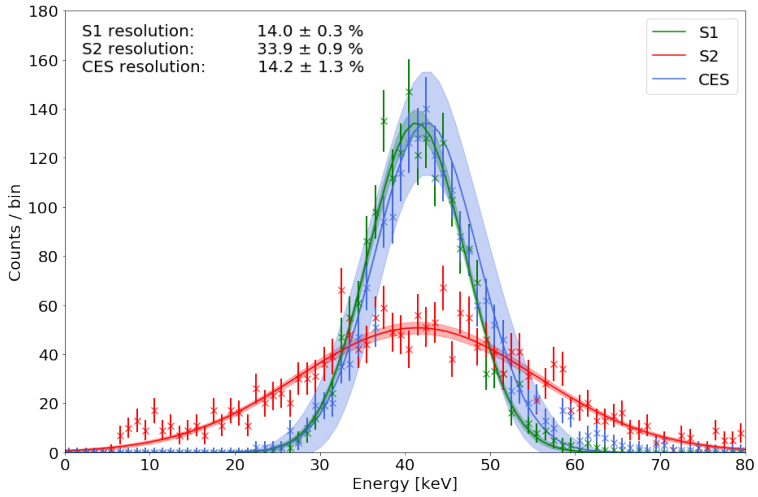


**Figure 5.30:** Energy resolution: The CES does not yield an improved resolution compared to the S1-only resolution, which is explained by the much worse S2 resolution with little information gain when combining with the S1 signals.

To summarize, the HUsXe detector was characterized in this section and shows a functionality comparable to other small- and large-scales TPCs. Besides fundamental studies of the PMT gains and krypton selection, which serve as a basis for investigating the TPC's hermeticity in the following section, LXe properties and detector-inherent gains were determined. Even though some results indicate the limitations of this TPC with its missing $x$-$y$ resolution, good results were obtained: the comparison of drift velocities, diffusion constants, and absolute scintillation and ionization yields agree well with the results reported by other large- and small-scale detectors.

## 5.5 HUsXe hermeticity and radon predictions for DARWIN

The results presented so far indicate the good functionality of the HUsXe TPC. Following the demonstration of the successful construction, this section is dedicated to studying its unique property: the hermeticity of the instrumented volume. The TPC chamber, mostly made of PTFE, was sealed by the concept of cryofitting, utilizing the different thermal expansion coefficients of the materials, explained in section 5.2.1. As indicated by pre-tests, this sealing concept does not yield vacuum tightness and a leakage flow between the two separated volumes is expected. This parameter is measured in the following section by using $^{83m}$Kr measurements. A realistic scaling up of HUsXe's hermeticity is further utilized to estimate DARWIN's $^{222}$Rn contamination assuming a semi-hermetic TPC as realized here. For that, a mathematical model is developed to describe the expected $^{83m}$Kr and $^{222}$Rn concentrations of HUsXe and DARWIN, respectively.

### 5.5.1 The hermeticity of HUsXe

In order to study HUsXe's hermeticity, $^{83m}$Kr is flushed through the gas system directly into the TPC, where it homogeneously mixes with the xenon target within $\mathcal{O}$(min). After stopping the krypton flow, a decrease in the number of krypton events over time is expected: besides the exponential decrease due to the krypton decay, an additional decrease is caused by the residual mass exchange flow $f$ between the two improperly separated volumes, diluting the krypton concentration in the xenon target. To extract the relevant information out of these measurements, a mathematical model describing the $^{83m}$Kr concentration is used. It represents the different components affecting the $^{83m}$Kr concentration in the target. A system of differential equations is set up and adapted to the initial conditions, described by the initial krypton filling of the inner volume; the data is afterward modeled using the solution of the differential equations, and the leakage flow is extracted.

Figure 5.31 presents the different contributions taken into account for the model. $M_i$ and $N_i$ denote the xenon mass and number of the krypton atoms of the inner ($i = 1$) and the outer ($i = 2$) xenon volume, respectively. A homogeneous krypton concentration in both volumes is assumed. The impact of the purification system is expected to be negligible due to the low xenon mass and the resulting low number of krypton atoms contained in its pipes. Since the system is enclosed, shows great long-term stability, and minor pressure differences between the two xenon volumes were recorded, the absolute leakage flow in both directions is assumed to be equal, i.e., $|f| = |f_{\text{out}}| = |f_{\text{in}}|$. The three source and drain terms affecting the $^{83m}$Kr concentration after the initial filling are:

- $-\lambda \cdot N_1$; $-\lambda \cdot N_2$: The krypton atoms in both volumes decay with their corresponding decay constant $\lambda$.
- $\pm f \cdot \frac{N_2}{M_2}$: The leakage flow $f$ streaming from the outer to the inner volume, defined as mass exchange per time unit, is scaled by the outer volume's krypton concentration. Its sign depends on the point of view, i.e., whether the term describes the evolution of the inner or outer volume's amount of krypton.
- $\pm f \cdot \frac{N_1}{M_1}$: The leakage flow from the inner to the outer volume is scaled by the inner volume's krypton concentration.

The resulting system of two differential equations presents the time evolution of the number of krypton atoms in the inner and outer volume, $N_1$ and $N_2$, respectively:

$$\frac{\partial N_1}{\partial t} = -\lambda N_1 - f \cdot \frac{N_1}{M_1} + f \cdot \frac{N_2}{M_2} \tag{5.23}$$

$$\frac{\partial N_2}{\partial t} = -\lambda N_2 - f \cdot \frac{N_2}{M_2} + f \cdot \frac{N_1}{M_1} \ . \tag{5.24}$$

The equations are solved and the integration constants are adapted to the initial conditions: $N_1(0) = N_0$ and $N_2(0) = 0$, where $N_0$ is the number of krypton atoms initially flushed into the TPC. $N_1(t)$ is expressed by

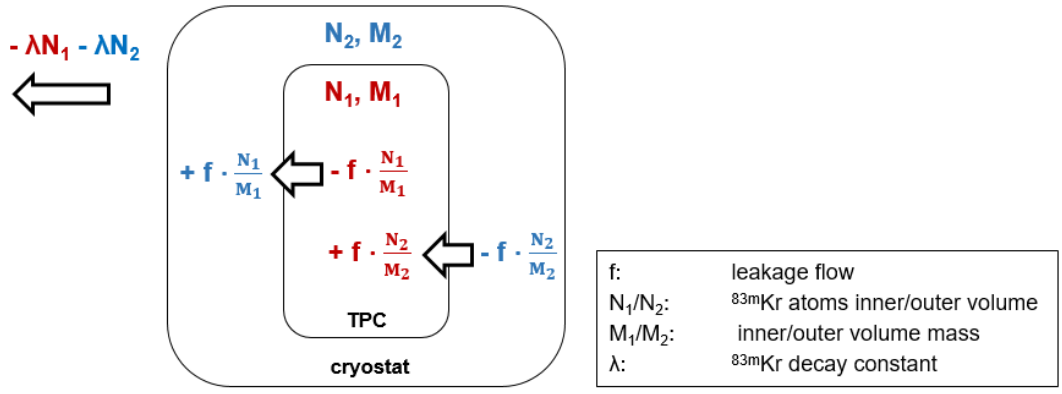


**Figure 5.31:** Scheme describing HUsXe's $^{83m}$Kr evolution contributions. The red (blue) terms represent the factors influencing the evolution of the number of krypton atoms $N_1$ and $N_2$ in the inner and outer volume, respectively. The absolute leakage flow $f$ is assumed to be equal in both directions and is scaled by the corresponding krypton concentration.

$$N_1(t) = \frac{N_0 \cdot e^{-\lambda t}}{M_1 + M_2} \cdot \left( M_1 + M_2 \cdot e^{\lambda t + \frac{(-f M_1 M_2 - f M_2^2 - \lambda M_1 M_2^2)t}{M_1 M_2^2}} \right) , \tag{5.25}$$

where $N_0$ is a free parameter and $f$ the leakage flow. The decay constant $\lambda$ is known, and the masses $M_1$ and $M_2$ are calculated by the TPC geometry and the filled amount of xenon. Since the number of recorded krypton events, the activity $A_1$, is directly proportional to $N_1(t)$, equation (5.25) allows to extract the leakage flow $f$. Several data sets are analyzed to cross-check the stability of this supposedly time-stable detector property. To provide consistent conditions for these different sets, a fixed measurement procedure was defined at the time of data taking: For the initial krypton flushing, valve V4 (compare figure 5.7) was opened for 1 min while the purification system of the inner xenon volume was operating with a speed of 1 SLM and transported the krypton into the TPC. After the krypton filling, 3 min measurements were recorded every 10 min for 5 h. Before starting a new data set and filling $^{83m}$Kr again into the TPC, a break of at least 5 h was foreseen. This interruption ensured stable starting conditions for each data set. Due to the more than 10 h time difference between the krypton flushes, $< 2.2\%$ of the krypton atoms are expected to remain in the xenon target.

We described in section 5.3.2 that the simultaneous operation of both gas systems yielded LXe level instabilities, while only purifying the inner volume yielded stable conditions. Therefore, the data was taken with the inner purification system in operation and the outer purification system being offline. In principle, the described measurements could also have been accomplished by recording the krypton leakage in the opposite direction. However, this would require filling the $^{83m}$Kr calibration source to the outer volume, which the LXe level instabilities prevented when operating the outer purification system.

The number of detected krypton events of several 3 min measurements is presented in figure 5.32, based on the krypton tagging algorithm described in section 5.4.2. In total, seven different data sets are shown. The data is described by equation (5.25), with the masses $M_1 = 0.9\,\text{kg}$ and $M_2 = 5.5\,\text{kg}$. $M_1$ corresponds to the total mass of the inner xenon volume, including the inactive xenon below the cathode. However, only events occurring between the cathode and gate electrodes are identified as krypton events since an S2 signal is required. The difference between instrumented and total inner xenon mass $M_1$ leads to an additional factor, which is not accounted for in equation (5.25) as it does not influence the extracted leakage flow $f$ but only changes the interpretation of the parameter $N_0$. The leakage flow $f$ is calculated for each data set, resulting in a mean flow of $f = (0.11 \pm 0.01)\,\text{kg/h}$. In order to show the impact of this mass exchange flow as an additional decay channel, the $^{83\text{m}}$Kr decay curve is also included in figure 5.32: its exponential decay clearly differs from the recorded data.

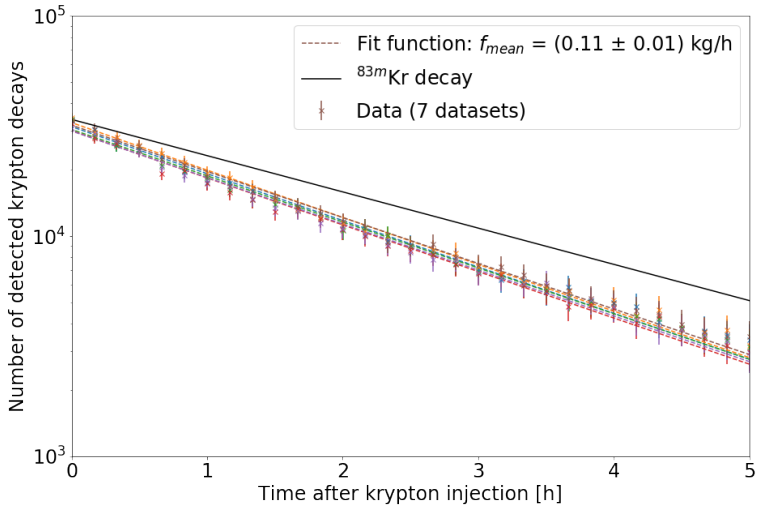


**Figure 5.32:** Extraction of the leakage flow $f$ by recording the time evolution of krypton decays happening in the xenon target. The black curve describes the expected behavior after the initial krypton filling in case of a hermetically sealed detector, while the data clearly shows the influence of the leakage, an additional krypton decrease. Its flow is extracted from the fit describing the data.

The measurements presented here were recorded during HUsXe's run 3. Similar data was also taken during run 1 and analyzed using a krypton S1-only tagger due to the small electron lifetimes obtained during hermetic operation. The result from this run, $f = (0.11 \pm 0.02)\,\text{kg/h}$, is in good agreement with the leakage flow presented here, which shows the repeatability of the measurement.

The leakage flow $f = (0.11 \pm 0.01)\,\text{kg/h}$ is considered to be a first hint towards feasible leakage flows. Its reduction should be possible by improving the sealing of the target; we present two ideas here: Firstly, potential leaks around the PMTs could be reduced by implementing a quartz plate, similar to the semi-sealed San Diego TPC described in section 5.1.1. The underlying idea is not to seal the single PMTs but instead the entire TPC cylinder with quartz plates at the top and bottom. This might be especially beneficial for large detectors with many photo-

sensors. Due to quartz' VUV light transmission of $> 90\%$ [212], the PMTs could be entirely operated in the outer xenon volume. Consequently, all radon emanated out of PMT surfaces would end up in the outer xenon buffer volume. Quartz's known low $^{226}$Ra contamination [267], resulting in low $^{222}$Rn emanation, makes this idea even more beneficial. However, the finite transparency and the technical feasibility of producing a quartz plate with a 2.6 m diameter introduce additional challenges. Secondly, the complete TPC could be housed in a hermetic vessel, such as an acrylic chamber with feedthroughs for detector installations. On the one hand, this idea would probably lead to a higher TPC radon concentration than a hermetically sealed TPC; on the other hand, it is much easier to design and build due to fewer boundary conditions and thus easier to seal. This approach was already applied for the much simpler DEAP-3600 single-phase detector (i.e., no electric fields), where an acrylic vessel was successfully installed around the 3.6 t argon target and the liquid argon scintillation light was guided by acrylic light guides to PMTs far away from the target [268].

### 5.5.2 $^{222}$Rn predictions for DARWIN

With its 5.6 cm diameter HUsXe differs significantly from the planned DARWIN detector size of a 260 cm diameter TPC. The obtained hermeticity result of $f = 0.11\,\mathrm{kg/h}$ from HUsXe can thus not be used to estimate DARWIN's radon budget assuming a semi-hermetic TPC. Therefore, different possibilities to scale up the HUsXe outcome to DARWIN are studied, differing in the assumed origin of the main leaks: If the major leaks were around the PMTs, HUsXe's flow would have to be scaled up with the number of PMTs or the area of the PMT arrays growing with $r^2$, in either case. This results in a factor of $\sim 1000$ and constitutes the most pessimistic case. Secondly, the main leaks could have appeared around the electrode support frames. Since enlarging the circumference of these frames from HUsXe to DARWIN scales with $r$, the primary leakage around the support frames would result in an expected leakage flow increase for DARWIN of a factor of $\sim 50$. Finally, the main leak could happen at the LXe valve or the stainless steel vessels containing the liquid level control. Applying the hermetic TPC concept for DARWIN would imply needing not more than one liquid level control and one LXe valve. Under these leak assumptions, the leakage flow would not have to be scaled up at all. Based on the data acquired in this work, it is impossible to distinguish between potential leakage origins. Thus, the following DARWIN radon estimations are shown as a function of leakage flow, highlighting the scaled-up flows of these three scenarios. For further investigations on the leakage flow origins, one could, e.g., change the TPC design. Implementing only one PMT or reducing the number of electrode support frames (thus evaluating the detector's hermeticity using S1 signals only) would help to identify the seals to be improved.

Using HUsXe's hermeticity results to predict DARWIN's radon concentrations involves changing the isotope from $^{83m}$Kr to $^{222}$Rn, which are both expected to homogeneously mix with the xenon target. Even though the more volatile krypton is enriched in the gaseous xenon phase, while the less volatile radon accumulates in the

liquid xenon [269], this is expected to have a minor impact on the final results due to the small mass of the gaseous layer. However, since slightly different contributions affect the concentration in the instrumented volume, a dedicated $^{222}$Rn model describing DARWIN's contamination is introduced here. Similar to the model presented in section 5.5.1, $N_i$ and $M_i$ denote the number of radon atoms and the xenon mass of the inner ($i = 1$) and outer ($i = 2$) volume. Due to $^{222}$Rn's half-life of $\sim 3.8$ days [9], homogeneous radon mixing within the LXe is expected even for a large-size detector such as DARWIN. Figure 5.33 presents the considered $^{222}$Rn contributions in the model. For the terms $-\lambda \cdot N_1$, $-\lambda \cdot N_2$, $\pm f \cdot \frac{N_2}{M_2}$, and $\pm f \cdot \frac{N_1}{M_1}$, the same descriptions as given in section 5.5.1 apply.

- $+k_1$; $+k_2$: Radon is emanated permanently out of surfaces. The terms introduced here describe the emanation rates in the TPC, $k_1$, and in the xenon buffer volume, $k_2$, both including the connected pipes and subsystems outside the cryostat.

- $-f_{rr} \cdot \frac{N_1}{M_1}$: Several experiments have already shown the successful installation of radon removal systems [208, 270]. Therefore, a radon reduction with a speed of $f_{rr}$ is assumed for the inner xenon volume. It is assumed to have a 100% efficiency.

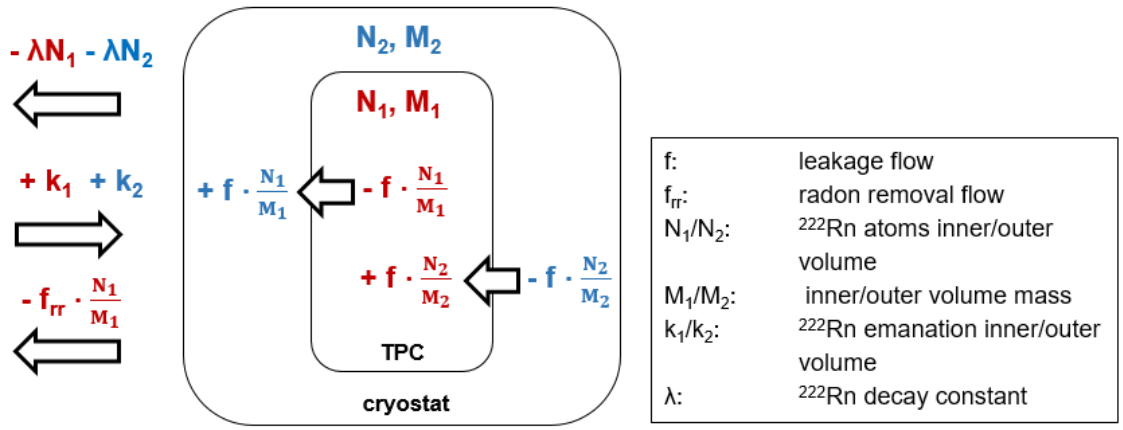


**Figure 5.33:** Scheme describing DARWIN's $^{222}$Rn evolution contributions. The red (blue) terms represent the factors influencing the evolution of the number of radon atoms $N_1$ and $N_2$ in the inner and outer volume, respectively. $k_1$ and $k_2$ describe the radon emanation in the volumes. A radon removal flow $f_{rr}$ is introduced to describe a radon removal system.

The resulting system of two differential equations describes the time evolution of the inner and outer volumes' number of radon atoms, $N_1$ and $N_2$, respectively:

$$\frac{\partial N_1}{\partial t} = -\lambda N_1 - f \cdot \frac{N_1}{M_1} + f \cdot \frac{N_2}{M_2} + k_1 - f_{rr} \cdot \frac{N_1}{M_1} \tag{5.26}$$

$$\frac{\partial N_2}{\partial t} = -\lambda N_2 - f \cdot \frac{N_2}{M_2} + f \cdot \frac{N_1}{M_1} + k_2 \ . \tag{5.27}$$

A crucial result is the radon concentration of the $N_1$ equilibrium level for $t \to \infty$, i.e., with continuous radon emanation, radon leakage into the outer volume, and radon removal:

$$\lim_{t\to\infty} N_1(t) = \frac{k_1 M_1 (f(k_2/k_1 + 1) + \lambda M_2)}{\lambda M_2 (f_{rr} + \lambda M_1) + f(f_{rr} + \lambda(M_1 + M_2))} \ . \tag{5.28}$$

To better understand this solution, three limit behaviors are examined first before studying the general case.

**No leakage and no radon removal:** Assuming a fully hermetic xenon target ($f = 0$) and an inoperative radon removal system ($f_{rr} = 0$), equation (5.28) simplifies to

$$N_1(f = 0, f_{rr} = 0) = \frac{k_1}{\lambda} \ . \tag{5.29}$$

This describes the known relation $N = \frac{A}{\lambda}$ between the number of radon atoms and the corresponding activity, where the activity is given by the emanation rate.

**Infinitely high leakage and no radon removal:** For an infinitely high leakage flow ($f \to \infty$) and an inoperative radon removal system ($f_{rr} = 0$), equation (5.28) reduces to

$$N_1(f \to \infty, f_{rr} = 0) = \frac{k_1 + k_2}{\lambda} \cdot \frac{M_1}{M_1 + M_2} \ . \tag{5.30}$$

Again, the solution characterizes the relation between activity and the total number of atoms in the entire xenon volume. This causes the fraction $M_1/(M_1 + M_2)$ of all radon atoms to be contained in the TPC.

**Infinitely high radon removal:** An infinitely large radon removal flow ($f_{rr} \to \infty$) causes a radon-free xenon target. As expected, equation (5.28) simplifies to

$$N_1(f_{rr} \to \infty) = 0 \ . \tag{5.31}$$

For the general case, a TPC radon emanation rate of $k_1 = 3\,\mathrm{mBq}$, a ten times higher emanation rate in the outer xenon volume, $k_2 = 30\,\mathrm{mBq}$, as well as a radon removal speed of $f_{rr} = 1000\,\mathrm{SLM} \approx 360\,\mathrm{kg/h}$ are assumed as default parameters, based on [201]. An $\sim 10$ times higher emanation in the outer volume than in the inner volume is expected due to the larger surfaces and less radio-pure materials, such as cables. Figure 5.34 shows the specific radon activity in the DARWIN TPC for varying leakage flows. Very high leakage flows, representing the case of a classical, non-hermetic TPC, yield a radon activity of more than $0.3\,\mu\mathrm{Bq/kg}$ - more than a factor of 3 higher than DARWIN's radon goal of $0.1\,\mu\mathrm{Bq/kg}$ [7]. In contrast, very low leakage flows, describing a hermetically sealed TPC, cause radon contaminations of $< 0.05\,\mu\mathrm{Bq/kg}$. This illustrates DARWIN's very challenging radon goal but also the great possibilities by realizing a hermetic TPC. Note that even a semi-hermetic TPC would significantly impact the final result: a TPC with a leakage flow of $f = 50 \cdot f_{\mathrm{HUsXe}}$ (orange line) causes a $^{222}$Rn reduction of approximately a factor of 6 compared to the non-sealed design and outperforms the radon goal. Obtaining

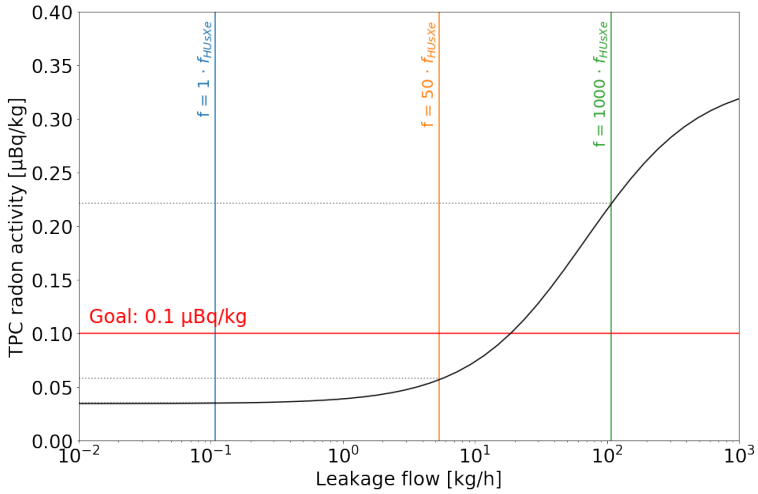


**Figure 5.34:** DARWIN predicted specific $^{222}$Rn activity depending on the leakage flow of a (semi-)hermetic TPC. Non-hermetic detectors, indicated by a high leakage flow, result in a radon activity of $> 3$ times the DARWIN goal. In contrast, a hermetically sealed TPC achieves a radon concentration below the design goal. The shown curve assumes a 3 mBq radon emanation rate in the TPC, a 1:10 emanation ratio between inner and outer volume, and a radon removal speed of 1000 SLM. The three vertical lines indicate the three tightness scenarios depending on the leakage origin, see text for details.

such a leakage flow is not unrealistic, as demonstrated by HUsXe and the suggestions of tightness improvements mentioned in section 5.5.1. Even a TPC with a 2-3 times higher leakage than the orange case would still lead to a significant radon reduction. Moreover, figure 5.34 shows that the (semi-)hermetic TPC concept must be applied to reach the goal if no significant improvement of other radon reduction techniques can be achieved.

The results shown in figure 5.34 depend on the parameter assumptions, which describe the performance of other radon mitigation techniques: the TPC emanation rates represent the influence of material selection and surface treatment, the radon removal speed describes the effect of radon distillation systems. To study their impact on the achievable radon activity, the parameters are varied separately, as presented in figure 5.35.

Figure 5.35 (a) shows the specific radon activity for four different TPC radon emanation rates $k_1$, fixing the radon removal speed to 1000 SLM and the ten times higher emanation of the outer volume $k_2 = 10 \cdot k_1$. Again, each model reaches radon concentrations below the DARWIN goal when assuming a hermetically tight TPC, while a classical TPC design ends up with too much contamination for each assumption. The scenario assuming $k_1 = 1$ mBq is very optimistic since an $\mathcal{O}(1\,\text{mBq})$ emanation rate is already expected by DARWIN's electrodes [201]. Changing emanation ratios between the inner and outer volume are shown in (b) with a fixed radon removal flow of 1000 SLM and a radon emanation rate of $k_1 = 3$ mBq. Similar to (a), even the most optimistic assumption, here $k_2 = 5 \cdot k_1$, leads to radon activities above the DARWIN goal for classical, non-hermetic TPCs. Figure 5.35 (c) presents

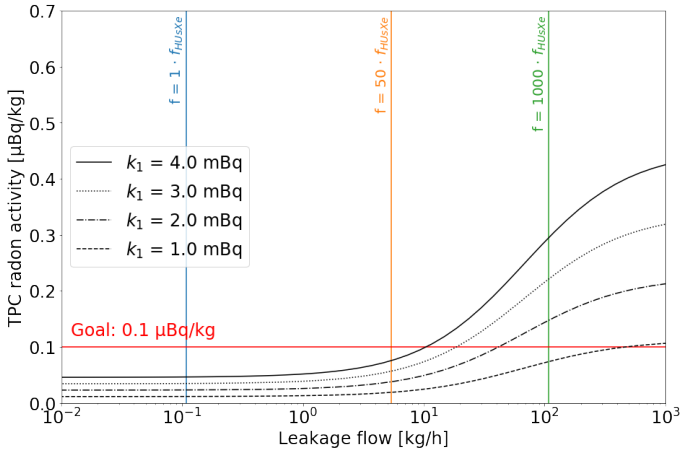


(a) Varying TPC emanation.

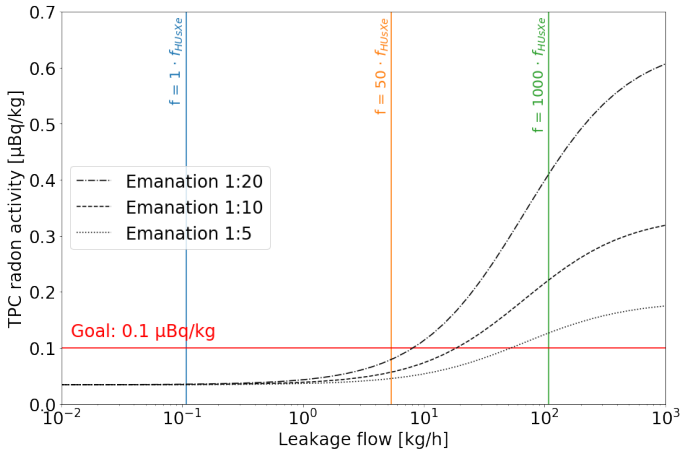


(b) Varying emanation ratio.

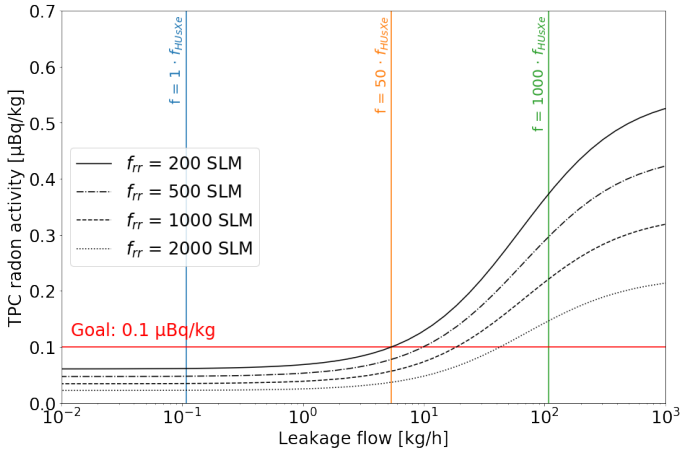


(c) Varying radon removal flow.

**Figure 5.35:** Impact of the variation of the parameters describing DARWIN's expected radon activity. Each plot presents the expected specific $^{222}$Rn activity for DARWIN. (a) varies the impact of the $^{222}$Rn emanation in the TPC, (b) different emanation ratios between inner and outer volume, keeping $k_1 = 3\,\mathrm{mBq}$, (c) varies the impact of different radon removal speeds. In general, all diagrams show the great impact of a hermetic TPC.

several radon removal speeds assuming $k_1 = 3\,\mathrm{mBq}$ and $k_2 = 10 \cdot k_1$. With a classical TPC design even a purification flow of 2000 SLM would not be sufficiently high to reach DARWIN's radon goal: $f_{rr} \sim 6000\,\mathrm{SLM}$ would be required, corresponding to purifying the entire xenon target within $\sim 25\,\mathrm{h}$. The radon removal speed $f_{rr}$ scales linearly in power consumption, resulting in a very cost-intensive radon mitigation technique. Again, a semi-hermetic concept with $f = 50 \cdot f_{\mathrm{HUsXe}}$ would allow reaching the DARWIN design goal with relatively modest flows $f_{rr}$.

To summarize, the shown DARWIN $^{222}$Rn activities are presented for different scenarios based on different assumptions. All studied scenarios show too large radon activities for fully non-hermetic TPC designs. Even with optimistic assumptions on the radon removal speed and the material coating/selection, the DARWIN goal of 0.1 $\mu$Bq/kg goal cannot be achieved. The presented results emphasize the need for a (semi-)hermetic TPC design. The scaled-up HUsXe results give guidance to the obtainable radon concentrations: even a 100 times larger leakage flow than the one achieved in the small-scale TPC would significantly impact DARWIN's specific radon activity. Addressing the challenge of sealing all components of a DARWIN detector is beyond the scope of this work. We highlight that the large amount of PTFE used for sealing would imply the need for a low-activity PTFE material, such as used for the EXO-200 detector [99]. Beyond the emphasis of applying a (semi-)hermetic TPC concept for DARWIN, the findings presented here yield insights into the impact of the individual radon reduction techniques, being a valuable input towards building the ultimate dark matter detector.

# Chapter 6

# Summary

Many experiments have been developed or planned in the last years with the primary goal of detecting dark matter. Among them there are several experiments employing a liquid xenon-filled time projection chamber (TPC), such as the proposed next-generation DARWIN experiment, which aim to directly detect weakly-interacting massive particles (WIMPs). With its large target mass, ultra-low background, and low energy threshold, DARWIN will also be sensitive to other rare processes beyond dark matter. This thesis was dedicated to the study of several DARWIN science channels and their background budget, as well as the investigation of a possible $^{222}$Rn reduction technique: the hermetic TPC.

As shown in [142], DARWIN, with its 40 t active liquid xenon target, will yield spin-independent WIMP-nucleon cross-sections of down to $\sim 10^{-49}\,\mathrm{cm}^2$. This requires the expected nuclear recoil background to be dominated by irreducible coherent elastic neutrino-nucleus scattering (CE$\nu$NS) events. The investigation of other reducible nuclear recoil sources - radiogenic and cosmogenic neutrons - in this thesis (see sections 4.2.2 and 4.3) yield the following strong suggestions towards building the DARWIN detector: Even though a first optimization study identified a low-background [176] titanium cryostat and hoop stiffening rings to minimize its wall thickness as the favorable option compared to stainless steel designs, it still constitutes the largest radiogenic neutron source. A further background reduction is necessary and could be feasible by follow-up optimization studies and an intense titanium material screening campaign, or by stronger target fiducialization what, however, will cause longer measurement times to achieve a certain exposure. Additionally, the need for implementing photomultiplier tubes (PMTs) and polytetrafluoroethylene (PTFE) components with contaminations lower than the ones installed in the XENON1T detector [175, 168] was shown. Assuming the low-background PTFE used by EXO-200 [99] and an improved PMT design with a ceramic mass decrease by a factor of five [185] would already suffice to reduce their backgrounds to a subdominant contribution. Combining these measures with a further cryostat background reduction by a factor of two would result in a total radiogenic neutron-induced background of $\mathcal{O}(10\%)$ of the CE$\nu$NS rate. The installation of a water shield with the minimal dimensions of $\varnothing\,12\,\mathrm{m} \times 12\,\mathrm{m}$ is required to reduce the background contribution of cosmogenic neutrons to $< 6\%$ of the CE$\nu$NS rate, assuming

the rock overburden of Laboratori Nazionali del Gran Sasso (LNGS). Employing the ø 18 m × 18 m water tank from Borexino would reduce the expected background to a negligible level. These findings thus show that LNGS can be a possible location for DARWIN's search for WIMPs.

However, the investigation of DARWIN's sensitivity to the neutrinoless double beta decay ($0\nu\beta\beta$) of $^{136}$Xe (see section 4.4) indicated that cosmogenic neutrons, which can be captured by $^{136}$Xe atoms and produce the $\beta$-decaying isotope $^{137}$Xe, could be a limiting factor for the $0\nu\beta\beta$ search at LNGS. For a baseline scenario, which assumes material activities measured by XENON1T and LZ and yields a sensitivity limit of $T^{0\nu}_{1/2} > 2.4 \cdot 10^{27}$ yr (90% C.L.) [10], materials contribute with 40% more events than $^{137}$Xe. However, this changes when assuming cleaner materials, as required for the WIMP search. The half-life limit of the material-dominated baseline scenario translates to an effective neutrino Majorana mass limit $m_{\beta\beta} = [18\text{-}46]$ meV. The ultimate scenario, which is described by an irreducible neutrino-dominated background and includes reducing other cosmogenic, material-induced, and xenon-intrinsic backgrounds, would yield $m_{\beta\beta} = [11\text{-}28]$ meV. This would cover the parameter space of the inverted neutrino ordering and thus could allow concluding on the neutrino mass ordering. In general, the predicted results for both the baseline and neutrino-dominated scenario indicate that DARWIN, whose primary science goal is the dark matter search, will reach sensitivities approaching those of dedicated tonne-scale future $0\nu\beta\beta$ experiments [86, 87]. In contrast to these experiments, DARWIN's target will not be isotopically enriched in its double beta-decaying isotope $^{136}$Xe.

A similar process providing information about the nature of the neutrino is the neutrinoless double electron capture ($0\nu$ECEC) of $^{124}$Xe. A first study presented in this work (see section 4.5), which investigates the new multiple scatter analysis technique and assumes the baseline material scenario, yields a sensitivity limit of $T^{0\nu}_{1/2} > 3.7 \cdot 10^{25}$ yr (90% C.L.). Improved sensitivities of $\mathcal{O}(10^{26}\,\text{yr})$ could be achieved by optimizing the signal tagging algorithm and by improving xenon-intrinsic and material contaminations. This is currently addressed in a follow-up study. However, this science channel will be limited in its sensitivity by the low natural abundance of $^{124}$Xe of only 0.09% [9] and thus will not be competitive with the search for $0\nu\beta\beta$ of $^{136}$Xe in terms of limits on $m_{\beta\beta}$. Nevertheless, the (unexpected) discovery of the $0\nu$ECEC could provide complementary information in determining the mechanism of lepton number violation [105].

Due to its low background and large target mass, DARWIN will also be able to detect five types of different solar neutrinos by elastic $\nu$-electron scatterings: *pp*, $^{7}$Be, $^{13}$N, $^{15}$O, and *pep* neutrinos [11], as presented in section 4.6. Even though their expected spectra will be shadowed by the two-neutrino double beta decay ($2\nu\beta\beta$) of $^{136}$Xe, which can only be reduced by isotopic depletion (which is detrimental to DARWIN's $0\nu\beta\beta$ sensitivity), the fluxes of the *pp* and $^{7}$Be neutrinos will be measured with high precision, exceeding the most precise measurements to date by a factor of 50 and 15, respectively [114, 200]. With its 0.15% precision after an experi-

ment run time of 10 yr, the *pp* neutrino flux can be used to calculate the electroweak mixing angle $\sin^2\theta_w$ and the $\nu_e$ survival probability $P_{ee}$ with uncertainties of 5.1% and 4.0%, respectively, in a previously non-measured energy range of $< 200$ keV.

A xenon-intrinsic $^{222}$Rn contamination of 0.1 $\mu$Bq/kg was assumed for all science channels investigated in this thesis, as this is a requirement defined by DARWIN's search for WIMPs ($^{222}$Rn background $\leq$ 10% of irreducible background from *pp* and $^{7}$Be neutrinos) [7]. To achieve this specific activity is one of the most challenging tasks towards realizing DARWIN and will only be feasible by combining several radon reduction techniques. In this work the concept of a hermetic TPC was investigated by building, operating, and analyzing the small-scale Hermetically Used Xenon TPC (HUsXe), see chapter 5. The instrumented liquid xenon target was mechanically separated from the xenon in contact with the rest of the detector materials. The sealing relied on the concept of cryofitting, which employs the different thermal expansion coefficients of the TPC materials. Due to the separation of the two xenon volumes, HUsXe was partially operated by two independent xenon supply and purification systems, which is to date a unique technique in the liquid xenon community. However, their simultaneous operation induced periodic pressure build-ups and liquid level changes of several millimeters (see section 5.3), which can be improved in the future by using independent cooling systems for both xenon volumes. Nevertheless, the operation of a single gas system purifying the liquid xenon target provided stable conditions and allowed for in-depth investigations of the detector performance.

Since HUsXe is a fully-functional TPC, its performance was examined in section 5.4 by characterizing the detector response using the meta-stable isotope $^{83m}$Kr as a calibration source. The detector-inherent gains $g1 = (0.089 \pm 0.004)$ PE/$\gamma$ and $g2 = (7.1 \pm 0.7)$ PE/$e^-$ were derived, indicating a good performance comparable to other small-scale TPCs. Furthermore, field-dependent liquid xenon properties, the electron drift velocity and longitudinal diffusion, were determined and agree well with data from other small- and large-scale experiments.

The hermeticity of HUsXe, which describes the level of its tightness, was determined in section 5.5 by filling the liquid xenon target with $^{83m}$Kr and recording the number of krypton decays over time. In addition to the exponential decay, a further decrease is expected due to $^{83m}$Kr atoms leaking to the outer xenon volume. The investigation yielded a leakage flow $f = (0.11 \pm 0.01)$ kg/h between the two separated xenon volumes; possibilities for improvements were discussed in section 5.5.1. This result was applied to a DARWIN-size TPC assuming different origins for mass leakage. It was used to give guidance to achievable DARWIN $^{222}$Rn activities, see section 5.5.2. Different performance scenarios for other radon reduction methods (material selection, surface coating, radon removal in distillation columns) were included in the study, which indicates that, for non-hermetic TPC designs, only very progressive assumptions on their performance would lead to $^{222}$Rn concentrations $< 0.1\,\mu$Bq/kg. A hermetic TPC notably reduces this activity: even a leakage flow 100 times larger than the one achieved in HUsXe would already result in a signifi-

cant $^{222}$Rn reduction. Besides the strong emphasis of designing a hermetic TPC for DARWIN, these calculations give valuable insights into the performance of individual radon reduction possibilities. Addressing the challenges of sealing the TPC components of a DARWIN-size hermetic detector is subject of future studies, which could be investigated at the DARWIN full-diameter or full-drift length detector test platforms PANCAKE and Xenoscope [149], respectively.

To summarize, this work investigated some of the many interesting challenges towards building the DARWIN detector. The shown sensitivity studies indicate the great possibilities of the next-generation DARWIN observatory, which could give important insights about the matter content in the Universe and the nature of the neutrino, and could thus provide the first proof for physics beyond the standard model. In order to build, construct, and operate such a next-generation dark matter detector, the XENON/DARWIN and LUX-ZEPLIN (LZ) collaborations have joint forces in 2021. Over the last two decades, experiments developed by these collaborations using liquid xenon targets have delivered world-leading results in the field of direct dark matter detection. The next-generation detector, whose physics objectives are discussed in detail in [141], aims to continue this pursuit by combining the most successful technologies, including those developed by the current-generation detectors XENONnT and LZ with the primary goal of exploring the experimentally accessible parameter space for spin-independent WIMP-nucleon interactions.

# Abbreviations

**0$\nu\beta\beta$** neutrinoless double beta decay

**0$\nu$ECEC** neutrinoless double electron capture

**2$\nu\beta\beta$** two-neutrino double beta decay

**2$\nu$ECEC** two-neutrino double electron capture

**ADC** analog-to-digital converter

**ALP** axion-like particles

**CE** collection efficiency

**CES** combined energy scale

**CE$\nu$NS** coherent elastic neutrino-nucleus scattering

**C.L.** confidence level

**CMB** cosmic microwave background

**CNO** carbon–nitrogen–oxygen

**CP** charge parity

**CY** charge yield

**DAQ** data acquisition

**DARWIN** DARk matter WImp search with liquid xenoN

**DM** dark matter

**DPE** double photoelectron

**DSN** diffuse supernova

**ER** electronic recoil

**FWHM** full width at half maximum

**GXe** gaseous xenon

**HUsXe** Hermetically Used Xenon TPC

**HV** high voltage

**IO** inverted ordering

**LCE** light collection efficiency

**$LN_2$** liquid nitrogen

**LNGS** Laboratori Nazionali del Gran Sasso

**LXe** liquid xenon

**LY** light yield

**MC** Monte Carlo

**MM** mass-mixing

**MS** multiple scatter

**m.w.e.** meter water-equivalent

**NEST** Noble Element Simulation Technique

**NO** normal ordering

**NR** nuclear recoil

**PE** photoelectron

**PEEK** polyetheretherketone

**PMNS** Pontecorvo-Maki-Nakagawa-Sakata

**PMT** photomultiplier tube

**PTFE** polytetrafluoroethylene

**QE** quantum efficiency

**RHC** right-handed current

**ROI** region of interest

**SD** spin-dependent

**SI** spin-independent

**SiPM** silicon photomultiplier

**SLM** standard liters per minute

**SM** standard model

**SPE** single photoelectron

**SS** single scatter

**TPC** time projection chamber

**TPE** triple photoelectron

**UA** under-amplified

**VUV** vacuum ultra-violet

**WIMP** weakly interacting massive particle

**XeBRA** Xenon-Based Research Apparatus

# Bibliography


[1] N. Aghanim et al. (Planck Collaboration): *Planck 2018 results. VI. Cosmological parameters*, *Astronomy & Astrophysics* 641, 6 (2020).

[2] J. Billard et al.: *Direct detection of dark matter - APPEC Committee report* (2021), arXiv: 2104.07634.

[3] E. Aprile et al. (XENON Collaboration): *Dark matter search results from a one tonne × year exposure of XENON1T*, *Phys. Rev. Lett.* 121, 111302 (2018).

[4] E. Aprile et al. (XENON Collaboration): *Projected WIMP sensitivity of the XENONnT dark matter experiment*, *JCAP* 11, 031 (2020).

[5] D.S. Akerib et al. (LUX-ZEPLIN Collaboration): *The LUX-ZEPLIN (LZ) experiment*, *Nucl. Instr. Meth. A* 953, 163047 (2020).

[6] Y. Meng et al. (PandaX-4T Collaboration): *Dark matter search results from the PandaX-4T commissioning run* (2021), arXiv: 2107.13438.

[7] J. Aalbers et al. (DARWIN Collaboration): *DARWIN: towards the ultimate dark matter detector*, *JCAP* 1611, 017 (2016).

[8] J. Billard et al.: *Implication of neutrino backgrounds on the reach of next generation dark matter direct detection experiments*, *Phys. Rev. D* 89, 023524 (2014).

[9] International Atomic Energy Agency - Nuclear Data Section: *Live Charts of Nuclids*, `https://www-nds.iaea.org/relnsd/vcharthtml/VChartHTML.html`, accessed: 2 October, 2021.

[10] F. Agostini et al. (DARWIN Collaboration): *Sensitivity of the DARWIN observatory to the neutrinoless double beta decay of* $^{136}Xe$, *Eur. Phys. J. C* 80, 808 (2020).

[11] J. Aalbers et al. (DARWIN Collaboration): *Solar neutrino detection sensitivity in DARWIN via electron scattering*, *Eur. Phys. J. C* 80, 1133 (2020).

[12] F. Kuger et al.: *Prospects of charge signal analyses in liquid xenon TPCs with proportional scintillation in the liquid phase* (2021), arXiv: 2112.11844.

[13] F. Zwicky et al.: *Die Rotverschiebung von extragalaktischen Nebeln*, *Helvetica Physica Acta* 6, 110 (1933).

[14] C.L. Cowan et al: *Detection of the free neutrino: a confirmation*, *Science* 124, 3212 (1956).

[15] K. Freese: *Review of observational evidence for dark matter in the Universe and in upcoming searches for dark stars*, *EAS Publications Series* 36, 113 (2009).

[16] V.C. Rubin et al.: *Rotation velocities of 16 Sa galaxies and a comparison of Sa, Sb and Sc rotation properties*, *Astrophysical Journal* 289, 81 (1985).

[17] A. Bosma: *21-cm line studies of spiral galaxies*, *Astronomical Journal* 86, 1825 (1981).

[18] K.G. Begeman et al.: *Extended rotation curves of spiral galaxies: dark haloes and modified dynamics*, *Mon. Not. R. Astr. Soc.* 249, 523 (1990).

[19] D. Clowe et al.: *A direct empirical proof of the existence of dark matter*, *Astrophysical Journal* 648, 109 (2006).

[20] A. Einstein: *Lens-like action of a star by the deviation of light in the gravitational field*, *Science* 84, 506 (1936).

[21] F. Kahlhoefer et al.: *Colliding clusters and dark matter self-interactions*, *Monthly Notices of the Royal Astronomical Society* 437, 2865 (2013).

[22] A.N. Taylor et al.: *Gravitational lens magnification and the mass of Abell 1689*, *Astrophysical Journal* 501, 539 (1998).

[23] J. Merten et al.: *Creation of cosmic structure in the complex galaxy cluster merger Abell 2744*, *Monthly Notices of the Royal Astronomical Society* 417, 333 (2011).

[24] M. Milgrom: *Dynamics with a nonstandard inertia-acceleration relation: an alternative to dark matter in galactic systems*, *Annals of Physics* 229, 384871 (1994).

[25] A.A. Penzias & R.W. Wilson: *A measurement of excess antenna temperature at 4080 Mc/s*, *Astrophysical Journal* 142, 419 (1965).

[26] D. Fixsen: *The temperature of the Cosmic Microwave Background*, *Astrophysical Journal* 707, 916 (2009).

[27] M. Safarzadeh & D.N. Spergel: *Ultra-light dark matter is incompatible with the Milky Way's dwarf satellites*, *Astrophysical Journal* 893, 21 (2020).

[28] G. Bertone et al.: *Particle dark matter*, Cambridge University Press, 2010.

[29] B. Audren et al.: *Strongest model-independent bound on the lifetime of dark matter*, *JCAP* 12, 028 (2014).

[30] T. Marrodan Undagoitia & L. Rauch: *Dark matter direct-detection experiments*, *J. Phys. G* 43, 013001 (2016).

[31] G. Jungman et al.: *Supersymmetric dark matter*, *Physics Report* 267, 195 (1996).

[32] G. Arcadi et al.: *The waning of the WIMP? A review of models, searches, and constraints*, *Eur. Phys. J. C* 78, 203 (2018).

[33] G. Steigman et al.: *Precise relic WIMP abundance and its impact on searches for dark matter annihilation*, *Phys. Rev. D* 86, 023506 (2012).

[34] G. Kane & S. Watson: *Dark matter and LHC: what is the connection?*, *Mod. Phys. Lett. A* 23, 2103 (2008).

[35] F. Kahlhoefer: *Review of LHC dark matter searches*, *Int. J. Mod. Phys. A* 32, 1730006 (2017).

[36] C. Pérez de los Heros: *Status, challenges and directions in indirect dark matter searches*, *Symmetry* 12, 1648 (2020).

[37] A. Ibarra et al.: *Indirect searches for decaying dark matter*, *International Journal of Modern Physics A* 28, 1330040 (2013).

[38] O. Adriani et al.: *Observation of an anomalous positron abundance in the cosmic radiation*, *Nature* 458, 607 (2009).

[39] M. Aguilar et al. (AMS Collaboration): *First result from the Alpha Magnetic Spectrometer on the International Space Station: precision measurement of the positron fraction in primary cosmic rays of 0.5–350 GeV*, *Phys. Rev. Lett.* 110, 141102 (2013).

[40] K. Blum et al.: *AMS02 results support the secondary origin of cosmic ray positrons*, *Phys. Rev. Lett.* 111, 211101 (2013).

[41] H. Abdallah et al. (H.E.S.S. Collaboration): *Search for dark matter annihilations towards the inner galactic halo from 10 years of observations with H.E.S.S.*, *Phys. Rev. Lett.* 117, 111301 (2016).

[42] M.L. Ahnen et al. (MAGIC Collaboration): *Indirect dark matter searches in the dwarf satellite galaxy Ursa Major II with the MAGIC telescopes*, *JCAP* 03, 009 (2018).

[43] S. Archambault et al. (VERITAS Collaboration): *Dark matter constraints from a joint analysis of dwarf spheroidal galaxy observations with VERITAS*, *Phys. Rev. D* 95, 082001 (2017).

[44] M. Ackermann et al. (Fermi-LAT Collaboration): *Search for gamma-ray spectral lines with the Fermi Large Area Telescope and dark matter implications*, *Phys. Rev. D* 88, 082002 (2013).

[45] M.G. Aartsen et al. (IceCube Collaboration): *Search for annihilating dark matter in the Sun with 3 years of IceCube data*, *Eur. Phys. J. C* 77, 146 (2017).

[46] K. Choi et al. (Super-Kamiokande Collaboration): *Search for neutrinos from annihilation of captured low-mass dark matter particles in the Sun by Super-Kamiokande*, *Phys. Rev. Lett.* 114, 141301 (2015).

[47] J. Conrad & O. Reimer: *Indirect dark matter searches in gamma- and cosmic rays*, *Nature Physics* 13, 224 (2017).

[48] J.D. Lewin & P.F. Smith: *Review of mathematics, numerical factors, and corrections for dark matter experiments based on elastic nuclear recoil*, *Astroparticle Physics* 6, 1 (1996).

[49] M. Schumann: *Direct detection of WIMP dark matter: concepts and status*, *J. Phys. G* 46, 103003 (2019).

[50] A.M. Green: *Astrophysical uncertainties on the local dark matter distribution and direct detection experiments*, *J. Phys. G* 44, 084001 (2017).

[51] M.C. Smith et al.: *The RAVE survey: constraining the local galactic escape speed*, *Monthly Notices of the Royal Astronomical Society* 379, 755 (2007).

[52] K. Freese et al.: *Colloquium: annual modulation of dark matter*, *Rev. Mod. Phys.* 85, 1561 (2013).

[53] D.N. Spergel: *The motion of the Earth and the detection of weakly interacting massive particles*, *Phys. Rev. D* 37, 1353 (1988).

[54] R.H. Helm: *Inelastic and elastic scattering of 187-MeV electrons from selected even-even nuclei*, *Phys. Rev.* 104, 1466 (1956).

[55] P. Klos et al.: *Large-scale nuclear structure calculations for spin-dependent WIMP scattering with chiral effective field theory currents*, *Phys. Rev. D* 88, 083516 (2013).

[56] C. Capelli: *Search for dark matter and neutrinoless double beta decay in XENON1T and calibration of the photosensors in XENONnT*, PhD thesis, Universität Zürich, 2020.

[57] K. Abe et al. (XMASS Collaboration): *A direct dark matter search in XMASS-I*, *Phys. Lett. B* 789, 45 (2019).

[58] P.-A. Amaudruz et al. (DEAP Collaboration): *DEAP-3600 dark matter search*, *Nuclear and Particle Physics Proceedings* 273, 340 (2016).

[59] K. Ueshima et al. (XMASS Collaboration): *Scintillation-only based pulse shape discrimination for nuclear and electron recoils in liquid xenon*, *Nucl. Instr. Meth. A* 659, 161 (2011).

[60] D.S. Akerib et al. (LUX-ZEPLIN Collaboration): *Results from a search for dark matter in the complete LUX exposure*, *Phys. Rev. Lett.* 118, 021303 (2017).

[61] X. Cui et al. (PandaX-II Collaboration): *Dark matter results from 54-ton-day exposure of PandaX-II experiment*, *Phys. Rev. Lett.* 119, 181302 (2017).

[62] P. Agnes et al. (DarkSide Collaboration): *DarkSide-50 532-day dark matter search with low-radioactivity argon*, *Phys. Rev. D* 98, 102006 (2018).

[63] E. Armengaud et al. (EDELWEISS Collaboration): *Constraints on low-mass WIMPs from the EDELWEISS-III dark matter search*, *JCAP* 05, 019 (2016).

[64] R. Agnes et al. (SuperCDMS Collaboration): *Results from the Super Cryogenic Dark Matter Search (SuperCDMS) experiment at Soudan*, *Phys. Rev. Lett.* 120, 061802 (2018).

[65] A.H. Abdelhameed et al. (CRESST Collaboration): *First results from the CRESST-III low-mass dark matter program*, *Phys. Rev. D* 100, 102002 (2019).

[66] A. Aguilar-Arevalo et al.: *The DAMIC dark matter experiment* (2015), arXiv: 1510.02126.

[67] C. Amole et al. (PICO Collaboration): *Dark matter search results from the PICO-60 $C_3F_8$ bubble chamber*, *Phys. Rev. Lett.* 118, 251301 (2017).

[68] R. Bernabei et al. (DAMA Collaboration): *First results from DAMA/LIBRA and the combined results with DAMA/NaI*, *Eur. Phys. J. C* 56, 333 (2008).

[69] J. Amare et al.: *Annual modulation results from three-year exposure of ANAIS-112*, *Phys. Rev. D* 103, 102005 (2021).

[70] G. Adhikari et al.: *Strong constraints from COSINE-100 on the DAMA dark matter results using the same sodium iodide target*, *Science Advances* 7, 46 (2021).

[71] G. Danby et al.: *Observation of high-energy neutrino reactions and the existence of two kinds of neutrinos*, *Phys. Rev. Lett.* 9, 36 (1962).

[72] K. Kodama et al. (DONUT Collaboration): *Observation of tau neutrino interactions*, *Phys. Lett. B* 504, 218 (2001).

[73] B. Pontecorvo: *Inverse beta processes and nonconservation of lepton charge*, *Sov. Phys. JETP* 7, 172 (1958).

[74] Y. Fukuda et al. (Super-Kamiokande Collaboration): *Evidence for oscillation of atmospheric neutrinos*, *Phys. Rev. Lett.* 81, 1562 (1998).

[75] Q.R. Ahmad et al. (SNO Collaboration): *Direct evidence for neutrino flavor transformation from neutral-current interactions in the Sudbury Neutrino Observatory*, *Phys. Rev. Lett* 89, 011301 (2002).

[76] R. Davis: *A review of the Homestake solar neutrino experiment*, *Progress in Particle and Nuclear Physics* 32, 13 (1994).

[77] P.F. de Salas et al.: *2020 global reassessment of the neutrino oscillation picture*, *JHEP* 71 (2021).

[78] M. Wurm: *Measuring the neutrino mass ordering in JUNO*, International School of Nuclear Physics, Erice, Italy, 2017.

[79] N. Ackerman et al. (EXO-200 Collaboration): *Observation of two-neutrino double-beta decay in Xe-136 with EXO-200*, *Phys. Rev. Lett.* 107, 212501 (2011).

[80] E. Aprile et al. (XENON Collaboration): *First observation of two-neutrino double electron capture in $^{124}$Xe with XENON1T*, *Nature* 568, 532 (2019).

[81] E. Majorana: *Teoria simmetrica dell'elettrone e del positrone*, *Il Nuovo Cimento* 14, 171 (1937).

[82] S.M. Bilenky & C. Guinti: *Neutrinoless double-beta decay: a probe of physics beyond the Standard Model*, *International Journal of Modern Physics A* 30, 1530001 (2015).

[83] F. del Aguila et al.: *Effective Lagrangian approach to neutrinoless double beta decay and neutrino masses*, *JHEP* 146 (2012).

[84] S. Dell'Oro et al.: *Neutrinoless double beta decay: 2015 review*, *Advances in High Energy Physics* 2162659 (2016).

[85] J. Engel & J. Menéndez: *Status and future of nuclear matrix elements for neutrinoless double beta decay: a review*, *Reports on Progress in Physics* 80, 046301 (2017).

[86] M.J. Dolinski et al.: *Neutrinoless double beta decay: status and prospects*, *Annual Review of Nuclear and Particle Science* 69, 219 (2019).

[87] M. Redshaw et al.: *Mass and double-beta-decay Q Value of* $^{136}$*Xe*, *Phys. Rev. Lett.* 98, 053003 (2007).

[88] S. Umehara et al.: *Neutrino-less double-*$\beta$ *decay of* $^{48}$*Ca studied by* $CaF_2$*(Eu) scintillators*, *Phys. Rev. C* 78, 058501 (2008).

[89] M. Agostini et al. (GERDA Collaboration): *Improved limit on neutrinoless double-*$\beta$ *decay of* $^{76}$*Ge from GERDA Phase II*, *Phys. Rev. Lett.* 120, 132503 (2018).

[90] A.S. Barabash & V.B. Brudanin (NEMO Collaboration): *Investigation of double beta decay with the NEMO-3 detector*, *Physics of Atomic Nuclei* 74, 312 (2011).

[91] J. Argyriades et al.: *Measurement of the two neutrino double beta decay half-life of Zr-96 with the NEMO-3 detector*, *Nucl. Phys. A* 847, 168 (2010).

[92] R. Arnold et al. (NEMO-3 Collaboration): *Results of the search for neutrinoless double-*$\beta$ *decay in* $^{100}$*Mo with the NEMO-3 experiment*, *Phys. Rev. D* 92, 072011 (2015).

[93] A.S. Barabash et al.: *Final results of the Aurora experiment to study* $2\beta$ *decay of* $^{116}$*Cd with enriched* $^{116}CdWO_4$ *crystal scintillators*, *Phys. Rev. D* 98, 092007 (2018).

[94] A. Giachero et al.: *New results from the CUORE experiment*, ICHEP, Prague, 2020.

[95] A. Gando et al. (KamLAND-Zen Collaboration): *Search for Majorana neutrinos near the inverted mass hierarchy region with KamLAND-Zen*, *Phys. Rev. Lett.* 117, 082503 (2016).

[96] R. Arnold et al. (NEMO-3 Collaboration): *Measurement of the* $2\nu\beta\beta$ *decay half-life of* $^{150}$*Nd and a search for* $0\nu\beta\beta$ *decay processes with the full exposure from the NEMO-3 detector*, *Phys. Rev. D* 94, 072003 (2016).

[97] F.T. Avignone et al.: *Next generation double-beta decay experiments: metrics for their evaluation*, *New J. Phys.* 7, 6 (2005).

[98] O. Cremonesi & M. Pavan: *Challenges in double beta decay*, *Advances in High Energy Physics* 951432 (2014).

[99] M. Auger et al. (EXO-200 Collaboration): *The EXO-200 detector, part I: detector design and construction*, *JINST* 7, 05010 (2012).

[100] N. Abgrall et al. (LEGEND Collaboration): *LEGEND-1000 preconceptual design report* (2021), arXiv: 2107.11462.

[101] J.B. Albert et al. (nEXO Collaboration): *Sensitivity and discovery potential of the proposed nEXO experiment to neutrinoless double beta decay*, *Phys. Rev. C* 97, 065503 (2018).

[102] A. Giuliani et al.: *Double beta decay APPEC Committee report* (2019), arXiv: 1910.04688.

[103] M. Doi & T. Kotani: *Neutrinoless modes of double beta decay*, *Progress of Theoretical Physics* 89, 139 (1993).

[104] D.A. Nesterenko et al.: *Double-$\beta$ transformations in isobaric triplets with mass numbers $A = 124, 130$, and 136*, *Phys. Rev. C* 86, 044313 (2012).

[105] C. Wittweg et al.: *Detection prospects for the second-order weak decays of $^{124}Xe$ in multi-tonne xenon time projection chambers*, *Eur. Phys. J. C* 80, 1161 (2020).

[106] J. Kotila et al.: *Neutrinoless double electron capture*, *Phys. Rev. C* 89, 064319 (2014).

[107] J. Katakura & Z.D. Wu: *Nuclear data sheets for $A = 124$*, *Nuclear data sheets* 109, 1655 (2008).

[108] J. Newstead et al.: *Atmospheric neutrinos in a next-generation xenon dark matter experiment* (2020), arXiv: 2002.08566.

[109] R.F. Lang et al.: *Supernova neutrino physics with xenon dark matter detectors: a timely perspective*, *Phys. Rev. D* 94, 103009 (2016).

[110] G. Settanta et al. (Borexino Collaboration): *First detection of CNO neutrinos with Borexino* (2021), arXiv: 2105.09211.

[111] D. Akimov et al. (COHERENT Collaboration): *Observation of coherent elastic neutrino-nucleus scattering*, *Science* 357, 1123 (2017).

[112] G. Bellini et al. (Borexino Collaboration): *Neutrinos from the primary proton–proton fusion process in the Sun*, *Nature* 512, 383 (2014).

[113] G. Bellini et al. (Borexino Collaboration): *First evidence of pep solar neutrinos by direct detection in Borexino*, *Phys. Rev. Lett.* 108, 051302 (2012).

[114] G. Bellini et al. (Borexino Collaboration): *Precision measurement of the $^7Be$ solar neutrino interaction rate in Borexino*, *Phys. Rev. Lett.* 107, 141302 (2011).

[115] M. Agostini et al. (Borexino Collaboration): *Improved measurements of $^8B$ solar neutrinos with 1.5 kt $\times$ y of Borexino exposure*, *Phys. Rev. D* 101, 062001 (2020).

[116] B. Aharmim et al. (SNO Collaboration): *Combined analysis of all three phases of solar neutrino data from the Sudbury Neutrino Observatory*, *Phys. Rev. C* 88, 025501 (2013).

[117] M. Anderson et al. (SNO+ Collaboration): *Measurement of the $^8B$ solar neutrino flux in SNO+ with very low backgrounds*, *Phys. Rev. D* 99, 012012 (2019).

[118] S. Abe et al. (KamLAND Collaboration): *Measurement of the $^8B$ neutrino flux with the KamLAND liquid scintillator detector*, *Phys. Rev. C* 84, 035804 (2011).

[119] K. Abe et al. (Super-Kamiokande Collaboration): *Solar neutrino results in Super-Kamiokande-III*, *Phys. Rev. D* 83, 052010 (2011).

[120] A. Serenelli: *Alive and well: a short review about standard solar models*, *Eur. Phys. J. A* 52, 78 (2016).

[121] E. Aprile et al. (XENON Collaboration): *The XENON dark matter search experiment*, *New Astronomy Reviews* 49, 2 (2005).

[122] J. Angle et al. (XENON Collaboration): *First results from the XENON10 dark matter experiment at the Gran Sasso National Laboratory*, *Phys. Rev. Lett.* 100, 021303 (2008).

[123] E. Aprile et al. (XENON Collaboration): *XENON100 dark matter results from a combination of 477 live days*, *Phys. Rev. D* 94, 122001 (2016).

[124] D.Y. Akimov et al.: *WIMP-nucleon cross-section results from the second science run of ZEPLIN-III*, *Phys. Lett. B* 709, 1 (2012).

[125] E. Aprile & T. Doke: *Liquid xenon detectors for particle physics and astrophysics*, *Rev. Mod. Phys.* 82, 2053 (2010).

[126] J.B. Albert et al. (EXO-200 Collaboration): *An improved measurement of the $2\nu\beta\beta$ half-life of Xe-136 with EXO-200*, *Phys. Rev. C* 89, 015502 (2014).

[127] F.V. Massoli: *The XENON1T experiment: Monte Carlo background estimation and sensitivity curves study*, PhD thesis, Università di Bologna, 2015.

[128] Air Liquide: *Xenon: physical properties*, `https://encyclopedia.airliquide.com/xenon`, accessed: 21 October, 2021.

[129] V.C. Antochi et al.: *Improved quality tests of R11410-21 photomultiplier tubes for the XENONnT experiment*, *JINST* 16, 08033 (2021).

[130] E. Aprile et al. (XENON Collaboration): *XENON1T dark matter data analysis: signal & background models, and statistical inference*, *Phys. Rev. D* 99, 112009 (2019).

[131] D.S. Akerib et al. (LUX Collaboration): *First results from the LUX dark matter experiment at the Sanford underground research facility*, *Phys. Rev. Lett.* 112, 650 (2014).

[132] J. Mock et al.: *Modeling pulse characteristics in xenon with NEST*, *JINST* 9, 04002 (2014).

[133] K. Fujii et al.: *High-accuracy measurement of the emission spectrum of liquid xenon in the vacuum ultraviolet region*, *Nucl. Instr. Meth. A* 795, 293 (2015).

[134] P.-A. Amaudruz et al. (DEAP Collaboration): *Measurement of the scintillation time spectra and pulse-shape discrimination of low-energy $\beta$ and nuclear recoils in liquid argon with DEAP-1*, *Astroparticle Physics* 85, 1 (2016).

[135] P. Agnes et al.: *Characterization of the scintillation time response of liquid argon detectors for dark matter search* (2021), arXiv: 2110.05350.

[136] A. Hitachi et al.: *Luminescence quenching in liquid argon under charged-particle impact: relative scintillation yield at different linear energy transfers*, *Phys. Rev. B* 46, 11463 (1992).

[137] W.-T. Chen et al.: *Measurement of the transverse diffusion coefficient of charge in liquid xenon*, *Defect and Diffusion Forum* (2011).

[138] J.B. Albert et al. (EXO-200 Collaboration): *Measurement of the drift velocity and transverse diffusion of electrons in liquid xenon with the EXO-200 detector*, *Phys. Rev. C* 95, 025502 (2017).

[139] E. Aprile et al.: *Observation of anti-correlation between scintillation and ionization for MeV gamma-rays in liquid xenon*, *Phys. Rev. B* 76, 014115 (2007).

[140] E. Conti et al.: *Correlated fluctuations between luminescence and ionization in liquid xenon*, *Phys. Rev. B* 68, 054201 (2003).

[141] R.F. Lang et al.: *A next-generation liquid xenon observatory for dark matter and neutrino physics*, *in preparation* (2022).

[142] M. Schumann et al.: *Dark matter sensitivity of multi-ton liquid xenon detectors*, *JCAP* 10, 016 (2015).

[143] V.N. Lebedenko et al. (ZEPLIN Collaboration): *Results from the first science run of the ZEPLIN-III dark matter search experiment*, *Phys. Rev. D* 80, 052010 (2009).

[144] S.A. Malik et al.: *Interplay and characterization of dark matter searches at colliders and in direct detection experiments*, *Physics of the Dark Universe* 9, 51 (2015).

[145] J.B. Dent et al.: *Inverse Primakoff scattering as a probe of solar axions at liquid xenon direct detection experiments*, *Phys. Rev. Lett.* 125, 131805 (2020).

[146] A. Derevianko et al.: *Axio-electric effect*, *Phys. Rev. D* 82, 065006 (2010).

[147] E. Aprile et al. (XENON Collaboration): *First axion results from the XENON100 Experiment*, *Phys. Rev. D* 90, 062009 (2014).

[148] F. Neves et al.: *Measurement of the absolute reflectance of polytetrafluoroethylene (PTFE) immersed in liquid xenon*, *JINST* 12, 01017 (2017).

[149] L. Baudis et al.: *Design and construction of Xenoscope - a full-scale vertical demonstrator for the DARWIN observatory*, *JINST* 16, 08052 (2021).

[150] Hamamatsu Photonics K. K.: *Data sheet: photomultiplier tube R11410-21.*

[151] L. Baudis et al.: *The first dual-phase xenon TPC equipped with silicon photomultipliers and characterisation with* $^{37}Ar$, *Eur. Phys. J. C* 80, 477 (2020).

[152] D. Ferenc et al.: *ABALONE*$^{TM}$ *photosensors for the IceCube experiment*, *Nucl. Instr. Meth. A* 954, 161498 (2018).

[153] E. Erdal et al.: *Recent advances in bubble-assisted liquid hole-multipliers in liquid xenon*, *JINST* 13, 12008 (2018).

[154] International Atomic Energy Agency: *Database of prompt gamma rays from slow neutron capture for elemental analysis*, `https://www-pub.iaea.org/MTCD/Publications/PDF/Pub1263_web.pdf`, accessed: 28 October, 2021.

[155] T. Yano: *Measurement of gamma-ray production from thermal neutron capture on gadolinium for neutrino experiments*, *Nucl. Instr. Meth. A* 845, 425 (2017).

[156] D. Ramírez García: *Monte Carlo simulations of a neutron veto for the XENONnT dark matter experiment*, Master's thesis, Johannes Gutenberg-Universität Mainz, 2017.

[157] M. v. Sivers et al.: *The GeMSE facility for low-background $\gamma$-ray spectrometry*, *JINST* 11, 12017 (2016).

[158] L. Baudis et al.: *Gator: a low-background counting facility at the Gran Sasso Underground Laboratory*, *JINST* 6, 08010 (2011).

[159] D. Budjáš et al.: *Highly sensitive gamma-spectrometers of GERDA for material screening: part 2* (2008), arXiv: 0812.0768.

[160] F. Boehm & P. Vogel: *Physics of massive neutrinos*, *University Press* (1992).

[161] J.B. Albert et al. (EXO-200 Collaboration): *Cosmogenic backgrounds to $0\nu\beta\beta$ in EXO-200*, *JCAP* 04, 029 (2016).

[162] E. Aprile et al. (XENON Collaboration): *Removing krypton from xenon by cryogenic distillation to the ppq level*, *Eur. Phys. J. C* 77, 275 (2017).

[163] E. Aprile et al. (XENON Collaboration): *Conceptual design and simulation of a water Cherenkov muon veto for the XENON1T experiment*, *JINST* 9, 11006 (2014).

[164] D.-M. Mei & A. Hime: *Muon-induced background study for underground laboratories*, *Phys. Rev. D* 73, 053004 (2006).

[165] M. Rajado Nunes da Silva: *Low background rare event searches with liquid xenon detectors*, Master's thesis, Albert-Ludwigs-Universität Freiburg, 2021.

[166] S. Agostinelli et al.: *GEANT4 - a simulation toolkit*, *Nucl. Instr. Meth. A* 506, 250 (2003).

[167] J. Allison et al.: *Recent developments in GEANT4*, *Nucl. Instr. Meth. A* 835, 186 (2016).

[168] E. Aprile et al. (XENON Collaboration): *Physics reach of the XENON1T dark matter experiment*, *JCAP* 04, 027 (2016).

[169] D.G. Madland et al.: *SOURCES 4A: a code for calculating (a,n), spontaneous fission, and delayed neutron sources and spectra*, `https://inis.iaea.org/collection/NCLCollectionStore/_Public/32/027/32027512.pdf?r=1`, accessed: 8 November, 2021.

[170] A. Kish: *Neutron production in materials*, Internal wiki note, 2012.

[171] M. Selvi: *Study of the performances of the shield and muon veto of the XENON1T experiment*, Identification of Dark Matter, Montpellier, France, 2010.

[172] M. Ester et al.: *A density-based algorithm for discovering clusters in large spatial databases with noise*, *KDD Proceedings* 226 (1996).

[173] M. Szydagis et al.: *NEST: a comprehensive model for scintillation yield in liquid xenon*, *JINST* 6, 10002 (2011).

[174] B. Lenardo et al.: *A global analysis of light and charge yields in liquid xenon*, *IEEE Trans. Nucl. Sci.* 62, 6 (2015).

[175] E. Aprile et al. (XENON Collaboration): *Material radioassay and selection for the XENON1T dark matter experiment*, *Eur. Phys. J. C* 77, 890 (2017).

[176] D.S. Akerib et al. (LUX-ZEPLIN Collaboration): *Identification of radiopure titanium for the LZ dark matter experiment and future rare event searches*, *Astroparticle Physics* 96, 1 (2017).

[177] C. Zhang et al.: *Cosmogenic activation of materials used in rare event search experiments*, *Astroparticle Physics* 84, 62 (2016).

[178] J. van Dongen: *Cryostat wall thickness estimation for the 40t DARWIN detector*, Nikhef Mechanical Technology, 2018.

[179] E. Aprile et al. (XENON Collaboration): *Energy resolution and linearity of XENON1T in the MeV energy range*, *Eur. Phys. J. C* 80, 785 (2020).

[180] L.E. Strigari: *Neutrino coherent scattering rate at direct dark matter detectors*, *New J. Phys.* 11, 105011 (2009).

[181] N. Vinyoles et al.: *A new generation of standard solar models*, *Astrophysical Journal* 835, 202 (2017).

[182] J. Aalbers et al.: *wimprates: v0.3.1*, `https://zenodo.org/record/3551727#.YeEwZ3XMJhE`, 2019.

[183] The MACRO Collaboration: *Measurement of the residual energy of muons in the Gran Sasso underground Laboratories*, *Astroparticle Physics* 19, 313 (2003).

[184] M. Haffke et al.: *Background measurements in the Gran Sasso Underground Laboratory*, *Nucl. Instr. Meth. A* 643, 36 (2011).

[185] DARWIN Collaboration, Internal wiki note, 2019.

[186] E. Aprile et al. (XENON Collaboration): *Study of the electromagnetic background in the XENON100 experiment*, *Phys. Rev. D* 83, 082001 (2011).

[187] B.J. Mount et al. (LUX-ZEPLIN Collaboration): *LUX-ZEPLIN (LZ) technical design report* (2017), arXiv: 1703.09144.

[188] K. Lesko: *The Sanford Underground Research Facility at Homestake (SURF)*, *Eur. Phys. J. Plus* 127, 107 (2012).

[189] J. Hall: *The SNOLAB underground laboratory*, *J. Phys.: Conf. Ser.* 1468, 012252 (2020).

[190] J.B. Albert et al. (EXO-200 Collaboration): *Search for neutrinoless double-beta decay with the upgraded EXO-200 detector*, *Phys. Rev. Lett.* 120, 072701 (2018).

[191] R. Arnold et al.: *Probing new physics models of neutrinoless double beta decay with SuperNEMO*, *Eur. Phys. J. C* 70, 927 (2010).

[192] L. Baudis et al.: *Neutrino physics with multi-ton scale liquid xenon detectors*, *JCAP* 01, 044 (2014).

[193] M. Tanabashi et al. (Particle Data Group): *Review of particle physics*, *Phys. Rev. D* 98, 030001 (2018).

[194] J. Ye: *The electronic recoil excess in XENON1T and the prospect to decipher it with XENONnT*, TAUP, 2021.

[195] J. Neyman: *A selection of early statistical papers of J. Neyman*, University of California Press, 2020.

[196] G.J. Feldman & R.D. Cousins: *Unified approach to the classical statistical analysis of small signals*, *Phys. Rev. D* 57, 3873 (1998).

[197] F. Capozzi et al.: *Global constraints on absolute neutrino masses and their ordering*, *Phys. Rev. D* 95, 096014 (2017).

[198] W.J. Marciano & Z. Parsa: *Neutrino-eletron scattering theory*, *J. Phys. G* 29, 2629 (2003).

[199] J.A. Formaggio & G.P. Zeller: *From eV to EeV: neutrino cross sections across energy scales*, *Rev. Mod. Phys.* 84, 1307 (2012).

[200] M. Redchuk et al. (Borexino Collaboration): *Comprehensive measurement of pp-chain solar neutrinos*, *Nature* 562, 505 (2018).

[201] E. Aprile et al. (XENON Collaboration): *$^{222}$Rn emanation measurements for the XENON1T experiment*, *Eur. Phys. J. C* 81, 337 (2021).

[202] E. Aprile et al. (XENON Collaboration): *Intrinsic backgrounds from Rn and Kr in the XENON100 experiment*, *Eur. Phys. J. C* 78, 132 (2018).

[203] S. Bruenner et al.: *Radon daughter removal from PTFE surfaces and its application in liquid xenon detectors*, *Eur. Phys. J. C* 81, 343 (2021).

[204] F. Joerg et al.: *Application of surface coatings for radon mitigation*, Low Radioactivity Techniques, 2019.

[205] K. Abe et al. (XMASS Collaboration): *Radon removal from gaseous xenon with activated charcoal*, *Nucl. Instr. Meth. A* 661, 50 (2012).

[206] M. Arthurs et al.: *Performance study of charcoal-based radon reduction systems for ultraclean rare event detectors*, *JINST* 16, 07047 (2021).

[207] Y. Nakano et al.: *Evaluation of radon adsorption efficiency values in xenon with activated carbon fibers*, *Prog. Theor. Exp. Phys.* 113, 01 (2020).

[208] E. Aprile et al. (XENON Collaboration): *Online $^{222}$Rn removal by cryogenic distillation in the XENON100 experiment*, *Eur. Phys. J. C* 77, 358 (2017).

[209] E. Aprile et al. (XENON Collaboration): *Light dark matter search with ionization signals in XENON1T*, *Phys. Rev. Lett.* 123, 251801 (2019).

[210] A. Kopec et al.: *Correlated single- and few-electron backgrounds milliseconds after interactions in dual-phase liquid xenon time projection chambers*, *JINST* 16, 07014 (2021).

[211] Y. Wei et al.: *Development and performance of a sealed liquid xenon time projection chamber*, *JINST* 16, 01018 (2021).

[212] K. Sato et al.: *Development of dual-phase xenon TPC with a quartz chamber for direct dark matter search*, *Prog. Theor. Exp. Phys.* 113, 02 (2020).

[213] P. Barrow et al.: *Qualification tests of the R11410-21 photomultiplier tubes for the XENON1T detector*, *JINST* 12, 01024 (2017).

[214] COMSOL: *Understand, predict, and optimize physics-based designs and processes with COMSOL Multiphysics®*, `https://www.comsol.com/comsol-multiphysics`, accessed: 1 October, 2021.

[215] I. Kaufmann: *Development of a setup required for filling, operating and recuperating a hermetic TPC*, Bachelor's thesis, Albert-Ludwigs-Universität Freiburg, 2019.

[216] E. Conti: *Collection of xenon properties*, `https://userswww.pd.infn.it/~conti/LXe.html`, accessed: 2 October, 2021.

[217] The Engineering ToolBox: *Linear expansion coefficients*, `https://www.engineeringtoolbox.com/linear-expansion-coefficients-d_95.html`, accessed: 31 October, 2021.

[218] Designerdata: *Data sheet: PTFE*, `https://designerdata.nl/materials/plastics/thermo-plastics/polytetrafluoroethylene-(teflon)`, accessed: 1 November, 2021.

[219] Leybold: *Fundamentals of leak detection*, `https://www.leyboldproducts.com/media/pdf/90/c7/87/Fundamentals_of_Leak_Detection_EN.pdf`, accessed: 31 October, 2021.

[220] P. Meinhardt: *Commissioning, operation, and characterization of a small-scale liquid xenon TPC and R&D studies on single-phase TPC operation*, PhD thesis, Albert-Ludwigs-Universität Freiburg, 2021.

[221] E. Aprile et al. (XENON Collaboration): *Measurements of proportional scintillation and electron multiplication in liquid xenon using thin wires*, *JINST* 9, 11012 (2014).

[222] B. Kaminsky: *Optimizing liquid xenon TPCs*, PhD thesis, Universität Bern, 2017.

[223] Hositrad: *Vacuum components*, `https://www.hositrad.com/`, accessed: 15 October, 2021.

[224] Inc. Cryogenic Control Systems: *Data sheet: Model 22C cryogenic temperature controller*, `https://www.cryocon.com/M22CProdFolder.php`, accessed: 2 October, 2021.

[225] KNF: *Data sheet: PM 28544-022*, `https://knf.com/fileadmin/Global_files/Downloads/Product_OEM_Process/Datasheets/Datenblatt_N_022_N_026_01-2019_web.pdf`, accessed: 3 October, 2021.

[226] Linde: *Data sheet: Entspannungsstation REDLINE® Typ S200*, `http://www.linde-gase.de/produkte/armat/Db-S200.pdf`, accessed: 3 October, 2021.

[227] Swagelok: *VCR components*, `https://www.swagelok.com/`, accessed: 15 October, 2021.

[228] SAES®: *Data sheet: MonoTorr PS3-MT3-R-2*, `https://puregasproducts.com/pdf/L130-013_-_484.pdf`, accessed: 3 October, 2021.

[229] Teledyne Hastings Instruments: *Data sheet: mass flow controller HFC-302*, https://www.schaefer-tec.it/sites/default/files/151-102009%20300_302--flwmtrs-contrllres.pdf, accessed: 3 October, 2021.

[230] *Doberman GitHub respository*, https://github.com/AG-Schumann/Doberman, accessed: 2 October, 2021.

[231] *Pinscher GitHub respository*, https://github.com/AG-Schumann/Pinscher, accessed: 2 October, 2021.

[232] P. Zappa et al.: *A versatile and light-weight slow control system for small-scale applications*, *JINST* 11, 09003 (2016).

[233] J. Grigat: *A robust and versatile slow control system for small- to medium-size experiments*, Master's thesis, Albert-Ludwigs-Universität Freiburg, 2020.

[234] CAEN: *Data sheet: N1470 power supply*, https://www.caen.it/products/n1470/, accessed: 27 October, 2021.

[235] CAEN: *Data sheet: SY5527 power supply*, https://www.caen.it/products/sy5527/, accessed: 27 October, 2021.

[236] CAEN: *Data sheet: V1724 digitizer*, https://www.caen.it/products/v1724/, accessed: 2 October, 2021.

[237] *Strax GitHub respository*, https://github.com/AG-Schumann/strax, accessed: 2 October, 2021.

[238] *Straxbra GitHub respository*, https://github.com/AG-Schumann/straxbra, accessed: 2 October, 2021.

[239] R. Glade-Beucke: *Characterization of XeBRA's dual-phase TPC for DARWIN R&D*, Master's thesis, Albert-Ludwigs-Universität Freiburg, 2021.

[240] L. Althüser et al.: *VUV transmission of PTFE for xenon-based particle detectors*, *JINST* 15, 12021 (2020).

[241] BATRONIX: *Data sheet: Rigol DG1022*, https://www.batronix.com/versand/funktionsgeneratoren/Rigol-DG1022.html, accessed: 5 October, 2021.

[242] R. Saldanha et al.: *Model independent approach to the single photoelectron calibration of photomultiplier tubes*, *Nucl. Instr. Meth. A* 863, 35 (2017).

[243] A. Manalaysay et al.: *Spatially uniform calibration of a liquid xenon detector at low energies using 83m-Kr*, *Rev. Sci. Intr.* 81, 073303 (2010).

[244] L.W. Kastens et al.: *Calibration of a liquid xenon detector with Kr-83m*, *Phys. Rev. C* 80, 045809 (2009).

[245] A. Chan et al. (DELPHI collaboration): *Performance of the HPC calorimeter in DELPHI*, *IEEE Trans. Nucl. Sci.* 42, 491 (1995).

[246] L. Baudis et al.: *Response of liquid xenon to Compton electrons down to 1.5 keV*, *Phys. Rev. D* 87, 115015 (2013).

[247] J. Aalbers: *Dark matter search with XENON1T*, PhD thesis, Universiteit van Amsterdam, 2018.

[248] E. Aprile et al. (XENON Collaboration): *Observation and applications of single-electron charge signals in the XENON100 Experiment*, *J. Phys. G: Nucl. Part. Phys.* 41, 035201 (2014).

[249] E. Aprile et al. (XENON Collaboration): *Analysis of the XENON100 dark matter search data*, *Astroparticle Physics* 54 (2014).

[250] F. Joerg et al.: *Characterization of alpha and beta interactions in liquid xenon* (2021), arXiv: 2109.13735.

[251] L. Baudis et al.: *A dual-phase xenon TPC for scintillation and ionisation yield measurements in liquid xenon*, *Eur. Phys. J. C* 78, 351 (2018).

[252] L.S. Miller et al.: *Charge transport in solid and liquid ar, kr and xe*, *Phys. Rev.* 166, 871 (1968).

[253] E. Gushchin et al.: *Emission of 'hot' electrons from liquid and solid argon and xenon*, *Sov. Phys. JETP* 55, 650 (1982).

[254] P. Sorensen: *Anisotropic diffusion of electrons in liquid xenon with application to improving the sensitivity of direct dark matter searches*, *Nucl. Instr. Meth. A* 635, 41 (2011).

[255] E. Hogenbirk et al.: *Field dependence of electronic recoil signals in a dual-phase liquid xenon time projection chamber*, *JINST* 13, 10031 (2018).

[256] O. Njoya et al.: *Measurements of electron transport in liquid and gas xenon using a laser-driven photocathode*, *Nucl. Instr. Meth. A* (2020).

[257] E. Grace et al.: *Index of refraction, Rayleigh scattering length, and Sellmeier coefficients in solid and liquid argon and xenon*, *Nucl. Instr. Meth. A* 867, 204 (2017).

[258] A. Bismark: *Simulation and characterization of a LXe TPC for DARWIN R&D*, Master's thesis, Albert-Ludwigs-Universität Freiburg, 2019.

[259] T. Doke et al.: *Estimation of Fano factors in liquid argon, krypton, xenon and xenon-doped liquid argon*, *Nucl. Instr. Meth.* 134, 353 (1976).

[260] E. Dahl: *The physics of background discrimination in liquid xenon, and first results from XENON10 in the hunt for WIMP dark matter*, PhD thesis, Princeton University, 2009.

[261] G. Anton et al. (EXO-200 Collaboration): *Measurement of the scintillation and ionization response of liquid xenon at MeV energies in the EXO-200 experiment*, *Phys. Rev. C* 101, 065501 (2020).

[262] L. Baudis et al.: *A measurement of the mean electronic excitation energy of liquid xenon*, *Eur. Phys. J. C* 81, 1060 (2021).

[263] E. Aprile et al. (XENON Collaboration): *Signal yields of keV electronic recoils and their discrimination from nuclear recoils in liquid xenon*, *Phys. Rev. D* 97, 092007 (2018).

[264] D.S. Akerib et al. (LUX Collaboration): *Tritium calibration of the LUX dark matter experiment*, *Phys. Rev. D* 93, 072009 (2016).

[265] E. Aprile et al. (XENON Collaboration): *The XENON1T dark matter experiment*, *Eur. Phys. J. C* 77, 881 (2017).

[266] D.S. Akerib et al. (LUX Collaboration): *Improved limits on scattering of weakly interacting massive particles from reanalysis of 2013 LUX data*, *Phys. Rev. Lett.* 116, 161301 (2016).

[267] K. Abe et al. (XMASS Collaboration): *Development of low radioactivity photomultiplier tubes for the XMASS-I detector*, *Nucl. Instr. Meth. A* 922, 171 (2019).

[268] P.-A. Amaudruz et al. (DEAP collaboration): *Design and construction of the DEAP-3600 dark matter detector*, *Astroparticle Physics* 108, 1 (2019).

[269] E. Aprile et al. (XENON Collaboration): *Application and modeling of an online distillation method to reduce krypton and argon in XENON1T* (2021), arXiv: 2112.12231.

[270] X. Cui et al.: *Design and commissioning of the PandaX-4T cryogenic distillation system for krypton and radon removal*, *JINST* 16, 07046 (2021).

# Acknowledgements

The years of my Ph.D. studies have been a wonderful experience and I am very grateful for the people I have met and the knowledge they have shared with me. Since writing this thesis would not have been possible without the help of others, I dedicate this last page to thank everybody who gave important input. Not everyone is mentioned by name since I want to keep this page directly work-related; however, I also appreciate the contributions of many other people.

First of all, I would like to express my special appreciation and thanks to Prof. Dr. Marc Schumann, who gave me the great opportunity to be part of his working group. His detailed knowledge and experience, as well as his trust in my work and continuous support have been the basis for the success of this thesis. Also, I am deeply grateful to apl. Prof. Dr. Horst Fischer for his motivating words to push for more. I would not have started these Ph.D. studies without his advice years ago and I am still delighted to have listened to him! I want to extend my thanks to Dr. Fabian Kuger for his continuous supervision and support. I have benefited greatly from the numerous discussions and his deep physical understanding taught me to always question and interpret results.

Moreover, many thanks go to all the other members of the Freiburg Astroparticle Physics group, of which I am proud to be part! Thanks to my office mates Daniel, Justin, and Patrick for their permanent support and helpful discussions; to Mariana for joining the HUsXe project and her work on the $0\nu$ECEC; to Jaron for his frequent help with slow control issues; to Robin for his input on the HUsXe data analysis; to Diego and Matthias for their help on MC- and computing-related questions, respectively, and to the rest of the working group Adam, Alexey, Arianna, Darryl, Fairhurst, Florian, Francesco, Julia, and Sebastian for many discussions and suggestions in meetings, proofreading this thesis, and all the detector shifts they took over. I enjoyed working with all of them and appreciated the friendly and cooperative atmosphere very much!

I would also like to thank the DARWIN Collaboration, particularly the members of the simulation group. Their feedback has been very valuable and their help enabled the investigation of the many science channels presented in this thesis.

Lastly, a big thank you also goes to the entire mechanical workshop of the physics institute for manufacturing HUsXe. Thanks for the great and detailed work, as well as for repeatedly enabling short-term changes.